**UC Santa Barbara**
**UC Santa Barbara Electronic Theses and Dissertations**

**Title**

Dopant Transport and Distribution in Semicrystalline Conductive Polymers

**Permalink**

https://escholarship.org/uc/item/6m31714m

**Author**

Nguyen, Phong Hien

**Publication Date**

2023

Peer reviewed|Thesis/dissertation

eScholarship.org Powered by the California Digital Library
University of California

UNIVERSITY OF CALIFORNIA

Santa Barbara

# Dopant Transport and Distribution in Semicrystalline Conductive Polymers

A dissertation submitted in partial satisfaction of the
requirements for the degree Doctor of Philosophy
in Chemical Engineering

by

Phong Hien Nguyen

Committee in charge:

Professor Michael L. Chabinyc, Co-Chair

Professor Rachel A. Segalman, Co-Chair

Professor Christopher M. Bates

Professor Glenn H. Fredrickson

March 2024

The dissertation of Phong Hien Nguyen is approved.

Professor Glenn H. Fredrickson

Professor Christopher M. Bates

Professor Rachel A. Segalman, Committee Co-Chair

Professor Michael L. Chabinyc, Committee Co-Chair

December 2023

Dopant Transport and Distribution in Semicrystalline Conductive Polymers

Copyright © 2024

by

Phong Hien Nguyen

# Acknowledgements

Thank you to my loved ones, family members, colleagues, mentors, and friends. Your unending support during this period of my life has made this accomplishment just as much yours as it is mine.

# Curriculum Vitae

Phong Hien Nguyen

December 2023

## EDUCATION

Doctor of Philosophy in Chemical Engineering, University of California, Santa Barbara, May 2024 (expected)

Bachelor of Science in Chemical Engineering, University of Missouri, Columbia, May 2019

## PROFESSIONAL EMPLOYMENT

2019-2023: Teaching Assistant, Department of Chemical Engineering, University of California, Santa Barbara

## AWARDS

| | |
|---|---|
| National Science Foundation Graduate Research Fellowship | Sept. 2021- Dec. 2023 |

## PUBLICATIONS

14. **Nguyen, P. H.**; Callan, D. H.; Plunkett, E. C.; Gruschka, M.; Alizadeh, N.; Landsmann, M. R.; Su, G.; Gann, E.; Bates, C. M.; Delongchamp, D.; Chabinyc, M. L. Dopant Distributions in Semicrystalline Conjugated Polymers from Resonant X-Ray Scattering. In preparation.

13. Choi, Y-J.; Warnock, S.; Alizadeh, N.; **Nguyen, P. H.**; Kottage, D.; Phillips, O.; Chen, Z.; Chabinyc, M. L.; Bates, C. M. Acid-Sensitive Molecular Glasses as Removable Thin-Film Protective Layers. *Chem. Mater.* **2023**, *35* (23), 10078-10085.

12. Oh, S.; **Nguyen, P. H.**; Tran, T. M.; DeStefano, A. J.; Tagami, K.; Yuan, D.; Nikolaev, A.; Condarcure, M.; Han, S.; Alaniz, J. R. de; Chabinyc, M. L. Interfacial Doping of Semiconducting Polymers with Phenothiazine-Based Polymeric Ionic Liquids. *J. Mater. Chem. C* **2023**, *11* (44), 15435-15442.

11. Pace, G.; Zele, A.; **Nguyen, P. H.**; Clément, R. J.; Segalman, R. A. Mixed Ion–Electron-Conducting Polymer Complexes as High-Rate Battery Binders. *Chem. Mater.* **2023**, *35* (19), 8101–8111.

10. Le, M. L.; Lapkriengkri, I.; Albanese, K. R.; **Nguyen, P. H.**; Tran, C.; Blankenship, J. R.; Segalman, R. A.; Bates, C. M.; Chabinyc, M. L. Engineering Soft, Elastic, and Conductive Polymers for Stretchable Electronics Using Ionic Compatibilization. *Chem. Mater.* **2023**, *35* (17), 7301–7310.

9. Pace, G.; Nordness, O.; **Nguyen, P. H.**; Choi, Y.-J.; Tran, C.; Clément, R. J.; Segalman, R. A. Tuning Transport via Interaction Strength in Cationic Conjugated Polyelectrolytes. *Macromolecules* **2023**, *56* (15), 6078–6085.

8. **Nguyen, P. H.***; Scheuermann, A. M.*; Nikolaev, A.; Chabinyc, M. L.; Bates, C. M.; Read de Alaniz, J. Reversible Modulation of Conductivity in Azobenzene Polyelectrolytes Using Light. *ACS Appl. Polym. Mater.* **2023**, *5* (7), 4698-4703. (*equal contribution)

7. **Nguyen, P. H.**; Schmithorst, M. B.; Mates, T. E.; Segalman, R. A.; Chabinyc, M. Diffusion of Brønsted Acidic Dopants in Conjugated Polymers. *J. Mater. Chem. C* **2023**, *11* (22), 7462–7470.

6. Yuan, D.; Plunkett, E.; **Nguyen, P. H.**; Rawlings, D.; Le, M. L.; Kroon, R.; Müller, C.; Segalman, R. A.; Chabinyc, M. L. Double Doping of Semiconducting Polymers Using Ion-Exchange with a Dianion. *Advanced Functional Materials* **2023**, *33* (29), 2300934.

5. Zokaei, S.; Kim, D.; Järsvall, E.; Fenton, A. M.; Weisen, A. R.; Hultmark, S.; **Nguyen, P. H.**; Matheson, A. M.; Lund, A.; Kroon, R.; Chabinyc, M. L.; Enrique, G. D.; Zozoulenko, I.; Müller, C. Tuning of the Elastic Modulus of a Soft Polythiophene through Molecular Doping. *Materials Horizons* **2022**, *9* (1), 433–443.

4. Thomas, E. M.; **Nguyen, P. H.**; Jones, S. D.; Chabinyc, M. L.; Segalman, R. A. Electronic, Ionic, and Mixed Conduction in Polymeric Systems. *Annual Review of Materials Research* **2021**, *51* (1), 1–20.

3. Torres Dominguez, E.; **Nguyen, P. H.**; Hylen, A.; Maschmann, M. R.; Mustapha, A.; Hunt, H. K. Design and Characterization of Mechanically Stable, Nanoporous TiO2 Thin Film Antimicrobial Coatings for Food Contact Surfaces. *Materials Chemistry and Physics* **2020**, *251*, 123001.

2. Beaudette, C. A.; Held, J. T.; Greenberg, B. L.; **Nguyen, P. H.**; Concannon, N. M.; Holmes, R. J.; Mkhoyan, K. A.; Aydil, E. S.; Kortshagen, U. R. Plasmonic Nanocomposites of Zinc Oxide and Titanium Nitride. *Journal of Vacuum Science & Technology A* **2020**, *38* (4), 042404.

1. Torres Dominguez, E.; **Nguyen, P. H.**; Hunt, H. K.; Mustapha, A. Antimicrobial Coatings for Food Contact Surfaces: Legal Framework, Mechanical Properties, and Potential Applications. *Comprehensive Reviews in Food Science and Food Safety* **2019**, *18* (6), 1825–1858.

# Abstract

Dopant Transport and Distribution in Semicrystalline Conductive Polymers

by

Phong Hien Nguyen

Ionically and electronically conducting polymers are celebrated for their distinct electronic characteristics, flexibility, and processability, making them vital in diverse fields such as ion exchange membranes, energy devices, and biomedical technologies. This dissertation delves into polymeric charge conduction materials, distinguishing them based on the type of charge carriers involved: ions, electronic charge carriers (polarons), or a combination of both. The study differentiates between electronic doping, which introduces polaronic and ionic charges, and purely ionic doping, achieved by adding small-molecule salts to introduce ionic charges. The first section of the study explores the structure-property relationships, illustrating how disordered polymer domains are linked to ionic charge carrier conduction and ordered domains to electronic conductivity. This section emphasizes the significance of the coexistence of these different phases within a single material, which facilitates mixed conduction.

A focal point of the research is the investigation of doping processes in polymers. The dissertation's second chapter examines the nuances of electronic doping, particularly the mechanisms of Brønsted acid-induced oxidation in conjugated polymer thin films. This investigation reveals that such doping leads to self-limiting diffusion, resulting in stable dopant concentration gradients, optimal for creating heterojunctions. Subsequently, the dissertation pivots to polyelectrolyte design, examining the interactions between ionic charge carriers ($Li^+$) and photoresponsive azo moieties attached to a polymer backbone. A notable discovery here is that semicrystalline polymers can achieve up to sevenfold higher conductivity than their amorphous counterparts due to $Li^+$ complexation, challenging the conventional wisdom that favors disorder for enhanced ionic conductivity. The final major contribution of this work is the development of resonant scattering techniques for simultaneous examination of both amorphous and crystalline domains in polymers. This method provides deep insights into the dopant ion distribution within different polymer domains. The research establishes a methodology for predicting polarized resonant soft X-ray scattering contrast, which resolves aspects of structure, orientation, and chemistry. The findings indicate that dopant counterions preferentially localize within ordered domains at equilibrium, with variations in localization dependent on dopant concentrations and chemical structure. In summary, this dissertation significantly advances our understanding of dopant-polymer interactions in ionically and electronically conducting polymers, highlighting the complex interplay between structure and function in these materials and marking a noteworthy advancement in the field of conductive polymers.

TABLE OF CONTENTS

Acknowledgements....................iv

Curriculum Vitae....................v

Abstract.................... vii

Chapter 1 – Introduction....................1

1.1 Abstract....................1

1.2 Introduction....................1

1.3 The principles of mixed conduction....................4

1.3.1 Transport fundamentals....................4

1.3.2 Ionically conducting polymers....................9

1.3.3 Electronically conducting polymers....................15

1.4 Ionic, electronic, and mixed conduction figures of merit....................21

1.4.1 Ionic transport....................21

1.4.2 Electronic transport....................22

1.4.3 Mixed conducting systems....................23

1.4.4 Measurement methods....................27

1.5 Emerging areas in mixed conduction....................29

1.5.1 Dynamic structural and morphological disorder....................29

1.5.2 Dielectric environment....................31

1.5.3 Mechanical properties....................32

1.6 Conclusions....................33

1.7 Acknowledgements....................33

Chapter 2 – Diffusion of Brønsted Acidic Dopants in Conjugated Polymers....................35

2.1 Abstract 35

2.2 Introduction 36

2.3 Results and Discussion 38

- 2.3.1 Diffusion-limited thickness dependence of electrical conductivity 38
- 2.3.2 Model of the Brønsted acidic doping process 40
- 2.3.3 Reaction rate in the absence of diffusion limitations 44
- 2.3.4 Stable dopant concentration gradients from diffusion-limited doping 48
- 2.3.5 Diffusion-reaction limited doping with increased film thickness 51
- 2.3.6 Dopant transport limitations from concentration depth profiles 54
- 2.3.7 Doping-induced structural changes at film surfaces 56

2.4 Conclusions 59

2.5 Acknowledgements 60

2.6 Appendix 61

- 2.6.1 Experimental methods 61
- 2.6.2 Kinetic models applied to UV-vis spectroscopy 63
- 2.6.3 High depth resolution DSIMS quantified via XPS 64
- 2.6.4 CP/MAS NMR of P3HT and Brønsted acid-doped P3HT 70
- 2.6.5 Angle-Resolved GIWAXS of H/DTFSI-doped P3HT films 72
- 2.6.6 AFM-measured texture of pristine and profiled P3HT films 74

Chapter 3 – Reversible Modulation of Conductivity in Azobenzene Polyelectrolytes using Light 77

3.1 Abstract 77

3.2 Introduction 78

3.3 Results and Discussion ....................................................................79

3.3.1 Design and Synthesis of Azobenzene-Containing Polymeric Ionic Liquids ....................................................................................79

3.3.2 Photoisomerization of Poly(azobenzene) and Poly(azo-*co*-IL)..81

3.3.3 Azobenzene Enables Reversible, Light-Mediated Ionic Conductivity in Polyelectrolytes...................................................................................83

3.3.4 Ionic Liquid Incorporation Reduces Azobenzene *Cis*-Isomer Metastability ........................................................................................84

3.3.5 Proposed Azo-Ion Coordination ...............................................86

3.4 Conclusions.........................................................................................88

3.5 Acknowledgments ..............................................................................88

3.6 Appendix............................................................................................89

3.6.1 Experimental Methods.............................................................89

3.6.2 Synthesis of Poly(azobenzene) and Poly(azo-*co*-IL) ................90

3.6.3 Reactivity Ratios in Copolymerization of PFPA and AzoAcMe103

3.6.4 Differential Scanning Calorimetry of Poly(azobenzene) and Poly(azo-*co*-IL) .....................................................................................104

3.6.5 Impedance Spectroscopy of Poly(azobenzene) and Poly(azo-*co*-IL) Thin Films ...............................................................................106

3.6.6 UV–Visible Spectroscopy of Poly(azobenzene) and Poly(azo-*co*-IL) Thin Films.......................................................................109

Chapter 4 – Dopant Distributions in Semicrystalline Conjugated Polymers from Resonant X-Ray Scattering...............................................................................113

4.1 Abstract........................................................................................113

4.2 Introduction.....................................................................................114

4.4 Results and Discussion ....................................................................118

4.4.1 P3HT Films with Controlled Crystallinity and Dopant Counterion Identity..............................................................................................118

4.4.2 Dopant Uptake with Varying Crystallinity and Counterion Identity ..........................................................................................................121

4.4.3 Scattering Anisotropy as a Measure of Bonding, Morphology, and Molecular Orientation of Doped P3HT Films ..................................123

4.4.4 Orientational Self-Contrast Between Fibrillar Crystals...........125

4.4.5 Experimental Scattering Anisotropy Varies with Crystallinity and Dopant Identity ...................................................................................129

4.4.6 Modelling Dopants in Semicrystalline Polymers .....................133

4.4.7 Simulation-Aided Interpretation of Scattering Anisotropy ......136

4.5 Conclusions......................................................................................141

4.6 Appendix..........................................................................................142

4.6.1 Materials and Methods ...........................................................142

4.6.8 Summary of P3HT Blend Composition, Crystallinity, and Dopant Counterion Concentration...................................................................146

4.6.9 Atomic Force Microscopy of Least and Most Crystalline P3HT Blend ..........................................................................................................147

4.6.10 X-Ray Photoelectron Spectroscopy Depth Profiling of Doped P3HT Films ..................................................................................................148

4.6.11 Atomic Force Microscopy of $F_4$TCNQ Vapor-Doped and $TFSI^-$ Anion Exchanged Films ........................................................................151

4.6.12 XPS Survey Spectra of $F_4$TCNQ Surface Layer on P3HT.....152

4.6.13 Fibril Orientations from Grazing Incidence Wide Angle X-Ray Scattering (GIWAXS) ........................................................................153

4.6.14 Simulated Near edge X-ray Absorbance Fine Spectra ...........158

4.6.15 Comparisons of Simulated and Experimentally Measured NEXAFS ........................................................................171

4.6.16 Effect of Annealing on Scattering Anisotropy .......................182

4.9.17 Experimental Scattering Anisotropy Across Blends and Doping183

4.6.18 Simulated Scattering Anisotropy Versus Dopant Distribution and Orientation ........................................................................186

Chapter 5 – Conclusions and Future Outlook..........................................................190

References........................................................................................................193

# LIST OF FIGURES

Figure 1. Polymer ion conduction mechanisms........................................................11

Figure 2. Temperature dependence of ion conduction mechanisms...........................13

Figure 3. Morphology of conjugated polymer crystallites .........................................17

Figure 4. Interfacial capacitance between crystalline and amorphous domains..........25

Figure 5. Platforms to characterize electronic and ionic transport .............................26

Figure 6. Dopant-induced ordering of regiorandom P3HT from GIWAXS ...............31

Figure 7. Schematic of immersion doping process....................................................38

Figure 8. Thickness dependent conductivity of immersion doped P3HT ...................39

Figure 9. Proposed mechanism of Brønsted acid doping ...........................................41

Figure 10. HTFSI immersion doping kinetics from *in-situ* UV-vis absorbance spectroscopy. ..........................................................................................................45

Figure 11. Concentration depth profiles of immersion doped P3HT films .................49

Figure 12. Diffusion-limited Brønsted acidic doping reaction fitting .........................52

Figure 13. Anomalous diffusion from time-correlated dopant uptake ........................54

Figure 14. Angle-dependent GIWAXS of surface-doped P3HT.................................58

Figure 15. Comparison of numerical and analytic kinetic model fits..........................63

Figure 16. Comparison of DSIMS and XPS fluorine depth profiles...........................65

Figure 17. Concentration depth profiles of H/DTFSI immersion-doped P3HT films.66

Figure 18. D retention in DTFSI-doped P3HT films..................................................67

Figure 19. Concentration depth profile comparisons between DTFSI-doped annealed and unannealed P3HT films .........................................................................68

Figure 20. TFSI$^-$ diffusion in surface-doped P3HT past 1 week ................................69

Figure 21. Solid state CP/MAS $^1H \rightarrow ^{13}C$ NMR spectra of pristine and HTFSI-doped P3HT ........................................................................................................70

Figure 22. Angle-Resolved GIWAXS for H/DTFSI-doped P3HT films ...................72

Figure 23. Radially integrated scattering peaks from GIWAXS measurements of P3HT films doped with HTFSI from the vapor phase. .........................................................74

Figure 24. AFM of pristine and sputtered HTFSI-doped P3HT film surfaces...........75

Figure 25. AFM of pristine and sputtered DTFSI-doped P3HT film surfaces...........76

Figure 26. A four-step synthesis of the poly(azo-*co*-IL) from AzoAcMe and PFPA. 81

Figure 27. UV-vis absorbance spectra of cis and trans poly(azo-*co-IL)* ....................82

Figure 28. Conductivity of *cis*/*trans* poly(azobenzene) and poly(azo-*co*-IL) ............84

Figure 29. Time-resolved conductivity relaxation of cis poly(azobenzene) and poly(azo-*co*-IL) ..........................................................................................................85

Figure 30. Bathochromic shifts in *cis* poly(azobenzene) and poly(azo-*co*-IL) absorbance due to ion coordination ..........................................................................87

Figure 31. Multi-step synthesis of AzoAcMe..........................................................90

Figure 32. $^1H$ NMR spectrum of Azo-Me-OH in $CDCl_3$. ..........................................91

Figure 33. $^1H$ NMR spectrum of Ac-Br in $CDCl_3$.....................................................92

Figure 34. $^1H$ (top) and $^{13}C[^1H]$ (bottom) NMR spectra of AzoAcMe in $CDCl_3$........94

Figure 35. Mass spectra of AzoAcMe. .....................................................................95

Figure 36. FT-IR spectra of AzoAcMe.......................................................................95

Figure 37. Free-radical polymerization of AzoAcMe to poly(azobenzene)...............96

Figure 38. $^1H$ NMR spectrum of the poly(azobenzene) in $CDCl_3$. ............................97

Figure 39. SEC of poly(azobenzene) .......................................................................97

Figure 40. Polymerization of PFPA and AzoAcMe measured using $^{19}$F and $^{1}$H NMR98

Figure 41. $^{1}$H NMR spectrum of the poly(azo-*co*-PFPA). ........................................99

Figure 42. $^{19}$F NMR spectrum of poly(azo-*co*-PFPA) ..............................................100

Figure 43. $^{1}$H NMR spectrum of the poly(azo-*co*-IL) in $CDCl_3$. ..............................101

Figure 44. $^{19}$F NMR spectrum of the poly(azo-*co*-IL) .............................................102

Figure 45. SEC of poly(azo-*co*-PFPA) and poly(azo-*co*-IL) ....................................103

Figure 46. Reactivity ratios of PFPA and AzoAcMe ...............................................104

Figure 47. $T_g$ of poly(azobenzene) and poly(azo-*co*-IL) .........................................105

Figure 48. DSC traces of poly(azobenzene) and poly(azo-*co*-IL) ............................105

Figure 49. Microscope images of poly(azobenzene) and poly(azo-*co*-IL) on interdigitated electrode array ..........................................................................................107

Figure 50. Equivalent circuit fits to poly(azobenzene) and poly(azo-*co*-IL) Nyquist impedance spectra ..........................................................................................................108

Figure 51. Constant phase element evolution due to *cis* poly(azobenzene) relaxation109

Figure 52. UV-vis absorbance spectra of as-cast, *cis*, and *trans* poly(azobenzene) and poly(azo-*co*-IL) ..........................................................................................110

Figure 53. Relaxation of *cis* poly(azobenzene) and poly(azo-*co*-IL) via time-resolved UV-vis spectroscopy ...........................................................................................112

Figure 54. Schematic of possible dopant distributions .............................................118

Figure 55. Control over aggregation via regio-regular/random P3HT blend composition assessed from UV-vis absorbance spectra .........................................................120

Figure 56. Schematic depiction of $F_4$TCNQ vapor doping and TFSI$^-$ anion exchange processes with corresponding dopant concentrations as a function of sample crystallinity121

Figure 57. Experimental scattering anisotropy of P3HT ........................................124

Figure 58. Comparisons between observed and possible sources of p-RSoXS scattering contrast.........................................................................................................127

Figure 59. (a) Experimental scattering anisotropy across crystallinity and dopant counterion identity. ....................................................................................................131

Figure 60. RSoXS simulation process involving a multi-step workflow. ................133

Figure 61. Comparisons between experimentally observed and simulated P3HT morphology. ..........................................................................................................135

Figure 62. Comparison of experimental and simulated scattering anisotropy in 37% crystalline P3HT films...........................................................................................137

Figure 63. Comparison of experimental and simulated scattering anisotropy in 37% crystalline P3HT films with varying $F_4TCNQ^{\bullet-}$ orientations relative to P3HT. ................140

Figure 64. Atomic force micrographs of least crystalline and most crystalline P3HT blend films demonstrating similar fibril dimensions. ................................................147

Figure 65. XPS Depth Profile of LiTFSI Exchanged, 100% Regioregular P3HT Film148

Figure 66. Quantified XPS Depth Profile of F4TCNQ Vapor Doped P3HT ...........149

Figure 67. Quantified XPS Depth Profile of Doped, TFSI- Anion Exchanged P3HT149

Figure 68. $F_4$TCNQ Vapor Doped P3HT and TFSI$^-$ Anion Exchanged Film Surface Texture from AFM Phase Contrast Images. .................................................................151

Figure 69. XPS Survey Spectra at $F_4$TCNQ Vapor-Doped Film Top Surface and Mid-Depth, Showing Excess $F_4$TCNQ at Sample Surface. ................................................152

Figure 70. 2D scattering pattern of P3HT under grazing incidence geometry. .........153

Figure 71. Shallow Angle GIWAXS Orientation Distributions ...............................154

Figure 72. Critical Angle GIWAXS Orientation Distributions ................................155

Figure 73. Deep Angle GIWAXS Orientation Distributions....................................156

Figure 74. Effect of $\theta$ Orientation Distribution ........................................................157

**Figure 75. $\pi$-Stacked P3HT Crystallite, Γ Point Sampling Only C K edge NEXAFS.** ..........................................................................................................158

Figure 76. $\pi$-Stacked P3HT Crystallite, $2 \times 2 \times 2$ $k$-Point Grid Sampling C K edge NEXAFS ..........................................................................................................160

Figure 77. Single P3HT Chain, $\Gamma$ Point Sampling Only C K edge NEXAFS ..........162

Figure 78. Single P3HT Chain, $2 \times 2 \times 2$ $k$-Point Grid Sampling C K edge NEXAFS164

Figure 79. $F_4$TCNQ C K Edge NEXAFS .................................................................166

Figure 80. $F_4$TCNQ$^{\bullet-}$ C K Edge NEXAFS ...............................................................168

Figure 81. TFSI$^-$ C K Edge NEXAFS .....................................................................170

Figure 82. P3HT C K Edge NEXAFS Comparisons.................................................171

Figure 83. P3HT S K Edge NEXAFS Comparisons ................................................172

Figure 84. $F_4$TCNQ C K Edge NEXAFS Comparisons...........................................173

Figure 85. $F_4$TCNQ N K Edge NEXAFS Comparisons...........................................174

Figure 86. $F_4$TCNQ F K Edge NEXAFS Comparisons ...........................................175

Figure 87. $F_4$TCNQ$^{\bullet-}$ C K Edge NEXAFS Comparisons .........................................176

Figure 88. $F_4$TCNQ$^{\bullet-}$ N K Edge NEXAFS Comparisons .........................................177

Figure 89. $F_4$TCNQ$^{\bullet-}$ F K Edge NEXAFS Comparisons..........................................178

Figure 90. TFSI$^-$ C K Edge NEXAFS Comparisons ................................................179

Figure 91. TFSI$^-$ N K Edge NEXAFS Comparisons ................................................ 180

Figure 92. TFSI$^-$ F K Edge NEXAFS Comparisons ................................................ 181

Figure 93. Effect of sample annealing (120 °C, 2 hours under an inert nitrogen atmosphere) on scattering anisotropy. ...................................................................... 182

Figure 94. C K Edge Scattering Anisotropy ............................................................ 183

Figure 95. N K Edge Scattering Anisotropy ............................................................ 184

Figure 96. F K Edge Scattering Anisotropy ............................................................ 184

Figure 97. Simulated Scattering Anisotropy Versus Dopant Distribution and Orientation for Doped P3HT at the C K-Edge ........................................................................ 186

Figure 98. Simulated Scattering Anisotropy Versus Dopant Distribution and Orientation for Doped P3HT at the C K-Edge ........................................................................ 187

Figure 99. Simulated Scattering Anisotropy Versus Dopant Distribution and Orientation for Doped P3HT at the C K-Edge ........................................................................ 188

## Permissions

Parts of this dissertation were reproduced in part with permissions from:

(1) Thomas, E. M.; Nguyen, P. H.; Jones, S. D.; Chabinyc, M. L.; Segalman, R. A. Electronic, Ionic, and Mixed Conduction in Polymeric Systems. *Annual Review of Materials Research* **2021**, *51* (1), 1–20. https://doi.org/10.1146/annurev-matsci-080619-110405.

(2) Nguyen, P. H.; Schmithorst, M. B.; Mates, T. E.; Segalman, R. A.; Chabinyc, M. Diffusion of Brønsted Acidic Dopants in Conjugated Polymers. *Journal of Materials Chemistry C* **2023**, *11* (22), 7462–7470. https://doi.org/10.1039/D3TC00415E.

(3) Nguyen, P. H.*; Scheuermann, A. M.*; Nikolaev, A.; Chabinyc, M. L.; Bates, C. M.; Read de Alaniz, J. Reversible Modulation of Conductivity in Azobenzene Polyelectrolytes Using Light. *ACS Appl. Polym. Mater*. **2023**, *5* (7), 4698-4703. https://doi.org/10.1021/acsapm.3c00265. (*equal contribution)

# Chapter 1 – Introduction

This chapter was reproduced in part with permissions from:

> Thomas, E. M.; Nguyen, P. H.; Jones, S. D.; Chabinyc, M. L.; Segalman, R. A. Electronic, Ionic, and Mixed Conduction in Polymeric Systems. *Annual Review of Materials Research* **2021**, *51* (1), 1–20.

## 1.1 Abstract

Polymers that simultaneously transport electrons and ions are paramount to drive the technological advances necessary for next-generation electrochemical devices including energy storage devices and bioelectronics. However, efforts to describe the motion of ions or electrons separately within polymeric systems become inaccurate when both species are present. Herein, we highlight the basic transport equations necessary to describe mixed transport and the multi-scale materials properties that influence their transport coefficients. Potential figures of merit are discussed that enable a suitable performance benchmark in mixed conducting systems, independent of end application. Practical design and implementation of mixed conducting polymers requires understanding the evolving nature of structure and transport with ionic and electronic carrier density to capture the dynamic disorder inherent in polymeric materials.

## 1.2 Introduction

The simultaneous transport of both electrons and ions is fundamental to the electrochemical processes that drive energy generation and storage devices. Several reviews have highlighted other applications for which mixed conduction is critical,[1,2] including polymer-based transistors,[3] supercapacitors,[4] and electrochromic devices.[5] Despite the potential for polymeric mixed conductors in these applications, a holistic understanding of how two charged components conduct in a materials system remains limited. Part of the knowledge gap arises from the unshared language between research communities. The design rules for ion conduction are different than those for electronic conduction, which leads to difficulty when the conduction of both carriers is necessary.

Polymers, historically considered insulating, are very different from their conducting ceramic and metallic counterparts. Their mechanical properties and processability make them especially promising for improving device design. Because of their unique conduction mechanisms, how these factors affect their ability to conduct both ions and electrons is not fully understood. The molecular design of these systems has primarily focused on the optimization of electronic properties in the absence of ionic motion, or the opposite. Current design rules for polymers with high ionic or electronic mobility stem from studying these charged species separately. Ionic conductivity is highly related to polymer segmental motion and is therefore dominated by motion through the amorphous fraction of a semicrystalline polymer.[6] Conversely, electronic mobility is highest in more ordered domains of the polymer, generally along a $\pi$-stacked direction of crystallinity.[7–9] A critical challenge is to understand if conduction of two charge carrier types simply requires optimization of their orthogonal design requirements, a heterogeneous material with optimized charge pathways, or a synergy between these conduction mechanisms.

Multicomponent mixed conducting polymer systems are often tailored to perform in hydrated, dry, or other environments. Differences in the intended application make it difficult to develop robust design principles that encapsulate the features of mixed conduction. The presence and concentration of added salt, solvent, water, and polymer in a given mixed conducting system will impact the transport mechanisms for both the electrons and ions. For example, aqueous systems such as hydrogels, polyelectrolytes, and PEDOT:PSS, typically exhibit ionic conductivity greater than $10^{-3}$ S/cm, but the conductivity drops precipitously as the water content decreases below 50% by weight.[10] Designs based on block copolymers,[11–13] polymer blends,[14,15] and homopolymers[16,17] with mixed ionic and electronic functionality have all been proposed. We choose not to focus on a specific mixed conductor architecture but identify a few examples of materials for which fundamental relationships have been found and comment on how these claims can be generalized to other classes of polymers.

Herein, we review the efforts made to design and understand mixed conducting polymers. We highlight concepts and insight from the literature on ion- and electron-conducting polymers that are relevant to mixed conduction in a single materials system and show that simultaneous optimization of ion and electronic conduction requires new design rules. The first section of this article describes the physics of electron- and ion-conducting polymeric systems. The second section describes the nomenclature and methods used to study these phenomena and efforts to describe simultaneous conduction in polymeric systems. The last section discusses interesting potential directions and considerations in future research on these materials systems.

## 1.3 The principles of mixed conduction

### 1.3.1 Transport fundamentals

Unlike transport of neutral species, the mechanisms of ionic and electronic transport depend on electrostatic interactions of all charged species with the local electric field. The transport of electronic charge carriers has been shown to range from hopping-like to delocalized transport at various temperature and doping regimes.[18–20] Reported charge carrier mobilities are longer range averages of these fundamental local processes. In the same vein, liquid-like mechanisms are responsible for ion transport in ion-conducting polymers. [18,21] Thus, the transport of both ionic and electronic charge carriers can be described by a species balance around a control volume within a polymer system:[22]

$$\partial c_i / \partial t = -\nabla \cdot N_i + R_i \qquad \text{Equation 1}$$

where $\partial c_i/\partial t$ is the rate of change of concentration, $\nabla \cdot N_i$ is the gradient of the flux through a control volume, and $R_i$ is a term that accounts for the generation and consumption of species $i$ (*e.g.*, chemical reactions).

Mixed-conducting polymers typically operate below the melting temperature, where both amorphous and crystalline phases exist. As such, the bulk of the system does not flow and the contributions of the velocity field to the flux can be neglected, as are usually generation and consumption terms. Frequently, the Nernst-Plank extension of Fick's law is used to describe the flux of ions and electronic charge carriers:[21–25]

$$N_i = -z_i \mu_i F c_i \nabla \Phi + c_i v - D_i \nabla c_i \qquad \text{Equation 2}$$

where $z_i$ is the integer charge, $\mu_i$ is the mobility, $F$ is the Faraday constant, $c_i$ is the concentration, $\nabla\Phi$ is the gradient of the electric potential, $v$ is the velocity field that the species moves with, $D_i$ is the diffusion coefficient, and $\nabla c_i$ is the concentration gradient.

From Equation 2, the net flux of either ions or electronic charge carriers is a linear sum of (1) drift (*i.e.*, migration) due to the electric potential, (2) convection due to the velocity field, and (3) diffusion due to the concentration gradient.

An equivalent representation of flux for electronic charge carriers is given by Ohm's law (where $v = 0$ and $\nabla c_i = 0$):[22]

$$j = \kappa \nabla \Phi, \;\; \kappa = F^2 \sum z_i^2 \mu_i p_i \qquad \text{Equation 3}$$

where $j$ is the current density, $\kappa$ is the conductivity, $\nabla\Phi$ is the electric potential gradient, $z_i$ is the integer charge, $\mu_i$ is the mobility, and $p_i$ is the charge carrier density (concentration).

To a first approximation, the diffusion and mobility of both ionic and electronic charge carriers are related by the Nernst-Einstein equation:

$$D_i = RT\mu_i \qquad \text{Equation 4}$$

where $D_i$ is the diffusion coefficient, $\mu_i$ is the mobility, $R$ is the ideal gas constant, and $T$ is the temperature.

Additionally, conductivity can be generalized to both ionic and electronic charge carrier transport. The measured ionic conductivity represents contributions from mobile cations and anions in the polymer, while the electronic conductivity is dominated by contributions from positively charged polarons (and possibly bipolarons)[26] and negatively charged electrons[27] in *p*- and *n*-type conducting polymers, respectively. The conductivity of a particular species, $i$, is given as:

$$\sigma_i = p_i e |z_i| \mu_i \qquad \text{Equation 5}$$

where $p_i$ is the ion concentration/charge carrier density, $e$ is the charge of an electron, $z_i$ is the integer charge, and $\mu_i$ is the mobility.

When the application of an electric potential bias drives the transport of more than one charged species, it is useful to define the fraction of charge carried by each species. The fraction of total current carried by a single species, $i$, is the species transport number:

$$t_i = \frac{\sigma_i}{\sigma_{\text{total}}} \qquad \text{Equation 6}$$

where $t_i$ is the transport number, $\sigma_i$ is the conductivity of species $i$, and $\sigma_{\text{total}}$ is the sum of bulk conductivity that results from the sum of all $\sigma_i$.

In semicrystalline polymers, the mobility of ions and electronic charge carriers may be different in the crystalline and amorphous phases. A study of polymeric osmium perchlorate ion-exchange membranes, where electrons are not delocalized but instead hop in a similar fashion to ions, has demonstrated the analysis of limiting cases where one diffusion coefficient is much greater than the other and where both are equal.[23] In either case where one species (either the ion or the electronic charge carrier) is more mobile than the other, the local field that results from the more mobile species drives the less mobile species to minimize the energy of the field. An important finding of this work is that in these limiting cases, the overall diffusion coefficient is proportional to the diffusion coefficient of the less mobile species. Table 1 summarizes these findings. For the case where the diffusion coefficients of the mobile species are equal, the overall diffusion coefficient is also the same. As expected, the species transport number is greater when the relative diffusion coefficient of the species is greater. When the diffusion coefficients are equal, the transport number scales non-linearly according to the relative concentrations of both the mobile ion and electronic charge carrier.

**Table 1. Scaling dependencies of the overall diffusion coefficient and the transference number depending on the relative mobility (diffusion coefficient) of the mobile ion and mobile charge carrier[23]**

*$D_X$, $D_e$, $D$ are the ion diffusion coefficient, charge carrier diffusion coefficient, and overall diffusion coefficient, respectively. $t_X$ is the transference number of the mobile ion and $t_e$ is the transference number of the mobile charge carrier. $c_e$ is the concentration of the mobile charge carrier and $c_t$ is the combined concentration of the mobile charge carrier and mobile ion.*

| **Relative diffusion coefficient** | **Overall diffusion coefficient scaling** | **Transference number scaling** |
|---|---|---|
| $D_X \gg D_e$ | $D \cong D_e$ | $t_X \cong 1, t_e \cong 0$ |
| $D_X = D_e$ | $D \cong D_e \cong D_X$ | $t_X = (c_t - c_e)/(c_t - c_e^2)$,<br>$t_e = (1 - c_e)c_e/(c_t - c_e^2)$ |
| $D_X \ll D_e$ | $D \cong D_X$ | $t_X \cong 0, t_e \cong 1$ |

Typically, the diffusion coefficient of the electronic charge carrier may be approximated as much greater than that of ions in mixed conducting systems. The diffusion coefficient for polarons in poly(3-hexylthiophene) (P3HT) ranges from $10^{-5}$ to $10^{-3}$ cm$^2$ s$^{-1}$ (mobility of $10^{-3}$ to $10^{-1}$ cm$^1$ V$^{-1}$ s$^{-1}$), depending on the carrier concentration.[28] The diffusion coefficient for perchlorate ($ClO_4^-$) in a polymer-ion-counterion system is on the order of $10^{-14}$ cm$^2$ s$^{-1}$.[29] When solvent is added, the diffusion coefficient of $ClO_4^-$ increases to values of $10^{-12}$ to $10^{-10}$ cm$^2$ s$^{-1}$.[30] These order-of-magnitude differences in the diffusion coefficient ions and electronic charge carriers indicate same-order differences in the time scales of transport; to a good approximation these processes can be decoupled in time.

Although Fickian transport is used to describe the motion of charges in several materials classes, the assumptions inherent to Fickian diffusion are not applicable in mixed conductors.

Fickian diffusion is typically well-defined only in the dilute limit, where interspecies interactions can be neglected. Recent work utilizing moving front experiments has provided evidence that ion transport in a conjugated polymer with glycolated side chains is non-Fickian, and in fact, reminiscent of ion transport in inorganic materials.[31] As will be discussed in subsequent sections, intermolecular interactions are unavoidable at the ion concentrations necessary for necessary for most applications (conductivity of $10^{-3}$ S/cm).[25,32]

### 1.3.2 Ionically conducting polymers

Ion conduction in polymer electrolytes is a hierarchical process impacted by both the meso- (~10-100 nm) and molecular-scale (< 10 nm) structure and dynamics of the electrolyte. At the molecular scale, ionic transport involves an interplay of polymer segmental dynamics and ion-polymer solvation interactions, which simultaneously dissociate ions. These effects allow for long-range migration in response to an electric potential bias and act as frictional sources for ions, limiting their mobility on certain timescales. Transport at mesoscopic length scales is believed to require percolated regions of ion-solvating sites. Since ion-solvation sites are not fixed within the material, long-range transport depends both on the equilibrium ionic structure of the material as well as its fluctuation dynamics.

Ion transport in amorphous polymers is traditionally viewed as a liquid-like mechanism, whereby the local frictional environment dictates long-range ion transport.[33,34] Consequently, the temperature dependence of ionic conductivity correlates with measures of segmental mobility, such as the inverse of the segmental relaxation timescale, $1/\tau_\alpha$.[6,35,36] As a result, ionic conductivity follows commonly-known relationships for the temperature dependence of polymer dynamics such as the Vogel-Tammann-Fulcher (or equivalent Williams-Landau-Ferry) relationship (Equation 7):[37]

$$\sigma = \sigma_0(T)\exp\left(-\frac{B}{T-T_0}\right) \text{ for } T > T_g \qquad \text{Equation 7}$$

where the fitting parameters, $\sigma_0$ relate to the number of mobile ions, *B* relates to the activation energy associated with segmental motion, and $T_0$ is a reference temperature corresponding to the temperature of zero configurational entropy and typically takes on universal values ($T_0 \cong T_g - 50$ K, where $T_g$ is the glass transition temperature).[38] It is common to either treat $\sigma_0$ as a temperature independent constant or to assign it to scale with $T^{-1/2}$ dependence. Figure 1a schematically depicts how polymer segmental motion gives rise to pathways for ion transport. Strategies to increase ionic conductivity of polymeric electrolytes include adding more salt,[39] increasing the dielectric constant,[38] and lowering $T_g$ through synthetic routes, which facilitates segmental relaxation.[6]

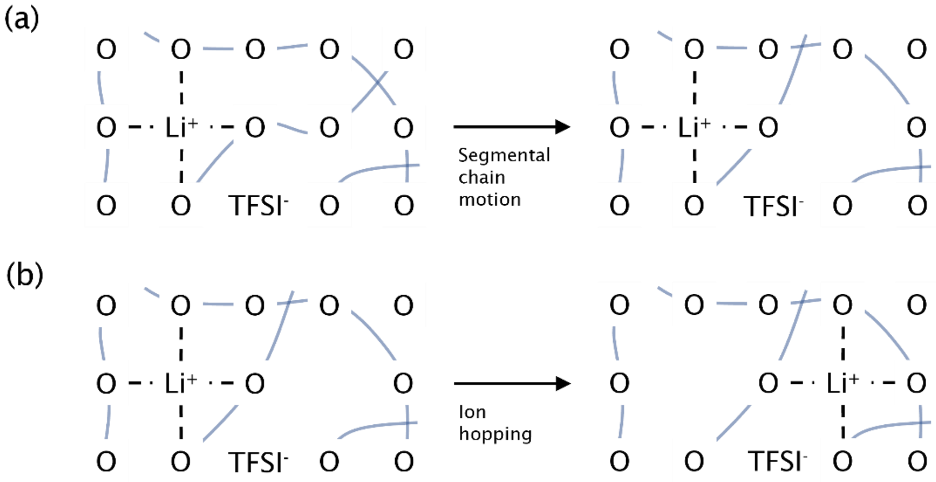

**Figure 1. Polymer ion conduction mechanisms**

*Mechanisms of ion conduction. (a) Ion transport is fostered by electrostatic interactions with electron withdrawing moieties on the polymer side chain. As segments of the polymer chain move, vacancies in the pseudo-matrix become available. (b) When nearby vacancies in the polymer pseudo-matrix are available, ions can hop from one site to another.*

The ionic conductivity polymer electrolytes far exceeds expectations from the liquid-like mechanism of ionic conduction in glassy and crystalline regions, suggesting an alternative transport mechanism where ion motion is decoupled from polymer relaxation.[40] In glassy or crystalline regions of the electrolyte, the temperature dependence of ion motion commonly follows an Arrhenius form (Equation 8):[38]

$$\sigma_0 = \sigma_0(T)\exp\left(-\frac{E_a}{k_B T}\right) \qquad \text{Equation 8}$$

where the activation energy ($E_a$) is now associated with ion hopping rather than segmental motion. Figure 1b schematically depicts how ions might hop via an Arrhenius hopping mechanism. For ordered phases, ions may hop to both free-volume sites and interstitial sites within the polymer matrix.

Polymeric mixed conductors are often semicrystalline; the bulk ionic conductivity is a sum of contributions to ionic conductivity in both the amorphous and crystalline phases. Below $T_g$, segmental chain motion is limited and ions are transported by hopping in both phases, as described by Equation 8. Because the energy barrier for ion hopping is much lower in the amorphous phase, the design rule for enhancing ionic conductivity in solely ion-transporting polymers is to reduce or remove the crystalline fraction. In mixed conducting polymers, the crystalline regions are helpful for conduction of electronic charge carriers. As a result, ion conduction in mixed conducting polymers is likely dominated by transport through amorphous domains. Above $T_g$, motion of polymer chain segments creates free-volume sites for ion motion, providing another contribution to ion conduction, as described by Equation 7. However, ion hopping can still occur in both phases. Figure 2 shows the various temperature regimes where significant differences in the mechanism on ionic conduction are observed and how the bulk ionic conductivity might arise from individual mechanistic contributions. An important distinction between ion conduction in solely ion-conducting polymers and in mixed conducting polymers is that in mixed conducting polymers there are at least two energy barriers to ion motion. Solely ion-conducting systems are often amorphous and so, the energy barrier is related to ion motion in the amorphous phase. Because mixed conducting polymers are usually semicrystalline, energy barriers for both ion hopping or segmental motion-mediated transport correspond to a crystalline phase and an amorphous phase.

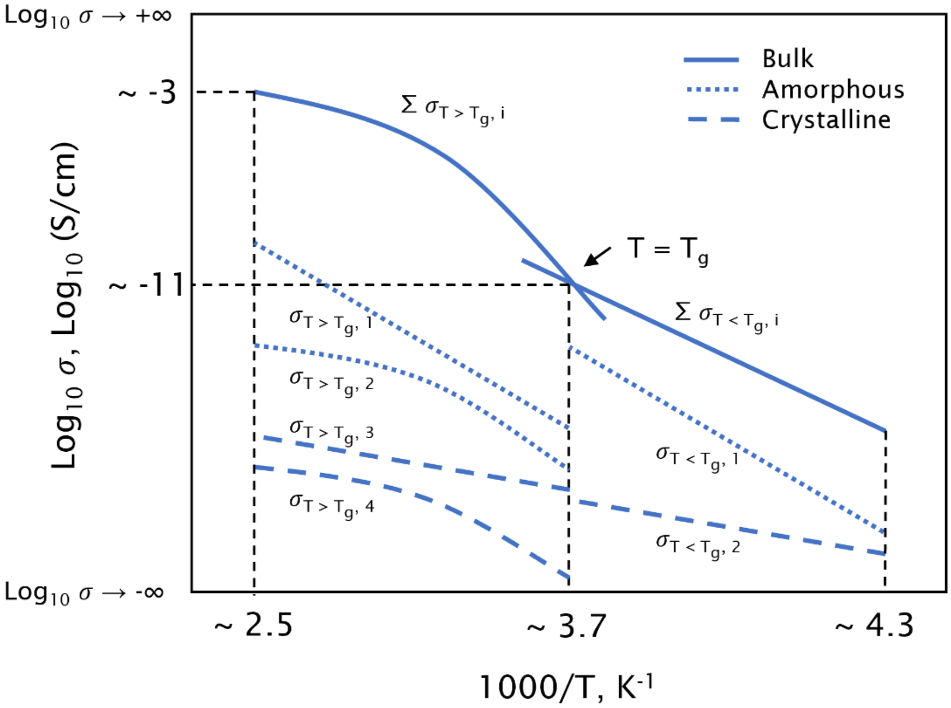

**Figure 2. Temperature dependence of ion conduction mechanisms**

*Arrhenius plot of temperature dependence of ionic conductivity in polymers. Approximate values are estimated from ionic conductivity in representative polymeric ionic liquids.(32) In semicrystalline polymers, the bulk ionic conductivity is a sum of individual contributions in both the crystalline and amorphous phases. At temperatures below* $T_g$*, ion hopping in both the amorphous* ($\sigma_{T < Tg,1}$) *and crystalline phases* ($\sigma_{T < Tg,2}$) *are the dominant mechanisms of ion transport. At temperatures above* $T_g$*, ion transport mediated by segmental chain motion* ($\sigma_{T > Tg,2}$, $\sigma_{T > Tg,4}$)*, along with ion hopping* ($\sigma_{T > Tg,1}$, $\sigma_{T > Tg,3}$) *can take place in both phases. Log-linear contributions in the Arrhenius plot describe ion hopping via the*

*Arrhenius equation, while non-linear contributions describe segmental chain motion-mediated transport via the Vogel-Tammann-Fulcher equation. Figure adapted with permission from Bocharova V. and Sokolov AP. 2020. Macromolecules. 53(11):4141–57; copyright 2020 American Chemical Society.*

Molecular-scale interactions between the polymer and mobile ion also contribute to ion transport. Because cations are typically the mobile ion of interest for many applications, strategies to increase the dielectric constant and introduce electron-rich moieties facilitate transport of cations in addition to segmental motion.[41] However, stronger interactions can detrimentally affect the relaxation processes of polymers,[42] potentially due to the change in chain dimensions at high salt concentration.[43] This effect likely contributes in the maximum ionic conductivity with salt concentration observed in many ion-conducting systems.[44] Pioneering simulation and experimental work has demonstrated aggregate structures ranging from isolated, spherical aggregates to percolated, stringy aggregates obtained through modifications in polymer repeat structure, ion identity, and polymer architecture.[45] Materials with ions tethered directly along the backbone (ionenes) can display highly-ordered ion structures, resulting in materials segregated into ion-rich domains[17] which displaying well-defined long-range order into unit cells with lattice parameters of ~3-7 nm below an order-disorder temperature.[46,47]

Analogously, mesoscale segregation of inhomogeneous polymers and polymer blends have been leveraged to generate materials with percolated ionically conductive domains on larger length scales (10-100 nm).[48,49] Though modification of an ion-conducting material such as PEO with an insulating domain is generally regarded to be detrimental to ionic conduction, insulating domains are often incorporated to impart structural rigidity. The effect of these insulating domains can range from a minimal impact on performance in the case of percolating morphologies to a dramatic insulating character in non-percolating morphologies.[50–52] These examples serve to demonstrate the importance of continuous connection of ion-conducting domains across all device length and time scales, demonstrating the hierarchical nature of ion conduction.

### 1.3.3 Electronically conducting polymers

In purely electron-conducting polymers, transport occurs through both delocalized $\pi$-orbitals along one chain and hopping between chains if sufficient $\pi$-$\pi$ overlap exists.[53] Since most conjugated polymers are semicrystalline, heterogenous electronic conduction between the amorphous and crystalline domains of the polymer results in complex behavior where the effects of separate mechanisms, such as charge transport along a polymer chain or charge hopping from one chain to another, are difficult to deconvolute. Additionally, several properties influence the observed electronic conductivity, including the morphology, the carrier concentration, and contour length of the polymer.[8]

To increase the electrical conductivity of polymers, carriers are introduced into the material through doping. Doping involves oxidation (reduction) of the backbone through an extrinsic molecule or an electrode, which forms a radical/hole (radical/electron) pair along the polymer backbone.[19,54,55] The charge-balancing moiety must exist in close proximity to the backbone charge, a phenomenon that differentiates doping in polymeric semiconductors from their inorganic counterparts. This coupling in space is discussed further in the context of double-layer capacitance on page 23. One central question in doping polymeric semiconductors is how the presence of these ions affects other material properties of the polymer, which impacts the resulting transport behavior.

The mobility of electronic charge carriers is known to be limited by the ordered domains. The specific transport mechanisms are ascertained through temperature-dependent measurements. Electronic mobility or electrical conductivity typically follow a power law ($T^{-a}$) or a stretched exponential ($\exp[-T^{-b}]$) with respect to temperature. Common models observed in temperature dependent measurements of semiconducting polymers include variable range hopping ($b = ¼ – ½$), nearest neighbor ($b = 1$), and band transport ($a \cong -1$). In-depth analyses of charge transport models in organic semiconductors has been published in several recent reviews and journal articles.[56–58] In contrast to most primarily ion-conducting polymers, semiconducting polymers often complicate the determination of a single transport mechanism at a given temperature due to their heterogenous morphology. Convoluting effects, such as changes in electronic charge carrier densities, can be monitored via thermopower measurements, which are related to the electronic density of states.[59–61]

The tendency for crystallization in polymers depends on the specific chemistry, including the stereo-regularity of the pendent groups along the polymer backbone, the introduction of other species, such as dopants, and effects of post processing.[62,63] The conjugated backbone and ring-like structures common in semiconducting and conducting polymers tends to stiffen the polymer backbone, which increases the propensity to form liquid crystalline phases and crystallize upon casting. As a result, mixed conducting polymer systems are often semicrystalline and few studies to-date have reported on electronic conduction at temperatures above $T_g$. Figure 3 shows how the molecular structure in ordered P3HT gives rise to the observed microscopic structure and how the alignment of polymer chains may lead to local anisotropy of electronic conductivity.

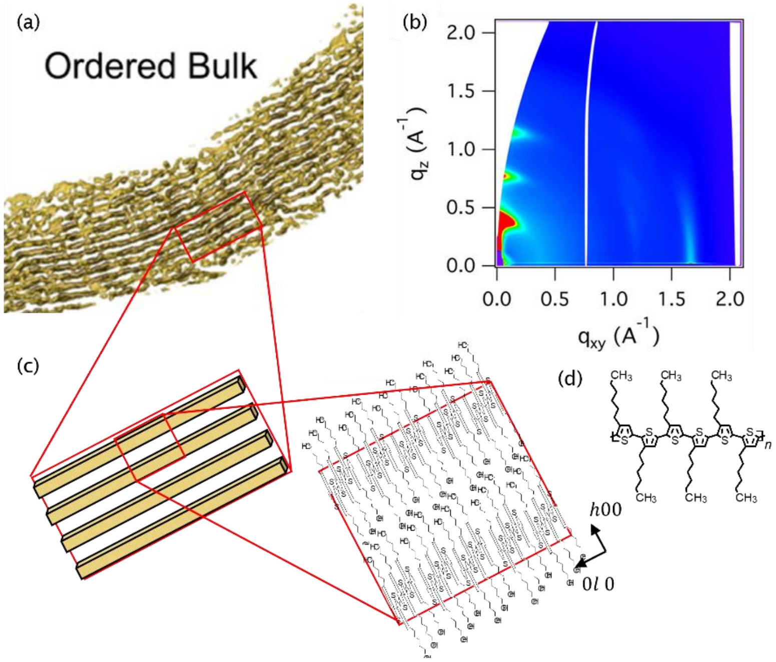

**Figure 3. Morphology of conjugated polymer crystallites**

*Structural orientation of P3HT in a crystallite. (a) 3D reconstruction of ordered domain nanostructure from an electron micrograph.*[64] *(b) Grazing incidence wide-angle X-ray scattering (GIWAXS) pattern for ordered P3HT. The signal near the* $q_z$ *direction corresponds to periodic stacking between adjacent polymer segments separated by alkyl side chains, while signal along the* $q_{xy}$ *direction corresponds to the* $\pi$-$\pi$ *stacking distance between adjacent polymer backbones. (c) The inset shows the projected ordering as a stack* *of high-aspect ratio rectangular prisms. Further magnification shows the molecular structure of P3HT oriented to match the nanostructure of ordered P3HT observed in a. Vectors showing the h00 and 0l0 direction are labeled to aid comparison to the GIWAXS pattern shown in b. (d) Molecular structure of P3HT, shown for comparison to the tomography image-aligned molecular structure in shown in c. In the electron tomography image, the polymer chain is viewed edge-on, and alkyl side chains extend between backbone stacks and are oriented orthogonally to the principal axis of the polymer. (a,c,d) Figure adapted with permission from Wirix MJM., et al. 2014. Nano Lett. 14(4):2033–38; copyright 2014 American Chemical Society. (b) Figure adapted with permission from Lim E., et al. 2019. Advanced Electronic Materials. 5(11):1800915; copyright 2019 WILEY-VCH Verlag GmbH & Co. KGaA, Weinheim.*

A holistic description of molecular-scale interactions between charged species and electronically-conducting polymers is complicated due to the fact that the electron (or hole) resides on the polymer itself while the counter-ion resides in proximity to the backbone.[55] Theoretical calculations can explore these effects separately. Recent simulations of P3HT oligomers using density functional theory (DFT) compared the $\pi$-stacking distance of the oligomers with and without polaronic charge on the backbone.[65] Calculations determined that even in the absence of dopant counter-ions, the presence of positive charge decreases the $\pi$-stacking distance by 0.02 – 0.08 Å, depending on the number of repeat units analyzed. The authors posited that the relaxation of the polaron between multiple chains leads to attractive forces between units, resulting in a decrease of the $\pi$-stacking distance. Although transport measurements were not completed in this work, experimental studies in conjugated donor-acceptor copolymers show that a smaller $\pi$-stacking distance leads to a concomitant increase in electronic mobility.[66] As a result, methods to reduce the $\pi$-stacking distance such as side chain engineering[67] and film processing[68] are expected to enhance these favorable interactions and improve electronic transport.

An understanding of how interactions between the charge carrier on the polymer and its counter-ion affect electronic mobility is still evolving. The counter-ions typically reside in the amorphous regions of the polymer due to the increased free volume of these domains or within the side chain region of polymeric crystallites. The low dielectric constant of most conjugated polymers (typically synthesized with alkyl side chains) can lead to localization the polaron on the polymeric backbone because of the Coulombic interaction with the counter ion, reducing its mobility. Efforts to mitigate these interactions such as increasing the polarity of the side chains[69,70] or using sterically bulky dopants[71] have shown promise to improve electrical conductivity in doped semiconducting polymers. These design principles may serve to improve other aspects of transport specific for mixed conduction, such as improving ion uptake in aqueous environments.[72]

The degree of crystallinity and connectivity between neighboring crystallites within semicrystalline polymers, both at molecular length scales and length scales on the order of 50 – 500 nm, largely governs the resulting electronic conductivity. Electronic mobility generally scales with the degree of crystallinity since trap states are induced by conformational disorder within the amorphous domains of the polymer. Processing strategies such as altering the casting solvent or the backbone regioregularity was found to influence the fraction of aggregated regions in the film and their free exciton bandwidth, which scaled with the electrical conductivity.[73,74] The distance over which polymeric backbones retain alignment with one another, defined as the orientation correlation length (OCL),[75] also influences the electrical properties of polymers. In contrast to the crystallites themselves, which are typically around 10 nm in size, the length scale over which they are connected is a strong determinant of the electronic conductivity even at similar carrier concentrations. The OCLs of pristine P3HT is typically below 50 nm[74], but can reach up to 350 nm in liquid crystalline semiconductors such as PBTTT.[76] Recent studies found that the doping method can degrade this long range order, influencing the maximum achievable electrical conductivity.[74,77] These results suggest that retaining the alignment between ordered domains when ions are present is critical for electronic as well as mixed conduction.

Tie chains, molecules which connect ordered regions, are also necessary to create a percolated pathway for electronic charge carriers. Tie chains must possess a sufficient contour length to connect two neighboring crystallites together, which requires a minimum degree of polymerization. In homopolymers, a discontinuous increase in electronic mobility typically occurs at around 12,000 – 15,000 g/mol, or about 70 – 90 repeats units for P3HT.[8] The same effect can be achieved through mixing small amounts of a high contour length polymer with the same polymer of lower contour length; analysis of P3HT blends found that only $10^{-3}$ of all chains need to act as tie chains for a percolated network to form, even when the degree of polymerization of the majority phase is as small as 30 repeat units.[78,79]

## 1.4 Ionic, electronic, and mixed conduction figures of merit

### 1.4.1 Ionic transport

While the total ionic conductivity is the most commonly reported metric of ionic transport in polymer electrolytes, actual electrolyte performance in energy storage and conversion devices heavily depends on a more comprehensive view of ion conduction. For example, in lithium-ion batteries, the motion of $Li^+$ ions are of primary interest and counterion motion can be detrimental to cell performance. Consequently, the transport number is an important parameter to define the fraction of the total current carried by the ion of interest (see Equation 6). This transport number is distinct from the transference number, though the quantities are often used synonymously in the literature.[80]

A quantity called the Haven ratio (Equation 9) is used to characterize the ratio of the measured ionic conductivity and the ionic conductivity reproduced from the Nernst-Einstein relation (Equation 4).

$$H = \frac{\sigma_{\mathrm{NE}}}{\sigma_{\mathrm{electrochem}}} = \frac{\sum_i n_i z_i^2 D_i}{kT\sigma_{\mathrm{electrochem}}} \qquad \text{Equation 9}$$

In Equation 9, $H$ is the Haven ratio, $\sigma_{\mathrm{NE}}$ is the Nernst-Einstein conductivity, $\sigma_{\mathrm{electrochem}}$ is the electrochemically-determined conductivity, $n_i$ is the number of charge carriers $i$, $z_i$ is the integer charge of the charge carrier, $D_i$ is the diffusion coefficient, $k$ is the Boltzmann constant, and $T$ is the temperature.

A discussion of methods to determine the Nernst-Einstein and electrochemically determined conductivity is provided on page 27. The Haven ratio often takes on a value of greater than unity for ionic liquids or molten salts,[81] but can take on values greater than unity for superionic conductors.[82] In some concentrated polymer electrolytes, Haven ratios of nearly unity are observed, but authors should take care to note that deviations from the Nernst-Einstein relation are likely to arise, particularly at high ionic strengths or in the presence of crystalline regimes. As such, Haven ratio values far from unity are indicative of intermolecular interactions that lead to differences between ionic diffusivity and charge diffusivity – such as ion aggregation.

### 1.4.2 Electronic transport

The electrical conductivity, $\sigma$, combines the concentration, mobility, and charge of the mobile species (Equation 5). For doped polymeric semiconductors, the electrical conductivity is the most commonly reported transport parameter and represents an average of all electronic conduction mechanisms that occur within the material. The highest reported values for doped polymers are between $10^4$ – $10^5$ S/cm at ambient temperatures.[83,84] The electrical conductivity at a single temperature does not reveal the complex relationship between the factors leading to it.[19,60]

Electronic mobility, $\mu$, provides a metric to understand how transport changes with carrier and counterion concentration. In lightly-doped polymeric semiconductors (charge carrier density of less than $10^{20}$ $\text{cm}^{-3}$),[28] many of the carriers are energetically trapped, leading to carrier mobility around $10^{-3}$ $\text{cm}^2\ \text{V}^{-1}\ \text{sec}^{-1}$. For comparison, the ionic mobility of $\text{ClO}_4^-$ in

P3HT is on the order of $10^{-14}$ cm$^2$ s$^{-1}$.[29] Adding more charge carriers leads to a superlinear increase in the electronic mobility, reaching up to ~0. 1 – 1 cm$^2$ V$^{-1}$ sec$^{-1}$ for some of the highest-performing semiconducting polymers. This superlinear trend is unique to polymeric semiconductors and has been rationalized by several mechanisms in recent literature.[85,86] Thus, the charge density is the true independent variable of transport phenomena in electron conduction and is necessary to quantify for electronic as well as ionic and mixed conduction.

### 1.4.3 Mixed conducting systems

When mixed conductors are applied to biological sensors and actuators, a fast response time may be important. In electrochromic devices, the contrast ratio of color and brightness may be a better metric for performance. Their application in ion pumps means that precise control over ion flux is crucial, while sensing applications depend on changes in electron or ion flux in response to external stimuli. Because of the range of potential applications, a single figure of merit to describe the performance of mixed conductors has not been established. In this section, we describe the typical device configurations used to characterize mixed conductors and describe the figures of merit that have arisen from these configurations.

The increasing utility of studying polymeric charge transport through organic electrochemical transistors (OECTs, Figure 5a), along with uncertainties in individual measurements of mobility, has bolstered the use of the transconductance as a figure of merit for mixed conduction. Since transistors are used as electrical amplifiers, the transconductance quantifies how much current is gained in the active layer for a given change in the gate voltage. Because $dI/dV_g$ depends on channel width and length, the transconductance is also a means to normalize across device dimensions. Several factors contribute to the device transconductance according to Equation 10:

$$g_m = (Wd/L)\mu C^{*}(V_{th} - V_g) \qquad \text{Equation 10}$$

where $\mu$ is the electronic mobility, $C^*$ is the volumetric capacitance of the active layer, $V_{th}$ is the threshold voltage, and $V_g$ is the gate voltage.

While transconductance yields utility in describing performance of transistors, capacitance is a more generalized figure of merit that can be used to benchmark performance for all mixed conducting devices. The chemical capacitance, defined by the change in chemical potential of the material for a change in carrier concentration[87], ultimately mediates other application-specific figures of merit such as the contrast ratio in electrochromics[88] and the flux in ion pumps and membranes.[89] Chemical capacitance is an extensive quantity and thus proportional to the volume of the sample and involves a redox reaction as well as diffusion of the external species into the surface and bulk.[90] Because all mixed conductors require this two-step mechanism, chemical capacitance may be one potential route for a generalized performance metric in mixed conductors.

Another form of capacitance, the electrical double layer (EDL) capacitance, arises from the accumulation of charges at the interface between an electrode and electrolyte material. In an electrolytic cell, a metal electrode is primarily responsible for electronic conduction whereas the electrolyte is primarily responsible for ionic conduction and the EDL is developed at their interface. Locally, the coupling between ions and charge carriers can be described by analogy between metal electrodes and crystalline regions and between electrolytes and amorphous regions. Figure 4 schematically shows how a positively charged hole might be balanced not only by a single anion molecule, but also complex electrostatic complexes, such as a hole-anion-cation-anion complex at the ordered-disorder interface. Because electrical fields and associated potential gradients couple ions and electronic charge carriers, these their distinct transport processes may be approximated as decoupled in time, but not in space.

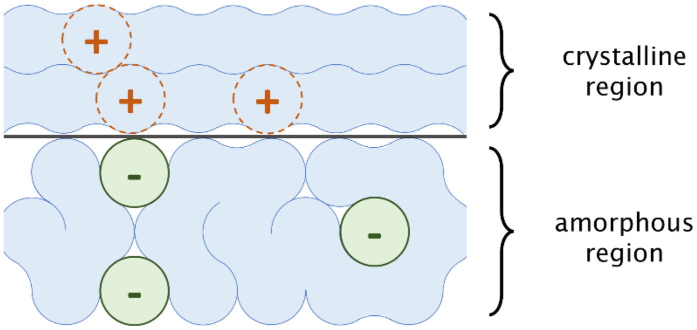

**Figure 4. Interfacial capacitance between crystalline and amorphous domains**

*Schematic depiction of a capacitance arising from a crystalline-amorphous interface in a mixed conducting polymer. In p-type mixed conductors, electrostatic interactions between anions (green) and polymer backbones with delocalized electrons (blue) lead to generation of charge conducting pathways (polarons, outlined in orange).*

It is apparent that EDL charging depends on both electronic and ionic species distributions and that this mutual dependence manifests through the condition for charge neutrality over the system bulk. Specifically, the applied potential in organic electronic devices drives ions towards ordered-disordered interfaces where charge carriers are induced and coupled with nearby dopant ions. Local electric fields arise from this separation of charge and can be accounted for in the boundary conditions necessary to solve Equation 1 and Equation 2.

Lastly, an important feature that is not often considered in OECTs is the kinetics of ion transport. Ion transport occurs on observable time scales ($10^{-3}$ s); limitations in their transport may significantly affect device performance and are observable through the transconductance.[91–93] The rate at which output and transfer characteristics (Figure 5b) are obtained is not often reported as the field of OECTs continues to expand, but understanding the kinetic component will be critical for rational design of high performance polymeric mixed conductors.[94,95]

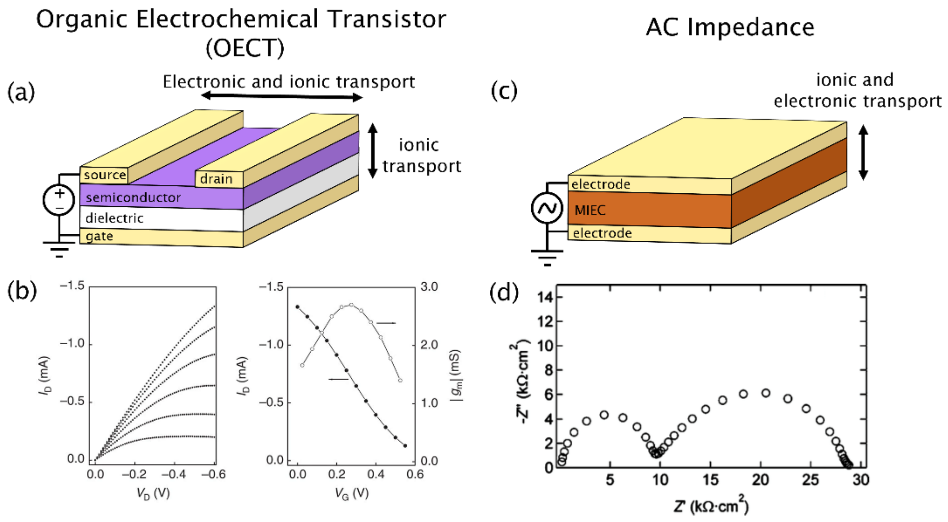

**Figure 5. Platforms to characterize electronic and ionic transport**

*Two common platforms to characterize ionic and electronic transport of polymeric semiconductors are the organic electrochemical transistor and symmetric cell. Ions and electrons travel in orthogonal directions within organic electrochemical transistors (a),* *which decouples ionic and electronic conduction. Output and transfer curves from OECT operation (b) yield information about the performance of the mixed conducting device.*[96] *Using AC impedance (c), both charge carriers travel in the same direction. A Nyquist plot (d) of the frequency-dependent response is one straightforward visualization of the contributions of electronic and ionic motion.*[97] *Presence of multiple semicircles in the Nyquist plot indicates motion of more than one chemical species in the sample. (b) Figure adapted with permission from Khodagholy D., et al. 2013. Nature Communications. 4(1):2133; copyright 2013 Springer Nature. (d) Figure adapted with permission from Patel SN., et al. 2012. ACS Nano. 6(2):1589–1600; copyright 2012 American Chemical Society.*

### 1.4.4 Measurement methods

The Bruce-Vincent method is a cell-based method frequently employed in the literature to determine the species-dependent transport.[17] This method employs a symmetric electrochemical cell (Figure 5c) and can relate the steady-state dc voltage of the cell to the transport of a specific species under dilute conditions. Consequently, this method does not give a true transport number at realistic conditions for most applications. The dilute condition approximation generally only applies at low ionic strengths (below 0.01), which is much less than the ionic strength typical for an electrolyte.[98] Despite the inability to extract faithful transport numbers under most usual conditions, this method has propagated widely and become standard in the field of ionically conducting polymers and the results of this experiment are important for benchmarking purposes and relevant for applications. Recent developments in cell-based methods may allow better estimation in concentrated solutions than the Bruce-Vincent method, including direct measurement of the concentration gradient along the transport direction and analysis based on concentrated solution theory.[99]

An alternative family of techniques to examine ion-specific transport utilizes measurements of ion self-diffusion constants and their contribution to conductivity is again calculated based upon the assumptions of the Nernst-Einstein equation. Techniques such as pulsed-field gradient NMR can measure the self-diffusion constants of ions.[100,101] Neglecting intermolecular interactions, the ionic conductivity contributions from individual species is directly related to this constant, their concentration, and valency allowing for facile computation of their contribution to the total conductivity. However, experimental reconstructions of the net ionic conductivity based on these results often fail to reconstruct the measured ionic conductivity, as discussed in the previous section.

As previously mentioned, OECTs are a unique platform to study the principles of mixed conduction relevant to many applications of ion/electron conductors. OECTs contain the same components as field-effect transistors and typically adopt similar geometries (Figure 5a). They are distinguished by the use of gate insulators that contain cations and anions that infiltrate the semiconducting layer upon application of a gate bias. Synthetically tethering the cation or anion species of the gate dielectric facilities control over ion diffusion into the semiconductor, preventing unwanted ion pair infiltration into the material.[28,102,103] As a result, the semiconductor can sustain charge throughout the bulk of the layer via ionic motion. OECTs also provide experimental control over the carrier density of ions and electrons critical in rationalizing the impact of ions on the mobility, morphology, and electronic structure of the semiconductor.[20,85,102]

## 1.5 Emerging areas in mixed conduction

There are several concepts of mixed conductors that are still not understood. This confusion arises from the fact that in polymers, electronic and ionic transport are not separate processes, and the impact of one transport mechanism necessarily impacts that of the other. This effect is less prevalent in other mixed conducting systems such as ceramics. Studies purely on one-component charge transport conclude that the material properties beneficial for one type of transport are detrimental to the other. Studies in polymeric mixed conductors have shown that this idea may not be the case, which is counter-intuitive to our current understanding.[104,105] This section details the sub-fields of mixed conductors that require more investigation.

### 1.5.1 Dynamic structural and morphological disorder

Previous sections have highlighted the importance of morphology for all forms of transport in polymeric semiconductors, consequently, the structural changes of semiconducting polymers upon ion incorporation are key to understanding transport in these materials. [106] It is of utmost importance then to understand how morphology evolves as more ionic species are added to the material. For example, interactions between electrically and ionically conducting domains can lead to structural rearrangement, contributing to an increase in mixed conduction. This effect was seen in P3HT:PEO block copolymers doped with LiTFSI salt.[97] Upon adding salt to the copolymer, both the electrical and ionic conductivity increased. While the increase in ionic conductivity is expected, the increase in electrical conductivity implies a structural rearrangement leading to improved electronic charge transport. Structural rearrangements due to solvent treatments also improve the mixed conductivity of PEDOT:PSS and PTHS.[3]

While many studies show an increasing degree of disorder upon adding salts or dopants in semicrystalline materials, few studies have probed the morphological effects of doping polymers that are already amorphous. Regiorandom P3HT is primarily amorphous on its own, but reversibly crystallizes and decrystallizes upon the addition and removal of the dopant 2,3,5,6-tetrafluoro-7,7,8,8-tetracyanoquinodimethane (F4TCNQ) (Figure 6).[74] These results suggest that the amorphous regions of conjugated polymers may be more structured than previously suggested and that a rigid amorphous phase may play a role in electronic conduction. Exploring these ideas may offer insight into the impact of semicrystallinity on the morphology of these polymers.[107,108]

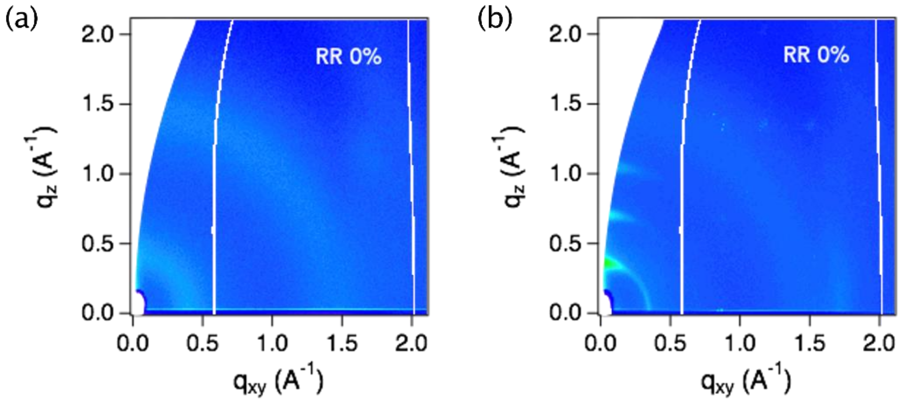

**Figure 6. Dopant-induced ordering of regiorandom P3HT from GIWAXS**

*Grazing incidence wide angle X-ray scattering measurements of P3HT indicate doping-induced reversible formation of crystallites.*[74] *Broad peaks are observed for regiorandom P3HT (a), while clear feaures near the* $q_z$ *axis appear upon doping with* $F_4TCNQ$ *(b). Figure adapted with permission from Lim E., et al. 2019. Advanced Electronic Materials. 5(11):1800915; copyright 2019 WILEY-VCH Verlag GmbH & Co. KGaA, Weinheim.*

### 1.5.2 Dielectric environment

The dielectric environment of charge carriers controls salt solvation and is known to impact ionic conductivity, but the impact of dielectric constant on electronic transport of mixed conductors is less clear. Enhancements in dielectric constant are linked to higher ionic conductivity since this leads to higher effective charge separations. Though recent work suggests that increases in dopant/polaron distance does not translate to higher electronic conductivity,[109] the recently demonstrated formation of dianions within highly polar thienothiophene-based polymers with ethylene-oxide side chains may lead to higher electrical performance.[110] This behavior may be a result of the increased dielectric constant of the polar side chains stabilizing the dianion, leading to fewer ionic charges per electronic charge. Similar results were observed in an EDOT-based polymer with oligoether side chains which shows solubility in several solvents, even in its charged state.[111] Understanding the impact of charge screening on electronic mobility will lead to insight into polymeric mixed conductor design.

### 1.5.3 Mechanical properties

The enhancement of transport performance of mixed conductors is often accompanied by tradeoffs in mechanical performance, which presents a challenge due to the demanding mechanical requirements for many applications of mixed conductors. Studies exploring the effect of strain on the electronic mobility of polymeric semiconductors have shown little change in electronic mobility at up to 100% strain.[112,113] In addition, ionic conductivity has been observed to increase as a result of increased strain through in situ studies, where through-plane and in-plane conductivity increases linearly with deformation of 200 µm PEO/LiClO4 electrolyte films.[114] Studies of polymeric actuators give some insight into the mechanical behavior of mixed conducting polymers.[115] Models to rationalize the effects of strain on the output characteristics of OECTs are also in development, which can elucidate fundamental relationships between conduction and mechanics of mixed conductors and establish practical boundaries for long-term operation. As with all performance metrics of mixed conducting polymers, the temperature dependence on the mechanical behavior of mixed conductors is crucial to elucidate the elastic and viscous response to an applied strain, which can evolve as a function of salt concentration.

## 1.6 Conclusions

The field of polymeric mixed conductors requires an interdisciplinary perspective that combines knowledge of electronic and ionic transport with principles distinct to mixed conduction. Polymers with a semicrystalline structure containing percolated pathways for both ions and electrons to conduct represents a clear design constraint for the morphology of mixed conductors; however, clear relationships between the morphology and various figures of merit for mixed conduction have yet to be elucidated. Expanding the structure-property relationships between these figures of merit and the percent crystallinity of polymers, which affects the capacitive component between ions and electrons in the material, has significant potential to create a unifying model for practical implementation of mixed conducting systems. This integrated picture is the ultimate path forward in designing polymeric materials to meet the demand of applications where mixed conduction is required. Knowledge from synthetic chemistry, electrochemistry, and solid-state physics informs the rational design and processing required for the multitude of applications for mixed conducting materials. The principles developed in the organic electronics and polymer electrolyte communities will be helpful in guiding this field, but some relationships distinct to mixed conduction have yet to be fully realized.

## 1.7 Acknowledgements

E.M.T. and P.H.N. acknowledge support for work on ionic and electronic interactions in semiconducting polymers from the Department of Energy, Office of Basic Energy Sciences, under grant DE-SC0016390. S.D.J. gratefully acknowledges support from the MRSEC Program of the National Science Foundation under Award No. DMR 1720256 for work on ionic conduction. Research was sponsored by the U.S. Army Research Office and accomplished under cooperative agreement W911NF-19-2-0026 for the Institute for Collaborative Biotechnologies. E.M.T. gratefully acknowledges support from an NSF Graduate Fellowship (DGE-1650114).

# Chapter 2 – Diffusion of Brønsted Acidic Dopants in Conjugated Polymers

Phong Nguyen, Michael Chabinc, and Rachel Segalman conceptualized the project and experiments. Phong Nguyen performed the experiments, analysis, and drafted the manuscript. Michael Schmithorst assisted with solid-state NMR experiments. Thomas Mates assisted with depth profiling measurements and analysis.

This chapter was reproduced in part with permissions from:

Nguyen, P. H.; Schmithorst, M. B.; Mates, T. E.; Segalman, R. A.; Chabinyc, M. Diffusion of Brønsted Acidic Dopants in Conjugated Polymers. *Journal of Materials Chemistry C* **2023**, *11* (22), 7462–7470.

## 2.1 Abstract

Many semiconductor devices (*e.g.*, light emitters and photovoltaics) utilize heterojunctions of doped and undoped layers or depend on gradients of electronic doping to control charge transport. Understanding of the formation and stability of gradients in doping requires an understanding of diffusion of dopants and the complex changes in polymer properties that arise during doping. Conjugated polymers can be electrically doped by strong acids, but the details of the reaction mechanism and subsequent stability are not understood. Here, we show a clear kinetic isotope effect in the doping of thin films of poly(3-hexylthiophene) (P3HT) by bis(trifluoromethane)sulfonimide (HTFSI) from solution indicating that this doping process is limited by proton transfer to the polymer. Dynamic secondary ion mass spectrometry (DSIMS) of doped films suggests that H/D can be retained

in doped films after the doping process. Complementary X-ray photoelectron spectroscopy and DSIMS depth profiling of dopant concentrations show definitive evidence of dopant enrichment at the P3HT surface. These surface-limited concentration profiles suggest that diffusivity of dopants vary inversely with dopant concentration due to doping-induced changes to the structure of the conjugated polymer.

## 2.2 Introduction

Electrical doping of organic semiconductors requires the incorporation of small molecules that chemically oxidize (*p*-type) or reduce (*n*-type) the organic semiconductor to form charge carriers. In many cases, dopants are added to solid thin films of semiconductors after film-casting (termed sequential doping) and consequently, controlled doping requires understanding of mass transport of the dopant into the film.[116] Doping induces complex changes to electronic, thermal, and mechanical properties alongside changes to crystalline and mesoscopic morphology.[117,118] Moreover, diffusion of dopants is a heterogeneous process owing to their semicrystalline nature which results in domains with varying electronic and ionic conductivity.[104,119] Improved control of doping requires an understanding of the reactive and diffusive driving forces for dopant transport, suitable approximations for continuum models, and consideration for the complex changes to polymer properties that arise from doping.

A common doping method involves either immersion of semiconducting polymer films in solutions of the dopant (immersion doping) or thermal evaporation/sublimation of the dopant into the polymer film (vapor doping). Both methods have been used as platforms to control and investigate the mass transport of various dopants, including 2,3,5,6-tetrafluoro-7,7,8,8-tetracyanoquinodimethane ($F_4TCNQ$),[18,120–123] molybdenum tris(1-(methoxycarbonyl)-2-(trifluoromethyl)ethane-1,2-dithiolene) (Mo(tfd-$CO_2$Me)$_3$),[124,125] and phosphomolybdic acid (PMA).[126] Within these studies, diffusion has been quantified in the context of: (1) diffusion of the dopant as it is introduced into the film and (2) diffusion of the dopant in the solid state following the doping process. Temperature, equilibrium between the neutral and ionized dopant, the size and shape of the dopant, the degree of solvent swelling, and doping reaction mechanism are all likely to affect the degree by which the dopant diffuses into the film.[121,123,125–128]

The most extensive models of dopant diffusion have examined the diffusion coefficients of both the neutral and ionized form of two common dopants ($F_4TCNQ$ and Mo(tfd-$CO_2$Me)$_3$), both of which oxidize the conjugated polymer by a charge transfer mechanism.[120,125,129] A study of diffusion of Mo(tfd-$CO_2$Me)$_3$ into poly(3-hexylthiophene) (P3HT) thin films and found that the surface concentration of Mo(tfd-$CO_2$Me)$_3^{\bullet-}$ saturates quickly and is essentially immobilized by coupling with the charged P3HT$^{\bullet+}$.[125] A study of the in-plane diffusion of $F_4TCNQ$ and a larger derivative ($F_4MCTCNQ$) in semiconducting polymers, found that the $F_4TCNQ$ diffuses approximately 1-2 orders more quickly than its radical anion.[120] Both considered dopant adsorption capacity and found that ionized dopants are the majority species, transported predominantly through the amorphous domains.

Here, we focus on the transport of a Brønsted acidic dopant, bis(trifluoromethane)sulfonimide (HTFSI), introduced into P3HT from the solution phase. To understand the individual contributions of doping reaction and diffusion to the overall process, we first investigated the proposed Brønsted acid doping mechanism and find that proton transfer limits the overall rate of the doping reaction. By measuring the depth-dependent dopant concentrations we find that deuterium (from a labeled acid dopant) is retained in significant quantities and that doping is diffusion-limited in films >100 nm in thickness. Complementary surface-sensitive grazing incidence X-ray scattering confirms that charge carrier-induced structural changes are most concentrated at the surface, likely due to doping induced rigidity that impedes further diffusion of dopants.

## 2.3 Results and Discussion

### 2.3.1 Diffusion-limited thickness dependence of electrical conductivity

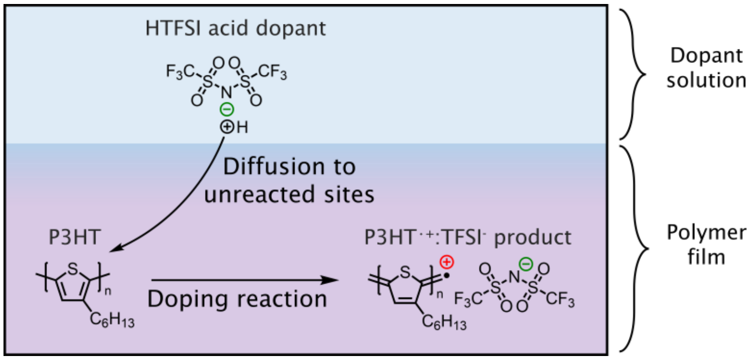

**Figure 7. Schematic of immersion doping process**

*First, dopants must diffuse into the polymer that is a mixture of reacted and unreacted units. Upon reaction, the polymer segment and neutral dopant are converted to the charge carrier-counterion product.*

The thickness dependence of the electrical conductivity of P3HT films doped by immersion in a solution of HTFSI suggests that diffusion can limit doping. Immersion doping is a diffusive-reactive process which requires diffusion of dopants past regions of reacted polymer (Figure 7). Upon diffusion to unreacted segments, the polymer segment and neutral dopant undergo a reaction to produce the charge carrier-counterion product. When 10 nm- and 265 nm-thick films of P3HT are immersed in a solution of the strong acid HTFSI, their conductivity varies inversely with film thickness. Undoped 265 nm thick films of P3HT exhibit electrical conductivities around $10^{-4}$ S/cm (10 nm films were 2 orders more conductive due to background doping, see Figure 8). For any given set of immersion times, the thinner films exhibit conductivities approximately an order greater than those of the thicker films. The limited conductivity of the thicker film is consistent with an estimate that only the surface layer is doped. A possible interpretation is that limited diffusion of dopants can result in conductivities which vary inversely with film thickness.

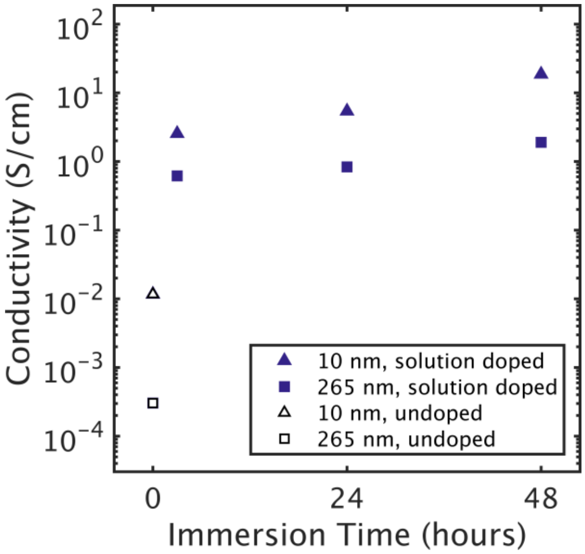

**Figure 8. Thickness dependent conductivity of immersion doped P3HT**

*Conductivity of 10 nm and 265 nm thick P3HT films immersed in acidic solutions [148 mM HTFSI ($CH_3OH$)] for varying times while exposed to air. The fact that a much thicker film exhibits limited conductivity suggests a surface-limited doping mechanism.*

### 2.3.2 Model of the Brønsted acidic doping process

The proposed mechanism of doping by strong Brønsted acids differs significantly from that of charge transfer dopants.[130–134] While charge transfer dopants can directly oxidize *p*-type conjugated polymers due to their high electron affinity, molecular doping via Brønsted acids have been suggested to follow a three-step mechanism, with the initial proton transfer and interchain oxidation mechanism expected to be endergonic and the final dehydrogenation step driving the reaction forward (see Figure 9).[131,132,134–136] A recent study reported direct observations of $H_2$ evolution during Brønsted acidic *p*-doping, though the rate limiting steps have yet to be confirmed experimentally.[137] Here we investigate the overall doping reaction to first determine the rate limiting step before considering diffusion limitations.

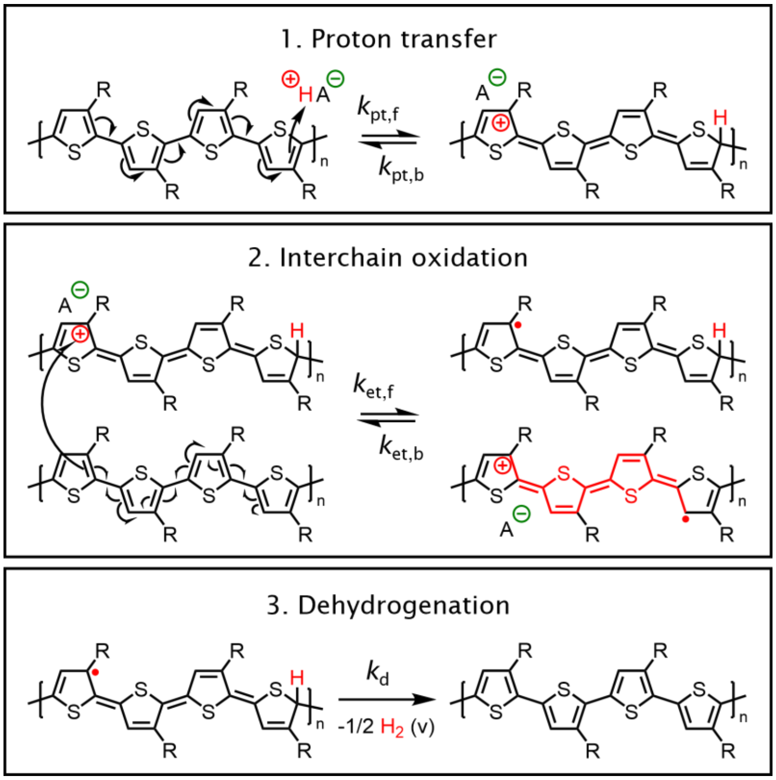

**Figure 9. Proposed mechanism of Brønsted acid doping**

*In the first step, the acid protonates a polymer segment, generating a charged intermediate. In the second step, the protonated intermediate oxidizes a nearby neutral segment, generating a polaron and a second hydrogenated radical intermediate. In proposed the third step, two radical intermediates react and* $H_2$ *gas is evolved.*

In the first step, the polythiophene backbone ($B$) is protonated by the acid ($H^+$), generating a positive charge delocalized along the polymer backbone ($HB^+$), compensated by the counterion ($A^-$) (Equation 11).

$$\mathrm{H}^{+} + A^{-} + B \leftrightharpoons \mathrm{H}B^{+}\!:\!A^{-} \qquad \text{Equation 11}$$

In the second step, the H$B^+$ intermediate oxidizes a nearby neutral chain ($B$), resulting in a hydrogenated radical intermediate (H$B^\bullet$) and polaron ($B^{\bullet+}$). Because of charge neutrality the counterion is associated with the polaron (Equation 12).

$$\mathrm{H}B^{+}\!:A^{-} + B \leftrightharpoons \mathrm{H}B^{\bullet} + B^{\bullet+}\!:A^{-} \qquad \text{Equation 12}$$

The proposed third dehydrogenation step, where two H$B^\bullet$ intermediates react and $H_2$ is evolved to regenerate the neutral polythiophene ($B$), is an exergonic step that drives the overall reaction forward (Equation 13).

$$\mathrm{H}B^{\bullet} \rightarrow B + 1/2\,\mathrm{H}_2\ (\mathrm{v}) \qquad \text{Equation 13}$$

To model the role of reaction rate on the immersion doping process, we consider the doping reaction by a Brønsted acid as follows. We model Equation 11 and Equation 12 with the assumption that the forward electron transfer is rapid and irreversible with the overall process limited by the forward rate of protonation (abbreviated as $k_{\mathrm{pt}}$). With this, the observed rate of reaction is limited by the forward rate of proton transfer ($k_{\mathrm{obs}} \approx k_{\mathrm{pt}}$) Equation 14.

$$\frac{dc_{B^{\bullet+}:A^{-}}}{dt} = k_{\mathrm{obs}} c_{\mathrm{H}^{+}} \qquad \text{Equation 14}$$

Neutral and ionized dopant transport throughout the polymer film is modeled using the diffusion-reaction equation (Equation 15).[129]

$$\frac{\partial c_i}{\partial t} = D_i \nabla^2 c_i + R_i \qquad \text{Equation 15}$$

In Equation 15, the change in concentration with time and space of species $i$ ($\partial c_i/\partial t$) is related Fickian diffusion ($D_i\nabla^2 c_i$) and reaction rate ($R_i$). $R_i$ is defined for the acid dopant ($H^+$), polymer repeat segment ($B$), and product ($B^{\bullet+}{:}A^-$)) with Equation 16.

$$R_{\mathrm{H}^+} = R_B = -R_{B^{\bullet+}:A^-} = -k_{\mathrm{obs}} c_{\mathrm{H}^+} \qquad \text{Equation 16}$$

In Equation 16, $k_{\mathrm{obs}}$ is the pseudo first-order rate constant of the overall reaction and $c_{\mathrm{H}^+}$ is the concentration of the acid in solution.

The immersion doping experiments were controlled for dopant concentrations, film thicknesses, and immersion times to test the model. Because of the strong acidity of HTFSI (pKa < 0),[138] it is leveled by the basicity of methanol, the solvent. For all deuterated acid solutions used here, 166 mM of HTFSI was dissolved in deuterated methanol (148 molecules of $CD_3OD$ per HTFSI) which resulted in a predominantly deuterated acid, *i.e.* $CD_3OD_2^+$. Both the acid and counter ion were tracked by DSIMS using $^{19}F$ and D (deuterium) as atomic labels to access the concentration profile of the dopant through the film depth.[139,140] For the diffusion-reaction model, the concentration of the acid at the film surface was approximated as constant owing to the large excess of solution relative to the total amount of polymer. The initial concentration of P3HT segments (reactant in this scenario) was varied as a fitting parameter and held fixed through each iteration. Specifically, the solid-state concentration of

P3HT repeat units is calculated from its density and divided by a stoichiometric parameter to represent the average number of repeat units consumed per dopant in a reaction. Lastly, we note that the presence of oxygen did not significantly affect the doping process overall, with differences in concentration depth profiles [Figure 18 (Appendix) exposed to air and Figure 20 (Appendix) entirely in $N_2$] unable to be resolved within the resolution of the depth profiling technique.

### 2.3.3 Reaction rate in the absence of diffusion limitations

First, we measured the primary kinetic isotope effect upon D exchange of the acidic proton to determine whether the proton transfer reaction is rate-limiting in polaron generation as assumed by the model.[141,142] To determine reaction kinetics from *in situ* UV-vis experiments, film thicknesses were minimized to 10 nm (in contrast to the 265 nm films used in depth profiling experiments). This ensures that diffusion limitations are minimized and that the changes in absorbance are determined primarily by the rate of the overall reaction. Later, relative reaction and diffusion rates were analyzed for homogeneous diffusive-reactive transport of dopants in thin films, showing that reaction kinetics can be reasonably determined from 10 nm-thick films.

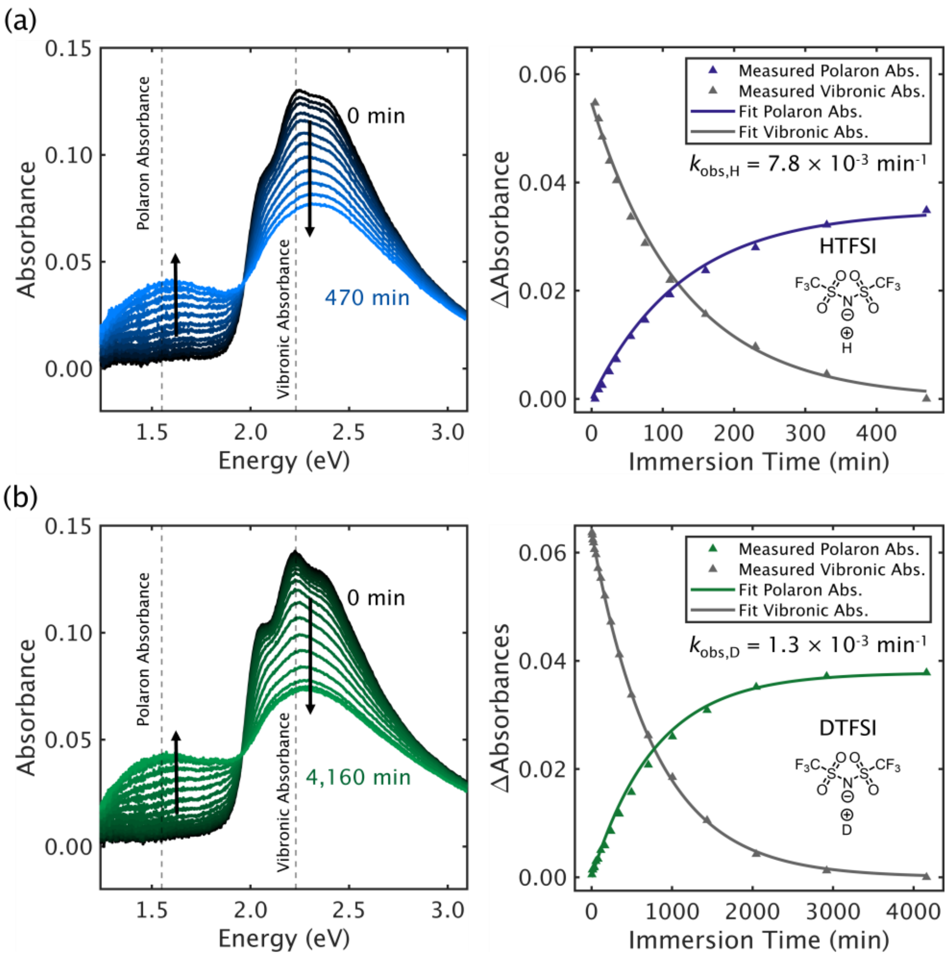

**Figure 10. HTFSI immersion doping kinetics from *in-situ* UV-vis absorbance spectroscopy.**

*(a) Time-resolved UV-vis spectra of 10 nm-thick P3HT film doped by immersion in a HTFSI solution (left). The polaron absorbance and neutral 0-1 vibronic absorbances are tracked at 1.55 and 2.23 eV, respectively, indicated by vertical dashed lines. The change in absorbance (right) reflects conversion the neutral P3HT to charged P3HT*$^{\bullet+}$ *with immersion-doping time and is fit to a pseudo-first order rate law. (b) Time-resolved UV-vis spectra of an identically prepared 10 nm-thick P3HT film in DTFSI solution (left) and corresponding change in polaron absorbance over time.*

Time-resolved UV-vis shows clear differences in the rate of polaron generation between films immersed in solutions of protonated and deuterated acid, with the DTFSI solution-doped film requiring 6 times longer than the HTFSI solution-doped film. To extract rate coefficients and assess the kinetic isotope effect, two models are employed: (1) a numerical solution to the Equation 15, to assess the full model implementation in the limiting case of no diffusion limitations, and (2) a simplified model assuming reaction-controlled kinetics and a pseudo-first order rate law.[135,143–145] The Damköhler number (Da), defined in Equation 17, describes the relative contributions of diffusion and reaction rates from Equation 15.

$$\mathrm{Da} = \frac{\text{reaction rate}}{\text{diffusion rate}} = \frac{k_{\mathrm{obs}} l^2}{D_{\mathrm{H^+}}} \qquad \text{Equation 17}$$

In Equation 17, $k_{\mathrm{obs}}$ is the pseudo first-order rate of the overall reaction (able to be converted to the second-order rate constant by normalizing by the solution concentration of the acidic dopant, $c_{\mathrm{H+},0}$), $l$ is the film thickness, and $D_{\mathrm{H+}}$ is the acid dopant diffusion coefficient. As a ratio of reaction and diffusion rates, Da $\gg$ 1 indicates a fast reaction and diffusion-limited process and Da $\ll$ 1 indicates the opposite. By minimizing the thickness of the film, the relative rate of reaction to diffusion can be minimized to allow reaction kinetics to control the time-dependent absorbance. We verify this for 10 nm P3HT films by fitting a solution to the differential mole balance that describes the time-dependent optical absorbance (Equation 18 and Equation 19).

$$A_B(t) = \varepsilon_B l c_B [\exp(-k_{\mathrm{obs}} t)] \qquad \text{Equation 18}$$

$$A_{B^{\bullet +}}(t) = \varepsilon_{B^{\bullet +}} l c_B [1 - \exp(-k_{\mathrm{obs}} t)] \qquad \text{Equation 19}$$

In Equation 18, $A_B(t)$ is the time-dependent change in the neutral vibronic absorbance of P3HT, $\varepsilon_B$ is the extinction coefficient of P3HT, $l$ is the film thickness, $c_B$ is the P3HT polymer segment concentration (assuming 10 repeat units per segment), $k_{\mathrm{obs}}$ is the pseudo first-order rate of the overall reaction, and $t$ is the reaction time. Similarly, in Equation 19, $A_{B^{\bullet +}}(t)$ is the time-dependent change in polaron absorbance and $\varepsilon_{B^{\bullet +}}$ is the extinction coefficient of the polaron product.

For the full diffusion-reaction system, the concentration profiles are numerically solved assuming $D_{\mathrm{H+}} \gg k_{\mathrm{pt}} l^2$ and converted to absorbance in the same way. Both fits to the diffusion-reaction equation (Equation 15) and the analytical solutions to the differential mole balance (Equation 18 and Equation 19) result in the same reaction rate and when plotted, give overlapping curves that reinforce that doping of 10 nm films is suitable for determining reaction rate kinetics [see Figure 15 (Appendix) for comparison of fits]. To fit changes in the polaron absorbance, 10 P3HT repeat units are assumed to form one reactive segment, commensurate with estimates from ENDOR measurements in similar systems.[136,146] Later, this stoichiometric parameter is varied when fitting the experimentally measured dopant concentration profiles further justifying that 10 repeat units per reactive segment is reasonable.

Upon fitting the reaction rate from protonated and deuterated acid doped films, a primary hydrogen kinetic isotope effect, $k_{\mathrm{pt,H}}/k_{\mathrm{pt,D}}$ of 6, was observed. While undoped, the P3HT films exhibits well-defined vibronic absorbances between 2 eV and 2.5 eV owing to the highly aggregated and semicrystalline morphology of P3HT in the solid state. Tracking the polaronic absorbance (centered at 1.55 eV) and neutral 0-1 vibronic transition (centered at 2.23 eV) enables generation of polarons and consumption of the neutral P3HT to be monitored. On the right side of Figure 10, the observed changes in polaron and vibronic absorbances are fit to Equation 5 assuming $D_{\mathrm{H+}} \gg k_{\mathrm{pt}}l^2$ ($D_{\mathrm{H+}} = 500$ nm$^2$ min$^{-1}$). The fits closely track the change in polaronic and vibronic absorbances for both protonated and deuterated acid doped films, differing significantly only in the reaction rates ($7.8 \times 10^{-3}$ min$^{-1}$ and $1.3 \times 10^{-3}$ min$^{-1}$, respectively). From this, we conclude that the electron transfer step is fast compared to the proton transfer step and that the initial proton transfer step limits the rate of the overall reaction in the absence of limits of mass diffusion. Lastly, we note that change in absorbance features follow from the second step, thus the third dehydrogenation step is silent in the UV-vis spectra.

### 2.3.4 Stable dopant concentration gradients from diffusion-limited doping

To study the fate of the proton from the acidic dopant after formation of the charge carrier, we measured the retention of D using dynamic secondary ion mass spectrometry (DSIMS) (Figure 11). In the case of complete retention of the acidic deuterium, D is expected to be retained in stoichiometric quantities with the TFSI$^-$ counterion. While the TFSI$^-$ concentration can be tracked by complementary XPS and DSIMS of fluorine, H/D are not accessible in XPS. Moreover, expected concentrations of D added by the labeled acid are low considering the expected doping levels and potential loss of D by the proposed dehydrogenation step. Assuming that completely doped P3HT$^{\bullet+}$ film contains 1 TFSI$^-$ per 10 repeat units, the TFSI$^-$ density should be ~$10^{20}$ molecules cm$^{-3}$. The corresponding expected concentration of H and

D (at natural abundance) are ~$10^{23}$ and ~$10^{19}$ $cm^{-3}$, respectively. Thus, D added by the doping process can be observed by DSIMS. Thicker P3HT films (265 nm) are used for depth profiling because of the resolution of DSIMS (~10 nm).

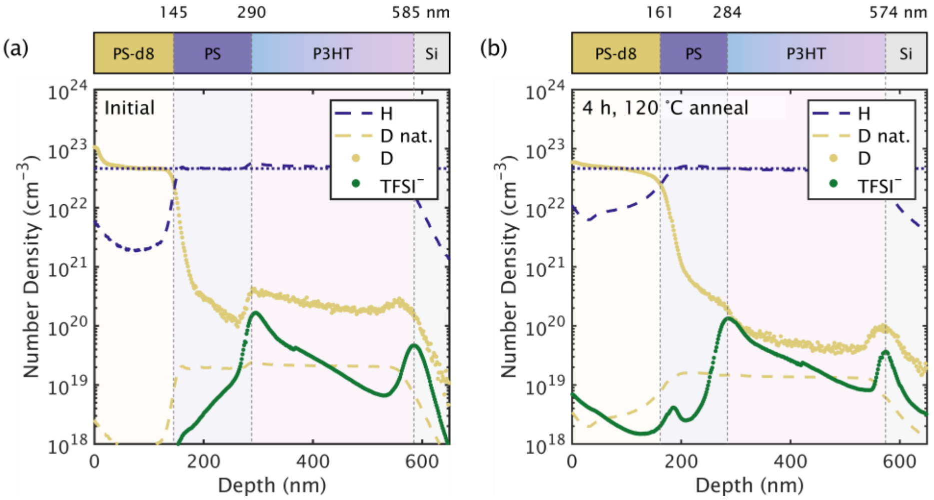

**Figure 11. Concentration depth profiles of immersion doped P3HT films**

*Concentration depth profiles of P3HT films immersion doped in DTFSI solution for 2 days, initial (a) and annealed (b) for 4 h at 120 °C. H and D concentrations are scaled to expected densities (shown as the dotted blue line) for polystyrene-d8 and polystyrene, respectively. The concentration of D expected at natural abundance (150 ppm relative to H) is shown as a reference dashed yellow line. TFSI⁻ concentrations are scaled to quantified XPS depth profiles of the same samples.*

Concentration depth profiles (Figure 11) show that the P3HT films are doped predominantly at the surface based on the TFSI⁻ concentration [additional profiles in Figure 17 (Appendix)]. For samples kept at ambient temperature, the TFSI⁻ signal peaks upon reaching the P3HT layer and then rapidly decays indicating both immediate surface enrichment and only very limited diffusion occurring after the initial doping treatments [see Figure 18 (Appendix)]. We further examined the change after thermal annealing at 120 °C for 4 hours. The similarities between the initial and annealed TFSI$^-$ profiles suggest that TFSI$^-$ diffusion is slow across a wide temperature range (ambient to 120 °C). Significant enrichment of TFSI$^-$ at the P3HT-substrate interface is an artifact of residual fluorine related to silicon wafer production.[147–149]

Our concentration depth profile measurements suggest modest D enrichment of the P3HT film from reaction with DTFSI. Samples doped by DTFSI exhibit D-enrichment as compared to HTFSI-doped samples [Figure 17 (Appendix)]. After drying ($10^{-8}$ torr at ambient temperature for 24 h), the total amount of D by integration [$(1.8 \pm 0.2) \times 10^{11}$] throughout the analyzed area of the P3HT film exceeds the total amount of TFSI$^-$ [$(2.3 \pm 0.9) \times 10^{10}$] by an order of magnitude (Figure 11a). We attribute this excess to residual $CD_3OD$; if all the D is attributed to $CD_3OD$, then there are ≈2 molecules of solvent per TFSI$^-$. The amount of D decreases substantially after thermal annealing [$(5.4 \pm 1.0) \times 10^{10}$ remaining, Figure 11b]. For comparison, control samples were immersed in $CD_3OD$ solvent only and otherwise processed identically. While both control and DTFSI solution doped samples exhibit D enrichment, the control samples exhibit much less residual $CD_3OD$ overall. This indicates that the counterion pair for the doping reaction ($CD_3OD_2^+$:TFSI$^-$) and doping of P3HT results in greater $CD_3OD$ uptake overall. After accounting for D enrichment in the control, remaining D in equivalently processed DTFSI-doped samples suggest modest D enrichment due to the doping reaction (see Figure 19 and Figure 20 in the Appendix).

The final proposed step of the doping reaction is evolution of hydrogen, but there is little direct evidence for this step in literature. Our attempts to determine the overall reaction product via NMR were inconclusive [see Figure 21 (Appendix)]. The increased amount of D in the doped samples relative to our undoped control samples could either be caused by residual $CD_3OD$ or by reaction products where the deuteron remains in the film. The D concentration profile is relatively higher than $TFSI^-$ through the film depth. This suggests it is possible that the proposed $HB^\bullet$ intermediate (Figure 9) leads to mobile $H^\bullet$ radicals that react through the thickness of the film. Given that any residual $CD_3OD$ cannot be separated from alternative reaction products, we cannot make a conclusive determination of the final products. We also note that any reaction products with the polymer could also be accompanied by side reactions due to residual trace metal species in the polymer from synthesis. For example, it has recently been shown that Pd/Ni nanoparticles impurities from synthesis in conjugated polymers can act as hydrogen evolution catalysts in other situations.[150,151] While hydrogen evolution cannot be completely ruled out, our results suggest that other reaction products may contribute and the overall reaction could be more complex than shown in Figure 9. We note that other semiconducting polymers with different backbone and sidechain designs can be doped by acids suggesting that the reaction products may vary depending on the specific material.[131,136,152–154]

### 2.3.5 Diffusion-reaction limited doping with increased film thickness

As shown in Figure 12, a much slower polaron generation rate is observed for thicker films. The absorbance of the neutral polymer for 265 nm films nearly saturates the detector, thus only the polaron absorbance is tracked. Extracting the polaron absorbance at 1.55 eV shows that the reaction continues past 3,800 minutes, as compared to the 10 nm-film which saturated around 1,000 minutes. The *in situ* UV-vis spectra shows a square-like polaron absorbance, indicative of localized polarons in low concentration.[136] Using the reaction rate fit to the thinner film, we find the diffusion of the $TFSI^-$ to be significantly slower than the neutral dopant owing to its coupling with $P3HT^{\bullet+}$. As a result, assuming diffusion of only the neutral dopant results in a best-fit diffusion coefficient of 1.0 $nm^2$ $min^{-1}$ ($1.7 \times 10^{-16}$ $cm^2$ $s^{-1}$) that approximately matches the observed rate of polaron generation. Other studies of diffusion in the solid state report the diffusion coefficient of neutral $F_4TCNQ$ (25 °C),[120] neutral $I_2$ (ambient temperature),[143] and PCBM (50 °C)[155] around $10^{-11}$ $cm^2$ $s^{-1}$ with other studies reporting similar values.[120,143,144,155,156] A study of diffusion of the dopant, $Mo(tfd\text{-}CO_2Me)_3$, considered a similar diffusion-reaction equation (Equation 15) and reported a diffusion coefficient between $10^{-15}$ – $10^{-16}$ $cm^2$ $s^{-1}$ and a reaction rate constant of $1.5 \times 10^{-2}$ $min^{-1}$ (as compared to $7.8 \times 10^{-3}$ $min^{-1}$ here).[125] We note that the dopant here is effectively the large methanoic acid-counterion pair ($CH_3OH_2^+$:$TFSI^-$) that results from the leveling effect and likely contributes to the slow diffusion observed.

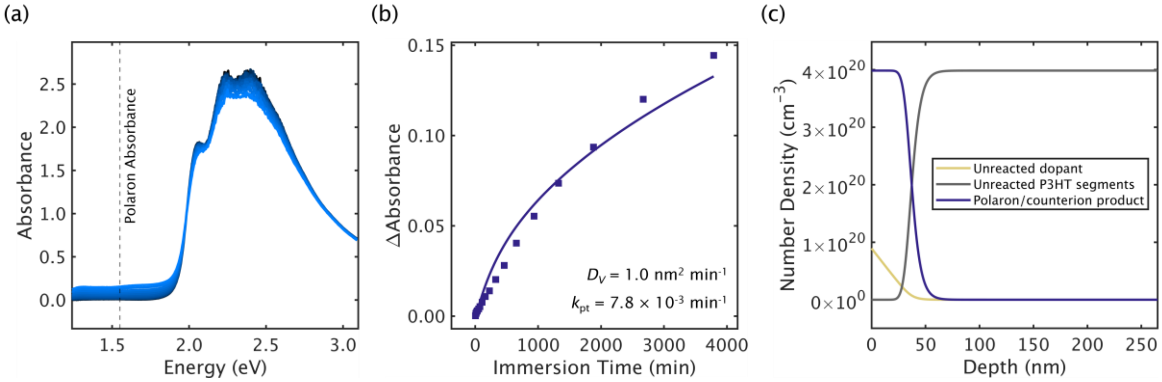

**Figure 12. Diffusion-limited Brønsted acidic doping reaction fitting**

*(a) In situ UV-vis of 265 nm-thick P3HT immersion-doped in HTFSI solution. (b) Change in polaron absorbance over time fit to the diffusion-reaction model (Equation 15), holding the same reaction rate as for the 10 nm film. (c) Predicted concentration profile from the diffusion-reaction model after 3,800 minutes (the latest data* Point *shown in (b)).*

Despite diffusion coefficient values similar those reported in literature for large dopant molecules,[120,125,143,144,155,156] our model overestimates polaron absorbance at short times and underpredicts at long times suggesting that additional considerations are needed to accurately model the rate of polaron generation. Moreover, the predicted concentration profile depicts a diffusion-limited process with a dopant saturated layer of approximately 40 nm thickness above an undoped P3HT layer (Figure 12c). Because optical spectroscopy measures the through plane average concentration, some possibilities (*e.g.*, concentration-dependent dopant diffusivities) are not observable and may manifest in an apparent lower diffusion coefficient. To consider limiting factors, we assess the dopant concentration through the film depth in the context of the diffusion-reaction model.

### 2.3.6 Dopant transport limitations from concentration depth profiles

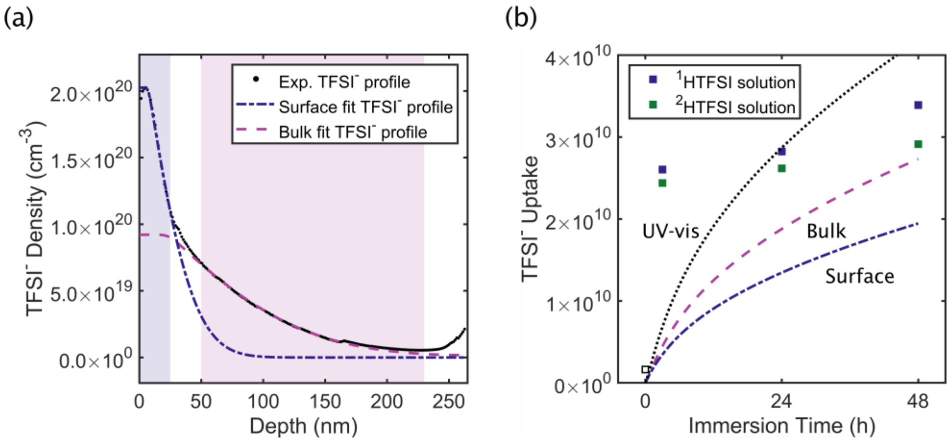

**Figure 13. Anomalous diffusion from time-correlated dopant uptake**

*(a) Depth profile of a 265 nm-thick P3HT film immersion-doped in HTFSI solution for 2 days while exposed to air. The depth profile can be fit by separating the top 20 nm (surface, blue-highlighted region) region and the remainder of the film (bulk, pink-highlighted region, 50 to 220 nm). (b) The experimentally measured total TFSI$^-$ uptake in 265 nm thick P3HT films for varying immersion times in acid solutions (blue and green squares for HTFSI and DTFSI solutions, respectively) are shown alongside theoretical dopant uptake results obtained from fitting time-resolved UV-vis spectra (dotted line), the surface layer (dash-dot line), and the bulk region (dashed line). The data* Point *at 0 minutes is a reference for the background fluorine observed in an undoped P3HT film. Details on integration and model scaling are provided in the Appendix.*

Upon analyzing the calibrated dopant concentration profile for the most highly doped sample (2 days of immersion in HTFSI solution with air exposure, Figure 13a), it is apparent that no combination of constant diffusion coefficients can produce the experimentally observed TFSI$^-$ profile. Fitting the surface region (highlighted in blue) requires approximately 5 P3HT repeat units per TFSI$^-$, reflecting the high concentration of dopants in this region. Compared to the results from fitting the change in polaron absorbance for a similarly processed UV-vis sample (Figure 12), the acid dopant diffusion coefficient ($D_{\mathrm{H+}}$, previously assumed responsible for all of the dopant uptake) is reduced from 1.0 to 0.1 nm$^2$ min$^{-1}$. This decrease in $D_{\mathrm{H+}}$ is accounted for with $D_{B\bullet+:A-}$ increased to 0.2 nm$^2$ min$^{-1}$ (previously assumed negligible). In contrast, when the region deeper within the film is considered (highlighted in pink), the ratio of P3HT repeat units to TFSI$^-$ ions is increased from 5 to 11, consistent with lower TFSI$^-$ concentration in this region. $D_{\mathrm{H+}}$ and $D_{B\bullet+:A-}$ are also increased from 0.1 to 0.5 nm$^2$ min$^{-1}$ and 0.2 to 1.8 nm$^2$ min$^{-1}$, respectively. Altogether, differences in the fits between the surface and bulk regions suggest that regions of lower dopant concentration exhibit higher dopant diffusivity.

Comparing the model-predicted curves for the varying fit diffusivities in Figure 13b to the experimentally measured dopant uptake show that concentration-dependent diffusion coefficients are needed to accurately describe dopant uptake. Earlier than 3 hours, the experimentally measured dopant uptake is much faster and drops off rapidly as compared to the model prediction. The apparent high diffusivity at short immersion doping times and apparent saturation with increasing immersion time suggest that dopant diffusivity has an inverse relationship with increasing dopant concentration. Lastly, the total TFSI$^-$ uptake between HTFSI and DTFSI solution-doped films at longer times appears to vary linearly in agreement with differences in their reaction rate. This is suggestive of a process where solutes must diffuse through reacted layers of increasing thickness before reaching reactive sites.[157]

Altogether, these results are also consistent with recent studies which found that molecular doping nominally increases the modulus of conjugated polymers, including P3HT with a variety of dopants.[117,158,159] We propose that the immersion doping process rapidly forms a doped layer at the film surface whose rigidity limits further diffusion of the dopant and thus restricts the reaction predominantly to the top 30 nm of the film.

### 2.3.7 Doping-induced structural changes at film surfaces

Evidence of surface-limited doped layers were further corroborated by angle resolved grazing incidence wide angle X-ray scattering (GIWAXS) measurements which show distinct doping-induced structural changes as a function of film depth. To evaluate the changes in structure of the doped films, known interplanar scattering features for pristine and doped P3HT were considered. More specifically, P3HT crystallizes with adjacent $\pi$-faces stacking in-plane and alkyl side chains stacking in the out-of-plane direction relative to the substrate.[160] For pristine P3HT, this results in scattering from the (020) and ($h$00) planes near 3.7 Å and 16.5 Å, respectively. Upon doping with HTFSI from the vapor phase, the alkyl chain stacking distance expands by about 1 Å from 16.5 Å and adjacent $\pi$-$\pi$ stacking distances are reduced by 0.1 Å from 3.79 Å [see Figure 23 (Appendix)]. Similar doping-induced structural changes have been observed for other conjugated polymers molecularly doped with TFSI$^-$.[152,161,162] This is consistent with other reports using a variety of different dopants where the increase in the alkyl stacking distance is attributed to dopant counterion incorporation between inter-alkyl side chains.[127] The reduction in $\pi$-$\pi$ stacking distance upon doping follows from polaron-induced attractive forces that assist in delocalizing polarons and helps to accommodate dopant counterions.[163] Because depth profiling measurements indicate a highly doped surface layer, differences in the structure at varying depths are expected using surface-sensitive angle resolved GIWAXS.[164–166]

Differences in the $\pi$-$\pi$ stacking distance, attributed to polaron formation, were observed predominantly at the surfaces of all films. In Figure 14, a complete angle resolved GIWAXS data set is shown for the most highly doped sample (a 265 nm P3HT film immersion doped in HTFSI solution for 2 days with air exposure), varying the grazing incidence angle from 0.05° to 0.13° in increments of 0.0025°. At angles less than the critical angle (0.10° for P3HT), the X-ray penetration depth is only a few nanometers, rapidly increasing to a few microns past the critical angle (Figure 14a).[167] As the incidence angle varies, the resultant scattering represents depth-weighted contributions of aggregates up to the X-ray penetration depth. Across all samples, an average difference of 0.2 Å between the (100) distance is observed at the shallowest and steepest angles, respectively (see Table 1). The modest increase in the dominant alkyl side chain stacking distance [(*h*00)] suggests that light doping throughout the film is sufficient to induce a majority of the observable inter-alkyl side chain expansion. In contrast, two $\pi$-$\pi$ stacking peaks centered at 1.68 Å$^{-1}$ and 1.75 Å$^{-1}$, respectively, are evident at the surface of all immersion-doped samples [Figure 22 (Appendix)]. We attribute the feature at 1.68 Å$^{-1}$ [labeled (020)] to a lightly doped aggregate population and the feature at 1.75 Å$^{-1}$ [(020)’] to more heavily doped aggregates. Changes to the (020) $\pi$-$\pi$ stacking distance vary distinctly at this doping regime, with the (020)’ feature predominant at the highly doped film surface and giving way to the (020) feature past the critical angle. This is reflected in Figure 14b by the relative intensity of peaks fit to each feature that vary consistently with decreasing doping levels as X-ray penetration depth increases. Similar shifts were observed during *in-situ* doping of P3HT in an organic electrochemical transistor with TFSI$^-$ as the counterion.[162]

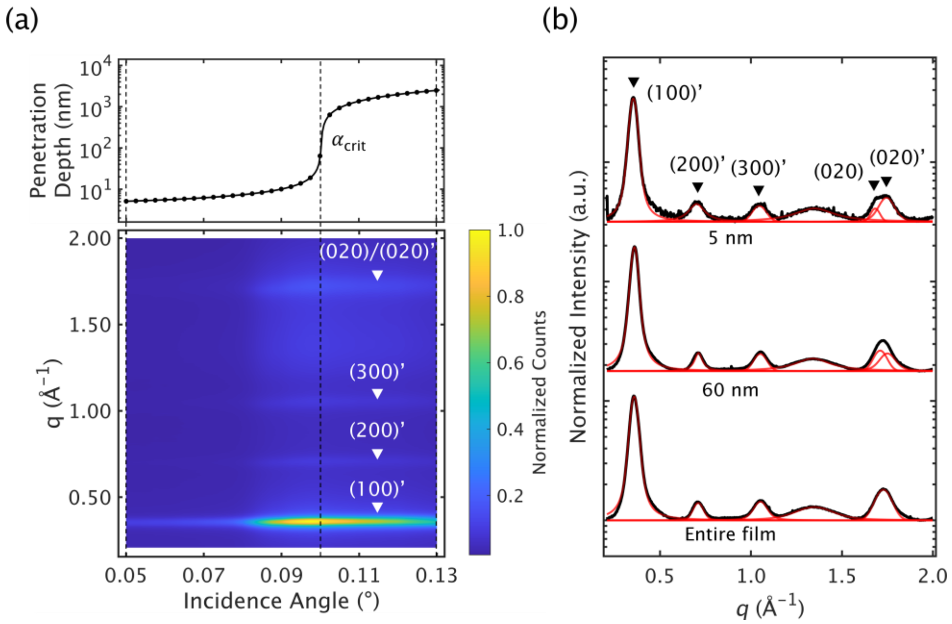

**Figure 14. Angle-dependent GIWAXS of surface-doped P3HT**

*(a) X-ray penetration depth varies with grazing incidence angle, scattering from the top few nanometers at shallow angles to the entirety of the film thickness at greater incidence angles (top). Black dots correspond to angles at which grazing incidence measurements were taken. Surface plot of radially integrated scattering intensity versus magnitude of the scattering vector, q, and grazing incidence angle (bottom). (b) Radially integrated scattering intensity at the shallowest angle (0.05°, c.a. 5 nm), critical angle (0.10°, c.a. 60 nm), and deepest angle measured (0.13°, entire film), showing differences in unit cell dimensions induced by doping at the surface.*

Lastly, we note that the structure of the acid doped P3HT is not significantly affected relative to other dopants. While NMR experiments were inconclusive in determining any chemical changes during doping, X-ray scattering suggests that it is unlikely to occur along the polymer backbone within ordered regions. For polythiophenes, trigonal $sp^2$ bonding results in a planar backbone geometry that helps facilitate $\pi$-$\pi$ stacking along the (020) direction. The doping-induced addition of a backbone proton bond would result in tetragonal $sp^3$ bonding that disrupts $\pi$-$\pi$ stacking structure. Instead, scattering from the acid-doped P3HT displays changes similar to those observed by other non-acidic dopants, *e.g.*, $F_4$TCNQ.[122] We suggest that within the doping regime here ($10^{19}$ to $10^{20}$ $cm^{-3}$), doping in the bulk of the film takes place predominantly within disordered regions and near the disordered-ordered interfaces based on comparison with *in-situ* measurements of P3HT electrochemically gated with $TFSI^-$ counterions.[162]

## 2.4 Conclusions

Sequential doping of conjugated polymer films is a complex process due to doping-induced changes in the polymer that concomitantly affect the transport of dopants. Here we found a significant kinetic isotope effect with Brønsted acid-based doping demonstrating that proton transfer limits the rate of polaron generation in the absence of limitations of diffusion. Modest amounts of acidic deuterium are retained in doped films suggesting other possible reactions than $H_2$ evolution proposed in the literature. Using thicker P3HT films, we consider both reaction and diffusion processes, finding that the doping process is diffusion limited in this system. Detailed measurements of the dopant concentration profile show that the dopants are predominantly confined to the P3HT surface, suggesting an inverse relationship between doping level and dopant diffusivity. These limitations manifest in limited conductivity of thick P3HT films (as compared to uniformly doped films) as well as surface-confined doping induced structural changes. This work demonstrates that both reactive and diffusive driving forces are important for understanding the efficiency of doping processes.

### 2.5 Acknowledgements

We acknowledge support from the U.S. Army Research Office and accomplished under cooperative agreement W911NF-19-2-0026 for the Institute for Collaborative Biotechnologies. This research made use the Stanford Synchrotron Radiation Lightsource, SLAC National Accelerator Laboratory, is supported by the U.S. Department of Energy, Office of Science, Office of Basic Energy Sciences under Contract No. DE-AC02-76SF00515. A portion of this work was performed in the UCSB Nanofabrication Facility, an open access laboratory. The research reported here made use of shared facilities of the National Science Foundation Materials Research Science and Engineering Center (MRSEC) at UC Santa Barbara (NSF DMR 1720256), which is a member of the Materials Research Facilities Network (www.mrfn.org). P.H.N gratefully acknowledges support from the National Science Foundation Graduate Research Fellowship Program under grant no. 2139319. Any opinions, findings, and conclusions or recommendations expressed in this material are those of the authors and do not necessarily reflect the views of the National Science Foundation.

## 2.6 Appendix

### 2.6.1 Experimental methods

#### 2.6.1.1 P3HT Film Preparation

P3HT (74 kDa, 2.2 PDI, 96% regioregular) was purchased from Rieke Metals. Solutions were made by dissolving P3HT in 1:1 (v:v) chlorobenzene:dichlorobenzene, stirred overnight at 120 °C in an $N_2$ glovebox. Solutions were cooled to room temperature and filtered through 0.45 μm PTFE filters prior to spin-casting. For GIWAXS and XPS/DSIMS samples, native oxide silicon substrates were cleaved from wafers and cleaned by sequential sonication in acetone, DI water, and isopropanol. UV-vis substrates were cut from thin quartz coverslips to fit in standard 1 cm quartz cuvettes and cleaned using the same procedure. For conductivity measurements, 15 × 15 mm quartz substrates were cleaned using the same procedure. After drying, substrates were plasma cleaned with 300 mTorr of air at 100 W, then immersed in isopropanol until immediately before spin casting. Thin (10 ± 2.4 nm thick) films were made by spin casting 5 mg/mL P3HT (in 1:1 chlorobenzene:dichlorbenzene) at 3,000. Thicker (265 ± 11 nm thick) films were spun from 35 mg/mL solutions at 1,000 RPM. Subsequently, all samples were annealed in $N_2$ at 120 °C for 30 minutes.

#### 2.6.1.2 Immersion Doping Procedure

Doping solutions were made by dissolving HTFSI (trifluoromethanesulfonimide, Sigma Aldrich) in either $CD_3OD$ (166.2 mM, 5 wt% HTFSI) or $CH_3OH$ (148.3 mM, 5 wt% HTFSI) in a $N_2$-filled glovebox and stirred overnight. Immersion doping was performed either in a fume hood or in an $N_2$-filled glovebox (samples exposed to air are noted explicitly throughout) by immersing P3HT films in 20 to 40 mL of dopant solution, and removed and dried after 3 hours, 1 day, and 2 days. Samples were further dried in high vacuum conditions ($10^{-8}$ torr, ambient temperature) overnight prior to analysis. For DSIMS samples, deuterated polystyrene (polystyrene-d8) D calibration and polystyrene (polystyrene) spacing layers are added by floating spun cast polystyrene and polystyrene-d8 films from quartz substrates onto water. The polystyrene and polystyrene-d8 films are lifted from the water bath using an O-ring, left to dry for 5 minutes, and overlaid onto the doped P3HT films to be depth profiled. After, samples were further dried overnight ($10^{-8}$ torr, ambient temperature) prior to depth profiling.

#### *2.6.1.3 In Situ* UV-Vis Spectroscopy

Film samples were placed in standard solution cuvettes such that the film surface was oriented towards the light source. Cuvettes fit with septum caps were filled with $N_2$-blanketed doping solutions and scans ranging from 190 nm to 1100 nm were acquired up to 4320 minutes (3 days). All UV-vis spectra were acquired using an Agilent Technologies Cary 60 UV-vis spectrometer and data analysis was conducted using custom MATLAB scripts. Polaron absorbance was tracked by subtracting the first spectra from all others to create difference spectra. The primary polaron absorbance and 0-1 vibronic absorbance at 1.55 eV and 2.23 eV, respectively, were tracked over time to extract doping reaction kinetics.

#### 2.6.1.4 Conductivity Measurements

For four-point probe conductivity measurements, shadow mask evaporation was used to deposit 30 nm gold electrodes (1 mm width, 0.2 mm length) using an Angstrom Engineering metal evaporator. Measurements were performed under inert $N_2$. Current ranging from 100 to

-100 μA, was supplied using a Keithley 6220 precision current source and voltage was measured using a Keithley 2400 source meter. Reported conductivities are the average of two measurements on each sample.

### 2.6.2 Kinetic models applied to UV-vis spectroscopy

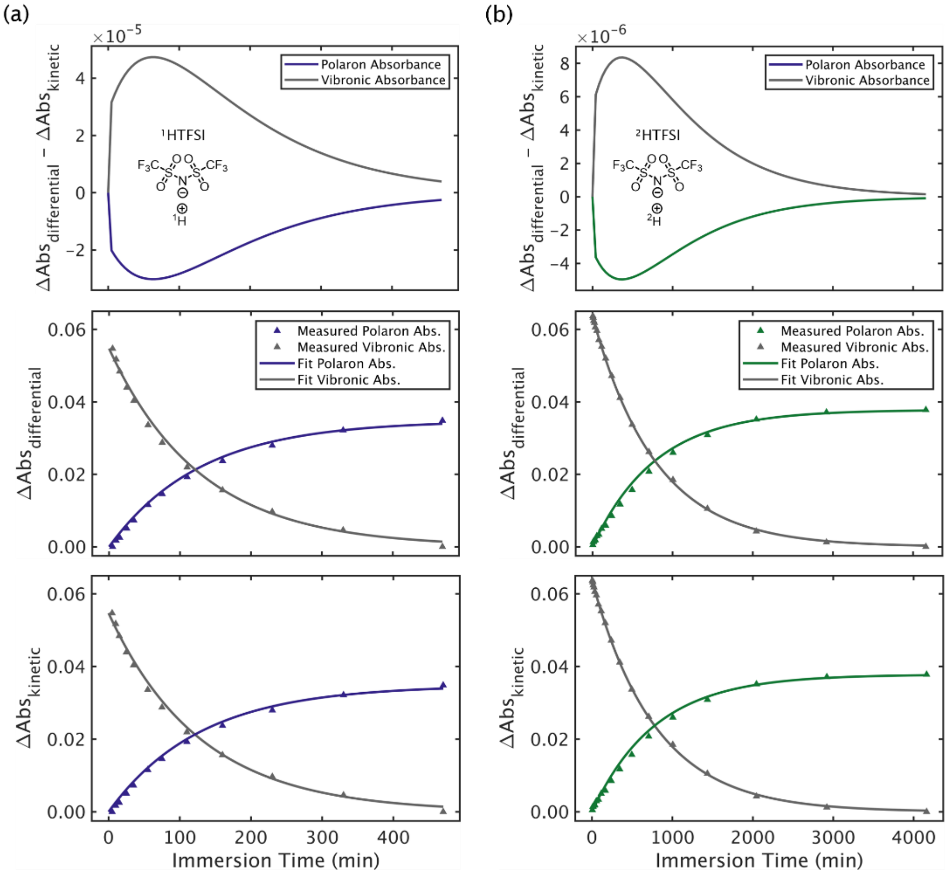

**Figure 15. Comparison of numerical and analytic kinetic model fits**

*(a) (Top) Differences between fit of the diffusion-reaction equation (Equation 15) ($\Delta Abs_{differential}$, middle) and differential mole balances (Equation 18 and Equation 19) ($\Delta Abs_{kinetic}$, bottom) for 10 nm P3HT films in (a) HTFSI ($CH_3OH$) and (b) DTFSI ($CD_3OD$) solutions.*

### 2.6.3 High depth resolution DSIMS quantified via XPS

Immersion-doped samples were cleaved in two for concurrent XPS and DSIMS depth profiling measurements. Additional polystyrene and deuterated polystyrene layers were floated onto DSIMS samples to provide deuterium calibration standards. F 1s atomic percentage was quantified from XPS depth profiles using the Avantage software suite provided by Thermo Fisher Scientific Inc. A complete XPS depth profile was taken for one sample to calibrate the etch time with etch depth using the known P3HT film thickness. Similarly, DSIMS depth profiles were converted from sputtering time to depth using the known P3HT film thickness. Least-squares fitting was performed to scale the $^{19}$F DSIMS profile to the F 1s XPS depth profile. All samples demonstrated good agreement between the XPS and SIMS fluorine profiles (Figure 16)**.** The XPS F 1s signal approaches the noise floor after approximately 1 atomic % at the survey scan conditions employed, corresponding to a noise floor of approximately $10^{20}$ cm$^{-3}$ and depth of 30 nm.

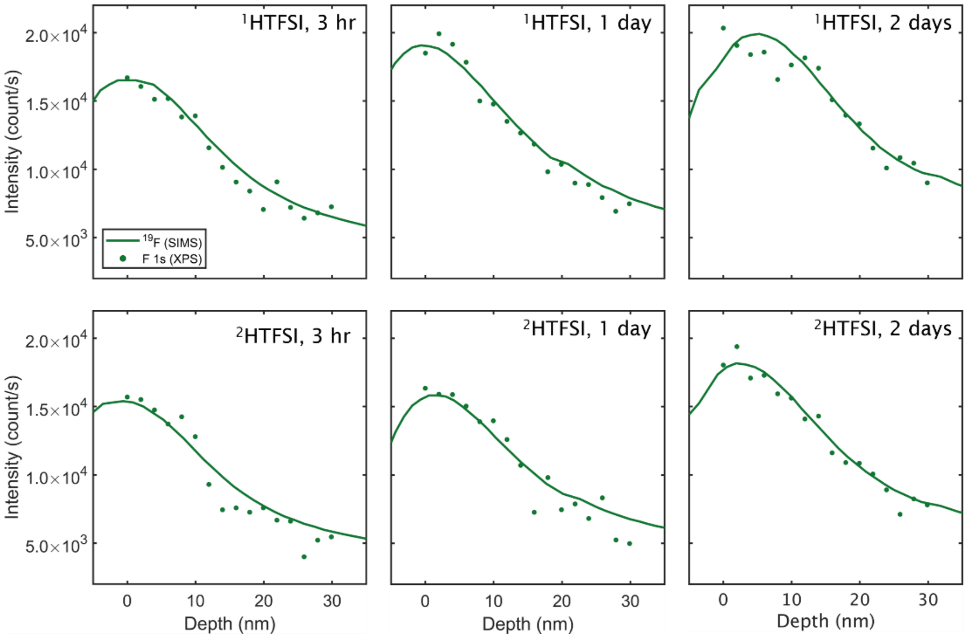

**Figure 16. Comparison of DSIMS and XPS fluorine depth profiles**

*Matching* $^{19}$*F and F 1s profiles from XPS and DSIMS depth profiling, respectively, for samples whose dopant uptake are summarized in Figure 13 of the main text. All samples were exposed to air during the doping process.*

The F 1s peak is quantified at each depth, allowing for the $^{19}$F profile to be scaled accordingly using least-squares fitting. Resulting depth profiles retain high depth resolution and signal-to-noise ratio while being stoichiometrically calibrated. Reported total D and TFSI$^-$ follow from integrating concentration depth profiles through the 265 nm P3HT region and accounting for the $3.1 \times 10^{-5}$ cm$^2$ regions analyzed by DSIMS. Model results (presented in Figure 13 of the main text) are scaled in the same way for direct comparison with experimental results.

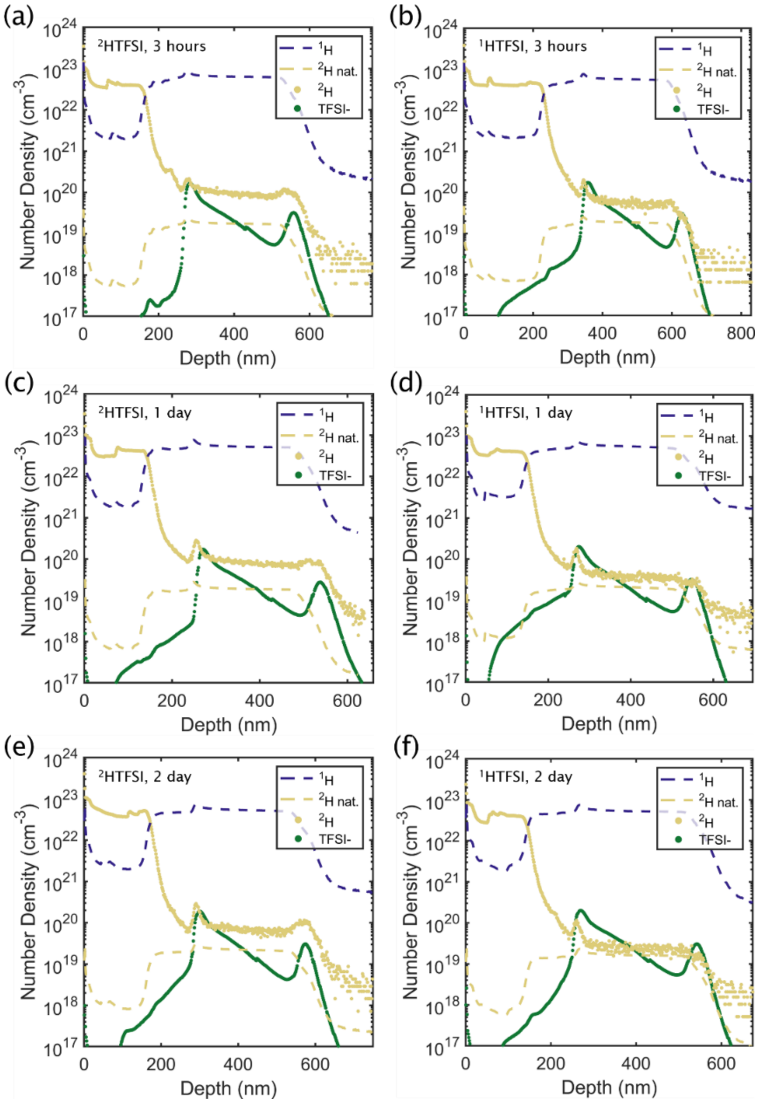

**Figure 17. Concentration depth profiles of H/DTFSI immersion-doped P3HT films**

*Concentration depth profiles of P3HT films immersion doped in in DTFSI (left column) and HTFSI (right column) solution 3 hours (a, b), 1 day (c, d), and 2 days (e, f), corresponding to dopant uptake measurements summarized in Figure 13 of the main text. All samples presented here were exposed to air during the doping process.*

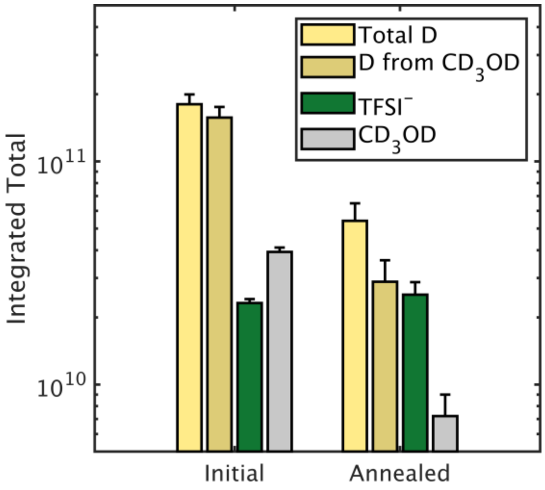

**Figure 18. D retention in DTFSI-doped P3HT films**

*Integrated D and TFSI⁻ throughout 265 nm P3HT films immersion doped in DTFSI solution. Error bars correspond to one standard deviation (N = 2).*

The integrated concentration of D throughout the P3HT film (light yellow bar) exceeds the amount of TFSI⁻ (green bar) by approximately an order of magnitude before annealing [$(1.8 \pm 0.2) \times 10^{11}$ vs $(2.3 \pm 0.9) \times 10^{10}$, respectively]. The D attributable to $CD_3OD$ (dark yellow bar) can be estimated by assuming the fraction of D originating from the doping reaction is equivalent to the amount of TFSI⁻ at most. Normalizing the remaining D provides an estimate of residual $CD_3OD$ content relative to TFSI⁻. Most of the residual $CD_3OD$ evaporates during annealing which suggests that D imparted by the doping reaction constitutes a significant fraction of the D signal after annealing.

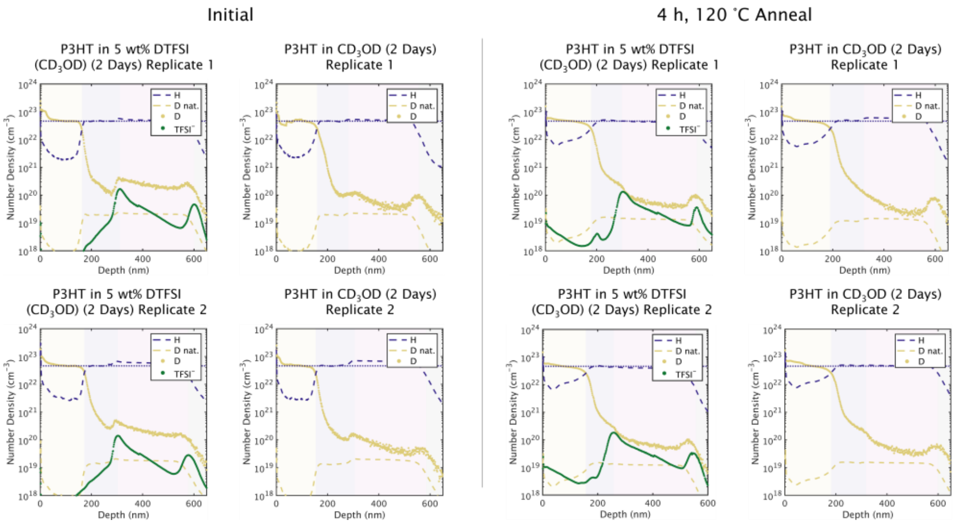

**Figure 19. Concentration depth profile comparisons between DTFSI-doped annealed and unannealed P3HT films**

*Concentration depth profiles of P3HT films immersed in DTFSI ($CD_3OD$) solution and in $CD_3OD$ solvent only. DTFSI-doped samples show significant D enrichment as compared to controls samples immersed only in $CD_3OD$ solvent (left). While most of the D disappears following the annealing process (right), residual D remains primarily at the P3HT top surface for both DTFSI-doped and control samples.*

A majority of the D enrichment from resulting from the doping process is attributable to residual $CD_3OD$ solvent (Figure 19). The annealing process removes most of the residual $CD_3OD$; however, a significant amount relative to $TFSI^-$ remains. While both annealed DTFSI-doped and control samples exhibit D-enrichment, the DTFSI-doped sample is significantly D-enriched throughout the film depth as compared to control samples. This suggests that excess D comes from the doping reaction.

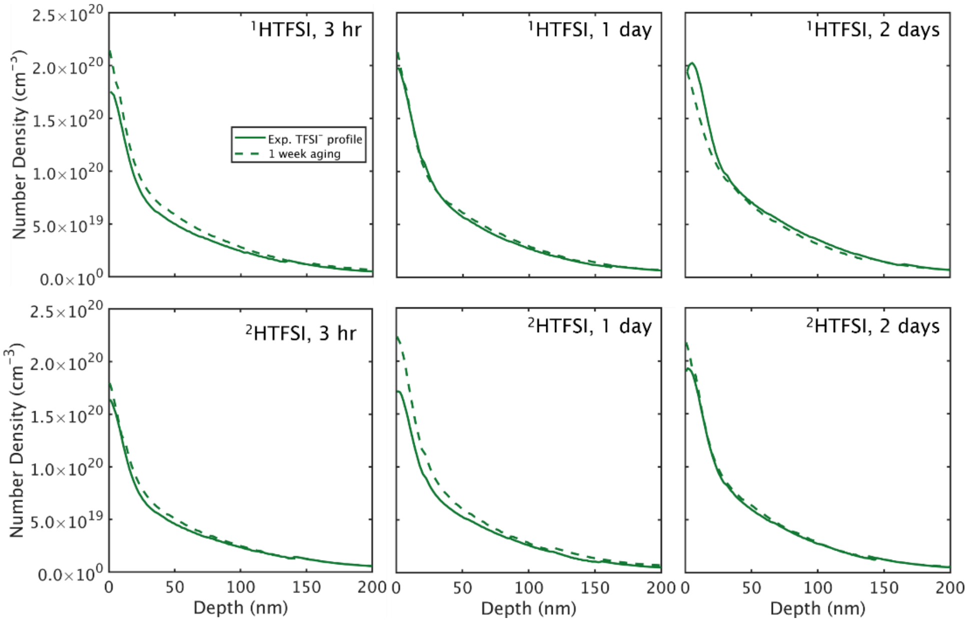

**Figure 20. TFSI$^-$ diffusion in surface-doped P3HT past 1 week**

*Effect of sample aging for 1 week. The same samples as reported in Figure 13 were measured using complementary XPS and DSIMS depth profiling.*

The quantified depth profile after 1 week of aging in an inert atmosphere at ambient temperature shows that TFSI$^-$ diffusion does not occur significantly within the 1-week time frame from sample doping to sample measurements. Deviations between the TFSI$^-$ profiles of the samples as reported and after 1 week are below the interfacial resolution of the technique.

### 2.6.4 CP/MAS NMR of P3HT and Brønsted acid-doped P3HT

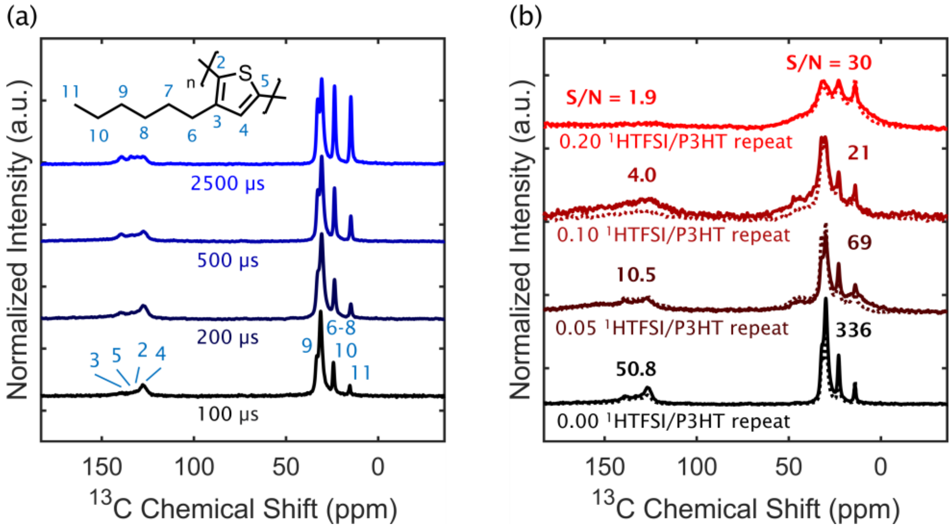

**Figure 21. Solid state CP/MAS $^{1}$H$\rightarrow$$^{13}$C NMR spectra of pristine and HTFSI-doped P3HT**

*Solid state cross-polarization magic angle spinning $^{1}$H$\rightarrow$$^{13}$C NMR spectra of (a) pristine and (b) HTFSI-doped P3HT. (a) Decreasing the cross-polarization contact time between $^{1}$H and $^{13}$C highlights carbons in proton-abundant environments. There is only one native proton on the P3HT backbone (position 4, P3HT repeat unit labeled on the inset) whose position is highlighted at short contact times. (b) Cross-polarization at short (200 µs) and long (500 µs) contact times for P3HT:HTFSI at different dopant to polymer repeat unit ratios. Signal-to-noise (S/N) ratios (for 200 µs contact time experiments, labeled aromatic and aliphatic regions) decrease with increasing dopant to polymer repeat unit ratios.*

$^{1}$H→$^{13}$C cross-polarization magic-angle-spinning NMR experiments were performed on a 500 MHz Bruker Avance NMR Spectrometer equipped with a double-resonance 4 mm NMR probe at a magnetic field strength of 11.7 T and a MAS frequency of 10 kHz. For the pristine

P3HT sample, 4096 scans were acquired with cross-polarization contact times of 100, 200, 500, and 2500 μs. For the HTFSI-doped P3HT samples of varying dopant levels, CP/MAS experiments with 200 μs and 500 μs contact times were acquired. For the 0.05 HTFSI/P3HT sample, 8192 scans were acquired, and for the 0.10 and 0.20 HTFSI/P3HT samples 16384 scans were acquired in order to observe signals above the noise level in the aromatic $^{13}C$ NMR spectrum region. The signal-to-noise (S/N) ratios listed in Figure 21b is normalized to 16384 scans for each sample for the purpose of comparison. A recycle delay of 1 s was used for all experiments, and SPINAL64 $^{1}H$ heteronuclear decoupling was applied during acquisition.

In the CP/MAS contact time experiment, polarization is transferred from abundant $^{1}H$ to $^{13}C$ to enhance signal. The length scale of polarization transfer varies with time; short contact times are able to highlight carbons in proton-rich environments. For any significant acidic proton retention, the proton is expected to bond to the P3HT backbone; however, CP/MAS NMR of HTFSI-doped P3HT does not unambiguously indicate additional protons added to any potential bonding sites (see Figure 21). Here, we also note that the signal-to-noise ratio decreases with increasing HTFSI/P3HT repeat ratio due to increasing concentration of paramagnetic species (the hole-radical polaron). Paramagnetic species can prematurely relax polarization, reducing polarization transfer from $^{1}H$ to $^{13}C$ and leading to lower signal-to-noise ratios. Because of this, the CP/MAS NMR of highly doped P3HT cannot conclusively indicate whether protons are added, even for scans spanning several hours.

### 2.6.5 Angle-Resolved GIWAXS of H/DTFSI-doped P3HT films

X-ray scattering was performed at experimental station 11-3 at the Stanford Synchrotron Radiation Lightsource using an X-ray energy of 12.7 keV. Angle-resolved GIWAXS scans were acquired with 100 second exposures at each incidence angle from 0.05° to 0.13° in increments of 0.0025°. During the acquisition, samples were continuously rocked in the direction perpendicular to the X-ray flux by ± 2 mm around the sample center to mitigate beam damage.

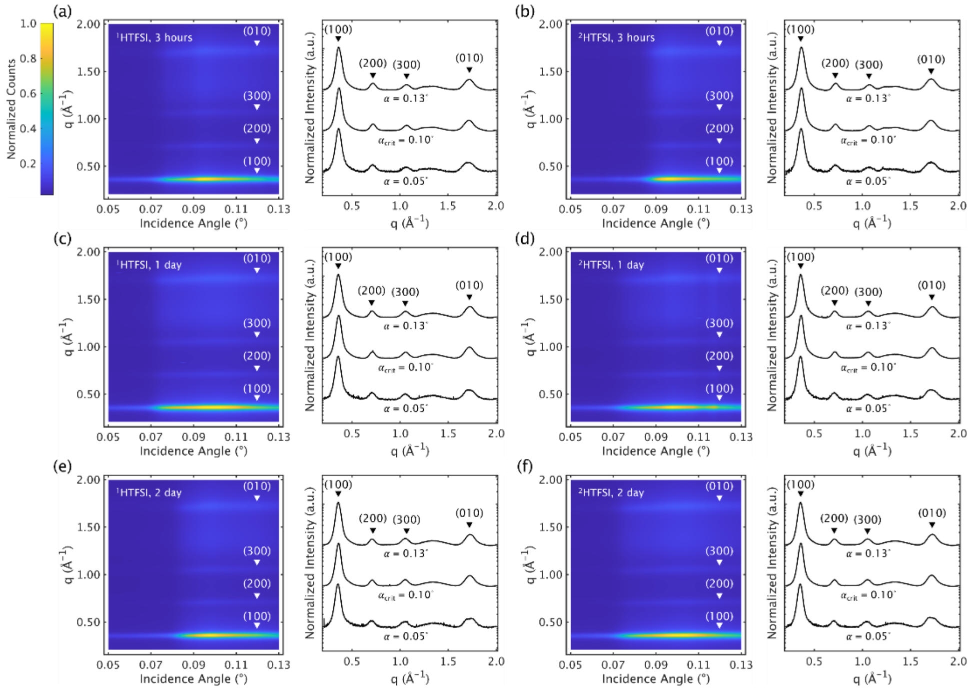

**Figure 22. Angle-Resolved GIWAXS for H/DTFSI-doped P3HT films**

*Angle-dependent GIWAXS of 265 nm P3HT immersion-doped in HTFSI solution (exposed to air) (a, c, e) and DTFSI solution (also exposed to air) (b, d, f) for 3 hours, 1 day, and 2 days. All samples exhibited an expanded (100) stacking distance and two peaks near 3.7 Å (1.7 Å$^{-1}$) at shallow incidence only, indicative of surface doping.*

## Table 2. Summary of P3HT lamellar stacking distances

*(100) stacking distances extracted from radially integrated GIWAXS data. (100) stacking distances are extracted from the average of the (100), (200), and (300) stacking distances. The reported (100) stacking distance is then the average of these at angles probing only the surface (incidence angle of 0.05° to 0.09°) and the film entirely/bulk (0.11° to 0.13°). Fitting is performed by subtracting background for each scan and least-squares fitting a Voigt line shape to (100), (200), (300), (020) and amorphous scattering using a custom MATLAB script.*

| **Dopant Solution** | **Immersion Time** | **Surface (100) stacking distance (Å)** | **Standard Deviation** | **Bulk (100) stacking distance (Å)** | **Standard Deviation** | **Average Difference** |
|---|---|---|---|---|---|---|
| Undoped | None | 16.18 | 0.04 | 16.15 | 0.05 | 0.03 |
| HTFSI | 3 hours | 17.58 | 0.05 | 17.4 | 0.019 | 0.16 |
| HTFSI | 24 hours | 17.89 | 0.41* | 17.7 | 0.080 | 0.24 |
| HTFSI | 48 hours | 17.86 | 0.03 | 17.7 | 0.016 | 0.17 |
| DTFSI | 3 hours | 17.45 | 0.02 | 17.3 | 0.008 | 0.11 |
| DTFSI | 24 hours | 17.76 | 0.06 | 17.6 | 0.022 | 0.17 |
| DTFSI | 48 hours | 17.91 | 0.03 | 17.7 | 0.020 | 0.23 |

*****Larger standard deviation attributed to stray cosmic radiation striking the X-ray detector (zinger), visible in the detector image.

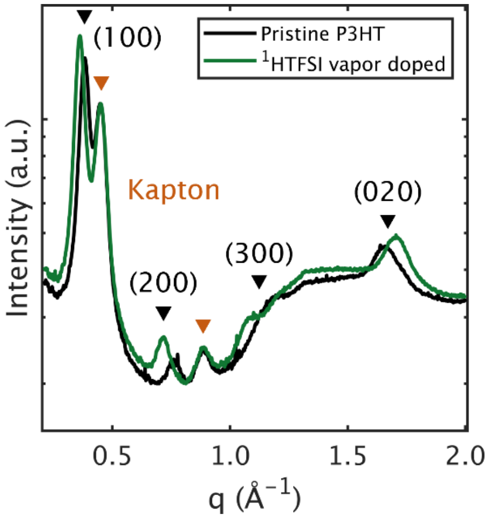

**Figure 23. Radially integrated scattering peaks from GIWAXS measurements of P3HT films doped with HTFSI from the vapor phase.**

*Data is taken at a grazing incidence angle of 0.13°, corresponding to the entire thickness of the film. Additional scattering peaks are from Kapton used to seal the scattering cell and are used for intensity normalization. Upon doping, the alkyl spacing shifts from 0.38* $Å^{-1}$ *(16.5 Å) to 0.36* $Å^{-1}$ *(17.5 Å), while the* $\pi$-$\pi$ *stacking shifts from 1.66* $Å^{-1}$ *(3.8 Å) to (1.70* $Å^{-1}$*) (3.7* $Å^{-1}$*).*

### 2.6.6 AFM-measured texture of pristine and profiled P3HT films

To assess whether DSIMS signal broadening throughout the depth was likely due to beam damage, atomic force micrographs were measured for pristine and doped P3HT films (see Figure 24 and Figure 25). Alignment of rows was performed using third-order polynomials. In both measurements, the sputtered surface is smoother than the pristine surface as quantified by the roughness average. While a rougher surface may be a byproduct of the immersion-doping process, these results also suggest that the elemental concentration profiles did not appreciably broaden due to beam damage.

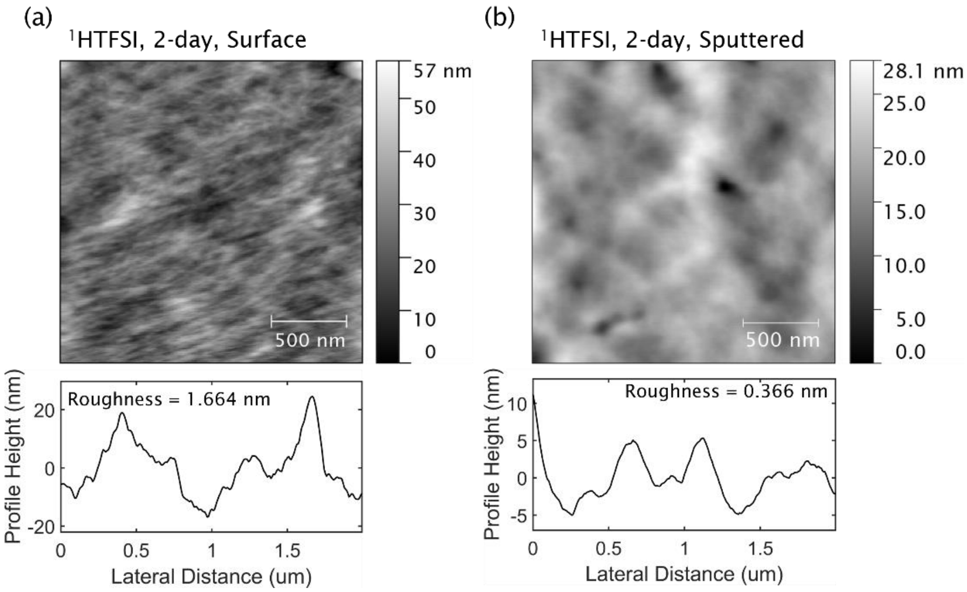

**Figure 24. AFM of pristine and sputtered HTFSI-doped P3HT film surfaces**

*Atomic force micrographs of pristine (a, top) and* $O_2^+$*-sputtered HTFSI immersion-doped P3HT films (b, top). Height profiles across micrograph mid*Points *show that depth profiling does not promote roughening of the sputtered surface. This suggests that sputtering-induced damage is not likely to cause broadening of the DSIMS depth profiles.*

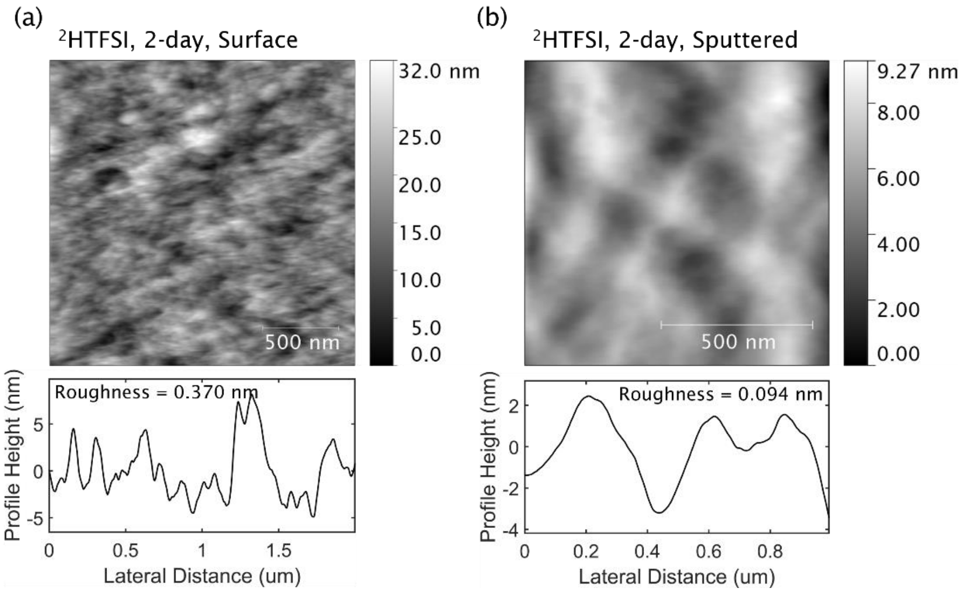

**Figure 25. AFM of pristine and sputtered DTFSI-doped P3HT film surfaces**

*Atomic force micrographs of pristine (a, top) and O2+-sputtered DTFSI immersion-doped P3HT films (b, top). Height profiles across micrograph mid*Points *show that depth profiling does not promote roughening of the sputtered surface. This suggests that sputtering-induced damage is not likely to cause broadening of the DSIMS depth profiles.*

# Chapter 3 – Reversible Modulation of Conductivity in Azobenzene Polyelectrolytes using Light

Angelique Scheuermann, Javier Read de Alaniz, and Christopher Bates designed the materials. Angelique Scheuermann and Andrei Nikolaev synthesized and purified the materials. Phong Nguyen and Angelique Scheuermann characterized materials. Phong Nguyen and Angelique Scheuermann drafted the manuscript.

This chapter was reproduced in part with permissions from:

> Nguyen, P. H.*; Scheuermann, A. M.*; Nikolaev, A.; Chabinyc, M. L.; Bates, C. M.; Read de Alaniz, J. Reversible Modulation of Conductivity in Azobenzene Polyelectrolytes Using Light. *ACS Appl. Polym. Mater.* **2023**, *5* (7), 4698-4703. (*equal contribution)

## 3.1 Abstract

Incorporating light-responsive azobenzene into polyelectrolytes couples photo-induced changes in steric interactions and polarity to ionic conductivity. The reversible isomerization of an azobenzene moiety yields a 2–7 times change in ion conductivity ($\sigma_{\text{trans}} > \sigma_{\text{cis}}$) depending on polymer composition. These trends cannot be explained by differences in the glass-transition temperatures of the polymers. Instead, UV–vis spectroscopy reveals a bathochromic shift in the $\pi \longrightarrow \pi^*$ transition of *cis*-poly(azobenzene) upon adding lithium bis(trifluoromethane)sulfonimide (LiTFSI) salt, suggesting coordination of the *cis* isomer with $Li^+$ is responsible for its lower conductivity. In summary, azobenzene is a simple and convenient functional unit to control the conductivity of polymeric materials using light.

## 3.2 Introduction

Polymer electrolytes (polyelectrolytes) are candidates for solid-state electrolytes owing to their thermal/chemical stability and synthetically tunable electrochemical and mechanical properties.[168] The ionic conductivity of polyelectrolyte materials is highly influenced by the degree of the segmental motion within the polymeric matrix, which is related to the glass transition temperature, $T_g$.[169,170] Here, we hypothesized that the photoisomerization of an azobenzene side-chain functionality would allow for light-induced modulation of ionic conductivity in composite materials containing polyelectrolytes. Introducing azobenzene as a light-responsive unit into a polyelectrolyte offers the capability to remotely change ionic conductivity via light irradiation with spatial and temporal control. Given that the photoisomerization of azobenzene is known to affect polarity[171,172] and sterics/crystallinity,[173–175] a key goal is to understand how these factors influence properties relevant to ion conduction in polyelectrolytes, including polymer $T_g$ and ion coordination.

Previously, we demonstrated the synthesis of polyelectrolytes containing azobenzene for use in photodetector applications,[176] which relied on the dye-sensitizing ability of azobenzene to stimulate charge transfer with a semiconducting polymer. Here, we leverage *trans–cis* isomerization to control ionic conductivity. Past work has reported the modulation of conductivity in solvated small-molecule ionic liquids based on azobenzene due to aggregation mediated by *trans–cis* isomerization.[177–179] When incorporated into polymers, the *trans–cis* isomerization of azobenzene also changes free volume and thus $T_g$.[180–183] Moreover, past studies have shown that *cis* azobenzene can coordinate with small molecules, including metal cations.[184–191] We thus hypothesized that light-mediated changes in $T_g$ and ion coordination could result in photoswitchable polyelectrolyte conductivity with azobenzene covalently attached to the side chain.

Herein, we describe the design, synthesis, and characterization of two poly(acrylate)-based polyelectrolytes with side-chain azobenzene functionality that exhibit reversible light-stimulated changes in ionic conductivity. One contains only azobenzene functionalized side chains [termed poly(azobenzene)] and the other also includes repeat units functionalized with the ionic liquid imidazolium bis(trifluoromethane)sulfonimide ($Im^+TFSI^–$) [poly(azo-*co*-IL)]. Ultraviolet (UV) light-induced *trans–cis* isomerization and a concomitant change in $T_g$ was characterized for both polymers via UV–visible spectroscopy and differential scanning calorimetry (DSC). Once both polymers were blended with additional LiTFSI, a reversible decrease in ionic conductivity was observed upon photoisomerization from *trans*-poly(azobenzene) to *cis*-poly(azobenzene) and vice versa. Though light does cause $T_g$ to change in these materials, cycling experiments suggests that coordination of *cis*-azobenzene with $Li^+$ dominates the observed trends in conductivity rather than the change in $T_g$ alone.

## 3.3 Results and Discussion

### 3.3.1 Design and Synthesis of Azobenzene-Containing Polymeric Ionic Liquids

To access light-responsive polyelectrolytes, we designed and synthesized copolymers of azobenzene acrylate (AzoAcMe) and pentafluorophenyl acrylate (PFPA) (Figure 26). Note that a methyl group was added at the *ortho* position in AzoAcMe to facilitate liquid-crystalline photo-melting as previously demonstrated with small-molecule powders;[192] synthetic details are provided in the Supporting Information.[182] In these copolymers, a high azobenzene content was targeted to disrupt the aggregation of *trans*-azobenzene before UV light irradiation.[193] Accordingly, AzoAcMe was copolymerized with PFPA in a 7:3 AzoAcMe:PFPA feed ratio using conventional free-radical polymerization initiated with 2,2-azobis(2-methylpropionitrile).[194] The resulting copolymer has a number-average molecular weight $M_\mathrm{n}$ = 18.3 kg/mol and molar-mass dispersity $Đ$ = 1.4 with 26 mol% PFPA as determined by $^{19}$F NMR spectroscopy. This material is a convenient platform for installing ionic-liquid functionality via activated-ester chemistry through post-polymerization modification.[195] Following complete base-catalyzed substitution with an amine nucleophile, amide formation at the PFPA sites was monitored with $^{19}$F NMR by the disappearance of broad polymeric PFPA resonances and the appearance of sharp peaks corresponding to pentaflourophenol. Subsequent methylation and salt metathesis afforded the new polyelectrolyte copolymer poly(azo-*co*-IL) with 26 mol% ionic liquid (IL) incorporation and a bis(trifluoromethane)sulfonimide (TFSI$^{-}$) counterion, supported by $^{1}$H and $^{19}$F NMR spectroscopy (see Figure 43 and Figure 44). As a control, homopolymers of the azobenzene polymer [poly(azobenzene)] were similarly synthesized without the aforementioned post-polymerization functionalization steps.

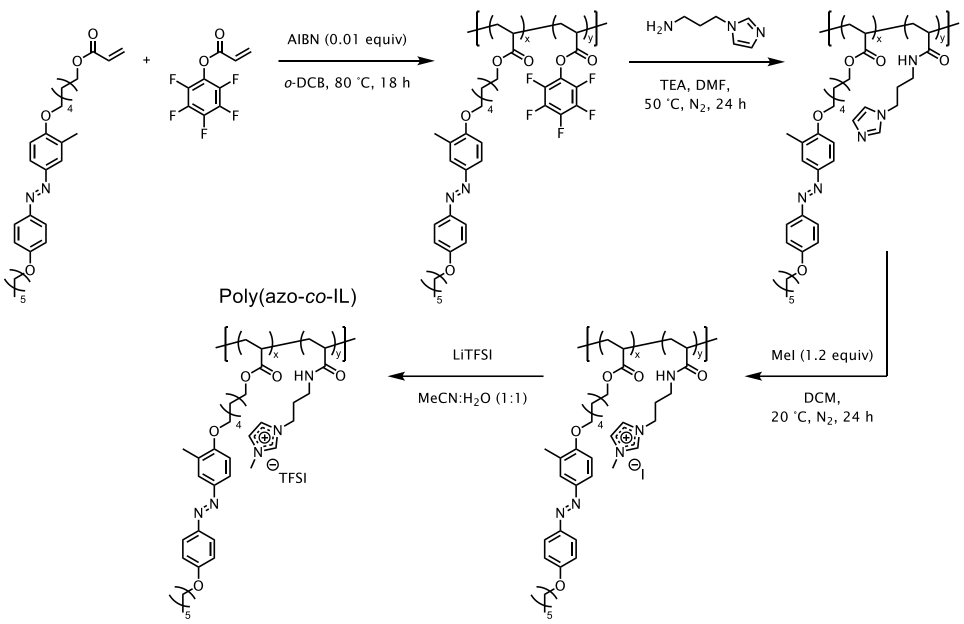

**Figure 26. A four-step synthesis of the poly(azo-*co*-IL) from AzoAcMe and PFPA.**

### 3.3.2 Photoisomerization of Poly(azobenzene) and Poly(azo-*co*-IL)

Following the synthesis and purification of poly(azobenzene) and poly(azo-*co*-IL), we confirmed azobenzene photo-isomerizes in the solid-state using UV- and visible-light irradiation to induce *cis* and *trans* isomers, respectively. As-cast films of poly(azo-*co*-IL) exhibit two absorption bands: a vibronic progression centered around 360 nm corresponding with a $\pi \longrightarrow \pi^*$ transition and a weakly absorbing $n \longrightarrow \pi^*$ transition in the visible near 460 nm, see Figure 27. These features are consistent with *trans* azobenzene. When exposed to UV irradiation (365 nm, 5 mW/cm$^2$ for 60 seconds), the $\pi \longrightarrow \pi^*$ transition bleaches and a stronger $n \longrightarrow \pi^*$ absorption is observed corresponding to a 53% isomerization of *trans*-to-*cis*-azobenzene (see Figure 52).[196,197] Signatures of vibronic absorbance are partially retained for UV-irradiated films, as a fraction of the *trans*-azobenzene remains.[176,182,198,199]

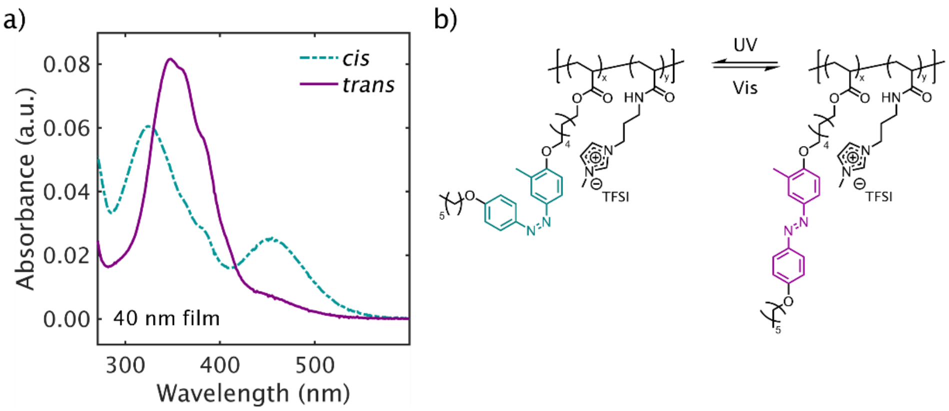

**Figure 27. UV-vis absorbance spectra of cis and trans poly(azo-*co-IL)***

*a) UV–vis absorbance of poly(azo-co-IL) in its b) two isomeric structures. At room temperature in equilibrium, the polymer absorbance is dominated by the trans isomer form. Upon irradiation with 365 nm UV light, the primary* $\pi \longrightarrow \pi^*$ *absorbance shifts to 319 nm (from 348 nm) and the n* $\longrightarrow \pi^*$ *absorbance at 455 nm increases, indicating the trans–cis isomerization.*

The glass-transition temperatures ($T_g$) of the *cis* and *trans* poly(azobenzene) and poly(azo-*co*-IL) adducts were measured using differential scanning calorimetry (DSC) to understand how illumination changes segmental motion. The $T_g$ of *cis* (4.6 °C) and *trans* (12.6 °C) poly(azobenzene) (see Figure 47) exhibits a similar trend as *cis* (7.4 °C) and *trans* (18.9 °C) poly(azo-*co*-IL). The lower $T_g$ of both *cis* isomers is consistent with the non-planar structure of *cis* azobenzene disrupting aggregation and increasing the free volume as compared to planar *trans* azobenzene. Notably, a blueshift in the $\pi \longrightarrow \pi^*$ transition (from 360 nm to 319 nm) also corroborates loss of vibronic absorbance from *trans* azobenzene.[199,200] Together, these results *cis* azobenzene isomers should yield an improved free–volume-mediated ionic conductivity.

### 3.3.3 Azobenzene Enables Reversible, Light-Mediated Ionic Conductivity in Polyelectrolytes

Next, impedance spectroscopy was used to study the ionic conductivity of poly(azobenzene) and poly(azo-*co*-IL). Each polymer was blended with 10 wt% LiTFSI in solution (10 mg/mL in a 1:2 mixture of acetonitrile:toluene) and spin coated onto interdigitated electrodes. These optically thin films were illuminated with 365 nm and 470 nm light to alternate between *cis* and *trans* isomers with impedance spectra collected in between. Equivalent circuit model fits indicate the ionic conductivity of *trans*-poly(azobenzene) is approximately 6–7 times higher than *cis*-poly(azobenzene) with a similar, less pronounced trend observed for poly(azo-*co*-IL) as well (see Figure 28). Films of both polymers required approximately 5 photoisomerization cycles before steady-state ionic conductivity values were reached. This initial transient period may be due to volume changes arising from isomerization which reach steady state as the films are cycled.[198,199] Additionally, optical micrographs of films cycled 10 times show a significant variation in texture between poly(azobenzene) and poly(azo-*co*-IL) with the latter being smoother (see Figure 48). We attribute this difference in film texture to the better solubility of LiTFSI in poly(azo-*co*-IL) due to the polymeric ionic-liquid functionality. The enhancement in salt solubility imparted by IL incorporation also results in poly(azo-*co*-IL) being approximately twice as ionically conductive as poly(azobenzene) overall.

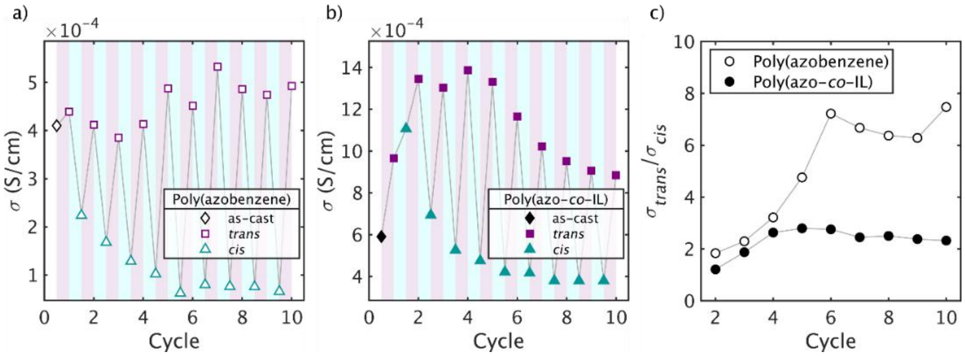

**Figure 28. Conductivity of *cis*/*trans* poly(azobenzene) and poly(azo-*co*-IL)**

*Ionic conductivity of (a) poly(azobenzene) and (b) poly(azo-co-IL). Films were cycled between cis and trans isomers by exposure to 365 nm and 470 nm light, respectively. Corresponding ratios of trans to cis conductivity are shown in (c). After 5 cycles, trans-poly(azobenzene) and trans-poly(azo-co-IL) are more conductive than cis-poly(azobenzene) and cis-poly(azo-co-IL).*

### 3.3.4 Ionic Liquid Incorporation Reduces Azobenzene *Cis*-Isomer Metastability

We evaluated the stability of *cis*-poly(azobenzene) and *cis*-poly(azo-*co*-IL) by continuously monitoring both the relaxation of impedance spectra (Figure 29) and thermal relaxation in the absence of electric fields (Figure 53) over time as both reach equilibrium (predominantly *trans*) isomer distributions. For poly(azobenzene), the conductivity resulting from equivalent model fits does not change appreciably over 45 hours and is consistent with the long half-life of other substituted *cis*-azobenzene derivatives in polymers.[193,201] The broadening of the impedance spectra of poly(azobenzene) is attributed to changes in the film pseudo-capacitance (see Figure 50). In contrast, the impedance spectra of poly(azo-*co*-IL) decreases over time, reflecting the relaxation of *cis* azobenzene to the more conductive *trans* azobenzene after ca. 35 hours.

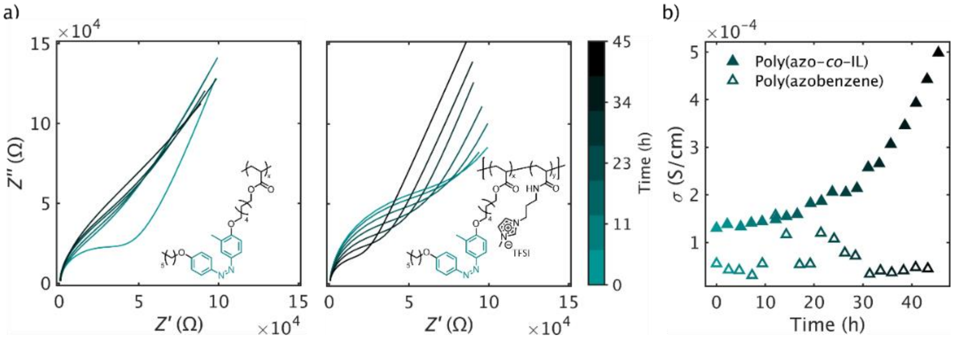

**Figure 29. Time-resolved conductivity relaxation of cis poly(azobenzene) and poly(azo-*co*-IL)**

*(a) Impedance spectra of initially UV-irradiated cis-poly(azobenzene) (left) and cis-poly(azo-co-IL) (right) linearly sampled over 45 h. Although the trans isomers are more conductive, the impedance spectra of UV-irradiated cis-poly(azobenzene) does not relax to lower impedances over 45 h of continuous measurement. In contrast, cis-poly(azo-co-IL) does relax to lower impedances. (b) Conductivity of initially UV-irradiated poly(azobenzene) and poly(azo-co-IL) over 45 hours. The extracted ionic conductivity of poly(azobenzene) does not show significant changes over 45 h, suggesting that the relaxation of the cis isomer is inhibited. In contrast, the conductivity of poly(azo-co-IL) increases with time, consistent with a relaxation to the trans isomer form.*

The increase in conductivity is greater than that observed in Figure 28 likely due to the concentration of $Li^+$ in high mobility domains at thermal equilibrium (40 °C) being greater than that resulting from the photostationary state induced by 470 nm light illumination.[196] This is corroborated by thermal relaxation measurements of the *cis* azobenzene UV-vis features to that of *trans* azobenzene. While both ionic conductivity (Figure 29) and *in-situ* UV-vis measurements (Figure 53) show that IL incorporation reduces *cis* azopolymer metastability, UV-vis measurements suggests that *cis* poly(azo-*co*-IL) equilibrates to the *trans* isomer after approximately 3 hours as compared to conductivity measurements (ca. 35 hours). The delayed relaxation to the higher ionic conductivities than afforded by *cis*-*trans* cycling is likely due to limited diffusion of mobile $Li^+$ imidazolium-rich domains during the time (10 minutes) between irradiation cycles in Figure 28.

### 3.3.5 Proposed Azo-Ion Coordination

Despite the *cis* isomer of poly(azobenzene) and poly(azo-*co*-IL) having a lower $T_g$, both *trans* forms show higher ionic conductivity. A similar effect has been observed in the past for azobenzene-containing vinyl polymers with a variety of metal cations.[184,185] In these examples, additional functionality attached to azobenzene can act as a ligand that complexes metal cations differently upon *trans*–*cis* photoisomerization. Here, we propose a similar effect, where the more polar nature of *cis*-azobenzene better coordinates $Li^+$ with the azo-nitrogen lone pairs.

To explore potential ion coordination effects, we measured UV–visible spectra of poly(azobenzene) and poly(azo-*co*-IL) films blended with LiTFSI. While the wavelength and intensity of the $\pi \longrightarrow \pi^*$ absorbance persists with added salt, a bathochromic shift from 319 nm to 337 nm was observed for *cis* poly(azobenzene) upon adding LiTFSI (Figure 30). Likewise, for poly(azo-*co*-IL), copolymerization of IL (imidazolium) causes a modest 5 nm bathochromic shift with additional blended LiTFSI increasing it another 11 nm. A similar shift in the $\pi \longrightarrow \pi^*$ transition has been observed in azobenzene–$BF_2$ complexes due coordination of $BF_2$ with an azo-nitrogen lone pair.[186] In the case of $BF_2$ coordination, increasing electron density induces a hypsochromic shift of the $\pi \longrightarrow \pi^*$ transition. Here, we suggest electron-deficient cations ($Im^+$ and $Li^+$) instead cause a bathochromic shift, the extent of which varies depending on azobenzene concentration. These effects were not present in *trans* films, where the same absorption features do not change with IL incorporation and added salt (Figure 51). Together, our results suggest *cis*-azobenzene likely coordinates with cations in both polymers.

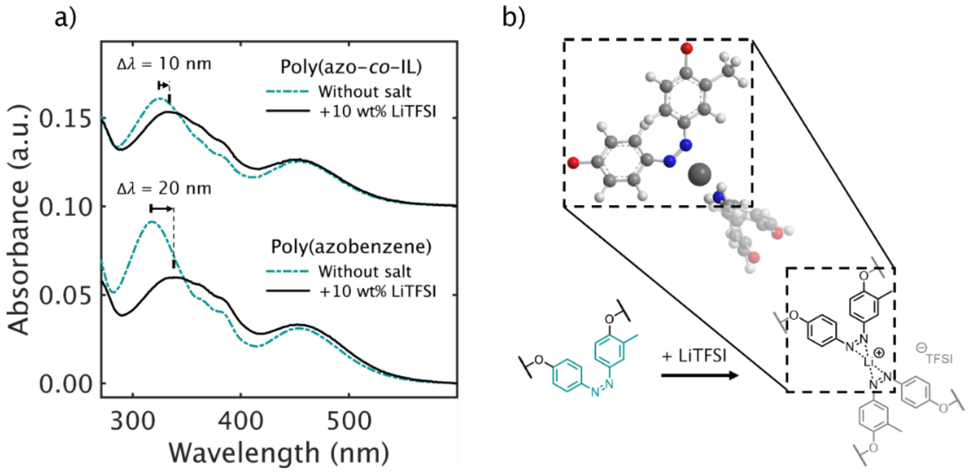

**Figure 30. Bathochromic shifts in *cis* poly(azobenzene) and poly(azo-*co*-IL) absorbance due to ion coordination**

*(a) UV–vis absorbance spectra of cis-poly(azo-co-IL) (top) and cis-poly(azobenzene) (bottom) with/without salt. Adding LiTFSI results in a bathochromic shift of the primary absorbance for both polymers, suggesting (b) an interaction between azobenzene and Li+ is likely responsible for the difference in ionic conductivity observed with cis and trans isomers.*

### 3.4 Conclusions

The conductivity of materials containing poly(azobenzene) and blended salt can be reversibly modulated with light. Poly(acrylate) homopolymers with azobenzene side chains undergo the most drastic change in ionic conductivity, namely a 6–7 times decrease upon isomerization from the *trans* to *cis* isomer. Incorporating a second, polymeric ionic-liquid (PIL) comonomer further increases absolute conductivity due to the improved solubility of added salt but attenuates differences between *trans* and *cis* to a factor of 2–3. Because *cis* isomers have a lower glass-transition temperature than *trans*, $T_g$ effects cannot explain these relative conductivity results. Instead, UV–visible spectroscopy suggests possible coordination of *cis*-azobenzene with cations as the dominant factor accounting for light-induced changes in ionic conductivity. The stability of *cis*-azobenzene also varies with IL incorporation, persisting for more than 45 h in a poly(azobenzene) homopolymer but relaxing back to *trans* after ca. 35 h with poly(azo-*co*-IL). In summary, azobenzene is a convenient platform for controlling the conductivity of polymeric materials using light.

### 3.5 Acknowledgments

The research reported here made use of shared facilities of the National Science Foundation Materials Research Science and Engineering Center (MRSEC) at UC Santa Barbara (NSF DMR 1720256, IRG-2), is a member of the Materials Research Facilities Network (www.mrfn.org). This work utilized NMR instruments supported by the National Science Foundation under award No. MRI-1920299. A portion of this work was performed in the UC Santa Barbara Nanofabrication Facility, an open access laboratory. P.H.N. and A.M.S. gratefully acknowledges support from the National Science Foundation Graduate Research

Fellowship Program under grant no. 2139319. Any opinions, findings, and conclusions or recommendations expressed in this material are those of the authors and do not necessarily reflect the views of the National Science Foundation.

## 3.6 Appendix

### 3.6.1 Experimental Methods

#### 3.6.1.2 Materials

Methanol, dichloromethane, acetonitrile, *ortho*-dichlorobenzene (DCB), deionized water (DI), ethanol, toluidine (99%), dimethylformamide (DMF), dichloromethane (DCM), 6-bromo alcohol, acryloyl chloride (97%, contains <210 MEHQ as stabilizer), sodium carbonate ($Na_2CO_3$), 4-hexyloxyaniline, *o*-cresol, triethylamine (TEA), sodium nitrite, hydrochloric acid (ACS Reagent, 37%), sodium hydroxide (NaOH), magnesium sulfate (anhydrous, ReagentPlus®, ≥99.5%), sodium iodide (ACS Reagent, >99.5%), 2-bromoethylamine hydrobromide, and 1-methylimidazole were purchased from Sigma-Aldrich and Fisher Scientific and used as received. Lithium bis(trifluoromethanesulfonimide) was obtained from Acros Organics. Toluene was freshly distilled for use. 2,2'-Azobis(2-methylpropionitrile) (AIBN, from Sigma-Aldrich) was recrystallized in methanol before use.

#### 3.6.1.3 Instrumentation

$^1$H NMR spectra were recorded on a Varian Unity Inova 500 MHz or a Varian Unity Inova AS600 500 MHz spectrometer at a regulated temperature of 25 °C. $^1$H NMR chemical shifts were calibrated to the resonances of $CDCl_3$ at δ = 7.26 ppm. $^{19}F$ NMR spectra were recorded on an Agilent Technologies 400-MR DD2 400 MHz with monofluorobenzene as an internal standard at δ = –113.15 for calibration. UV–Vis spectra were recorded on an Agilent Cary 60 UV–Vis Spectrometer. To induce photochemical isomerizations, a 365 nm Thorlabs collimated LED lamp (80 mW/cm$^2$) and a 470 nm Thorlabs collimated LED lamp (0.2 W/cm$^2$). Glass transition temperatures were measured on a TA Instruments DSC 250. Impedance spectra were collected using Solartron 1260 and 1287 potentiostats in tandem with ZPlot software on polymer films spun cast onto custom fabricated interdigitated electrodes.

## 3.6.2 Synthesis of Poly(azobenzene) and Poly(azo-*co*-IL)

### 3.6.2.1 Synthesis of Azo-Me-OH

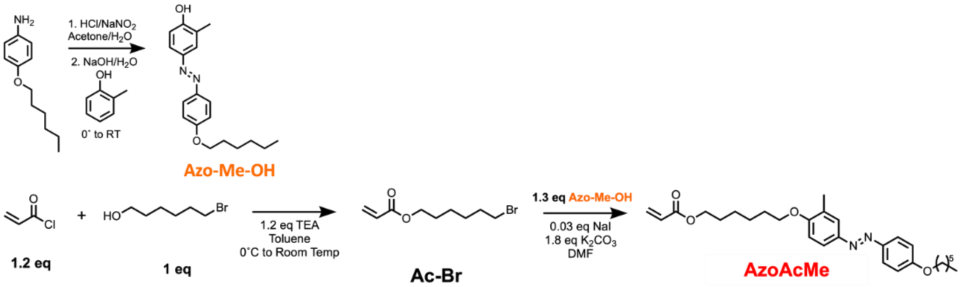

Figure 31. Multi-step synthesis of **AzoAcMe**.

The synthesis of Azo-Me-OH was adapted from Ishiba *et al.*[202] In a 500 mL 3-necked round bottom flask, 4-hexyloxyaniline (4.99 g, 25.8 mmol, 1 eq.) was dissolved 2:1 acetone: water (100 mL) and placed in an ice bath at 0 °C. 5.13 mL 37% HCl (77 mmol, 3 eq) was added to the round bottom flask slowly. To this solution, sodium nitrite in 50 mL $H_2O$ (2.36

g, 34.3 mmol, 1.33 eq) was added and the mixture turned from a brown color to a clear gray/black solution over ~5 min. Upon which, a solution containing both *o*-cresol (3.57 mL, 35.6 mmol, 1.34 eq) and NaOH (3.17 g, 79.3 mmol, 3.07 eq) in 60 mL $H_2O$ was added dropwise, resulting the formation of a red precipitate. After 24 hours, the solution was neutralized with 10 wt% HCl and the dark red precipitate was isolated. The crude precipitate was purified via column chromatography (eluded with 100% dichloromethane (DCM)) to afford a dark red crystalline product (2.86 g, 35% yield).

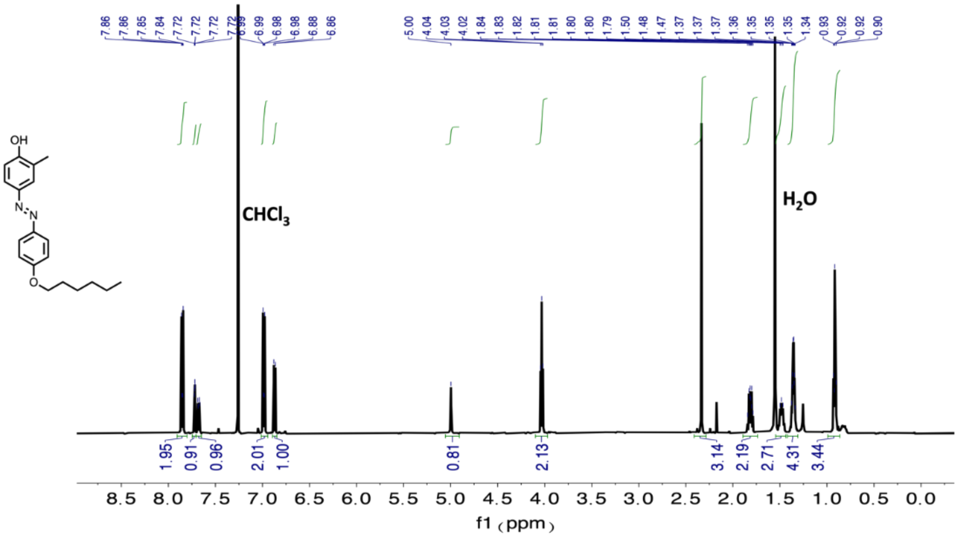

**Figure 32. $^1$H NMR spectrum of Azo-Me-OH in $CDCl_3$.**

### 3.6.2.2 Synthesis of Ac-Br

The following procedure was adapted from the literature.[203] In an oven dried 3-necked 500 mL round bottom flask, 6-bromoalcohol (6.4 mL, 48.9 mmol, 1 eq) and dry triethylamine (7.5 mL, 53.8 mmol, 1.1 eq) were dissolved in dry toluene (200 mL). The flask was lowered into an ice bath at 0 °C, and a solution containing acryloyl chloride (4.5 mL, 55.7 mmol, 1.14

eq) and 30 mL dry toluene was added dropwise to the first solution via addition funnel. After 24 hours, the reaction was quenched with the addition of 50 mL DI $H_2O$. The organic layer was collected and sequentially washed with 5% $Na_2CO_3$ in water (3x40 mL), 5% HCl (30 mL), and brine (50 mL). The organic layer was collected after washing, dried with $MgSO_4$, and reduced under reduced pressure to afford the Ac-Br product as a slightly yellow liquid (9.4 g, 81 % yield), which was used without further purification.

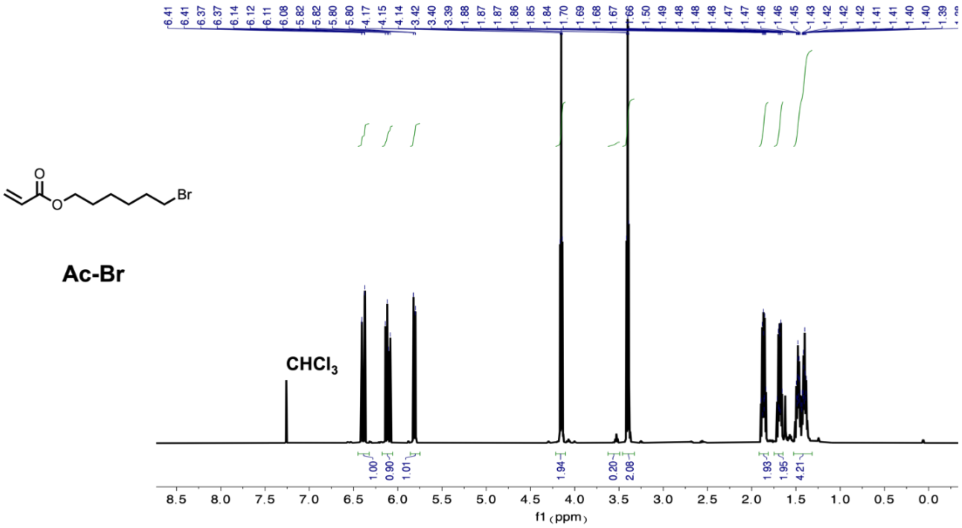

**Figure 33. $^1H$ NMR spectrum of Ac-Br in $CDCl_3$.**

### 3.6.2.3 Synthesis of AzoAcMe

Ac-Br (3 g, 11.8 mmol, 1 eq), Azo-Me-OH (4.8 g, 15.4 mmol, 1.3 eq), NaI (53.2 mg, 0.03 eq), $K_2CO_3$ (2.94 g, 21.3 mmol, 1.8 eq) were dissolved in 60 mL DMF in a 200 mL round bottom flask. The reaction was sparged with $N_2$, a reflux condenser was attached to the flask, and the reaction was heated to 115 °C for one hour. The reaction was found complete by $^1H$ NMR spectroscopy after the one hour mark. Water was then added to the reaction mixture, and the reaction was poured into a 500 mL separation flask, and ethyl acetate (5 × 40 mL) was used to extract the product. The organic layer was collected, washed with brine (40 mL), dried with $MgSO_4$, filtered and solvent removed with a rotovap. The crude reaction mixture was purified via column chromatography (eluded with 100% dichloromethane (DCM)) to afford as AzoAcMe as an orange-yellow powdery solid (4.35 g, 79% yield.)

#### 3.6.2.4 Characterization of AzoAcMe

$^1$H NMR ($CDCl_3$) $\delta$ 7.84 (d, 2H, $J_{HH}$ = 9 Hz, Ar*H*), 7.73 (m, 2H, Ar*H*), 6.98 (d, 2H, Ar*H*), 6.89 (d, 1H, Ar*H*), 6.40 (dd, 1H, $J_{HH}$ = 18 Hz, 1.5 Hz, alkene-*H*), 6.14 (q, 1H, $J_{HH}$ = 10.4 Hz, alkene-*H*), 5.80 (q, 1H, $J_{HH}$ = 10.4 Hz, 1.5 Hz), alkene-*H*), 4.19 (t, 2H, $J_{HH}$ = 7 Hz, OC$H_2$), 4.06 – 4.02 (overlapping mult., 4H, OC$H_2$), 2.29 (s, 3H, Ar-C$H_3$), 1.89 – 1.78 (overlapping mult. 4H, C$H_2$) 1.73 (pentet, 2H, $J_{HH}$ = 7 Hz), 1.60 – 1.53 (mult., 2 H, C$H_2$), 1.51 – 1.45 (mult., 4 H, C$H_2$), 1.35 (pentet, $J_{HH}$ = 4 Hz, C$H_2$), 0.92 (t, 3H, $J_{HH}$ = 7 Hz, –$CH_3$). $^{13}$C[$^1$H] NMR ($CDCl_3$) $\delta$ 166.55, 161.34, 159.00, 147.23, 146.69, 130.76, 128.84, 127.71, 124.48, 123.74, 125.67, 114.90, 110.75, 68.56, 66.56, 66.26, 64.75 31.84, 29.44, 29.40, 28.84, 26.10, 26.00, 25.96, 22.85, 16.65, 14.29.

FT-IR (neat) ν ($cm^{-1}$) 3072, 3060, 3055, 2938, 2864, 1718, 1635, 1596, 1500, 1489, 1462, 1416, 1390, 1320, 1296, 1244, 1150, 1139, 1104, 1075, 1057, 986, 936, 904, 843, 807, 787, 748, 729, 671, 635, 593, 582, 542. MS (ESI-TOF) m/z = 467.3 [M+H]+, 489.3 [M+$Na^+$].

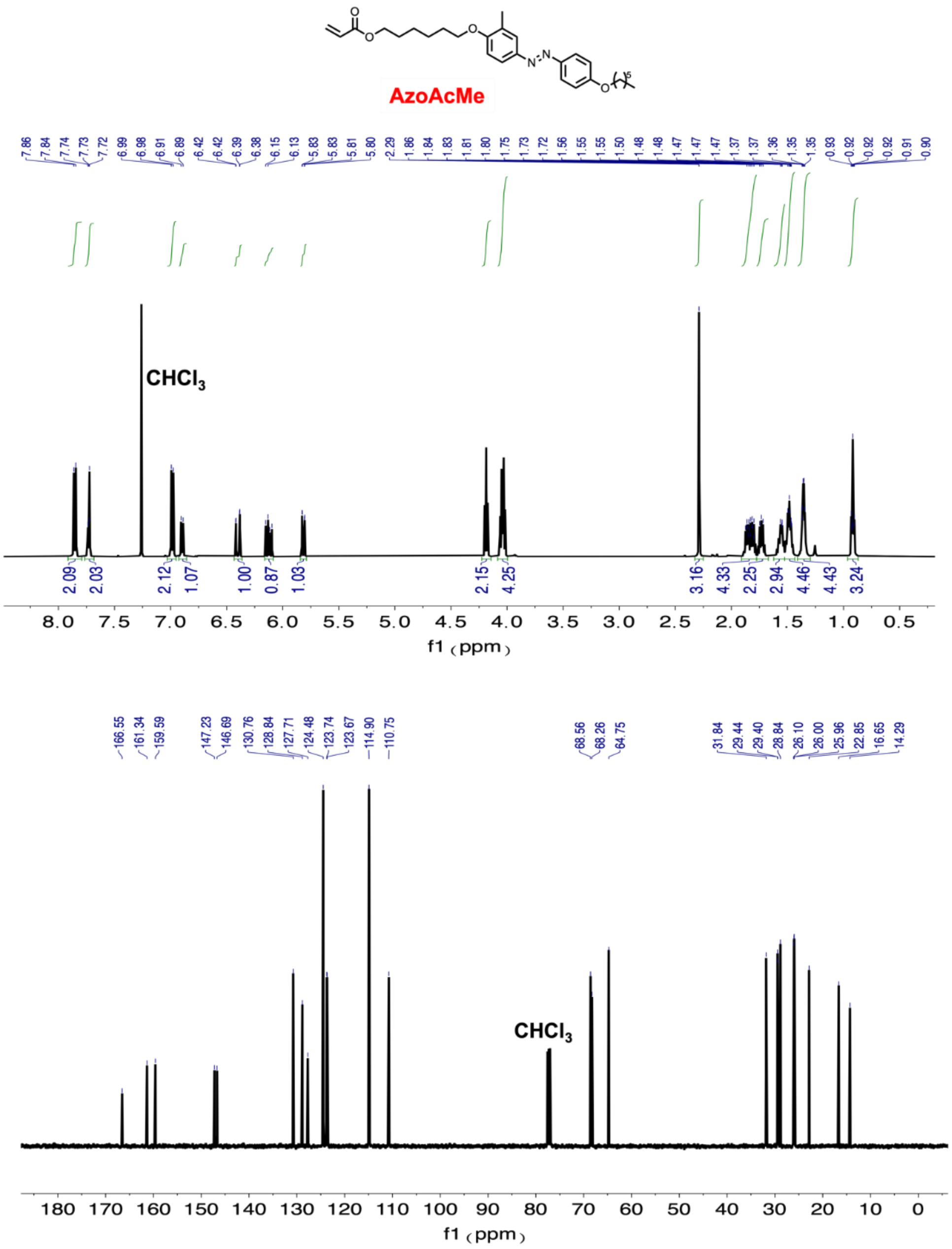

**Figure 34.** $^1$**H (top) and** $^{13}$**C[**$^1$**H] (bottom) NMR spectra of AzoAcMe in CDCl**$_3$**.**

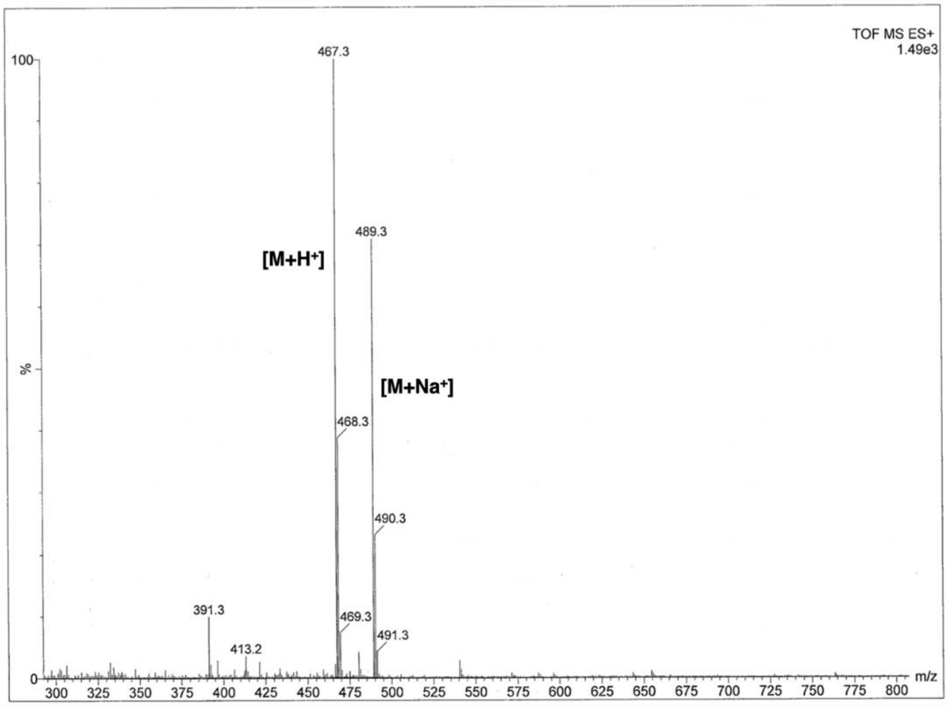

**Figure 35. Mass spectra of AzoAcMe.**

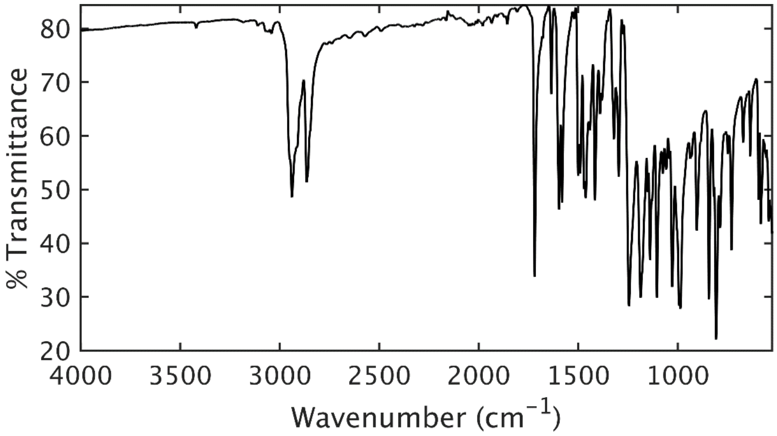

**Figure 36. FT-IR spectra of AzoAcMe.**

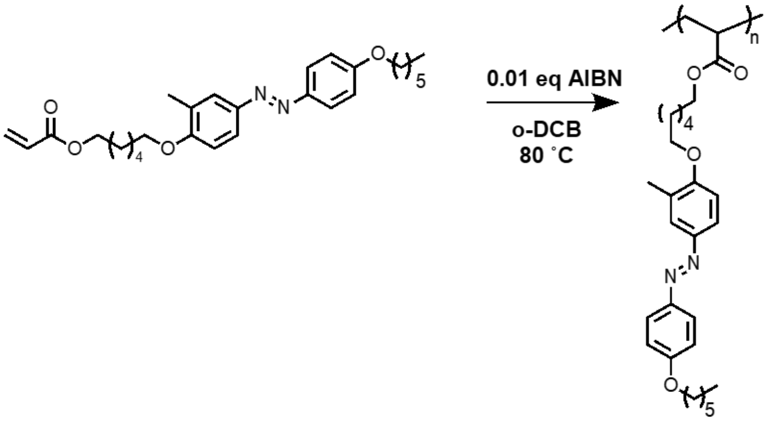

**Figure 37. Free-radical polymerization of AzoAcMe to poly(azobenzene).**

### 3.6.2.5 Synthesis of poly(azobenzene)

The pentafluorophenyl acrylate (PFPA) monomer was synthesized according to literature.[204] To a flame-dried 25 mL Schlenk flask, AzoAcMe (500 mg, 0.89 mmol, 4 eq) and AIBN (3.5 mg, 0.025 mmol, 0.1 eq), and 1 mL *o*-DCB were added. The reaction mixture was subjected to 4 freeze-pump-thaw cycles and under vacuum, the reaction was placed in an oil bath at 80 °C. After 17 hours of heating, the majority of o-DCB was removed under vacuum for 24 hours. The reaction mixture was dissolved in minimal DCM and purified via two successive precipitations: (1) pure hexane and (2) 1:1 hexane:diethyl ether, and centrifuged down in each precipitation. The final polymer was reconstituted in DCM and then dried in a 20 mL vial to reveal the PFPA-Azo copolymer as an orange solid (400 mg, 38% mass recovery, $M_n$ = 11 kDa, PDI = 1.4).

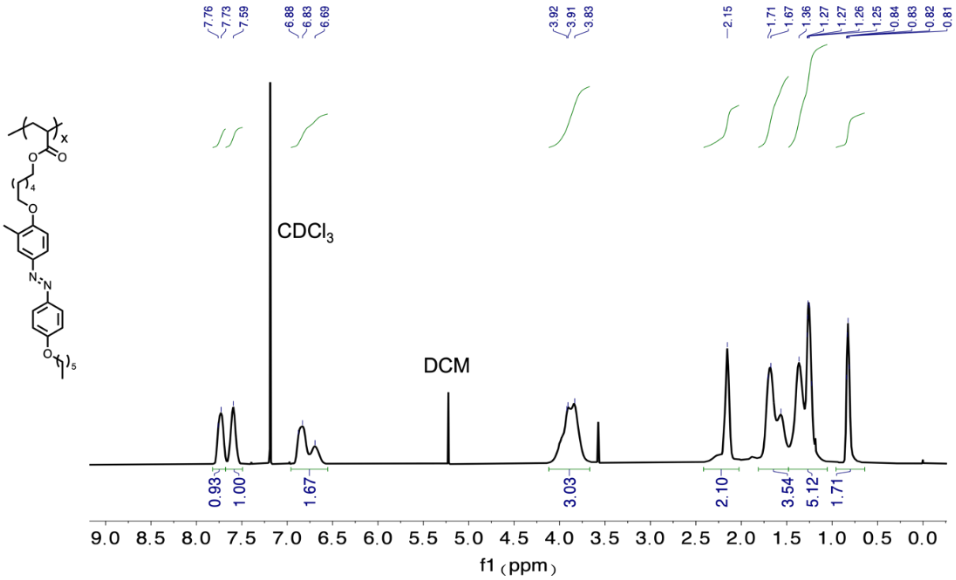

**Figure 38.** $^1$H NMR spectrum of the poly(azobenzene) in CDCl$_3$.

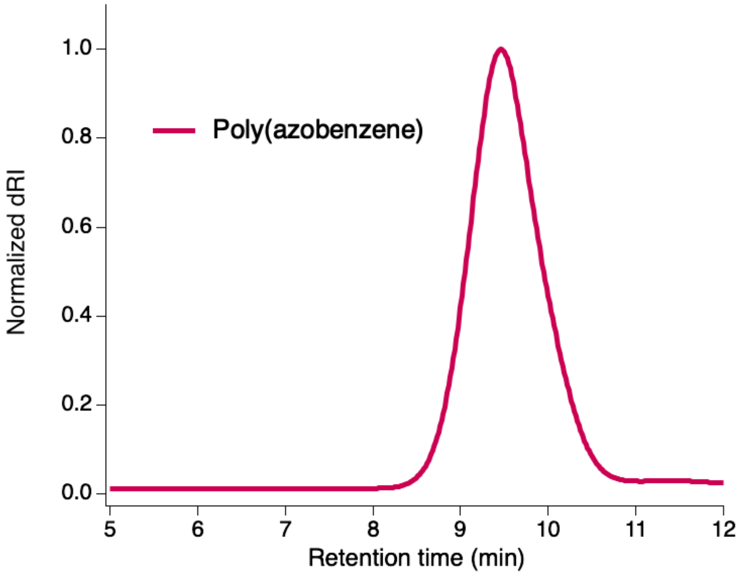

**Figure 39. SEC of poly(azobenzene)**

*Size-exclusion chromotagram (normalized differential refractive index signal) of poly(azobenzene).*

### 3.6.2.6 Synthesis of poly(azo-*co*-PFPA)

The pentafluorophenyl acrylate (PFPA) monomer was synthesized according to literature.[204] AzoAcMe (481 mg, 1.03 mmol, 4 eq), PFPA (61.4 mg, 0.26 mmol from a 124 mg PFPA in *o*-DCB solution, 1 eq), AIBN (4.2 mg, 0.025 mmol, 0.1 eq), and 1.2 mL *o*-DCB were added to a flame-dried 25 mL Schlenk flask. The reaction mixture was subjected to 4 freeze-pump-thaw cycles and subsequently heated in an oil bath at 80 °C under vacuum. After 17 hours of heating, the majority of *o*-DCB was removed under vacuum for 24 hours. The reaction mixture was dissolved in minimal DCM and purified via two successive precipitations: (1) pure hexane and (2) 1:1 hexane:diethyl ether, and centrifuged down in each precipitation. The final polymer was reconstituted in DCM and then dried in a 20 mL vial to reveal poly(azo-*co*-PFPA) as an orange solid (270 mg, 49% mass recovery, $M_n$ = 15 kDa, PDI =1.4)

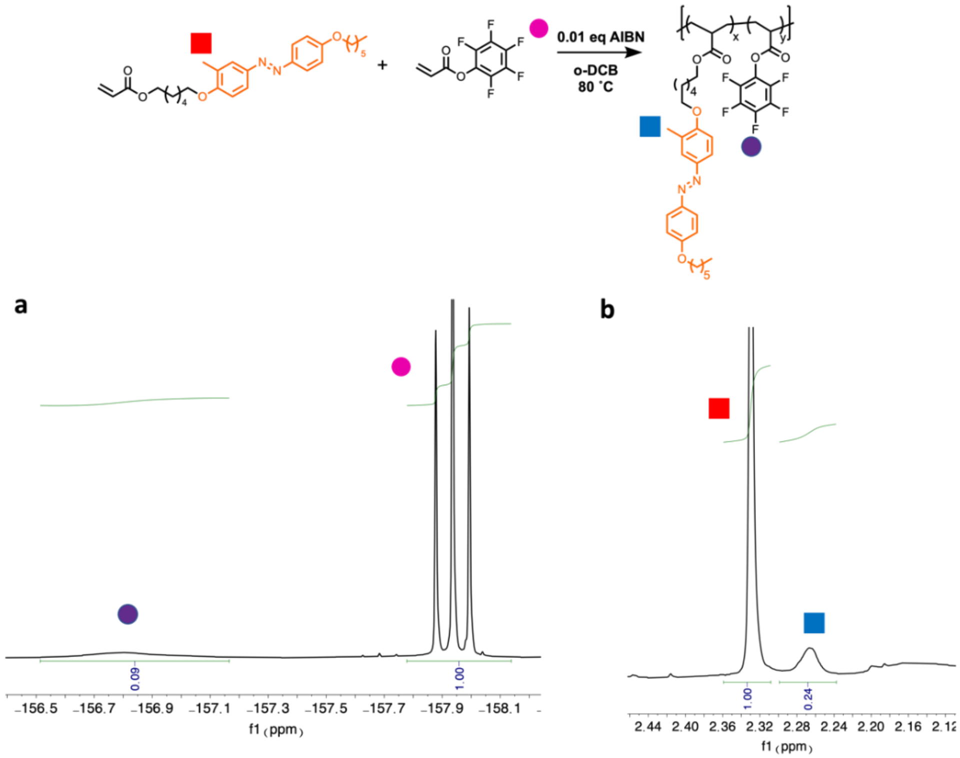

**Figure 40. Polymerization of PFPA and AzoAcMe measured using $^{19}$F and $^{1}$H NMR**

*Conversion of the PFPA monomer to polymer was monitored using* $^{19}F$ *NMR spectroscopy via (a) the integration of the fluorine at the para position. Conversion of the AzoAcMe monomer polymer was monitored using* $^{1}H$ *NMR spectroscopy via (b) the integration of the methyl on azobenzene.*

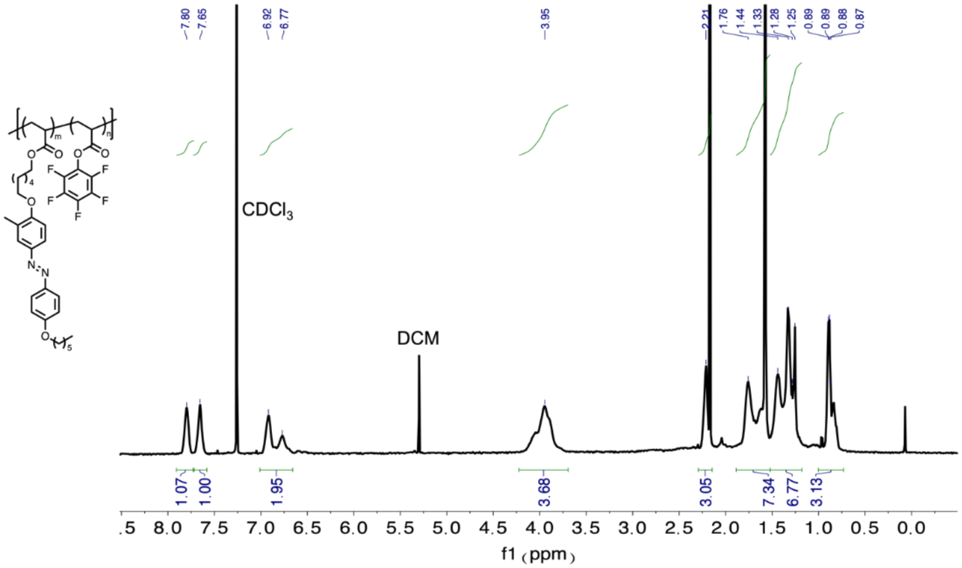

**Figure 41.** $^{1}$**H NMR spectrum of the poly(azo-*co*-PFPA).**

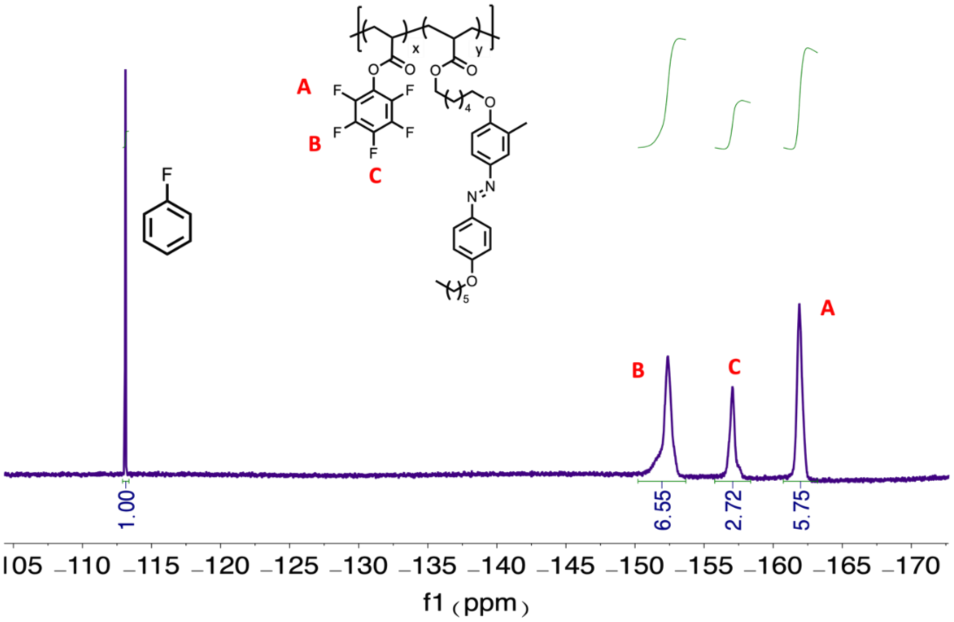

**Figure 42. $^{19}$F NMR spectrum of poly(azo-*co*-PFPA)**

*Quantitative $^{19}$F NMR measurements of poly(azo-co-PFPA) were completed by adding a known amount of monofluorobenzene as an internal standard (δ = –113.15 ppm) and comparing the relative integration of monofluorobenzene to the integration of fluorine on the PFPA monomer.*

### 3.6.2.7 Synthesis of poly(azo-*co*-IL)

A solution of poly(azo-*co*-PFPA) (270 mg, 1 eq), triethylamine (0.104 g, 1.03 mmol, 4 eq), and 1-(3-aminopropyl)imidazole (0.128 g, 1.03 mmol, 4 eq) in DMF was added to a flame-dried 25 mL round bottom flask. This reaction mixture was placed in an oil bath preheated to 50 °C and stirred for 24 hours under a nitrogen atmosphere. The DMF solvent was removed under vacuum and the polymer was precipitated from MeOH, redissolved in DCM, and reacted with methyl iodide (0.055 g, 0.39 mmol, 1.5 eq) at ambient temperature under nitrogen atmosphere overnight. The DCM solvent was evaporated and the resultant polymer was dissolved in (1:1) MeCN:$H_2O$ followed by the addition of lithium bis(trifluoromethanesulfonyl)imide (0.075 g, 0.26 mmol, 1 eq) and stirred at ambient temperature for 2 hours. The top layer was separated and concentrated under vacuum to yield the poly(azo-*co*-IL) as an orange solid (230 mg, 65% mass recovery, $M_n$ = 13 kDa, PDI = 1.14).

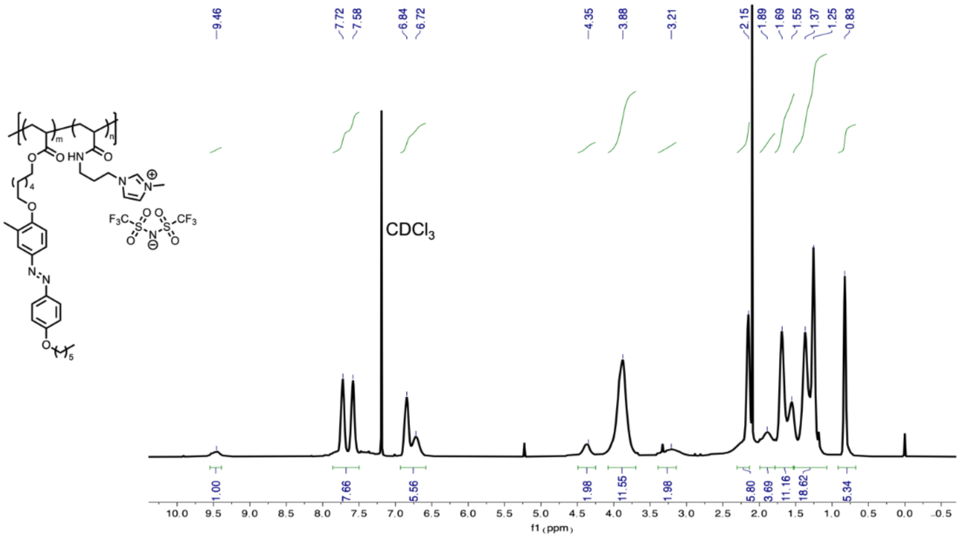

**Figure 43. $^1$H NMR spectrum of the poly(azo-*co*-IL) in $CDCl_3$.**

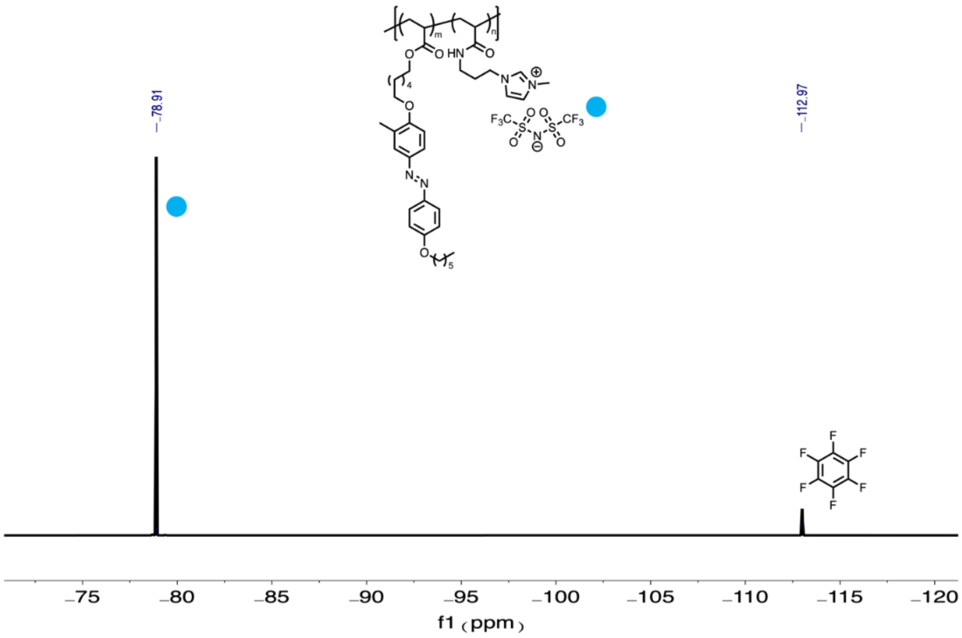

**Figure 44. $^{19}$F NMR spectrum of the poly(azo-*co*-IL)**

*$^{19}$F NMR spectrum of the poly(azo-co-IL) monofluorobenzene included as an internal standard (δ = –113.15 ppm).*

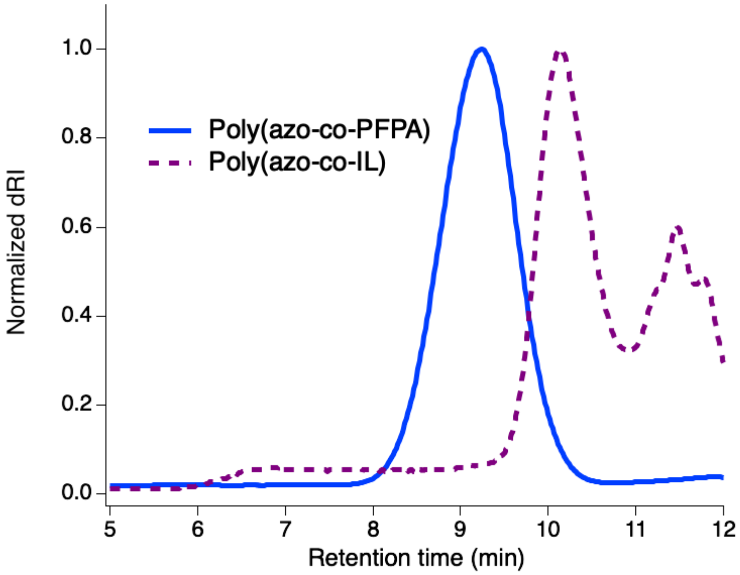

**Figure 45. SEC of poly(azo-*co*-PFPA) and poly(azo-*co*-IL)**

*Size-exclusion chromatogram (normalized differential refractive index signal) of poly(azo-co-PFPA) and poly(azo-co-IL).*

### 3.6.3 Reactivity Ratios in Copolymerization of PFPA and AzoAcMe

Reactivity ratios were found using Jaacks' method.[205] For the reactivity ratio of PFPA, a ratio of 9:1 PFPA:AzoAcMe was used in the free-radical polymerization and aliquots were taken for NMR spectroscopy every 5 minutes up to 30 minutes. The reactivity ratio of AzoAcMe was measured similarly. The conversion of the PFPA was monitored via $^{19}$F NMR spectroscopy and the conversion of AzoAcMe was monitored via $^{1}$H NMR spectroscopy.

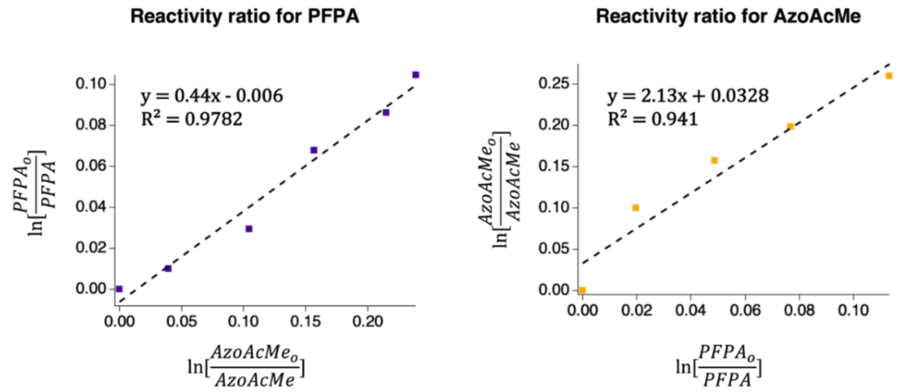

**Figure 46. Reactivity ratios of PFPA and AzoAcMe**

### 3.6.4 Differential Scanning Calorimetry of Poly(azobenzene) and Poly(azo-*co*-IL)

Both poly(azobenzene) and poly(azo-*co*-IL) were filtered and dissolved in toluene at 30 mg/mL. Samples were irradiated with 365 nm UV light (7.5 mW/cm$^2$, 15 minutes, stirring) to photoisomerize polymers to the *cis* isomer form. UV-irradiated solutions were cast into Teflon wells and dried under vacuum at ambient temperatures. Once dry, 5–8 mg of *cis* poly(azobenzene) and *cis* poly(azo-*co*-IL) were placed into hermetic aluminum pans and annealed at 25 % humidity under dark for 30 minutes. Samples were hermetically sealed prior to calorimetry measurements.

All DSC measurements were carried out using a TA Instruments DSC 250. Reported glass transition temperatures ($T_g$) were calculated using TA Instruments Trios software with half-height analysis. Samples were (1) equilibrated at -20 °C, (2) heated to 40 °C at 10 °C/min, (3) cooled to -20 °C at -10 °C/min, (4) heated to 40 °C at 20 °C/min, (5) cooled to -20 °C at -20 °C/min, (6) heated to 110 °C at 10 °C/min to induce thermal relaxation of *cis* azobenzene and melt aggregates, (7) rapidly quenched to -20 °C at -50 °C/min to minimize aggregation, (8) heated to 110 °C at 20 °C/min, and (9) finally cooled to -20 °C at 20 °C/min. $T_g$ of the *cis* and *trans* isomers are calculated from traces of the 4th and 8th steps, respectively (see Figure 48).

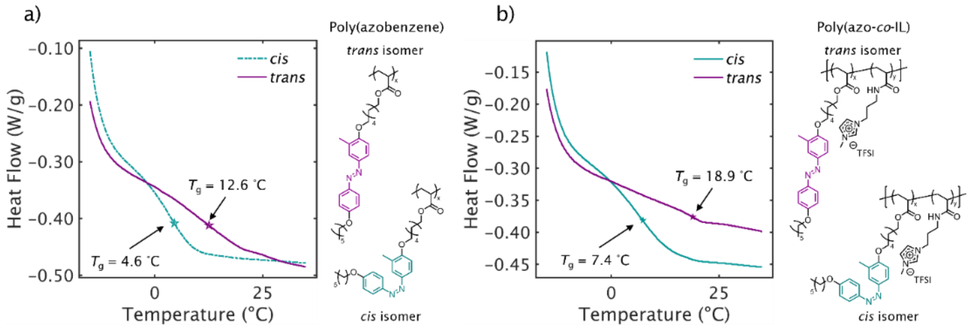

**Figure 47. $T_g$ of poly(azobenzene) and poly(azo-*co*-IL)**

*For both poly(azobenzene) (a) and poly(azo-co-IL) (b), the cis isomer exhibits a lower glass transition temperature ($T_g$) than the trans isomer. For poly(azobenzene), the $T_g$ of the cis isomer occurs at 4.6 °C while the $T_g$ of the trans isomer is at 12.6 °C. For poly(azo-co-IL), the cis and trans isomer $T_g$ are increased to 7.4 °C and 18.9 °C, respectively.*

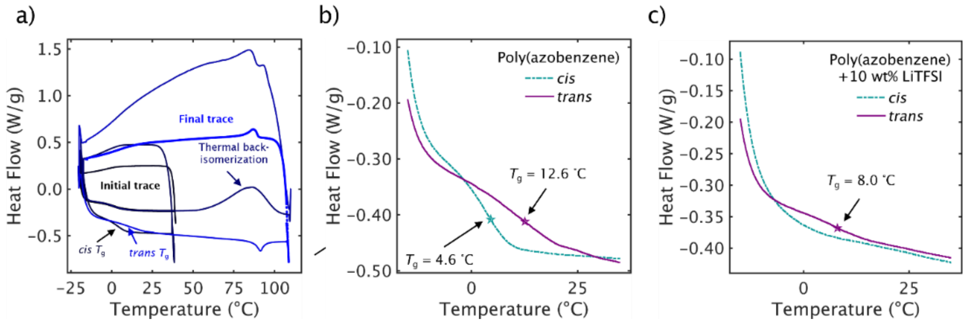

**Figure 48. DSC traces of poly(azobenzene) and poly(azo-*co*-IL)**

*(a) Differential scanning calorimetry (DSC) traces of cis poly(azobenzene) showing the initial cis isomer* $T_g$*, thermal back-isomerization onset around 50 °C and subsequent trans isomer* $T_g$*. (b) The cis isomer exhibits a lower glass transition temperature (*$T_g$*) than the trans isomer for poly(azobenzene). The* $T_g$ *of the cis isomer occurs at 4.6 °C while the* $T_g$ *of the trans isomer is at 12.6 °C. Upon adding 10 wt% LiTFSI to poly(azobenzene), the glass transition becomes less pronounced, at 8 °C for the trans isomer and not observable for the cis isomer.*

### 3.6.5 Impedance Spectroscopy of Poly(azobenzene) and Poly(azo-*co*-IL) Thin Films

Thin films of poly(azobenzene) and poly(azo-*co*-IL) were cast from 10 mg/mL (11:19 (v:v) acetonitrile:toluene, 10 wt% LiTFSI) solutions onto custom fabricated interdigitated electrodes following procedures adapted from Sharon *et al.*[206] Electrodes were fabricated using direct-write lithography (Heidelberg MLA 150) with a 5 nm adhesion layer of Ti and 40 nm of Au above a 300 nm dry chlorinated silicon oxide layer. Interdigitated electrodes consisted of 250 gold digits (125 pairs of opposite polarity) with 5 μm spacing, 5 μm width, and 1 mm length. Substrates were cleaned with sequential sonication in acetone, DI water, and isopropanol followed by 100 W plasma cleaning for 30 seconds prior to casting polymer solutions. Polymer solutions were spun cast at 1,000 RPM, 500 RPM/s for 2 minutes resulting in 26.1 nm and 15.3 nm films of poly(azobenzene) and poly(azo-*co*-IL), respectively. Film thicknesses were measured on bare silicon oxide regions using a Bruker Dektak XT stylus profilometer. Optical micrographs of films on interdigitated electrodes are shown in Figure 50).

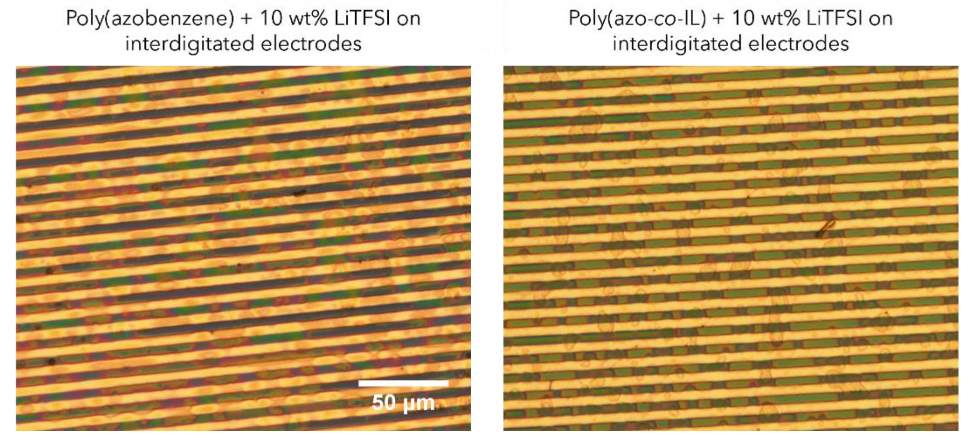

**Figure 49. Microscope images of poly(azobenzene) and poly(azo-*co*-IL) on interdigitated electrode array**

*Brightfield reflectance optical micrographs of poly(azobenzene) (left) and poly(azo-co-IL) (right) on interdigitated electrodes. Variations in color arise due to differences in texture, suggesting that the more uniform poly(azo-co-IL) is able to solubilize more LiTFSI than poly(azobenzene).*

Impedance measurements (100 Hz to 500,000 Hz, 100 mV AC amplitude) were carried out using Solartron 1260 and 1287 potentiostats in tandem with ZPlot software. Sample temperatures were maintained at 40 °C using a vacuum plate with active 25 % humidity controlled $N_2$ gas flow. Power densities for 365 nm and 470 nm monochromatic lamps were calibrated using a Thor labs thermal power meter. Impedance spectra of films were measured as-cast before cycling with 30 second exposures of 470 nm light at 5 mW/cm$^2$ and 365 nm light at 9 mW/cm$^2$. After each irradiation, films were allowed to equilibrate for 30 seconds in dark before AC measurements were applied. 20 measurements (resulting in 10 *trans–cis* photoisomerization cycles) were taken for each film reported. Resulting impedance spectra were fit to an equivalent circuit model using a custom MATLAB script accounting for contact resistance ($R_c$) through instrumentation, constant phase elements for non-ideal interfacial ($CPE_{int}$) and film ($CPE_{film}$) capacitance, film resistance ($R_{film}$), and parasitic capacitance ($C_{sub}$) (see Figure 49).

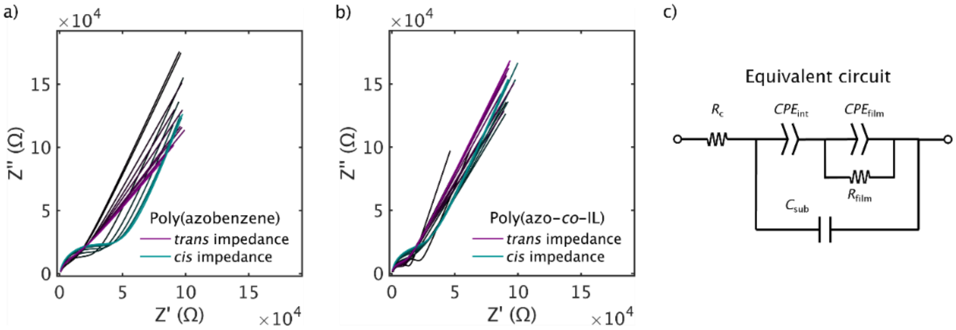

**Figure 50. Equivalent circuit fits to poly(azobenzene) and poly(azo-*co*-IL) Nyquist impedance spectra**

Cycling between UV light (365 nm) and visible light (470 nm) irradiated poly(azobenzene) (a) and poly(azo-*co*-IL) (b) leads to distinct differences in the impedance spectra of the cis and trans isomers. The equivalent circuit (c) consists of contact resistance ($R_c$) through instrumentation, constant phase elements for non-ideal interfacial ($CPE_{int}$) and film ($CPE_{film}$) capacitance, film resistance ($R_{film}$), and parasitic capacitance ($C_{sub}$).

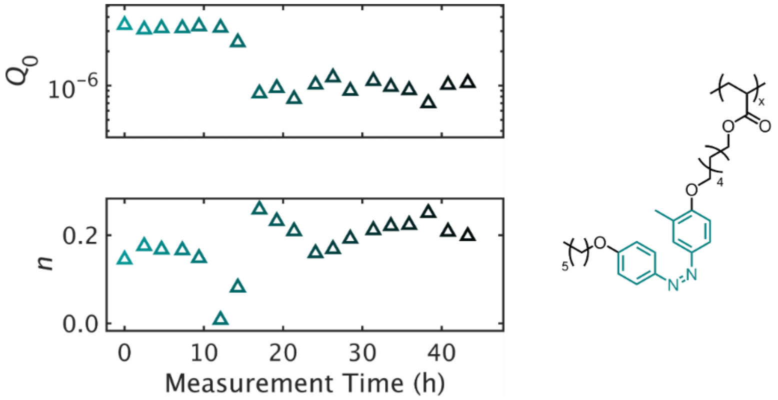

**Figure 51. Constant phase element evolution due to *cis* poly(azobenzene) relaxation**

*Changing constant phase element values fit to the equivalent circuit reflect the broadening of the cis-poly(azobenzene) impedance spectra over time.*

### 3.6.6 UV–Visible Spectroscopy of Poly(azobenzene) and Poly(azo-*co*-IL) Thin Films

Thin films of poly(azobenzene) and poly(azo-*co*-IL) were cast from 10 mg/mL (toluene) solutions. Thin films of poly(azobenzene) (10 wt% LiTFSI) and poly(azo-*co*-IL) (10 wt% LiTFSI) were cast from 10 mg/mL (11:19 (v:v) acetonitrile:toluene) solutions. All films were prepared using the same conditions outlined above for impedance spectroscopy measurements. UV–visible spectra were taken with an Agilent Technologies Cary 60 UV–visible spectrometer. UV–visible spectra are shown in Figure 52. We estimate extinction coefficients from known film thicknesses and an approximate density of 1.2 g/cm$^3$ For poly(azobenzene) with repeat unit molecular weight 466.62 g/mol and poly(azo-*co*-IL) with composition average repeat unit molecular weight 468.64 g/mol, this corresponds to an extinction coefficient (at 363 nm) of 10820 (M azobenzene)$^{-1}$ cm$^{-1}$ for *trans* poly(azo-*co*-IL) [assuming nearly unity *trans* fraction as-cast] and 8565 (M azobenzene)$^{-1}$ cm$^{-1}$ for *trans* poly(azobenzene) [assuming nearly unity *trans* fraction as-cast]. These estimates are consistent with previously reported extinction coefficients and are used to estimate that 53% of *trans* azobenzene has isomerized following 30 seconds of 365 nm illumination (9 mW/cm$^2$) giving a solid-state concentration of 1.0 M *cis* azobenzene at the photostationary state.

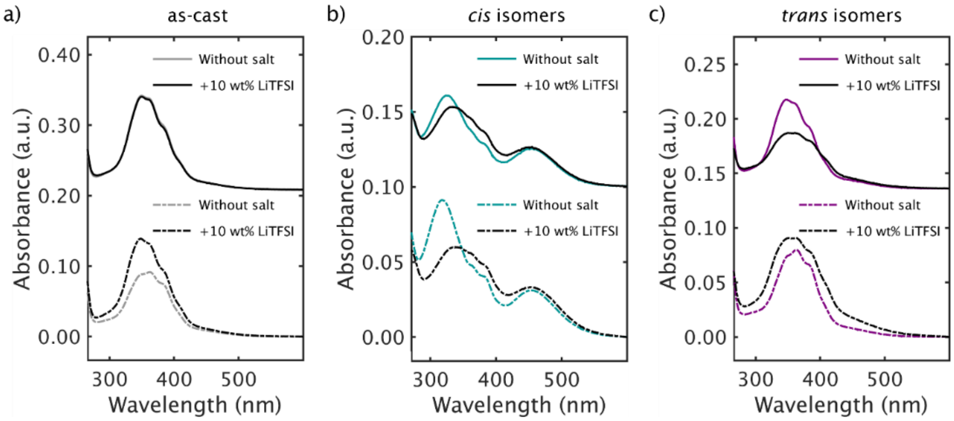

**Figure 52. UV-vis absorbance spectra of as-cast, *cis*, and *trans* poly(azobenzene) and poly(azo-*co*-IL)**

*Absorbances of as-cast (a), cis isomers (b), and trans isomers (c) of poly(azo-co-IL) (top) and poly(azobenzene) (bottom), respectively. The absorbances of the as-cast films are similar between those with and without LiTFSI. The trans isomers show minor differences in absorbance. In contrast, the cis isomers show differences in the position of the primary* $\pi \longrightarrow \pi^*$ *absorbance between films with and without LiTFSI.*

Thermal relaxation of poly(azobenzene) and poly(azo-*co*-IL) (both with 10 wt% LiTFSI) following 30 seconds of 365 nm illumination (9 mW/cm$^2$) were measured in the absence of an electric field. The same conditions as in Figure 29 of the main text were closely matched, including active 25 % humidity controlled $N_2$ gas flow at 40 °C. Thermal relaxation was measured via absorbance at 363 nm, which corresponds to the vibronic absorbance present for both visible and UV-irradiated films (see Figure 52). At 363 nm, this vibronic absorbance is suppressed in the *cis* isomer form relative to *trans* and is expected to increase over time as *cis* azobenzene relaxes to the equilibrium *trans* isomer form. Similar to Figure 29, poly(azo-*co*-IL) relaxes much faster than poly(azobenzene) where the relatively low absorbance of the *cis* isomer persists for more than the measurement period (60 hours). While these trends are similar, poly(azo-*co*-IL) relaxes after approximately 3 hours as measured by *in-situ* UV-vis as compared to the *ca.* 35 hours via conductivity measurements. Previous studies have concluded that *cis* isomer is unstable under applied voltages, with reductive potentials tending towards *trans* azobenzene.[207,208] Given this, we conclude that the 100 mV (vs open circuit) AC amplitude used for impedance measurements does not significantly affect *cis-trans* thermal back isomerization kinetics and that these processes may be offset by diffusion of $Li^+$ from azobenzene to imidazolium-rich domains.

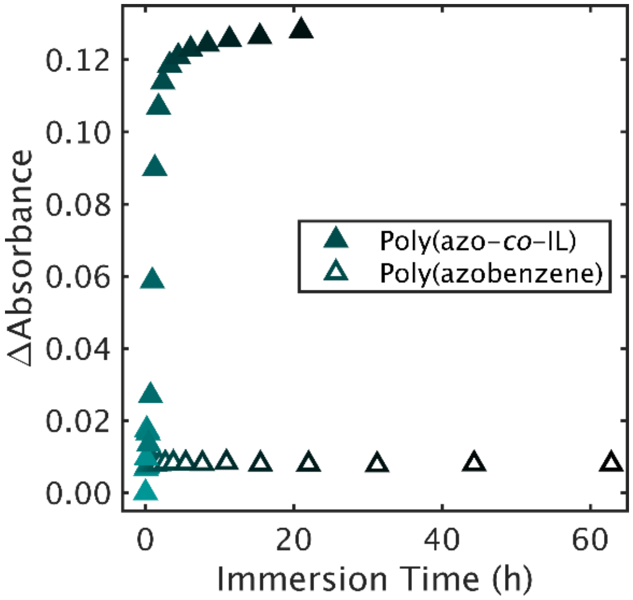

**Figure 53. Relaxation of *cis* poly(azobenzene) and poly(azo-*co*-IL) via time-resolved UV-vis spectroscopy**

*Relaxation of reduced absorbance of cis poly(azo-co-IL) and poly(azobenzene) at 363 nm. Like Figure 29 of the main text, cis poly(azo-co-IL) decays to its trans isomer form rapidly (after c.a. 3 hours) as compared to poly(azobenzene) whose cis isomer absorbance at 363 nm persists for more than 60 hours.*

# Chapter 4 – Dopant Distributions in Semicrystalline Conjugated Polymers from Resonant X-Ray Scattering

Phong Nguyen drafted the manuscript, simulated X-ray optical constants, and performed experimental characterization and final simulations. Devon Callan and Max Gruschka assisted with developing doped P3HT morphology simulations. Evan Plunkett conceptualized the initial outline of the project, fabricated experimental samples, optimized the doping processes, and assisted with characterization. Nima Alizadeh performed atomic force microscopy of all samples. Matt Lansman and Greg Su assisted with simulating X-ray optical constants. Michael Chabinyc, Rachel Segalman, Dean DeLongchamp, and Eliot Gann Provided guidance throughout the work.

## 4.1 Abstract

The distribution of dopant counterions within semicrystalline conductive polymers, such as poly(3-hexylthiophene-2,5-diyl) (P3HT), plays a pivotal role in understanding the mechanisms of charge conduction. These polymers feature a combination of amorphous domains, which enable ion transport, and ordered domains that facilitate high electronic mobility, alongside the need for local charge neutrality between electronic charge carriers and dopant counterions. This complex structure prompts questions about the role of dopant distributions in shaping the energetic landscape for charge conduction. Traditional methods for concurrently probing these domains have been limited. Our study presents a comprehensive model of P3HT morphology and assesses how dopant distribution affects resonant scattering. Crucially, we investigate the role of dopant chemical structure by

incorporating isotropic trifluoromethanesulfonimide (TFSI-) and planar, conjugated 2,3,5,6-tetrafluoro-7,7,8,8-tetracyanoquinodimethane (F4TCNQ•-), examining how these distinct dopant counterions modulate the scattering profiles of doped P3HT films. Our findings reveal that the inherent scattering anisotropy of P3HT, driven by density differences between crystalline and amorphous regions, is significantly affected by dopant placement. This dopant-driven modulation of scattering anisotropy, combined with dopant absorbance, offers a straightforward method to map dopant distribution across both domains, revealing a preference for crystallite incorporation. Moreover, by leveraging the anisotropic refractive indices of F4TCNQ•- at the N and F K-edges, we show that its conjugated planes align perpendicularly to that of the P3HT backbone. This approach underscores the capabilities of polarized resonant soft X-ray scattering in identifying orientation, structural, and compositional distributions within doped conjugated polymers and we introduce a workflow to model and interpret resonant scattering that is broadly extendable to other soft matter systems.

## 4.2 Introduction

Electrical doping of conjugated polymers introduces charge carriers and adjacent counterions. Understanding the interplay between these carriers—often localized as polarons—and counterions across local structural regions is essential for optimizing the conductive properties of these materials. One primary challenge is determining how the charge carriers and counterions are distributed across these regions of the polymer. Dopants and counterions infiltrate the conjugated polymer during the doping process. This infiltration is influenced by mass transport, which is governed by free volume and polymer segmental dynamics, suggesting that these species are more readily transported through disordered, amorphous domains than in ordered domains. The resulting charge carriers have higher mobility in the ordered domains, making it crucial to understand the distribution of counterions and charge carriers post-doping. Here, we focus on the distribution and organization of dopant counterions [trifluoromethanesulfonimide ($TFSI^-$) and 2,3,5,6-tetrafluoro-7,7,8,8-tetracyanoquinodimethane ($F_4TCNQ^{\bullet-}$)] within these crystalline and amorphous domains in a model conjugated polymer, poly(3-hexylthiophene) (P3HT).

Given the low dielectric constant ($2 < \varepsilon_r < 4$) of typical polymers, long-range electrostatic interactions between the charge carriers and counterions are prevalent. These interactions lead to electrostatic trapping, significantly influencing carrier mobility depending on dopant concentration.[209] The Bjerrum length—where electrostatic and thermal energies balance—ranges from 14 to 30 nm at room temperature in conjugated polymers. The length scale between crystalline domains in P3HT is approximately 20 nm and comparable to the electrostatic length scale,[210] suggesting an overlap with the electrostatic length scale. This overlap implies that electrostatic interactions and carrier concentration are key factors in charge transport, especially at high charge carrier densities ($\sim 10^{20}$ $cm^{-3}$) that lead to high electrical conductivity, where screening effects can alter the interactions between carriers and counterions, affecting dopant distributions across polymer domains.

Recent work has shown a correlation between structural disorder and electrical conductivity.[211] Contrary to initial expectations, ion size—a factor coupled to electrostatic trapping—plays a subordinate role compared to the effect of structural order.[127,211] The introduction of dopant counterions can lead to planarization of the polymer backbone and increased structural order overall.[163,212,213] A dependence on the level of doping further complicates this picture. For example, the ratio of polymer repeat units to carriers can range widely from $4 \times 10^5$ at low doping levels ($10^{16}$ cm$^{-3}$) to as high as 4 ($10^{21}$ cm$^{-3}$). Consequently, the average distance between counterions can vary from as high as 45 nm to as low as 1 nm. Fluctuations from these average distances can arise from doping that is localized within either crystalline or amorphous domains. Crystalline domains in *p*-type polymers are more readily doped via integer charge transfer with dopants due to their lower barrier to ionization, whereas amorphous domains may preferably form charge transfer complexes.[214–216] This distinction in charge transfer mechanisms has significant implications for the electronic transport properties of doped films. Thus, a comprehensive understanding of structural disorder and dopant distribution are necessary for optimizing the macroscopic charge transport properties.

While there have been notable advancements in understanding dopant distribution in conjugated polymers, current methodologies often focus on either crystalline or amorphous domains, not both, limiting a comprehensive understanding of dopant distribution. X-ray scattering excels in probing changes within the crystallites of conjugated polymers, yet cannot probe amorphous domains.[162,217] Conversely, electrochemical strain microscopy offers valuable insights on swelling behavior, particularly in amorphous domains.[218,219] The insights gained to date are relatively consistent showing a preference for dopants to localize within either crystalline or amorphous domains. These range from highly crystalline polymers, like PBTTT, to those engineered for enhanced polarity to incorporate ions, such as P3MEEMT.[145,152,216,219–228] The differences between materials depend on factors including the relative redox potentials of polymer domains and dopants, as well as dopant counterion chemistry and size. Despite the significant body of work correlating structural changes in conjugated polymers to doping,[219] a comprehensive perspective integrating both domain types, along with dopant identity and levels, is still lacking. Considering these observations, our approach aims to study dopant distributions simultaneously across both crystalline and amorphous regions in a single material and as a function of dopant identity.

We employed polarized resonant soft X-ray scattering (PRSoXS) to examine the nanostructure of doped P3HT films, leveraging its unique ability to combine X-ray absorption and scattering. While PRSoXS offers rich insights, its interpretation is complex, requiring direct computational methods.[229–233] Using P3HT as a defined model system, we outline a workflow for simulating PRSoXS and its application in resolving the distributions of counterions with two distinct chemical structures in doped P3HT films. We developed a model system using blends of P3HT that allowed us to control the size and concentration of ordered domains and a computational real-space analog for simulation. The model allowed us to explore the expected scattering from PRSoXS arising from different polymer–dopant orientations and distributions. Our analysis, supported by supplementary techniques, isolates the effects of various hypothetical dopant distributions, such as those schematically drawn in Figure 54, providing a clearer understanding of dopant preferences. This integrated approach not only reveals that dopants preferentially reside within crystalline domains but also suggests specific dopant geometries may influence dopant orientations relative to P3HT crystallites, providing a roadmap for future studies aimed at optimizing the properties of semicrystalline organic electronic materials.

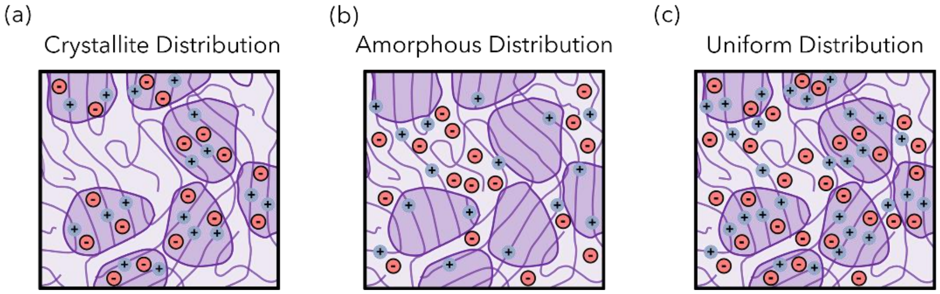

**Figure 54. Schematic of possible dopant distributions**

*(a) Dopants localized within crystallites. (b) Dopants in amorphous regions. (c) Uniformly distributed dopants. Ordered domains are highlighted in darker purple, while lighter purple regions denote disordered domains. Polarons are depicted as blue with a positive charge. Red counter anions are outlined to highlight their distribution within domains.*

## 4.4 Results and Discussion

### 4.4.1 P3HT Films with Controlled Crystallinity and Dopant Counterion Identity

Our goal is to understand how dopants or counterions are distributed between ordered and disordered regions in a model conjugated polymer. The counterion that balances a positively charged carrier in a conjugated polymer typically results from an electron-transfer reaction between a neutral segment of the polymer and a dopant. Figure 54 presents a schematic representation, specifically illustrating hypothetical distributions of resultant counterions between crystalline and amorphous phases in the case of *p*-doping. For P3HT, the crystallites have the smallest ionization energy and are more readily oxidized than the amorphous regions. With a relatively weak dopant like $F_4TCNQ$ there is likely to be a preference for doping of ordered domains. This understanding guided our choice of a model system that would allow us to control the ordered and disordered regions in a semiconducting polymer, thereby enabling an in-depth analysis of how counterions distribute between these domains using various methods.

We chose a model system based on blends of regioregular (RRe) and regiorandom (RRa) P3HT. Low molecular weight RRe P3HT (4.5 kDa) was chosen to be below the contour length of the high molecular weight RRe P3HT (23 kDa) in the blend.[234,235] This choice sets the nominal width of fibrillar crystals formed by the low molecular weight P3HT chains, as confirmed via atomic force microscopy (see Figure 64). The minor amount of high molecular weight RRe P3HT facilitates connections between crystallites, with the remainder of the blend composition consisting of RRa P3HT. The range of blends from 25% to 100% RRe P3HT was selected to systematically vary the degree of crystallinity. We used UV–vis absorbance spectra to estimate the mole fraction of crystalline to amorphous P3HT as the mole fraction of aggregates, ranging between approximately 20% and 40% (see Figure 55).[236] Notably, the ratio of H to J aggregates remained consistent across blends, reinforcing that the blend composition primarily influences the fraction of aggregates rather than the structural type of aggregation. Table 3 summarizes the varying P3HT blend compositions utilized in this study and the resultant levels of aggregation.

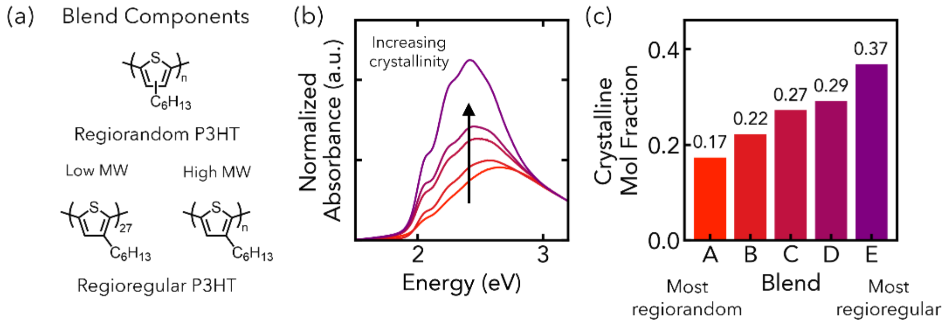

**Figure 55. Control over aggregation via regio-regular/random P3HT blend composition assessed from UV-vis absorbance spectra**

*(a) Regiorandom (RRa) and regioregular (RRe) P3HT are blended to control the total degree of crystallinity. (b) UV-vis absorbance spectra of a series of blends showing increased vibronic absorbance with increasing RRe P3HT. (b) Mol fraction of crystalline P3HT blends corresponding to spectra shown in (a).*

To investigate how counterions distribute in electronically doped blends of P3HT, we chose two structurally dissimilar species. Initially, $F_4TCNQ$ vapor was applied to dope the P3HT blend. The counterion in the doped film was changed using an anion exchange process with a LiTFSI solution that removes the initial counterion $F_4TCNQ^{\bullet-}$ (see Figure 56). Our choice of $F_4TCNQ^{\bullet-}$ and $TFSI^-$ as counterions allowed us to investigate their spatial distribution within the crystalline and amorphous phases of doped P3HT because of the molecular contributions to optical properties and PRSoXS contrast. $F_4TCNQ$ is nominally planar and possesses a conjugated structure, similar to P3HT, thus potentially leading to specific alignment or association within crystalline domains.[216,217,221–223,227] In contrast, $TFSI^-$ is nonplanar with multiple conformers, leading to a different set of interactions and potentially varied distributions within both crystalline and amorphous phases. The resulting differences in X-ray refractive indices and their contributions to features observed in PRSoXS are discussed later.

### 4.4.2 Dopant Uptake with Varying Crystallinity and Counterion Identity

We verified that the doping was uniform throughout the depth of the P3HT blend films before and after ion exchange. We utilized X-ray Photoelectron Spectroscopy (XPS) in conjunction with ion sputtering to analyze the concentration throughout the film depth of $F_4$TCNQ after doping and $TFSI^-$ after ion exchange. The analysis spot size, here 400 × 400 $\mu m^2$, does not offer detailed lateral spatial resolution; instead, it gives a lateral average view of the relative dopant concentrations. Our XPS and ion sputtering analyses revealed consistent dopant distribution throughout the entire depth of P3HT films doped with $F_4$TCNQ, and a nearly complete transition to $TFSI^-$ after prolonged immersion in LiTFSI solution, as detailed in Figure 65 – Figure 67 (Appendix).

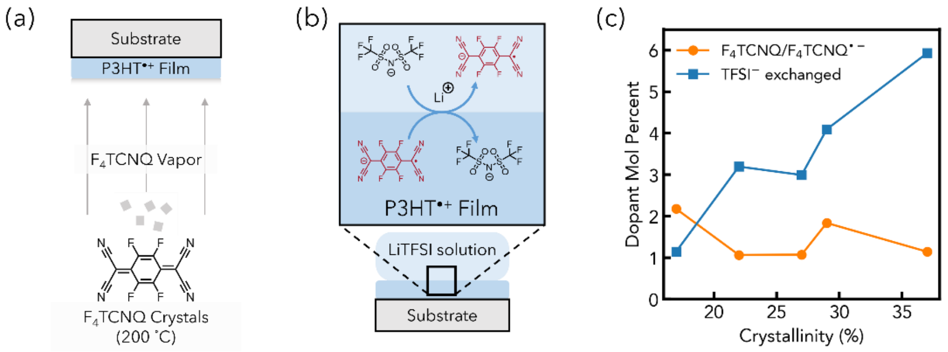

**Figure 56. Schematic depiction of $F_4$TCNQ vapor doping and $TFSI^-$ anion exchange processes with corresponding dopant concentrations as a function of sample crystallinity**

*(a) Schematic depiction of the $F_4TCNQ$ vapor doping process, where $F_4TCNQ$ crystals are sublimated onto a P3HT film, achieving uniform doping, and depositing a small excess of neutral $F_4TCNQ$ on top. (b) Schematic depiction of the ion-exchange process to exchange $F_4TCNQ^{\bullet-}$ for $TFSI^-$ using an LiTFSI solution. (b) Mid-film dopant concentration (relative to P3HT repeat units) versus sample crystallinity.*

Interestingly, while the concentration of $F_4TCNQ/F_4TCNQ^{\bullet-}$ remained relatively consistent across different blend compositions and levels of film crystallinity, we observed an increase in $TFSI^-$ concentration correlating with greater film crystallinity. A potential explanation is the incorporation of excess neutral LiTFSI, along with $TFSI^-$ to replace $F_4TCNQ^{\bullet-}$, but XPS analysis reveals only negligible amounts of $Li^+$ in the samples most rich in $TFSI^-$ [refer to Figure 65 (Appendix)]. Instead, AFM measurements of doped film surfaces[see Figure 68 (Appendix)] indicate a loss of fibril texture following $F_4TCNQ$ vapor doping, which we attribute to the deposition of excess neutral $F_4TCNQ$. Subsequent anion exchange in LiTFSI solution appears to restore the fibril texture. Our estimates for a 1,000 nm thick film with 5.9 mol% $TFSI^-$ (9.6 vol%, based on a doped film density of 1.1 g/cm$^3$) and 1.1 mol% $F_4TCNQ^{\bullet-}$ (1.9 vol%) suggest an approximately 50 nm layer of excess $F_4TCNQ$ (1.6 g/cm$^3$ bulk density) distributed about the film surface, which has an average roughness of about 25 nm. Our estimates of a $F_4TCNQ$ top layer are further corroborated by XPS measurements [Figure 69 (Appendix)]. We propose that presence of excess $F_4TCNQ$ provides the necessary oxidant to allow for greater incorporation of $TFSI^-$ via ion exchange doping as observed in literature.[226,237,238]

### 4.4.3 Scattering Anisotropy as a Measure of Bonding, Morphology, and Molecular Orientation of Doped P3HT Films

We characterized the nanostructure of the P3HT blends before and after doping using PRSoXS in a transmission geometry. We observe energy-dependent changes to the 2D scattering profile due to resonance between different transition dipole moments of the constituents of the blends and polarized resonant soft X-rays. These transition dipoles represent the directionality of electronic excitations of P3HT and the counterions in doped films, and their alignment with the polarization of the incident X-rays leads to anisotropic scattering patterns. The length scale of scattering anisotropy is tied to the periodicity of resonant scatterers, which are centers of molecular excitation/de-excitation (depolarization) processes filtered by relative alignment of X-ray polarization and transition dipole moments.[229,239,240] For example, the 2D scattering profiles shown on the left side of Figure 57 show scattering from polarized 285.25 eV X-rays, which correspond to the C 1s → $\pi^*_{C=C}$ transition dipole moment of an undoped P3HT blend film. Both detector images were captured for the same sample (undoped 37% crystalline P3HT) in the same position and orientation, changing only the direction of X-ray polarization. The fact that high-$q$ scattering follows the X-ray electric field polarization indicates that the scattering anisotropy is due to orientational correlations. For fibrillar P3HT, this orientational correlation length has to do with the periodic distance between aligned fibrils, a connection that follows from the normal of the P3HT thiophene plane being parallel to the fibril long axis.[239,241] As such, we observe anisotropic scattering length scales that reflect periodic distances between aligned fibrils, between 0.01 to 0.1 Å$^{-1}$ for P3HT.[241]

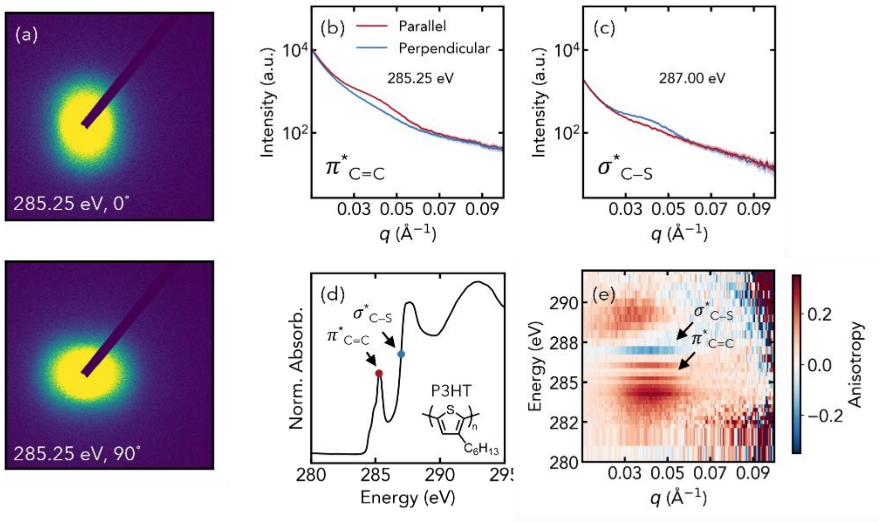

**Figure 57. Experimental scattering anisotropy of P3HT**

*X-ray detector images from a 37% crystalline P3HT blend film using 285.25 eV X-rays, changing only X-ray polarization between 0° (top) and 90° (bottom). Integrated scattering intensity (within a 45° wedge) parallel and perpendicular to the X-ray polarization, showing inversions of scattering anisotropy at 285.25 eV (b) and 287 eV (c). These energies are correlated with the C 1s →* $\pi^*_{C=C}$ *and C 1s →* $\sigma^*_{C—S}$ *transition energies as indicated in the isotropic P3HT NEXAFS in (d). Mapping the anisotropy (e) across energies and q clearly correlates the scattering anisotropy with the transition dipole moments of these transitions.*

The sensitivity of scattering anisotropy to alignment between different transition dipole moments and X-ray polarization is made clear when comparing the scattering at different resonant energies that correspond to orthogonal transition dipole moments. For example, the C 1s → $\sigma^*_{C\text{-}S}$ transition is predominantly in the plane of a thiophene ring as opposed to the out-of-plane C 1s → $\pi^*_{C=C}$ transition.[230,242] As such, the direction of scattering anisotropy compared at 285.25 eV and 287 eV are inverted, with C 1s → $\sigma^*_{\text{C-S}}$ transition resonant at 287 eV (see integrated scattering intensity profiles in Figure 57). The periodic length scale between aligned transition dipole moments is related to the scattering vector $q$. To quantify scattering anisotropy across energies, $E$, and $q$, we use the definition of scattering anisotropy in Equation 20.[229,239,241]

$$A(q,E) = \frac{I_{\parallel}(q,E) - I_{\perp}(q,E)}{I_{\parallel}(q,E) + I_{\perp}(q,E)} \qquad \text{Equation 20}$$

In Equation 20, $A(q, E)$ is the scattering anisotropy, $I_{\parallel}$ is the integrated scattering intensity about a 45° wedge centered along the X-ray polarization direction, and $I_{\perp}$ is the integrated scattering intensity about a 45° wedge centered 90° from the X-ray polarization direction. As such, $A(q, E)$ quantifies oriented scattering, capturing features of the length scales of the morphology (inherited from X-ray scattering) and molecular orientation (imparted by polarization of the incident X-ray electric field). We later show both experimentally and from simulation, that $A(q, E)$ in doped films is related to the counterions and their orientation, allowing us to discern dopant distribution from hypothesized models.

### 4.4.4 Orientational Self-Contrast Between Fibrillar Crystals

Scattering anisotropy, by itself, is a difficult metric to interpret, as it combines information about electronic transitions within the material, spatial correlations, and orientation of transition dipole moments relative to the X-ray polarization. To interpret the sources of scattering anisotropy and later model them, it is helpful to analyze the total scattering intensity as a function of energy and test this against predicted scattering contrast from different X-ray absorbance spectra. This analysis allows us to distinguish which sources of scattering contribute most. The total scattering intensity as a function of incident X-ray energy, $Q(E)$, defined in Equation 21.

$$Q(E) = \int_0^\infty I(q, E) q^2 \, dq \propto |\Delta n_{AB}(E)|^2 \qquad \text{Equation 21}$$

In Equation 21, $Q(E)$ is the energy-dependent Porod invariant [approximated with the total scattering intensity (TSI) in Figure 58] and $|\Delta n_{\mathrm{AB}}(E)|^2 = (\delta_{\mathrm{A}} - \delta_{\mathrm{B}})^2 + (\beta_{\mathrm{A}} - \beta_{\mathrm{B}})^2$, with $\delta_i$ and $\beta_i$ being the real and imaginary components of the complex refractive indices. $Q(E)$ can be interpreted as the Lorentz-corrected scattering across all $q$ and thus represents the total population of scatterers as a function of incident X-ray energy. In hard X-ray scattering, $Q(E)$ arises from differences in electron density between different phases/components. Within PRSoXS, a chemically homogeneous sample with anisotropic refractive indices can be treated similarly with each orientation (possessing orientation-dependent X-ray absorbance spectra) treated essentially as a different phase. We note that the determination of $Q(E)$ assumes only scattered coherent X-rays and thus accurate measurements of $Q(E)$ require filtering of incoherent X-rays. To accomplish this, we fit a power-law scattering form factor at high $q$ and subtracted the constant offset to remove signals of isotropic fluorescence.[243]

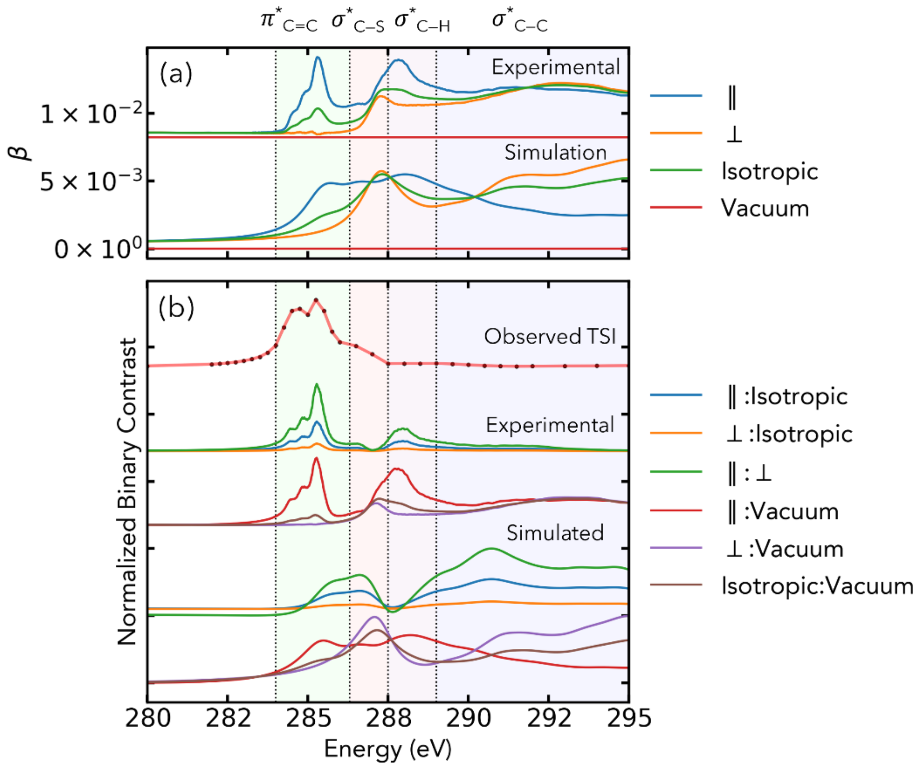

**Figure 58. Comparisons between observed and possible sources of p-RSoXS scattering contrast.**

*(a) Experimentally extrapolated (top) and directly simulated (bottom) NEXAFS of P3HT, with X-ray electric fields parallel, perpendicular, or isotropic relative to the C 1s →* $\pi^*_{\text{C=C}}$ *transition dipole moment. Trends show strong agreement, particularly below 288 eV, where the dominant source of scattering contrast appears. (b) Comparison of the observed total scattering intensity and potential sources of binary scattering contrasts for both experimentally extrapolated and simulated P3HT NEXAFS.*

In Figure 58, we compare the observed total scattering intensity (TSI), an approximation of $Q(E)$, with experimentally extrapolated and simulated P3HT NEXAFS, showing that the energies with the most scattering correspond to the C 1s → $\pi^*_{\text{C=C}}$ followed by the C 1s → $\sigma^*_{\text{C-S}}$ transition and that the source of this scattering is orientational self-contrast.[210] To aid interpretation, the energy axis is aligned between experimentally extrapolated and simulated NEXAFS (above) and various binary scattering contrasts (below). This approach enables hypothesis testing of the most likely sources of scattering contrast and provides a key for determining which transition dipole moments are significant. Here, we utilize the uniaxial optical tensor approximation with the normal to the thiophene plane (corresponding to the C 1s → $\pi^*_{\text{C=C}}$ transition dipole moment) defined as parallel (∥) and remaining two orthogonal directions are averaged and denoted as perpendicular (⊥). The isotropic NEXAFS is the weighted average of the parallel and perpendicular NEXAFS.

We observe a high degree of contrast in X-ray absorbance as the X-ray polarization varies from parallel to perpendicular. The antibonding orbitals labeled above the plot in Figure 58 were assigned based on simulation [see Figure 75 – Figure 78 (Appendix)] and are in agreement with previous assignments for P3HT.[239,242,244,245] We compare both experimentally extrapolated NEXAFS and directly simulated NEXAFS, highlighting that each approach captures different aspects of the observed PRSoXS. While the $\pi^*_{\text{C=C}}$ features are similar between experimental and simulated NEXAFS, there are notable deviations at higher energies. The simulated NEXAFS show that the C 1s → $\sigma^*_{\text{C-S}}$ transition dipole moment is dominant at 287 eV, in agreement with the inversion of scattering anisotropy seen in Figure 57. We note that the simulated NEXAFS is not accurate past 288 eV, where $\sigma^*_{\text{C-H}}$ and $\sigma^*_{\text{C-C}}$ features dominate.

From the TSI shown in Figure 58, we observe minimal scattering contrast past 288 eV which indicates (1) that the alkyl P3HT side chain is, on average, isotropic such that there is little orientational contrast due to transition dipole moments originating from C-H and C-C bonding and (2) that vacuum contrast is insignificant. The experimentally extrapolated NEXAFS predicts this isotropic side-chain conformation and is apparent when considering the possible binary contrasts shown directly below the observed TSI. In contrast, the binary contrasts from the simulated NEXAFS ($3^{rd}$ set of traces below TSI) presume that the alkyl side chains are ordered and outstretched and thus exhibit strong anisotropy—a feature of the simulated ordered P3HT unit cell. Next, we note minimal scattering contrast past the primary absorption edge, a feature which indicates minimal vacuum contrast/surface roughness as compared to bulk scattering. Vacuum, when treated as a material with no absorbance, gives way to binary contrast that is the $n_i^2$ and thus should give a step edge past the absorption onset when vacuum contrast is significant. Thus, as a first approximation, we neglect scattering from surface roughness in our simulations. Lastly, we use the experimentally extrapolated NEXAFS for PRSoXS simulations discussed later, noting limitations here in the accuracy of predicting scattering anisotropy near 287 eV.

### 4.4.5 Experimental Scattering Anisotropy Varies with Crystallinity and Dopant Identity

Studies of scattering anisotropy in undoped conjugated polymers have led to a robust understanding that orientational correlations between aligned domains contribute to anisotropic scattering within PRSoXS. For example, previous studies involving blends of P3HT with relatively isotropic PCBM, a fullerene derivative prevalent in organic photovoltaics, have demonstrated that scattering anisotropy necessitates molecular alignment correlated with domain boundaries to produce anisotropic scattering patterns.[246] For many semicrystalline conjugated polymers, the source of scattering anisotropy is attributed to the C 1s → $\pi^*_{\mathrm{C=C}}$ transition dipole, which disrupts isotropic symmetry at the molecular level along the direction normal to the conjugated plane of the polymer backbone.[241,247,248] This has facilitated the differentiation between various types of fibrillar crystallites, where the alignment between the fibril long axis and the C 1s → $\pi^*_{\mathrm{C=C}}$ transition dipole moment may vary.[241] Furthermore, the cited studies emphasize that within a chemically homogeneous system, *e.g.*, undoped P3HT, a variance in density between ordered and disordered phases can lead to distinct domains of varying optical density necessary for scattering anisotropy.

Analysis of PRSoXS data from undoped P3HT films reveals a clear trend: as the degree of crystallinity increases, so does the magnitude of scattering anisotropy up to the C 1s → $\sigma^*_{\mathrm{C\text{-}S}}$ transition at 287 eV, as illustrated in Figure 59. This observation is in line with predictions of previously established models: that increasing crystallinity leads to a greater number of orientationally correlated crystalline domains, culminating in a more pronounced scattering anisotropy.[210,233] This is exemplified by both increased negative scattering anisotropy at the C 1s → $\sigma^*_{\mathrm{C\text{-}S}}$ transition (287 eV), and greater positive scattering anisotropy at the C 1s → $\pi^*_{\mathrm{C=C}}$ transition (285.25 eV) which highlights the orthogonality of the two transition dipole moments. The specific value of $q$ at which this anisotropy emerges is affected by the proportion of RRe P3HT in the blend; a higher proportion leads to smaller amorphous regions between the crystallites, which, in turn, shifts the scattering anisotropy to higher $q$ values. This pattern is consistent with what we observe in both samples of greater crystallinity and annealed samples [Figure 93 (Appendix)].[233] Figure 59 shows scattering anisotropy data for only our least and most crystalline samples; however, a full set of scattering anisotropy data for all blend compositions are available [Figure 94 (Appendix)].

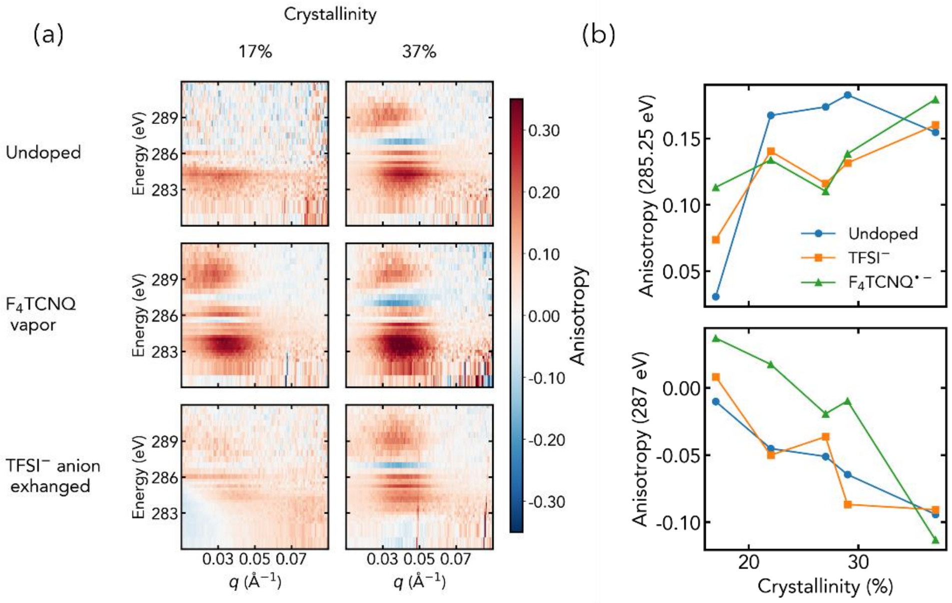

**Figure 59. (a) Experimental scattering anisotropy across crystallinity and dopant counterion identity.**

*Trends in scattering anisotropy across energies and q as a function of blend compositions and doping. (b) Anisotropy as a function of blend composition at 285.25 eV (top), and 287 eV (bottom), corresponding to the C 1s* $\rightarrow \pi^*_{C=C}$ *and C 1s* $\rightarrow \sigma^*_{C—S}$ *transitions, respectively.*

In films doped with $F_4TCNQ^{\bullet -}$ counterions, the scattering anisotropy below 283 eV is significantly enhanced across all levels of sample crystallinity, consistent with similar levels of $F_4TCNQ^{\bullet -}$ uptake measured across all blends. This enhancement is attributed primarily to

$F_4TCNQ^{\bullet-}$ having greater X-ray optical absorbance; its incorporation makes the samples more optically dense, presumably where $F_4TCNQ^{\bullet-}$ is most concentrated. At the N and F K edges, scattering anisotropy at the same length scale is observed for $F_4TCNQ$-doped samples, indicating that $F_4TCNQ^{\bullet-}$ counterions are likely structurally aligned relative to P3HT crystallites [Figure 95 and Figure 96 (Appendix)]. In contrast, when $TFSI^-$ is the counterion, minimal changes in the magnitude of the scattering anisotropy are observed. $TFSI^-$ lacks a carbon-based $\pi$ system, in contrast to planar $F_4TCNQ^{\bullet-}$, and has a more ellipsoidal geometry, resulting in relatively isotropic NEXAFS [simulated $TFSI^-$ NEXAFS are shown in Figure 81 and Figure 90 (Appendix)]. This isotropy can be seen from a comparison of scattering anisotropy for undoped P3HT and $TFSI^-$-containing doped P3HT in Figure 59, as well as N and F K-edge anisotropy maps, where little to no scattering anisotropy is observed [Figure 95 and Figure 96 (Appendix)]. Opposite from the $F_4TCNQ^{\bullet-}$ case, $TFSI^-$ incorporation leads to an inversion in scattering anisotropy below 283 eV, a feature correlated with the weaker absorbance of $TFSI^-$ relative to P3HT, such that the addition of $TFSI^-$ acts to lower the X-ray optical density where it is distributed. We also note that $TFSI^-$ was introduced using an ion-exchange process from films initially doped with $F_4TCNQ$ and we may expect only small changes in the overall nanostructure of P3HT, making the comparison of the two cases more robust.

From our NEXAFS simulations and observed scattering anisotropy, it is clear that the relative X-ray absorbance of the dopants affects the resultant changes to scattering anisotropy due to either a concentration or dilution of X-ray absorbance in the amorphous/crystalline P3HT domains that these dopants occupy. Much of the inherent scattering anisotropy in undoped P3HT comes from differences in density between crystalline and amorphous regions.[241] We hypothesized that selective distributions of dopants to either only crystallites or amorphous regions would result in distinct changes to scattering anisotropy requiring simulation to uncover the origin of these experimental observations.

### 4.4.6 Modelling Dopants in Semicrystalline Polymers

To aid in interpreting doping-induced changes to experimental scattering anisotropy maps, we developed a methodology using a digital twin of our model system for PRSoXS simulations. For this process, we employ the voxel-defined morphology framework of the NIST RSoXS Simulation Suite (NRSS) in the four-step workflow as outlined in Figure 60.[231]

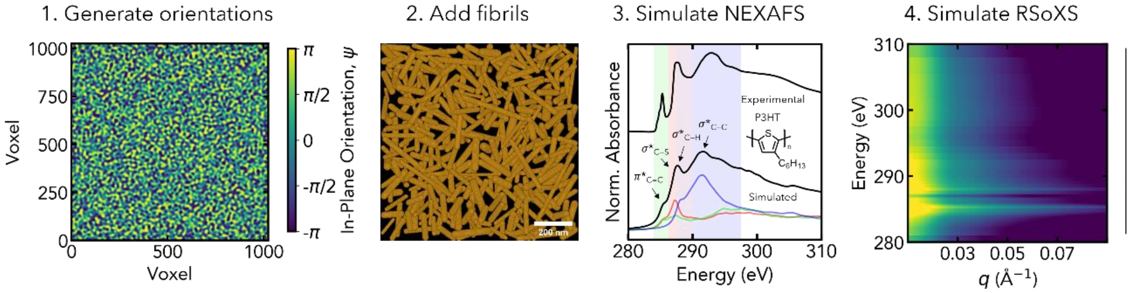

**Figure 60. RSoXS simulation process involving a multi-step workflow.**

*First, the generation of orientation fields seeds the simulation space for fibril orientation. Secondly, Poisson disk sampling facilitates the random distribution of fibrils with prescribed minimum distances, inheriting orientation during placement. Fibrils grow lengthwise until reaching another fibril or the predefined maximum length. The final morphology distinguishes between fibrillar (crystalline P3HT) and amorphous phases.*

*Third, the calculated X-ray refractive indices were applied to different phases, and the combined morphology and refractive indices finally enable the simulation of RSoXS patterns.*

We initiated the simulation by defining a box and voxel pitch that represent the PRSoXS experimental length scales, specifically within a $q$-range of 0.01 to 0.1 Å$^{-1}$ corresponding to periodicities from 63 to 6.3 nm. Orientation fields were employed to seed fibrils and ensure in-plane isotropy (random $\psi$) and orientation with respect to the substrate normal ($\theta$) as inferred from GIWAXS data. The orientation fields were generated using a power spectral density and normalized with a cumulative distribution function. Figure 74 (Appendix) demonstrates the simulated scattering anisotropy versus edge-on character, highlighting minor variances between the least and most edge-on aligned samples and minimal changes to edge-on character upon doping. Thus, the average orientation distribution across all samples was used to isolate the effect of dopant distribution and identity. Within the defined simulation box, voxelized fibrils were introduced sequentially. These fibrils possess a Gaussian distribution of diameters (15 ± 3 nm) and an initial length of 100 nm, growing lengthwise until they either achieve a maximum length of 400 nm or encounter another fibril. Voxels within the fibrillar areas are classified as crystalline, with their C 1s $\rightarrow \pi^{*}_{\mathrm{C=C}}$ transition dipole moments aligned along the fibril length.[239] The surrounding matrix is identified as amorphous with 10% less density than crystalline P3HT and exhibits isotropically-averaged P3HT optical properties.[241] A Gaussian filter with a standard deviation of 3 was employed at the crystalline–amorphous boundary to define interfacial volume fraction and orientation gradients. Figure

61 presents a rendered, illustrative example of the simulated morphology, providing a comparison with fibril texture measured by AFM.

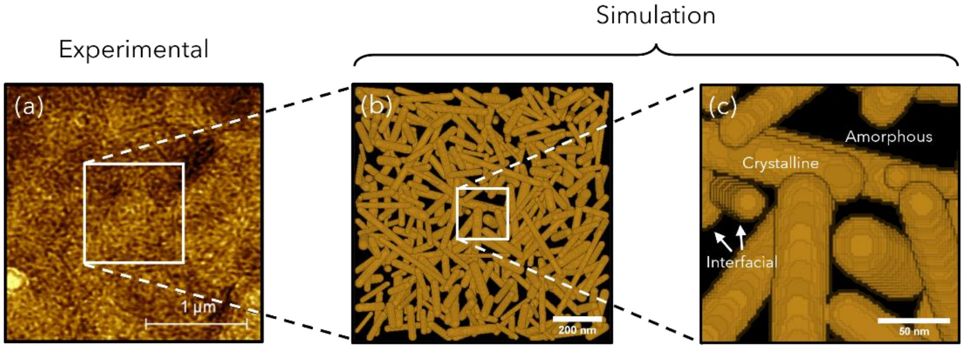

**Figure 61. Comparisons between experimentally observed and simulated P3HT morphology.**

*(a) Atomic force microscopy phase contrast image showing fibrillar crystallites of P3HT. (b) Simulated P3HT morphology, directly comparable to the region highlighted in (a). (c) Zoomed inset of simulated morphology, showing individual voxels composing crystalline, amorphous, and interfacial domains.*

For dopant incorporation, we replaced certain fractions of P3HT volume either uniformly, within crystallites, or within amorphous regions. The total dopant concentration was normalized to XPS measurements, as discussed above. The orientation of isotropic $TFSI^-$ and $F_4TCNQ^{\bullet-}$ is randomized, while aligned $F_4TCNQ^{\bullet-}$ shares orientation with P3HT (parallel C 1s → $\pi^*_{C=C}$ transition dipole moments). We also consider perpendicularly oriented $F_4TCNQ^{\bullet-}$ with an offset of +90° for $\psi$. The results for different combinations of dopant distribution and orientation are discussed later.

### 4.4.7 Simulation-Aided Interpretation of Scattering Anisotropy

To better understand the dopant-induced changes to the scattering anisotropy of the P3HT blends, we adopted the direct simulation approach outlined above. Specifically, our models simulate scattering anisotropy resulting from three distinct scenarios for the dopant distribution, as illustrated in Figure 54: a uniform distribution across the polymer, localization within crystallites, and localization within amorphous regions. In each scenario, we maintained a consistent doping level, ensuring that the total dopant concentration remains equivalent across all distributions by proportionately replacing the material in a specified phase (crystalline, amorphous, or uniform) with dopant. We first examine the case of $TFSI^-$ to probe the effect of dopant distribution alone, given its relatively isotropic X-ray optical constants at the C K edge [Figure 90 (Appendix)]. Subsequently, we explore the effect of dopant orientation with three distinct relative alignments of the C 1s $\rightarrow \pi^*_{C=C}$ transition dipole moments between P3HT and $F_4TCNQ^{\bullet-}$: unaligned, parallel, and perpendicular. It is important to note that these orientations are defined with respect to the crystalline P3HT, ensuring that the orientation of $F_4TCNQ$ is consistently measured against the P3HT C 1s $\rightarrow \pi^*_{C=C}$ transition dipole moments. We find that at the $F_4TCNQ$ concentrations observed (< 2.5 mol% $F_4TCNQ/F_4TCNQ^{\bullet-}$ relative to P3HT repeat units), scattering anisotropy at the C K edge does not sufficiently distinguish between the three cases for the orientation. Lastly, we acknowledge that the model's accuracy in predicting scattering anisotropy is limited to the three specific dopant distributions and orientations explored and does not encompass all possible configurations. Additionally, the P3HT refractive indices used do not reflect inversion of scattering anisotropy at 287 eV, and simulated fibrils based on random orientation fields do not perfectly capture orientational correlation lengths. Despite these limitations, our simulations distinctly delineate the effects of various dopant distributions.

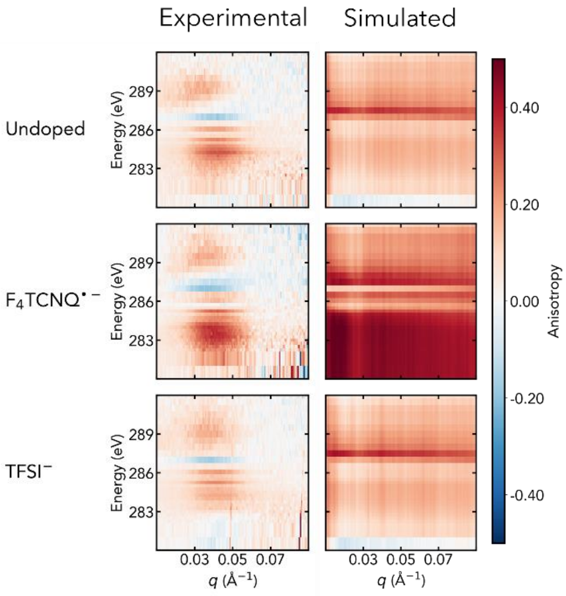

**Figure 62. Comparison of experimental and simulated scattering anisotropy in 37% crystalline P3HT films.**

*Simulated scattering anisotropy corresponds undoped P3HT (top), anti-aligned* $F_4TCNQ^{\bullet -}$ *counterions localized within crystallites (center), and uniformly distributed, randomly oriented* $TFSI^-$ *counterions (bottom).*

In Figure 62, we show the most consistent models (based on approximately 37% crystalline simulated morphologies) compared to experimentally observed scattering anisotropy for 37% crystalline P3HT containing $F_4TCNQ^{\bullet -}$ and $TFSI^-$ counterions. Our initial focus examines the changes to scattering anisotropy arising from varying dopant distributions. For $TFSI^-$, which exhibits relatively isotropic X-ray optical properties, the primary effect of differing distributions—whether uniform across the polymer, localized within crystallites, or localized within amorphous regions—is a modulation of the effective optical density in these areas. Differences in density contrast between crystalline and amorphous P3HT have previously been assigned to account for scattering anisotropy.[241] Given that $TFSI^-$ exhibits roughly half the absorbance of P3HT at the C K-edge [see Figure 82 and Figure 90 for P3HT and $TFSI^-$ refractive indices, respectively (Appendix)], the replacement of P3HT with $TFSI^-$ within the voxels of our model effectively diminishes the optical density at sites of $TFSI^-$ localization. Uniform doping negligibly impacts scattering anisotropy, which is still dominated by P3HT itself, correlating well with the experimental observations shown in Figure 59. Localized $TFSI^-$ within amorphous domains leads to pronounced positive scattering anisotropy below 283 eV; in contrast, $TFSI^-$ confined to crystallites results in negative scattering anisotropy at sub-283 eV energies [Figure 97 (Appendix)]. In the case of isotropic, randomly oriented $F_4TCNQ^{\bullet-}$, which exhibits an absorption approximately 4× that of P3HT, a reversed trend is observed: positive scattering anisotropy below 283 eV when localized within crystallites, and an inversion when $F_4TCNQ^{\bullet-}$ is within amorphous regions. These observed variations in scattering anisotropy for isotropic dopants highlight that the direction and magnitude of scattering anisotropy can distinctly differentiate between dopant distributions due to the influence of changing optical densities in different phases.

The X-ray refractive indices can vary with different orientations of molecular units within a solid film because of the orientation of their transition dipoles. Because of this, various orientations of the same material act as if they were separate material phases, *i.e.*, orientational self-contrast. As a dopant that resides predominantly within crystallites, we explore the possibility that the planar structure of $F_4TCNQ^{\bullet-}$ may lead to specific orientation within the P3HT crystallites. We specifically examine scenarios involving $F_4TCNQ^{\bullet -}$ in unoriented, parallel, and perpendicular configurations (refer to Figure 63 for visualization). Our C K-edge simulations indicate that the scattering anisotropy patterns of these orientations are not sufficiently distinct to determine the dopant orientation within a crystallite. This suggests that at the C K edge, scattering anisotropy is predominantly influenced by variations in optical density rather than the orientation of the dopant. However, at the N and F K edges—where P3HT does not absorb, making the dopant's contribution more pronounced—we observe clearer evidence of dopant orientation. Particularly at the N K edge, both experimental and simulated data of perpendicular configurations reveal a transition from positive to negative scattering anisotropy around 401 eV, indicative of a predominant perpendicular orientation of $F_4TCNQ^{\bullet -}$ within crystallites, as illustrated in Figure 63b. Similar patterns are observed at the F K edge, corroborating the significance of dopant orientation. Additionally, we note that across varying blend compositions, the scattering anisotropy exhibits a consistent structure (see Figure 94 – Figure 96). Minor shifts in the location of the scattering anisotropy maxima and intensity fluctuations scale with crystallinity, as discussed above.

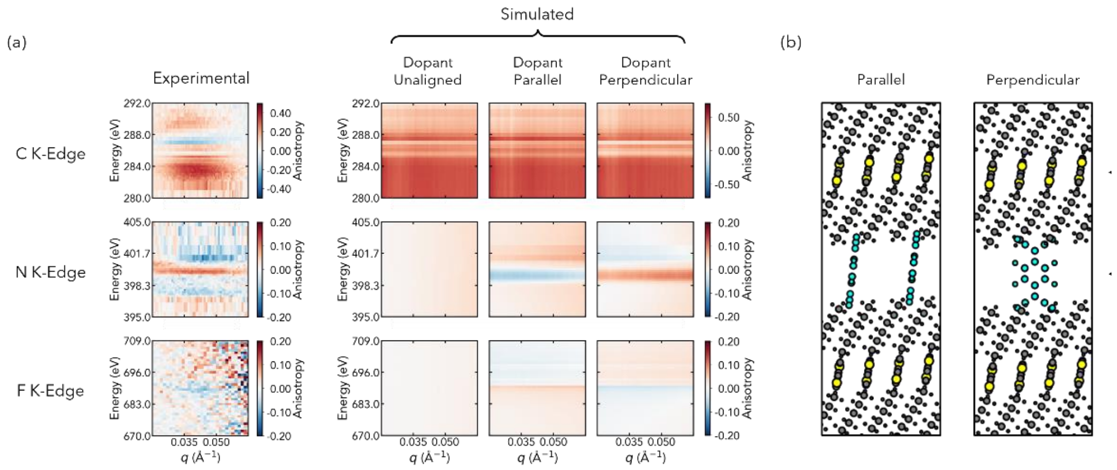

**Figure 63. Comparison of experimental and simulated scattering anisotropy in 37% crystalline P3HT films with varying $F_4TCNQ^{\bullet-}$ orientations relative to P3HT.**

*(a) Experimental scattering anisotropy maps at the C, N, F K edges shown next to simulated scattering anisotropy maps for unaligned, parallel, and perpendicular* $F_4TCNQ^{\bullet-}$ *relative to P3HT. (b) Schematic representations of the relative alignments of* $F_4TCNQ^{\bullet-}$ *to P3HT within a crystallite; not intended to depict exact crystal structures.*

In conclusion, our findings illustrate that for P3HT and the dopants considered here, the orientational self-contrast is less significant than the effect of changing optical density at the C K-edge X-rays, which presents a challenge in resolving both aspects using a single X-ray edge. However, by focusing on the unique orientational self-contrast at the N and F K edges, which are distinct to $F_4TCNQ$ in this experimental system, we successfully isolated and discerned dopant orientation. This insight not only advances our comprehension of scattering anisotropy but also underscores the intricate interplay among dopant distribution, orientation, and the resultant X-ray optical properties in doped conjugated polymer systems.

### 4.5 Conclusions

To understand the distribution of dopant counterions within the crystalline and amorphous phases of P3HT, we developed a range of P3HT blends, adjusting crystallinity and incorporating distinct dopant counterions: isotropic $TFSI^-$ and planar, conjugated $F_4TCNQ^{\bullet-}$. Our investigation utilized Polarized Resonant Soft X-Ray Scattering (PRSoXS), a technique that merges X-ray absorbance spectroscopy with X-ray scattering, making it well-suited for probing the structural, compositional, and orientational distributions in doped P3HT blends. To isolate the effect of dopant identity and distribution, we complemented PRSoXS with Atomic Force Microscopy (AFM) for morphological insight, UV–visible spectroscopy (UV–vis) to assess aggregation, X-Ray Photoelectron Spectroscopy (XPS) for dopant concentrations, and Grazing Wide-Angle X-ray Scattering (GIWAXS) for P3HT out-of-plane orientation. Our findings reveal that the inherent scattering anisotropy of P3HT, primarily driven by density variations between crystalline and amorphous regions, can be modulated by dopant distribution. Specifically, $TFSI^-$, with its lower absorbance at the C K edge, uniformly distributes across P3HT without significantly affecting its anisotropy. Conversely, $F_4TCNQ$ increases scattering anisotropy through its incorporation within crystallites. By leveraging the anisotropic refractive indices of $F_4TCNQ$ at the N and F K edges, we confirmed its conjugated planes are oriented perpendicularly to that of P3HT. Importantly, we outline a workflow for creating morphological models and integrating orientation-dependent refractive indices into PRSoXS simulations, crucial for understanding the complex effects of orientation, composition, and structure. This methodology not only highlights the unique sensitivity of PRSoXS but potentially paves the way for future workflows to capitalize on its unique insights to develop structure-property relationships across soft matter systems.

## 4.6 Appendix

### 4.6.1 Materials and Methods

#### 4.6.1.1 Materials and Processing Conditions

We use low molecular weight regioregular (RRe) P3HT (4.5 kDa, PDI = 1.6), high molecular weight RRe P3HT (23 kDa, PDI = 1.8), and regiorandom (RRa) P3HT (16.3 kDa, PDI = 2.5), which were dissolved in an equal-volume mixture of chlorobenzene and dichlorobenzene. P3HT solutions of varying blend composition were drop cast onto substrates to form 700 nm – 1,000 nm thick films. P3HT films are doped in an inert nitrogen glovebox atmosphere, enclosing the film and *c.a.* 3 mg of $F_4TCNQ$ crystals within a jar in the orientation depicted in Figure 56.[122] The jar was heated to 200 °C for 45 minutes, allowing for sublimation of $F_4TCNQ$ to oxidize the P3HT film. $TFSI^-$-containing samples are further anion exchanged in a concentrated LiTFSI solution (3 wt% in acetonitrile) for 120 minutes at 60 °C. Table 3 summarizes the varying P3HT blend compositions utilized in this study, resultant levels of aggregation, and dopant counterion concentrations measured.

#### 4.6.1.2 UV-Vis Absorbance Spectroscopy

All UV-vis spectra were acquired using an Agilent Technologies Cary 60 UV-vis spectrometer. Samples were drop cast from solution onto quartz substrates to form optically transparent films. Spectra for P3HT films of varying composition were fit to the Spano model via a custom Python script to quantify aggregate mole fractions.[236,249,250]

#### 4.6.1.3 X-Ray Photoelectron Spectroscopy

X-ray photoelectron spectroscopy (XPS) measurements were performed using an Escalab Xi+ Spectrometer from ThermoFisher Scientific. The spectrometer operated under a high vacuum condition of $10^{-8}$ Torr and utilized a monochromatic aluminum Kα X-ray source. To stabilize charge during the measurements, we used a dual ion-electron low-energy flood source. For acquiring survey spectra, we set the pass energy to 100 eV and conducted five scans at intervals of 0.25 eV, each with a dwell time of 50 ms. Depth profiling was done using an ion gun with a 1,000-atom $Ar^+$ cluster and an ion energy of 6,000 eV. Ion sputtering covered a square region measuring $1.5 \times 1.5$ $mm^2$. Within this area, we collected photoexcited electrons from the inner $400 \times 400$ $\mu m^2$ region to selectively isolate signal from crater centers.

#### 4.6.1.4 Grazing Incidence Wide Angle X-Ray Scattering

Grazing incidence wide angle X-ray scattering (GIWAXS) was performed at experimental station 11-3 at the Stanford Synchrotron Radiation Lightsource using an X-ray energy of 12.7 keV. Angle-resolved GIWAXS scans were acquired with 120 second exposures at grazing incidence angles of 0.05°, 0.10°, and 0.13°. 2D detector images were remapped to *q*-space using Nika and the WAXSTools Igor packages.[251] Partial pole figure analysis was done using a custom open-source python package (https://github.com/phonghnguyen/GIWAXS_Tools). See Figure 70 – Figure 74 (Appendix) for more details of the analysis and representative partial pole figures used for model morphology development.

#### 4.6.1.5 Resonant Diffraction

Resonant soft X-ray scattering experiments were performed at the Spectroscopy Soft and Tender (SST-1) beamline funded and operated by the National Institute of Standards and Technology (NIST) at the National Synchrotron Light Source II (NSLS-II).[252] Data reduction was performed using PyHyperScattering (https://github.com/usnistgov/PyHyperScattering), an open source package for hyperspectral scattering reduction and analysis.[253] Thin film samples on transparent silicon nitride windows were mounted normal to the incident X-ray beam with samples measured in transmission mode under high vacuum conditions.

#### 4.6.1.6 NEXAFS Simulations

Near edge X-ray Absorption Fine Structure (NEXAFS) simulations were carried out using the PWscf and XSpectra software packages of the Quantum ESPRESSO distribution.[254–258] The NEXAFS simulation process consists of (1) sourcing equilibrated or equilibrating atomic coordinates for a given molecule,[259] (2) obtaining the electronic structure for each core-hole configuration of the molecule, and (3) calculating the polarization-dependent X-ray absorbance spectra for each core-hole configuration. The configuration-specific spectra are offset by their relative total energies. The sum of spectra for each polarization direction are experimentally offset to tabulated absorption onsets (*e.g.*, the C 1s $\rightarrow \pi^*_{\mathrm{C=C}}$ peak measured at 285.25 eV) to obtain oriented NEXAFS. The NEXAFS are normalized to the bare atom scattering factors to obtain the imaginary component of the refractive indices, $\beta_i$, which can be solved for the real portion, $\delta_i$, using the Kramers-Kronig relations.[260,261]

To calculate P3HT NEXAFS, atomic coordinates for unit cells of low-energy crystalline polymorphs of P3HT were sourced from literature.[160,259] We adopt the approach of using a supercell consisting of 3-hexylthiophene 8-mer with periodic boundary conditions to represent a single polymer chain.[160,259] This is consistent with prior work demonstrating that 6 repeat units is sufficient to isolate adjacent core-hole excitons.[242] Our tests also confirmed that $\pi$-stacking effects are minimal and that $k$-point sampling density variations produce negligible spectral changes (Figure 75 – Figure 78). This further confirms that the chosen supercell is sufficient to capture key attributes of the simulated NEXAFS.

For the simulations involving dopant counterions, atomic coordinates were geometrically optimized through a relaxation calculation in Quantum ESPRESSO. A single dopant molecule within a sufficiently large cubic lattice was used to ensure the isolation of core-hole exciton effects. The optimization process employed the generalized gradient approximation (GGA), following the Perdew-Burke-Ernzerhof (PBE) scheme, and utilized a plane-wave cutoff energy of 30 Ry. Corroborative X-ray absorbance spectra and comparisons with experimental results are provided in the Appendix (Figure 82 – Figure 92).

#### 4.6.1.7 PRSoXS Simulations

PRSoXS simulations were carried out using the NIST RSoXS Simulation Suite (NRSS) which incorporates tools to validate input models and CyRSoXS, a virtual beamline instrument.[231] Simulated morphologies were generated using a custom software (https://github.com/devoncallan/DopantModeling).

### 4.6.8 Summary of P3HT Blend Composition, Crystallinity, and Dopant Counterion Concentration

**Table 3. Summary of P3HT blend composition, crystallinity, and dopant/dopant counterion mol fractions.**

| Blend ID | Composition (5 kDa/23 kDa/RRa) | Crystalline Mole Fraction | $F_4TCNQ$/ $F_4TCNQ^{\bullet-}$ Mole Fraction | $TFSI^-$ Mole Fraction |
|---|---|---|---|---|
| A | 20/5/75 | 0.17 | 0.022 | 0.019 |
| B | 40/5/55 | 0.22 | 0.011 | 0.053 |
| C | 50/5/45 | 0.27 | 0.011 | 0.049 |
| D | 70/0/30 | 0.29 | 0.018 | 0.067 |
| E | 100/0/0 | 0.37 | 0.011 | 0.096 |

### 4.6.9 Atomic Force Microscopy of Least and Most Crystalline P3HT Blend

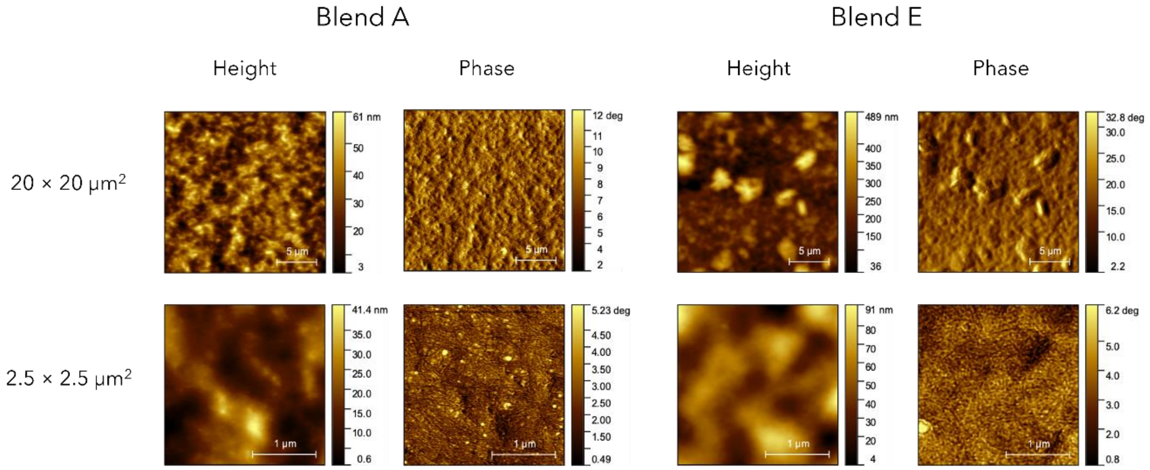

**Figure 64. Atomic force micrographs of least crystalline and most crystalline P3HT blend films demonstrating similar fibril dimensions.**

### 4.6.10 X-Ray Photoelectron Spectroscopy Depth Profiling of Doped P3HT Films

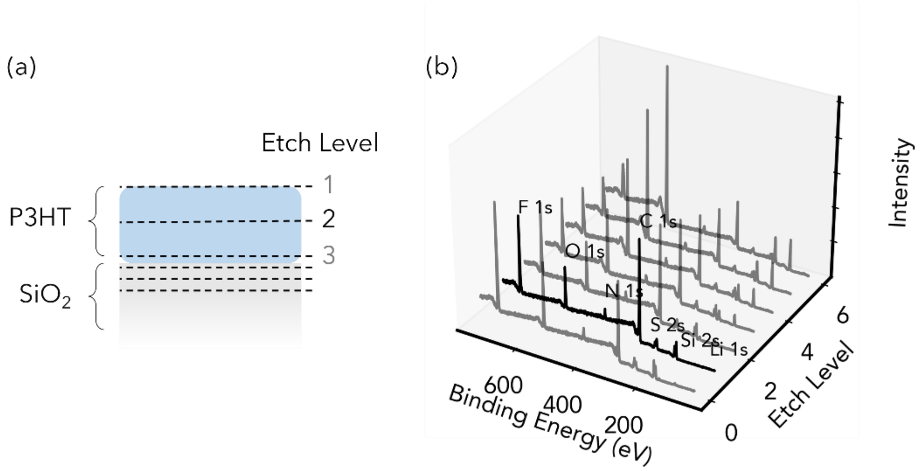

**Figure 65. XPS Depth Profile of LiTFSI Exchanged, 100% Regioregular P3HT Film**

*(a) Schematic P3HT film on SiO₂ substrate showing relative etch level locations corresponding to survey spectra in (b). The mid-P3HT survey spectra (at etch level 1) and the locations of various core-orbitals in the spectra are highlighted in (b). Dopant concentrations reported in the main text (Figure 56) correspond to the concentrations measured at etch level 1, past the surface and before the substrate. The lack of significant Li signal suggests negligible incorporation of neutral LiTFSI during the anion exchange process depicted in Figure 56.*

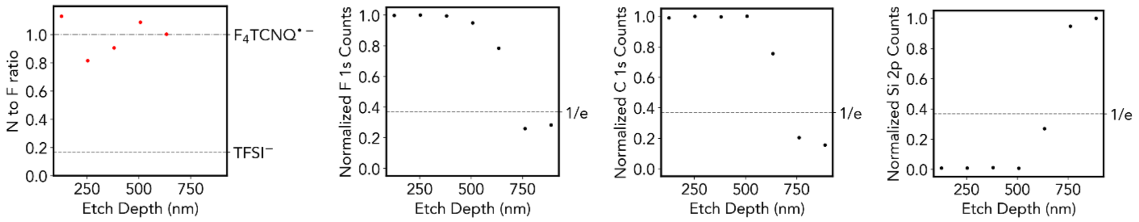

**Figure 66. Quantified XPS Depth Profile of F4TCNQ Vapor Doped P3HT**

*(a) Ratio of quantified nitrogen (N) to fluorine (F) in a $F_4$TCNQ vapor doped P3HT film as a function of etch depth. N and F are atomically unique to dopant/counterion species with a stoichiometric N to F ratio of 1/6 for TFSI$^-$ and 1 for $F_4$TCNQ/$F_4$TCNQ$^{\bullet-}$. $F_4$TCNQ vapor doped P3HT shows consistent N to F ratios for $F_4$TCNQ/$F_4$TCNQ$^{\bullet-}$ throughout the film depth. (b), (c), (d) Normalized F 1s, C 1s, and Si 2p count as a function of etch depth. The depth at which C 1s counts decreases past 1/e and Si 2p increases past 1/e indicates that the thickness of the film. The uniformity before reaching the $SiO_2$ substrate indicates uniform doping of P3HT through the film depth.*

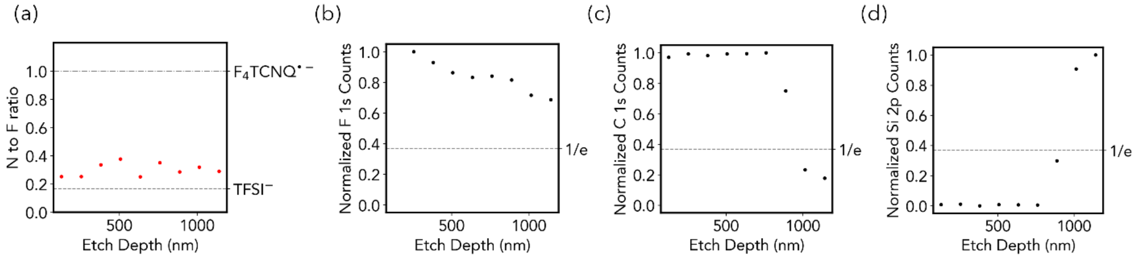

**Figure 67. Quantified XPS Depth Profile of Doped, TFSI- Anion Exchanged P3HT**

*(a) Ratio of quantified nitrogen (N) to fluorine (F) in a doped, TFSI$^-$ anion exchanged P3HT film as a function of etch depth. N and F are atomically unique to dopant/counterion*

*species with a stoichiometric N to F ratio of 1/6 for TFSI*$^-$ *and 1 for* $F_4TCNQ/F_4TCNQ^{\bullet-}$. *Doped, TFSI*$^-$ *anion exchanged P3HT shows consistent N to F ratios for TFSI*$^-$ *throughout the film depth. (b), (c), (d) Normalized F 1s, C 1s, and Si 2p count as a function of etch depth. The depth at which C 1s counts decreases past 1/e and Si 2p increases past 1/e indicates that the thickness of the film. The uniformity before reaching the* $SiO_2$ *substrate indicates uniform exchange of* $F_4TCNQ^{\bullet-}$ *for TFSI*$^-$.

### 4.6.11 Atomic Force Microscopy of $F_4TCNQ$ Vapor-Doped and $TFSI^-$ Anion Exchanged Films

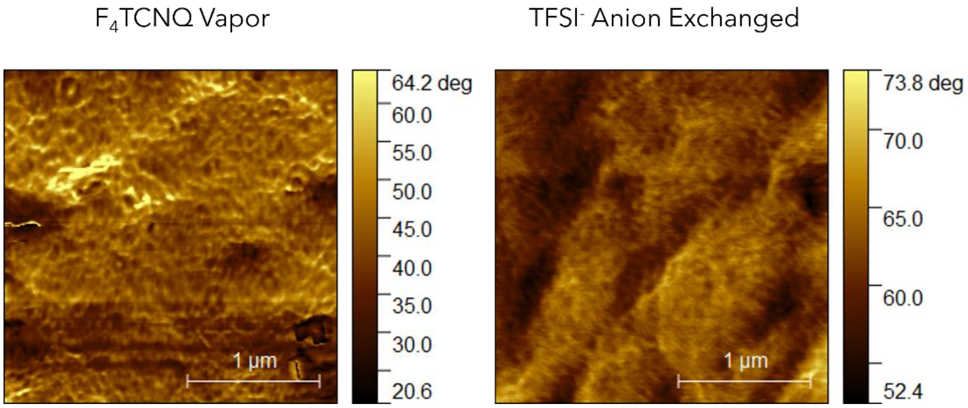

**Figure 68. $F_4TCNQ$ Vapor Doped P3HT and $TFSI^-$ Anion Exchanged Film Surface Texture from AFM Phase Contrast Images.**

*Atomic force micrographs of most crystalline P3HT blend films following $F_4TCNQ$ vapor doping (left) and anion exchange in LiTFSI solution (right), showing a substantial change in film texture, with reduced fibril texture upon $F_4TCNQ$ vapor doping and return of fibril texture following $TFSI^-$ anion exchange.*

### 4.6.12 XPS Survey Spectra of $F_4$TCNQ Surface Layer on P3HT

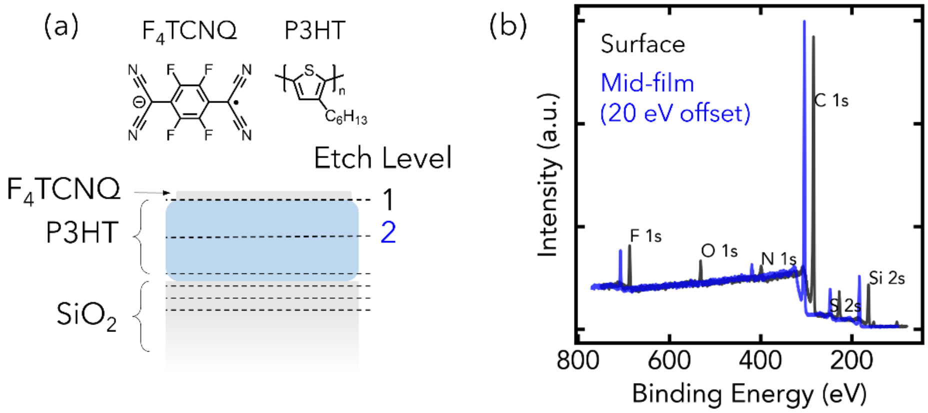

**Figure 69. XPS Survey Spectra at $F_4$TCNQ Vapor-Doped Film Top Surface and Mid-Depth, Showing Excess $F_4$TCNQ at Sample Surface.**

*Comparison of XPS survey spectra at film top surface and approximate mid*Point *for a* $F_4$*TCNQ vapor doped P3HT film. A horizontal offset of 20 eV for the film mid*Point *spectra allows for direct comparison of the F 1s and C 1s peaks. While film surfaces usually contain additional carbon contamination, the surface profile shows increased F 1s to C 1s signal relative to the mid-film survey spectra, indicating a significant enrichment of* $F_4$*TCNQ at the film top surface.*

### 4.6.13 Fibril Orientations from Grazing Incidence Wide Angle X-Ray Scattering (GIWAXS)

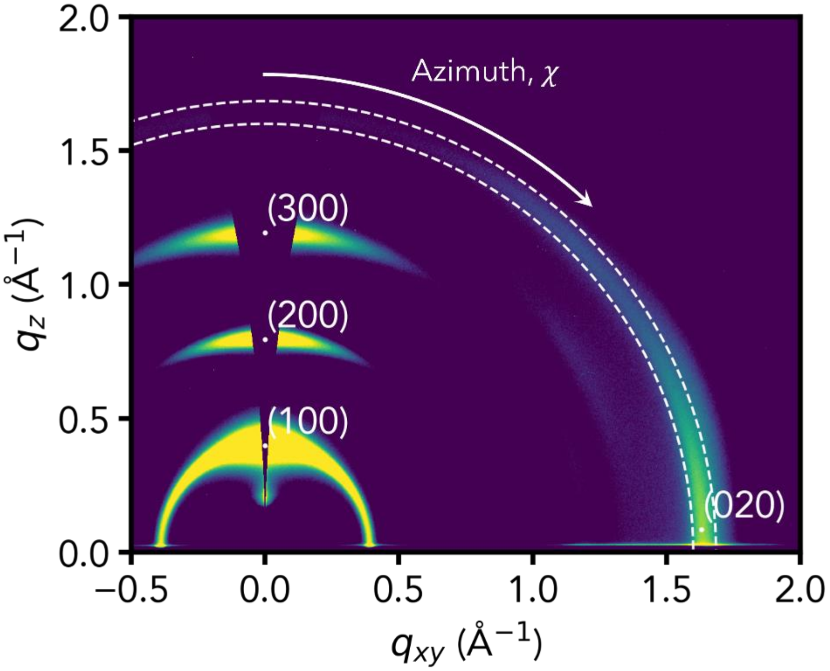

**Figure 70. 2D scattering pattern of P3HT under grazing incidence geometry.**

*The (100), (200), and (300) scattering peaks correspond to lamellar stacking in the out-of-plane direction ($q_z$). The (020) scattering peak corresponds to π-stacking in the in-plane direction ($q_{xy}$). The azimuthal angle, χ, is the angle from the $q_z$ towards the $q_{xy}$ axis. The population-corrected scattering intensity is used to measure the distribution of π-stack (i.e., fibril long axis) orientations.*

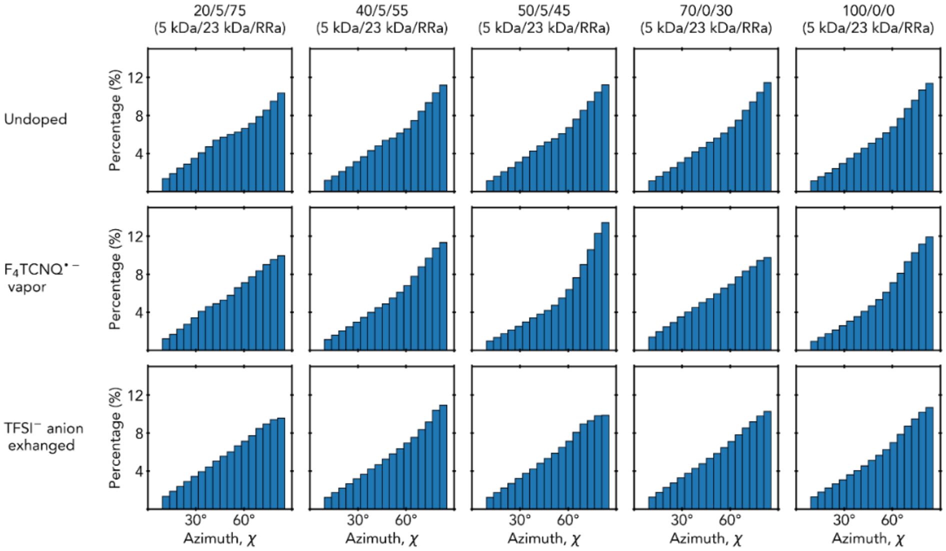

**Figure 71. Shallow Angle GIWAXS Orientation Distributions**

*Partial pole of the P3HT (020) peak as a function of azimuthal angle, χ, for undoped, $F_4$TCNQ-vapor doped, and TFSI$^-$ anion exchanged P3HT blends at a grazing incidence angle of 0.05°. At the shallow angle (0.05°), the X-ray penetration depth is limited to the top few nanometers and reflects P3HT fibril orientation at the film top surface.*

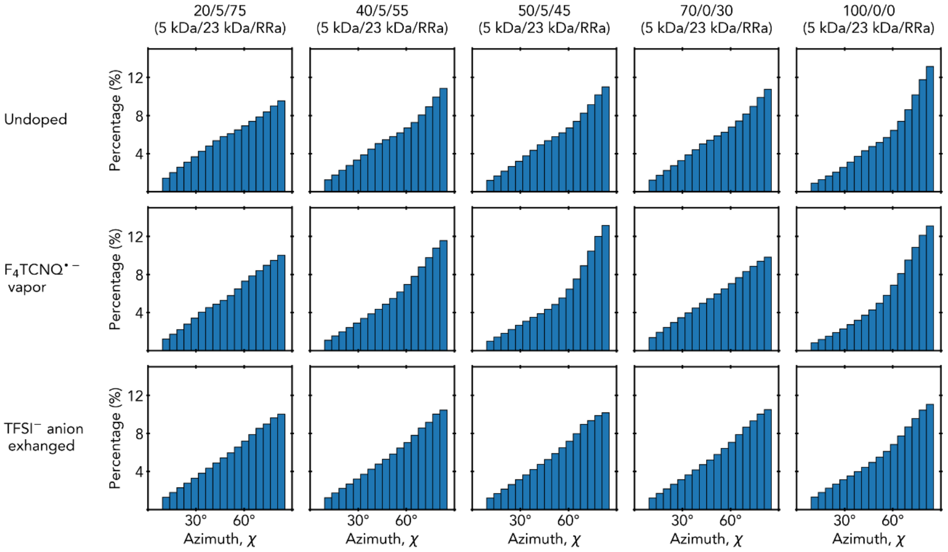

**Figure 72. Critical Angle GIWAXS Orientation Distributions**

*Partial pole of the P3HT (020) peak as a function of azimuthal angle, $\chi$, for undoped, $F_4$TCNQ-vapor doped, and $TFSI^-$ anion exchanged P3HT blends at a grazing incidence angle of 0.10°. At the shallow grazing incidence angle of 0.10°, the X-ray scattering reflects the depth-weighted contributions of aggregates up to the X-ray attenuation depth of 60 nm.*

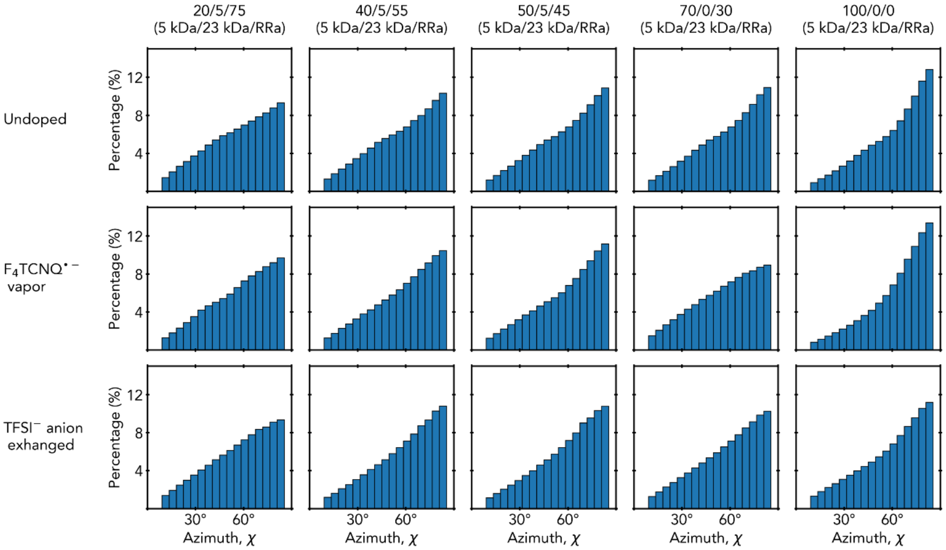

**Figure 73. Deep Angle GIWAXS Orientation Distributions**

*Partial pole of the P3HT (020) peak as a function of azimuthal angle, χ, for undoped, $F_4$TCNQ-vapor doped, and $TFSI^-$ anion exchanged P3HT blends at a grazing incidence angle of 0.13°. At the shallow grazing incidence angle of 0.13°, the X-ray scattering reflects the depth-weighted contributions of aggregates up to the X-ray attenuation throughout the film depth.*

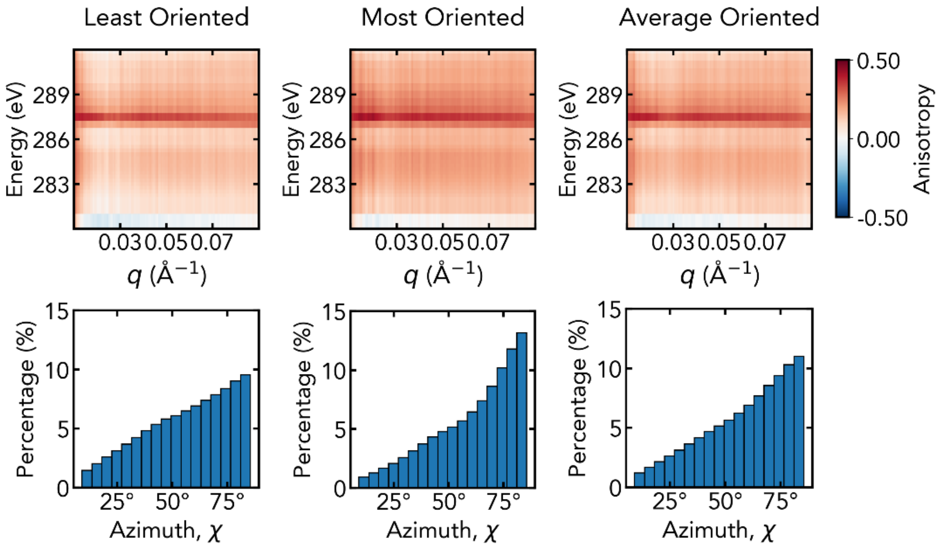

**Figure 74. Effect of *θ* Orientation Distribution**

*Effect of θ orientation distributions on simulated P3HT C K edge p-RSoXS scattering anisotropy. θ represents the angle between the substrate normal and the P3HT fibril long axis/thiophene plane normal. θ orientation distributions represent partial pole figures measured by GIWAXS at the grazing critical angle of 0.1° for P3HT, where scattering intensity is highest.*[262] *The effect of varying θ between samples containing the least and most RRe P3HT is minimal, with a small increase in scattering anisotropy for the least oriented distribution and a shift to higher q for the most oriented distribution. All other simulated p-RSoXS shown in this Appendix and main text use an average orientation distribution.*

### 4.6.14 Simulated Near edge X-ray Absorbance Fine Spectra

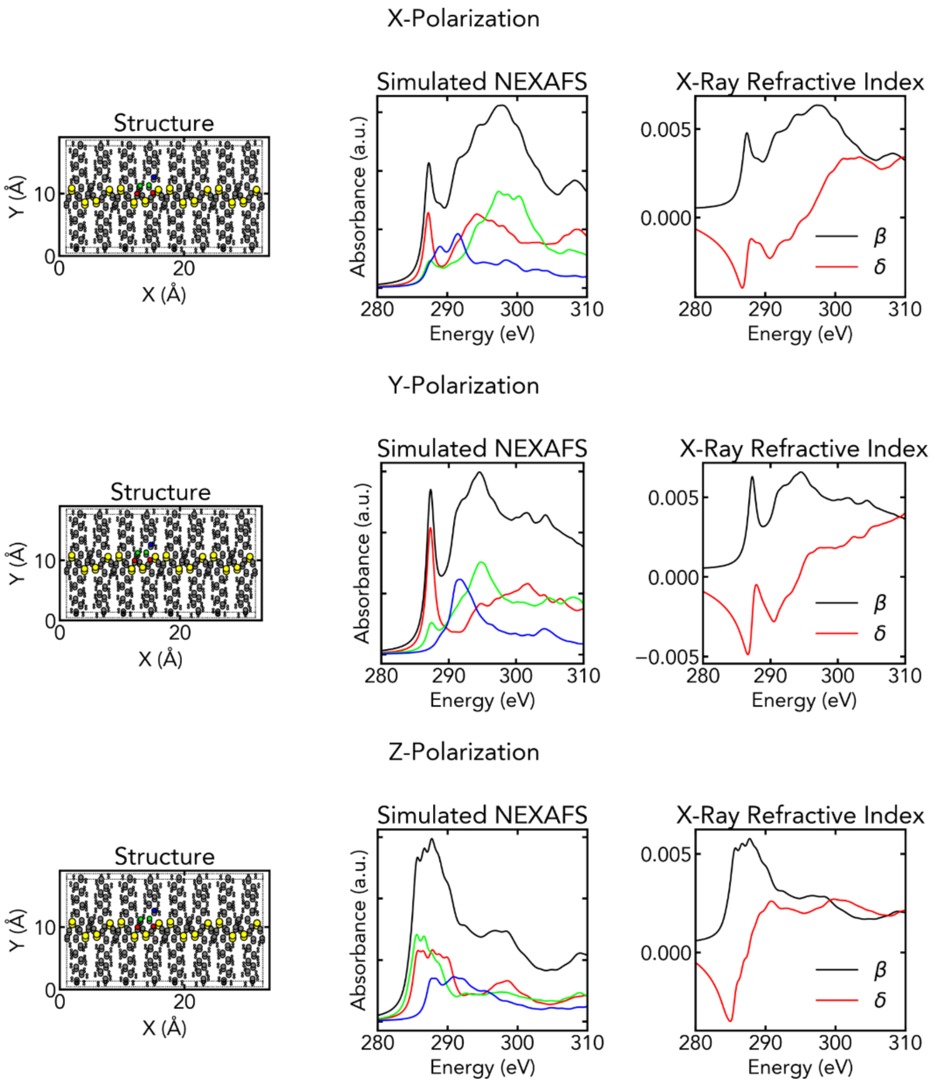

**Figure 75. π-Stacked P3HT Crystallite, Γ Point Sampling Only C K edge NEXAFS.** *Simulated P3HT C K edge NEXAFS using literature-reported P3HT structure.*[160,259] *Sulfur, carbon, and hydrogen atoms are represented by yellow, gray, and white atoms, respectively. Red, green, and blue carbon atoms are color-matched to the individual spectra of the simulated NEXAFS (center) with the overall spectra in black. The bare-atom normalized absorbance (β) and reflectance (δ, obtained from the Kramers-Kronig relations) are shown*

*on the right. The supercell (left) assumes 4 π-stacked, 8-mers of P3HT and translational symmetry. The X-ray absorbance calculation samples the Γ Point* only.

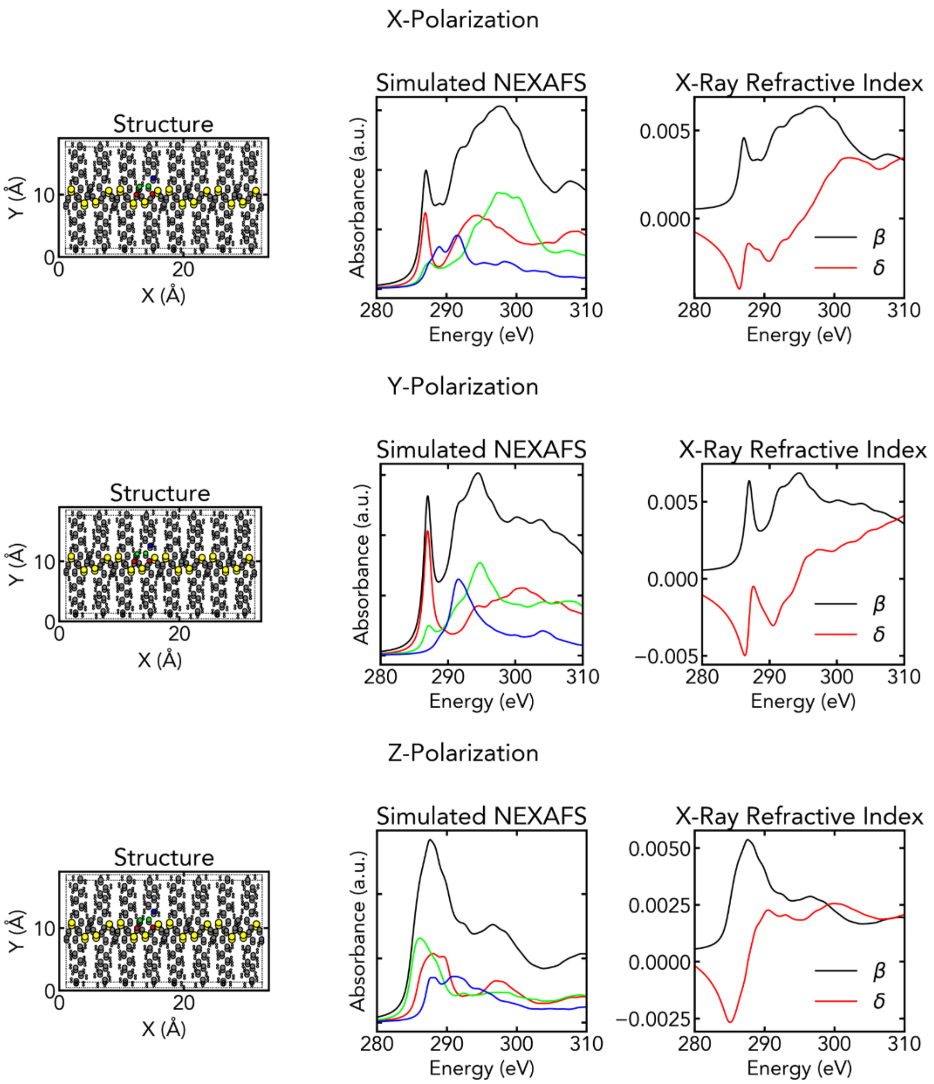

**Figure 76. *π*-Stacked P3HT Crystallite, 2 × 2 × 2 *k*-Point Grid Sampling C K edge NEXAFS**

*Simulated P3HT C K edge NEXAFS using literature-reported P3HT structure.*[160,259] *Sulfur, carbon, and hydrogen atoms are represented by yellow, gray, and white atoms, respectively. Red, green, and blue carbon atoms are color-matched to the individual spectra of the simulated NEXAFS (center) with the overall spectra in black. The bare-atom normalized absorbance (β) and reflectance (δ, obtained from the Kramers-Kronig relations) are shown* *on the right. The supercell (left) assumes 4 π-stacked, 8-mers of P3HT and translational symmetry. The X-ray absorbance calculation samples a 2 × 2 × 2 k-Point Grid centered about the Γ-point.*

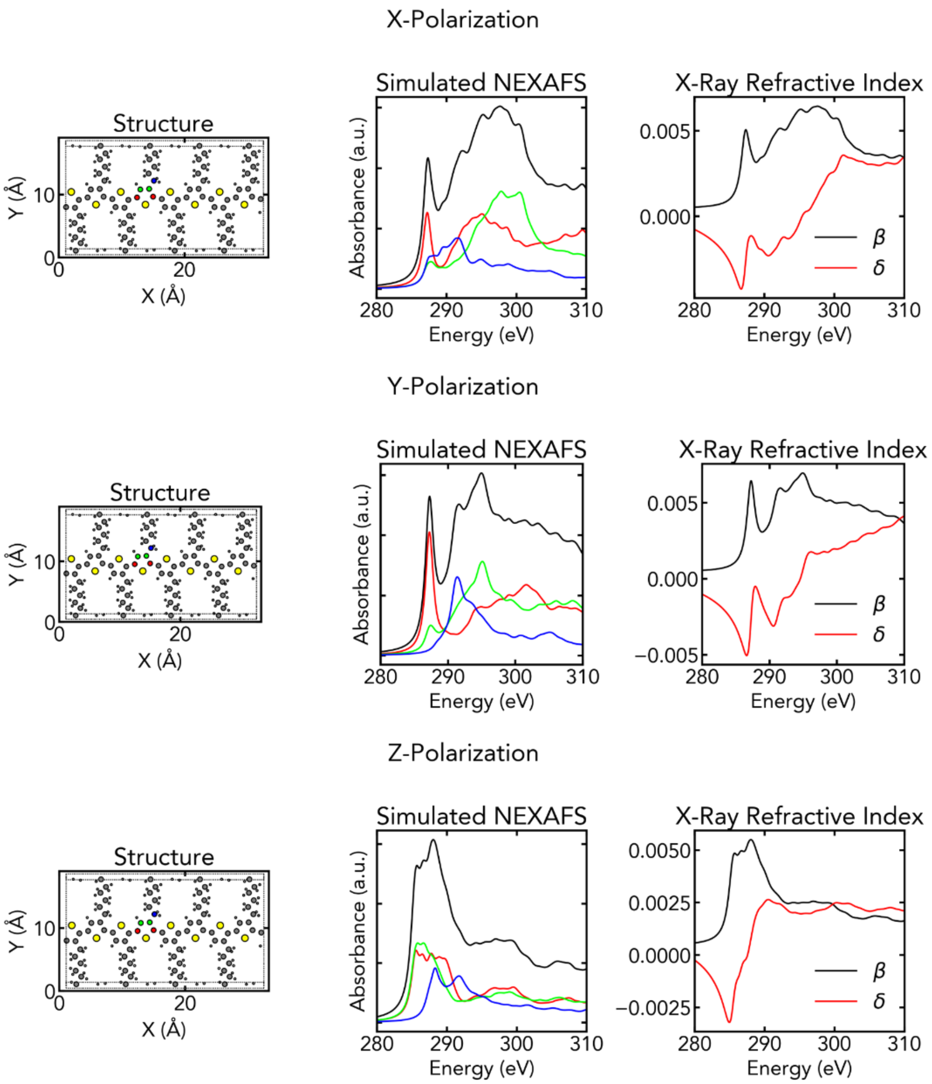

**Figure 77. Single P3HT Chain, *Γ* Point Sampling Only C K edge NEXAFS**

*Simulated P3HT C K edge NEXAFS using literature-reported P3HT structure.*[160,259] *Sulfur, carbon, and hydrogen atoms are represented by yellow, gray, and white atoms, respectively. Red, green, and blue carbon atoms are color-matched to the individual spectra of the simulated NEXAFS (center) with the overall spectra in black. The bare-atom normalized absorbance (β) and reflectance (δ, obtained from the Kramers*-Kronig *relations) are shown* *on the right. The supercell (left) assumes a single 8-mer of P3HT and translational symmetry. The X-ray absorbance calculation samples the Γ Point only.*

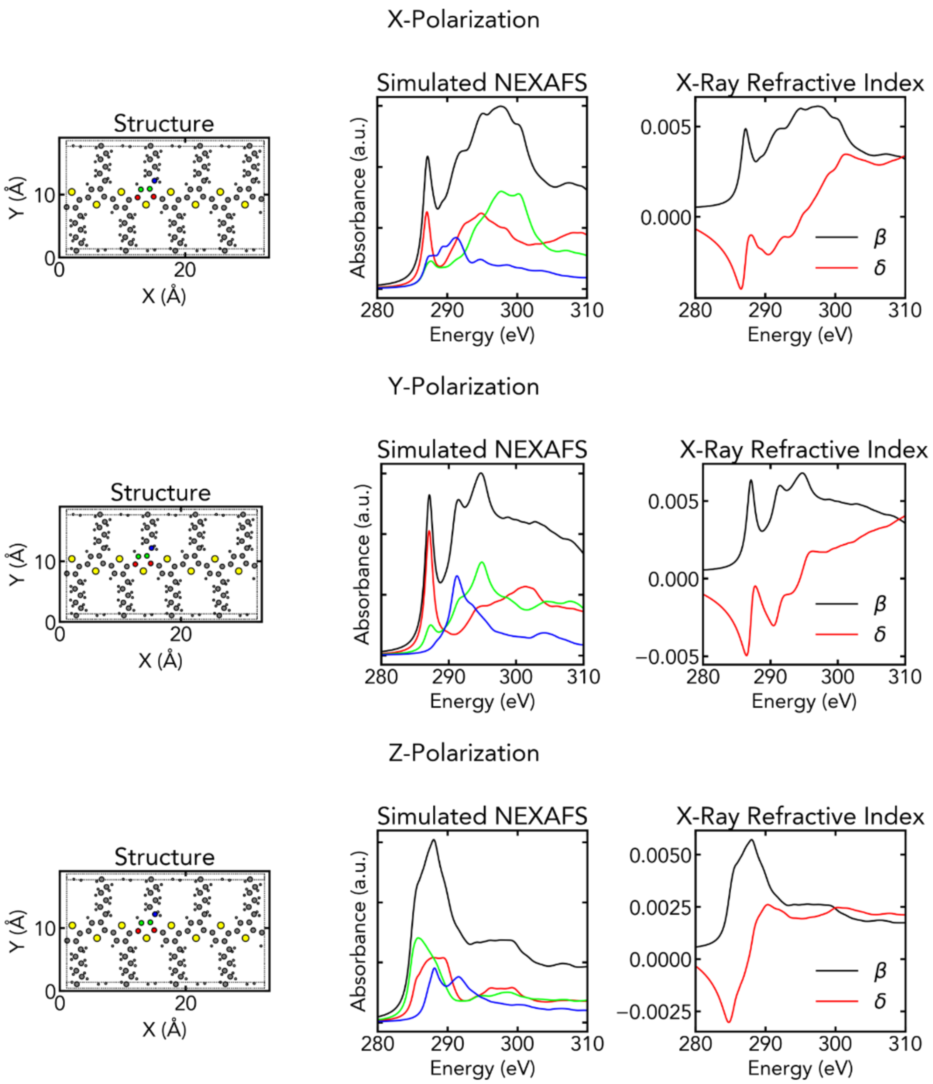

**Figure 78. Single P3HT Chain, 2 × 2 × 2 *k*-Point Grid Sampling C K edge NEXAFS**

*Simulated P3HT C K edge NEXAFS using literature-reported P3HT structure.*[160,259] *Sulfur, carbon, and hydrogen atoms are represented by yellow, gray, and white atoms, respectively. Red, green, and blue carbon atoms are color-matched to the individual spectra of the simulated NEXAFS (center) with the overall spectra in black. The bare-atom normalized absorbance (β) and reflectance (δ, obtained from the Kramers-Kronig relations) are shown on the right. The supercell (left) assumes a single 8-mer of P3HT and translational* *symmetry. The X-ray absorbance calculation samples a 2 × 2 × 2 k-Point Grid centered about the Γ-point.*

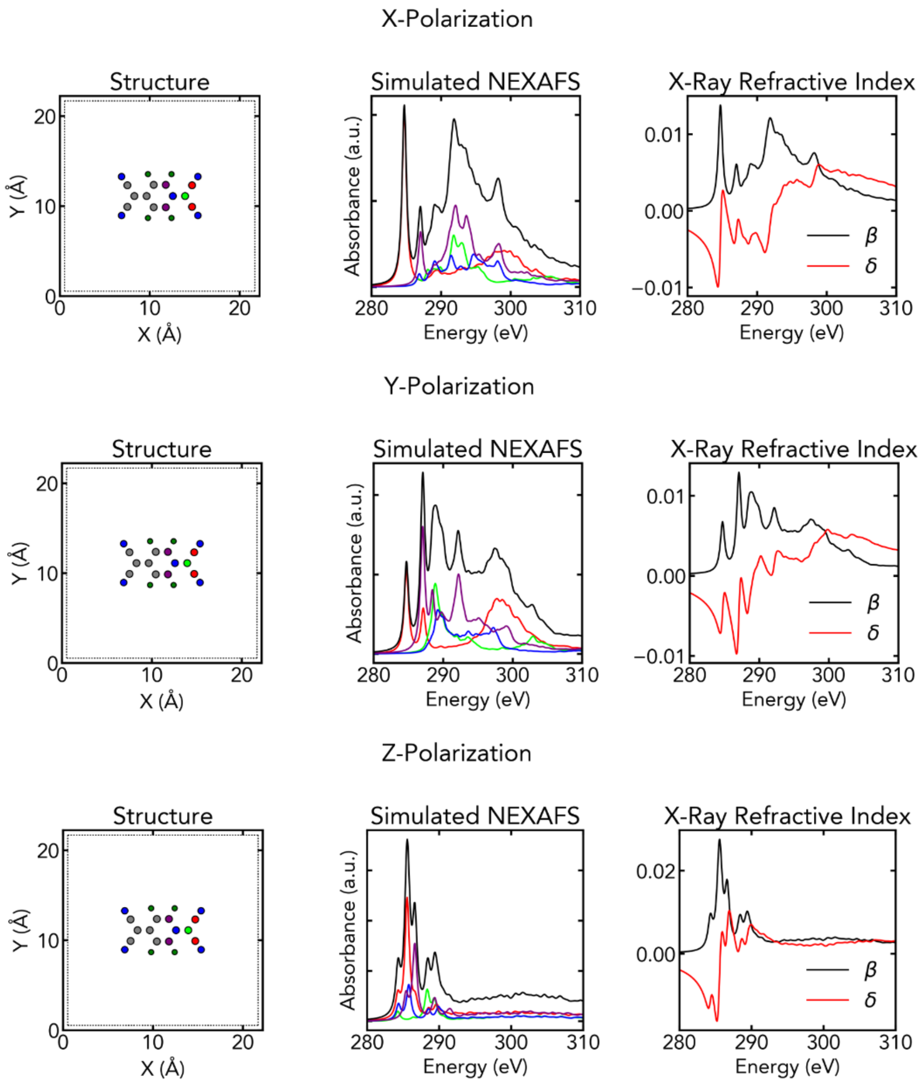

**Figure 79. F$_4$TCNQ C K Edge NEXAFS**

*Simulated F$_4$TCNQ C K edge NEXAFS. Carbon, nitrogen, and fluorine atoms are represented by gray, blue, and green atoms, respectively. Red, green, blue, and purple carbon atoms are color-matched to the individual spectra of the simulated NEXAFS (center) with the overall spectra in black. The bare-atom normalized absorbance (β) and reflectance (δ, obtained from the Kramers-Kronig relations) are shown on the right. The supercell (left)* *assumes a single molecule in a simple cubic lattice and translational symmetry. The X-ray absorbance calculation samples the Γ Point only.*

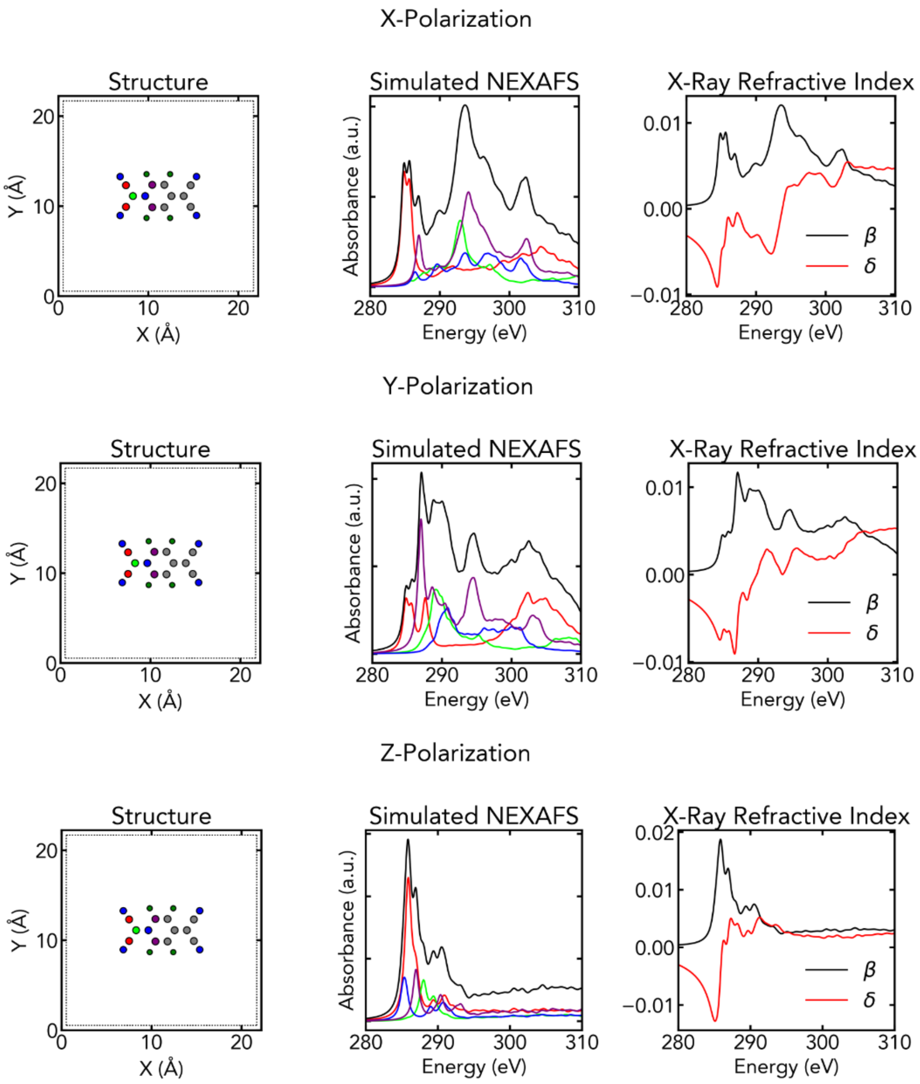

**Figure 80. $F_4TCNQ^{\bullet-}$ C K Edge NEXAFS**

*Simulated $F_4TCNQ^{\bullet-}$ C K edge NEXAFS. Carbon, nitrogen, and fluorine atoms are represented by gray, blue, and green atoms, respectively. Red, green, blue, and purple carbon atoms are color-matched to the individual spectra of the simulated NEXAFS (center) with the overall spectra in black. The bare-atom normalized absorbance (β) and reflectance (δ, obtained from the Kramers-Kronig relations) are shown on the right. The supercell (left)* *assumes a single molecule in a simple cubic lattice and translational symmetry. The X-ray absorbance calculation samples the $\Gamma$ Point only.*

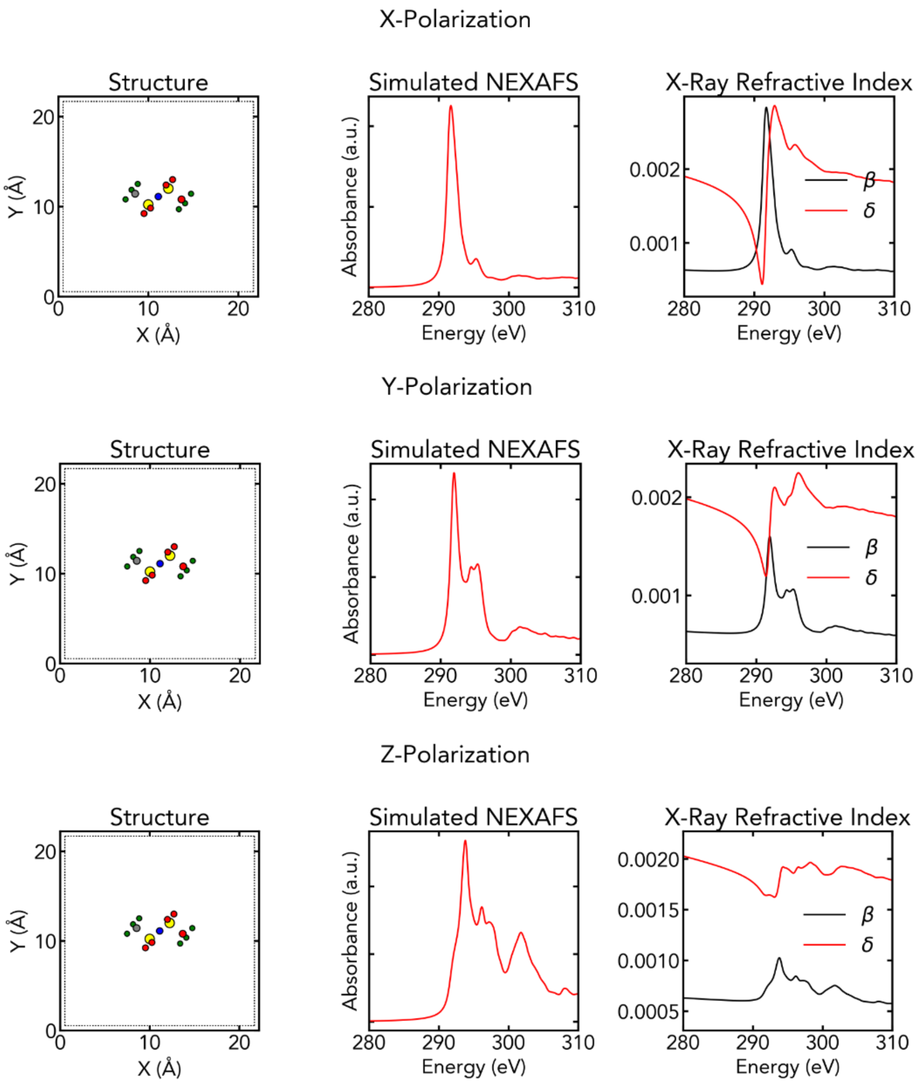

**Figure 81. TFSI$^-$ C K Edge NEXAFS**

*Simulated TFSI$^-$ C K edge NEXAFS. Carbon, nitrogen, fluorine, and sulfur atoms are represented by gray, blue, green, and yellow atoms, respectively. The red carbon atom is color-matched to the spectra of the simulated NEXAFS (center). The bare-atom normalized absorbance (β) and reflectance (δ, obtained from the Kramers-Kronig relations) are shown on the right. The supercell (left) assumes a single molecule in a simple cubic lattice and translational symmetry. The X-ray absorbance calculation samples the Γ Point only.*

### 4.6.15 Comparisons of Simulated and Experimentally Measured NEXAFS

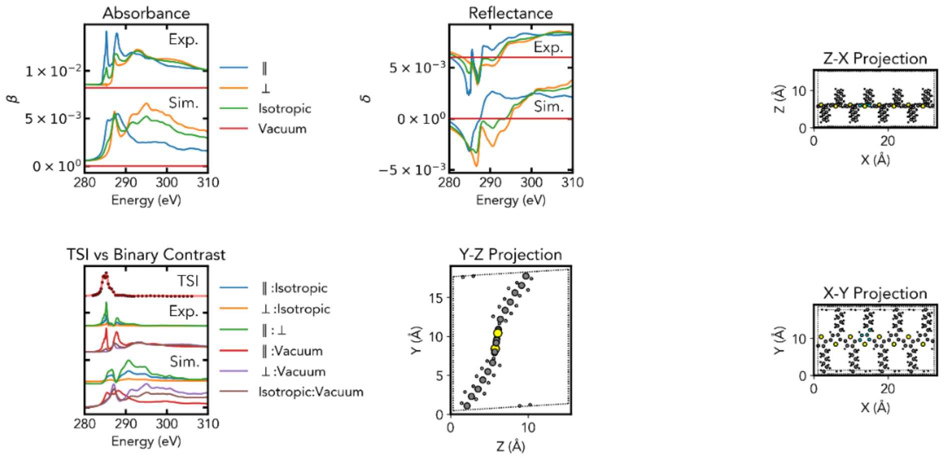

**Figure 82. P3HT C K Edge NEXAFS Comparisons**

*Simulated P3HT C K edge NEXAFS using uniaxial optical tensor approximations compared to experimentally measured X-ray absorbance and scattering contrast. The bare-atom normalized absorbance (β) and reflectance (δ, obtained from the Kramers-Kronig relations) are shown in the upper left and upper center plots, respectively. Parallel (∥), perpendicular (⊥), and isotropic spectra follow the convention described in the main text. The total scattering intensity (TSI) and binary contrasts shown in the lower left plot are calculated as described in the main text. Z-X, Y-Z, and X-Y projections of the unit cell are shown in the upper right, lower center, and lower right plots, respectively. Carbon, sulfur, and hydrogen atoms are shown as gray, yellow, and white respectively with the unit cell boundary shown as a dashed line. Core-hole excitons are simulated at the highlighted cyan atoms.*

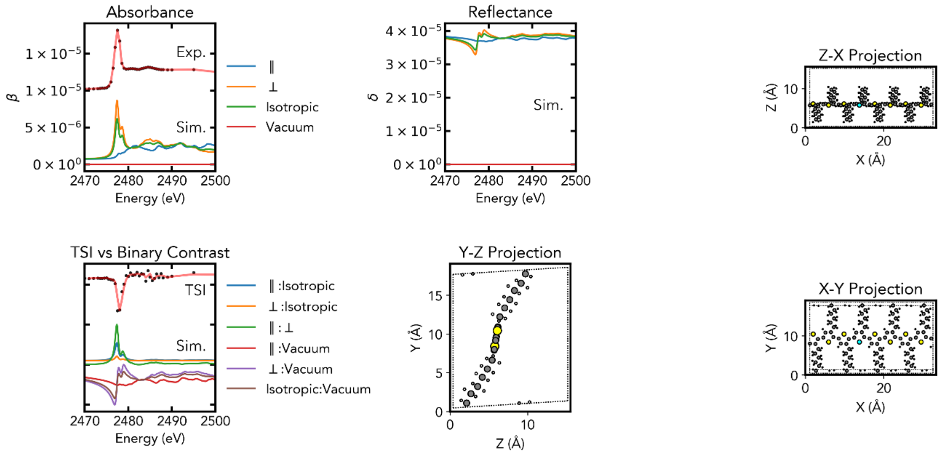

**Figure 83. P3HT S K Edge NEXAFS Comparisons**

*Simulated P3HT S K edge NEXAFS using uniaxial optical tensor approximations compared to experimentally measured X-ray absorbance and scattering contrast. The bare-atom normalized absorbance (β) and reflectance (δ, obtained from the Kramers-Kronig relations) are shown in the upper left and upper center plots, respectively. Parallel (//), perpendicular (⊥), and isotropic spectra follow the convention described in the main text. The total scattering intensity (TSI) and binary contrasts shown in the lower left plot are calculated as described in the main text. Z-X, Y-Z, and X-Y projections of the unit cell are shown in the upper right, lower center, and lower right plots, respectively. Carbon, sulfur, and hydrogen atoms are shown as gray, yellow, and white respectively with the unit cell boundary shown as a dashed line. Core-hole excitons are simulated at the highlighted cyan atom.*

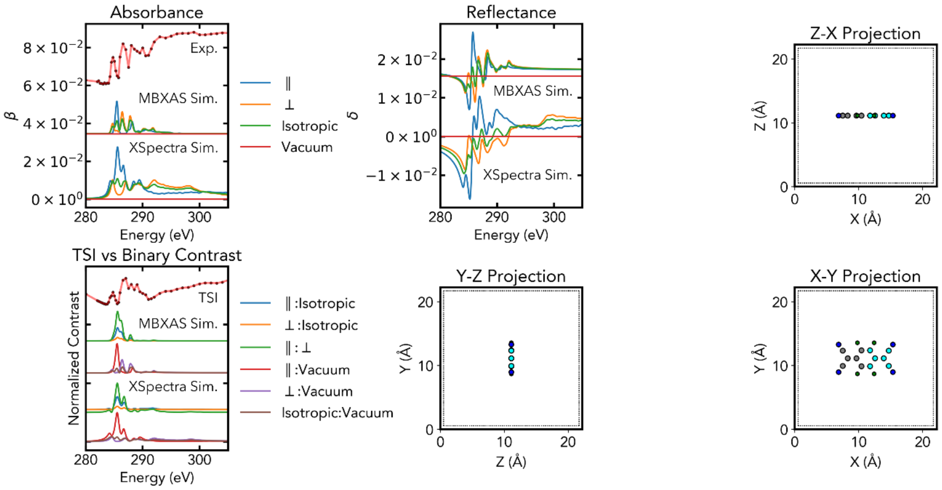

**Figure 84. $F_4$TCNQ C K Edge NEXAFS Comparisons**

*Simulated $F_4$TCNQ C K edge NEXAFS using uniaxial optical tensor approximations compared to experimentally measured X-ray absorbance and scattering contrast. The bare-atom normalized absorbance (β) and reflectance (δ, obtained from the Kramers-Kronig relations) are shown in the upper left and upper center plots, respectively. Parallel (//), perpendicular (⊥), and isotropic spectra follow the convention described in the main text. The total scattering intensity (TSI) and binary contrasts shown in the lower left plot are calculated as described in the main text. Z-X, Y-Z, and X-Y projections of the unit cell are shown in the upper right, lower center, and lower right plots, respectively. Carbon, nitrogen, and fluorine atoms are shown as gray, blue, and green respectively with the unit cell boundary shown as a dashed line. Core-hole excitons are simulated at the highlighted cyan atom.*

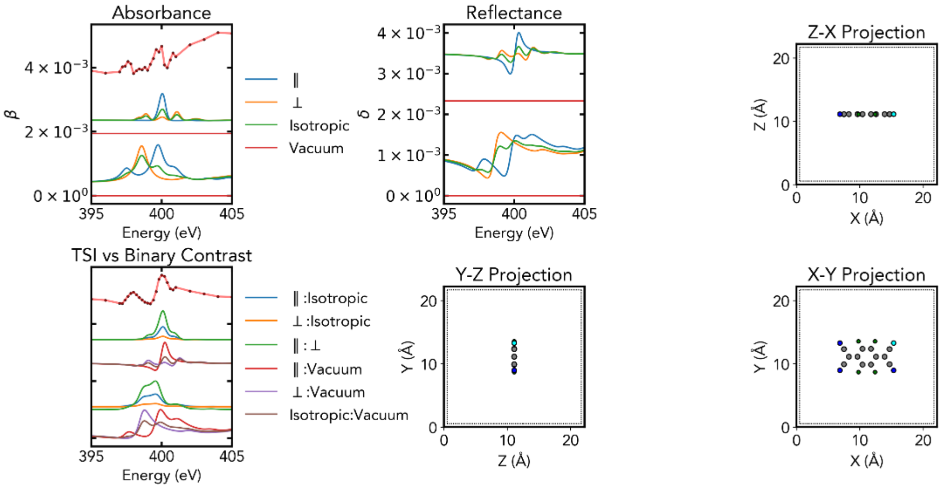

**Figure 85. F4TCNQ N K Edge NEXAFS Comparisons**

*Simulated $F_4TCNQ$ N K edge NEXAFS using uniaxial optical tensor approximations compared to experimentally measured X-ray absorbance and scattering contrast. The bare-atom normalized absorbance (β) and reflectance (δ, obtained from the Kramers-Kronig relations) are shown in the upper left and upper center plots, respectively. Parallel (//), perpendicular (⊥), and isotropic spectra follow the convention described in the main text. The total scattering intensity (TSI) and binary contrasts shown in the lower left plot are calculated as described in the main text. Z-X, Y-Z, and X-Y projections of the unit cell are shown in the upper right, lower center, and lower right plots, respectively. Carbon, nitrogen, and fluorine atoms are shown as gray, blue, and green respectively with the unit cell boundary shown as a dashed line. Core-hole excitons are simulated at the highlighted cyan atom.*

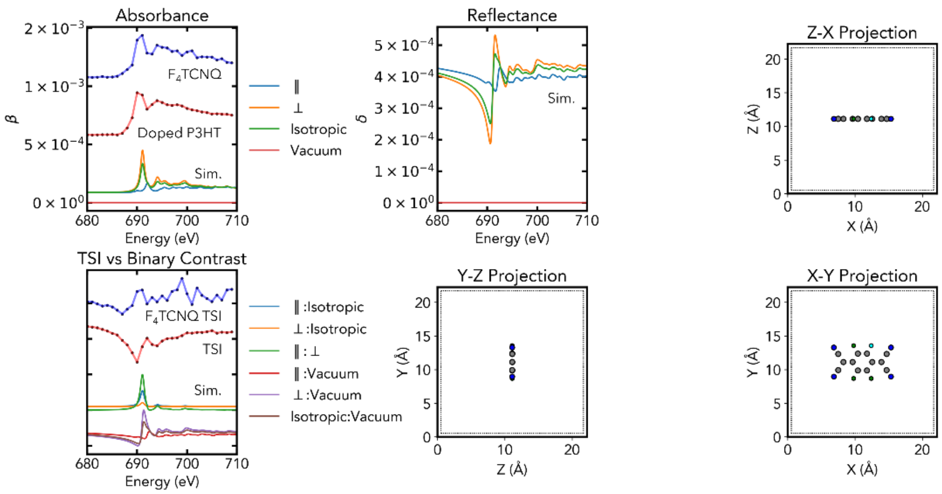

**Figure 86. $F_4$TCNQ F K Edge NEXAFS Comparisons**

*Simulated $F_4$TCNQ F K edge NEXAFS using uniaxial optical tensor approximations compared to experimentally measured X-ray absorbance and scattering contrast. The bare-atom normalized absorbance (β) and reflectance (δ, obtained from the Kramers-Kronig relations) are shown in the upper left and upper center plots, respectively. Parallel (∥), perpendicular (⊥), and isotropic spectra follow the convention described in the main text. The total scattering intensity (TSI) and binary contrasts shown in the lower left plot are calculated as described in the main text. Z-X, Y-Z, and X-Y projections of the unit cell are shown in the upper right, lower center, and lower right plots, respectively. Carbon, nitrogen, and fluorine atoms are shown as gray, blue, and green respectively with the unit cell boundary shown as a dashed line. Core-hole excitons are simulated at the highlighted cyan atom.*

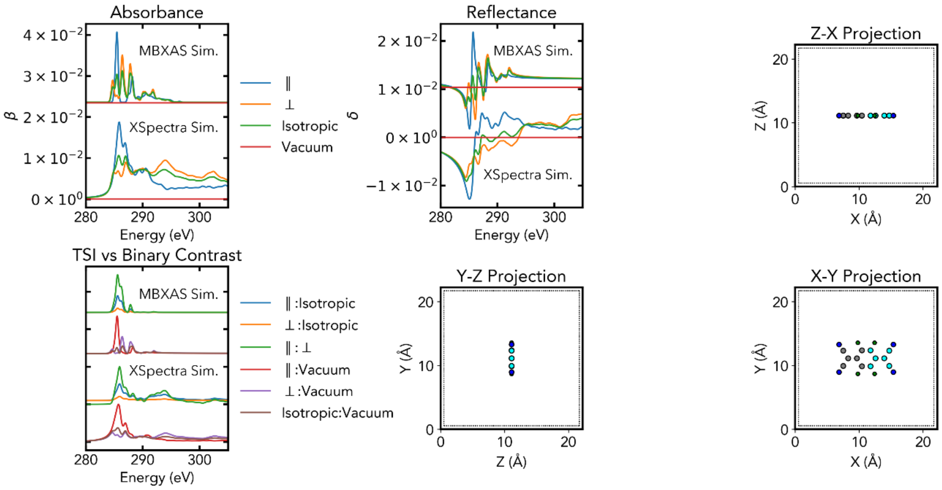

**Figure 87. $F_4TCNQ^{\bullet -}$ C K Edge NEXAFS Comparisons**

*Simulated $F_4TCNQ^{\bullet -}$ C K edge NEXAFS using uniaxial optical tensor approximations compared to experimentally measured X-ray absorbance and scattering contrast. The bare-atom normalized absorbance (β) and reflectance (δ, obtained from the Kramers-Kronig relations) are shown in the upper left and upper center plots, respectively. Parallel (∥), perpendicular (⊥), and isotropic spectra follow the convention described in the main text. The total scattering intensity (TSI) and binary contrasts shown in the lower left plot are calculated as described in the main text. Z-X, Y-Z, and X-Y projections of the unit cell are shown in the upper right, lower center, and lower right plots, respectively. Carbon, nitrogen, and fluorine atoms are shown as gray, blue, and green respectively with the unit cell boundary shown as a dashed line. Core-hole excitons are simulated at the highlighted cyan atom.*

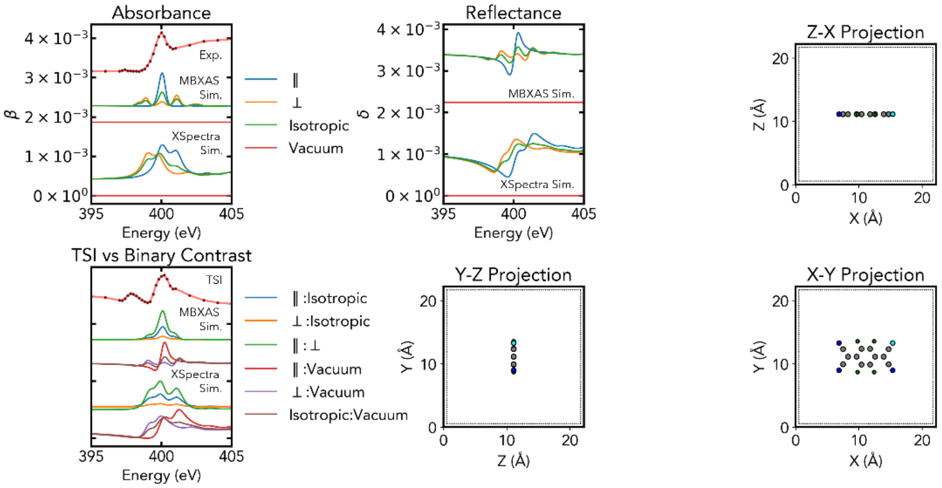

**Figure 88. $F_4TCNQ^{\bullet -}$ N K Edge NEXAFS Comparisons**

*Simulated* $F_4TCNQ^{\bullet -}$ *N K edge NEXAFS using uniaxial optical tensor approximations compared to experimentally measured X-ray absorbance and scattering contrast. The bare-atom normalized absorbance (β) and reflectance (δ, obtained from the Kramers-Kronig relations) are shown in the upper left and upper center plots, respectively. Parallel (//), perpendicular (⊥), and isotropic spectra follow the convention described in the main text. The total scattering intensity (TSI) and binary contrasts shown in the lower left plot are calculated as described in the main text. Z-X, Y-Z, and X-Y projections of the unit cell are shown in the upper right, lower center, and lower right plots, respectively. Carbon, nitrogen, and fluorine atoms are shown as gray, blue, and green respectively with the unit cell boundary shown as a dashed line. Core-hole excitons are simulated at the highlighted cyan atom.*

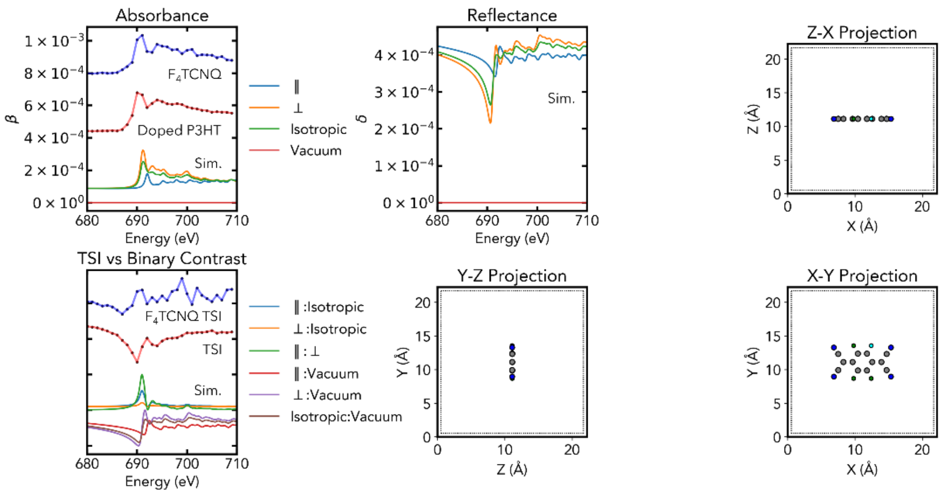

**Figure 89. $F_4TCNQ^{\bullet-}$ F K Edge NEXAFS Comparisons**

*Simulated $F_4TCNQ^{\bullet-}$ F K edge NEXAFS using uniaxial optical tensor approximations compared to experimentally measured X-ray absorbance and scattering contrast. The bare-atom normalized absorbance (β) and reflectance (δ, obtained from the Kramers-Kronig relations) are shown in the upper left and upper center plots, respectively. Parallel (//), perpendicular (⊥), and isotropic spectra follow the convention described in the main text. The total scattering intensity (TSI) and binary contrasts shown in the lower left plot are calculated as described in the main text. Z-X, Y-Z, and X-Y projections of the unit cell are shown in the upper right, lower center, and lower right plots, respectively. Carbon, nitrogen, and fluorine atoms are shown as gray, blue, and green respectively with the unit cell boundary shown as a dashed line. Core-hole excitons are simulated at the highlighted cyan atom.*

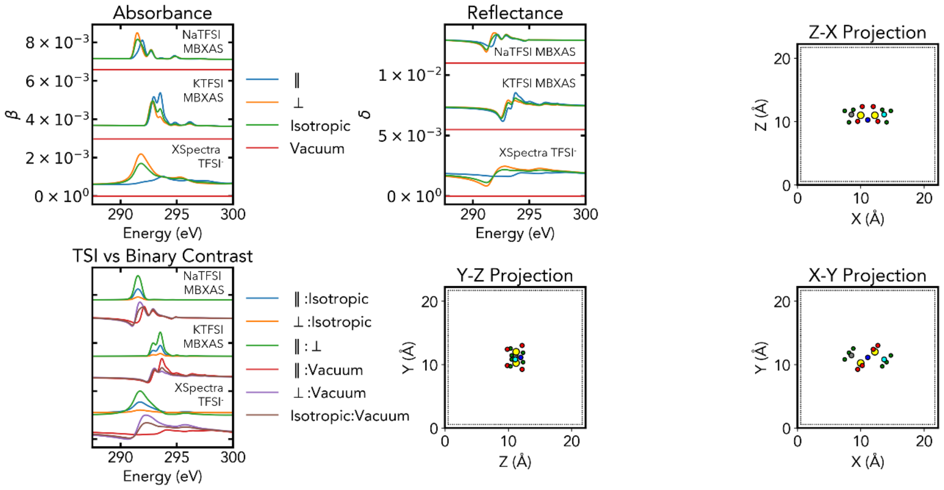

**Figure 90. TFSI$^-$ C K Edge NEXAFS Comparisons**

*Simulated TFSI$^-$ C K edge NEXAFS using uniaxial optical tensor approximations compared to experimentally measured X-ray absorbance and scattering contrast. The bare-atom normalized absorbance (β) and reflectance (δ, obtained from the Kramers-Kronig relations) are shown in the upper left and upper center plots, respectively. Parallel (∥), perpendicular (⊥), and isotropic spectra follow the convention described in the main text. The total scattering intensity (TSI) and binary contrasts shown in the lower left plot are calculated as described in the main text. Z-X, Y-Z, and X-Y projections of the unit cell are shown in the upper right, lower center, and lower right plots, respectively. Carbon, nitrogen, fluorine, and sulfur atoms are shown as gray, blue, green, and yellow atoms respectively with the unit cell boundary shown as a dashed line. Core-hole excitons are simulated at the highlighted cyan atom.*

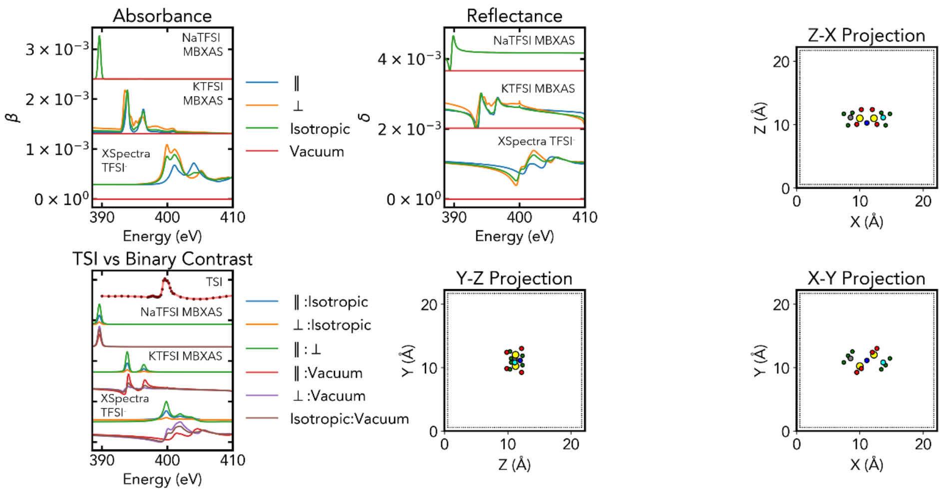

**Figure 91. TFSI$^-$ N K Edge NEXAFS Comparisons**

*Simulated TFSI$^-$ N K edge NEXAFS using uniaxial optical tensor approximations compared to experimentally measured X-ray absorbance and scattering contrast. The bare-atom normalized absorbance (β) and reflectance (δ, obtained from the Kramers-Kronig relations) are shown in the upper left and upper center plots, respectively. Parallel (∥), perpendicular (⊥), and isotropic spectra follow the convention described in the main text. The total scattering intensity (TSI) and binary contrasts shown in the lower left plot are calculated as described in the main text. Z-X, Y-Z, and X-Y projections of the unit cell are shown in the upper right, lower center, and lower right plots, respectively. Carbon, nitrogen, fluorine, and sulfur atoms are shown as gray, blue, green, and yellow atoms respectively with the unit cell boundary shown as a dashed line. Core-hole excitons are simulated at the highlighted cyan atom.*

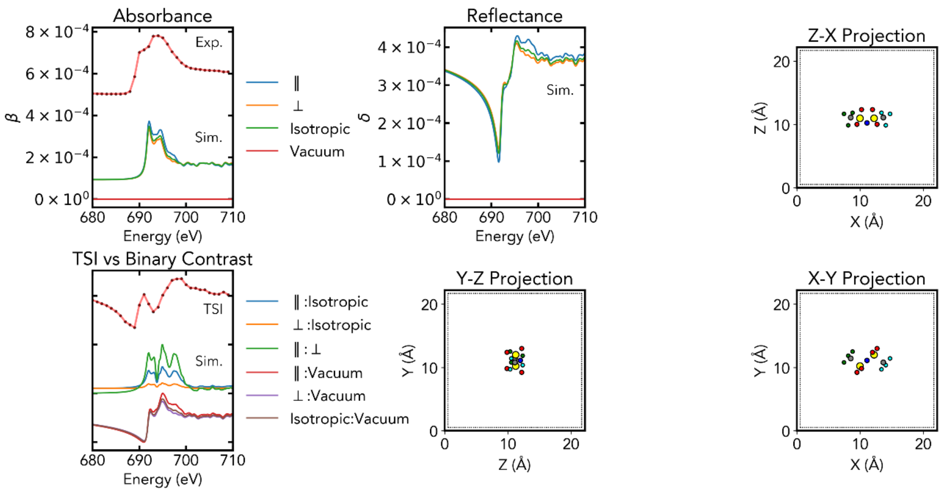

**Figure 92. TFSI$^-$ F K Edge NEXAFS Comparisons**

*Simulated TFSI$^-$ F K edge NEXAFS using uniaxial optical tensor approximations compared to experimentally measured X-ray absorbance and scattering contrast. The bare-atom normalized absorbance (β) and reflectance (δ, obtained from the Kramers-Kronig relations) are shown in the upper left and upper center plots, respectively. Parallel (∥), perpendicular (⊥), and isotropic spectra follow the convention described in the main text. The total scattering intensity (TSI) and binary contrasts shown in the lower left plot are calculated as described in the main text. Z-X, Y-Z, and X-Y projections of the unit cell are shown in the upper right, lower center, and lower right plots, respectively. Carbon, nitrogen, fluorine, and sulfur atoms are shown as gray, blue, green, and yellow atoms respectively with the unit cell boundary shown as a dashed line. Core-hole excitons are simulated at the highlighted cyan atom.*

### 4.6.16 Effect of Annealing on Scattering Anisotropy

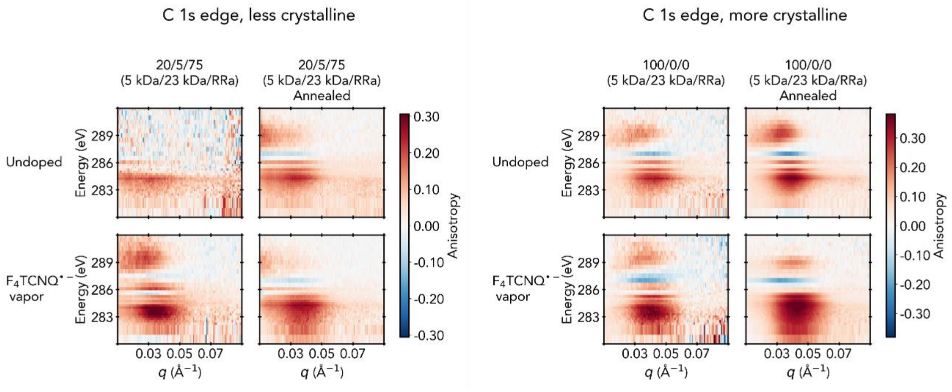

**Figure 93. Effect of sample annealing (120 °C, 2 hours under an inert nitrogen atmosphere) on scattering anisotropy.**

*Scattering anisotropy for samples containing the least (left) and most (right) regioregular low molecular weight P3HT are shown, including undoped and* $F_4$*TCNQ-vapor doped samples. For the undoped samples, annealing has the effect of increasing the magnitude of scattering anisotropy (top row). For* $F_4$*TCNQ-doped samples, annealing has the effect of increasing the area below 285 eV where positive scattering anisotropy is observed (bottom row), consistent with increasing incorporation of* $F_4TCNQ^{\bullet-}$ *counterions within crystallites, as described in the main text.*

### 4.9.17 Experimental Scattering Anisotropy Across Blends and Doping

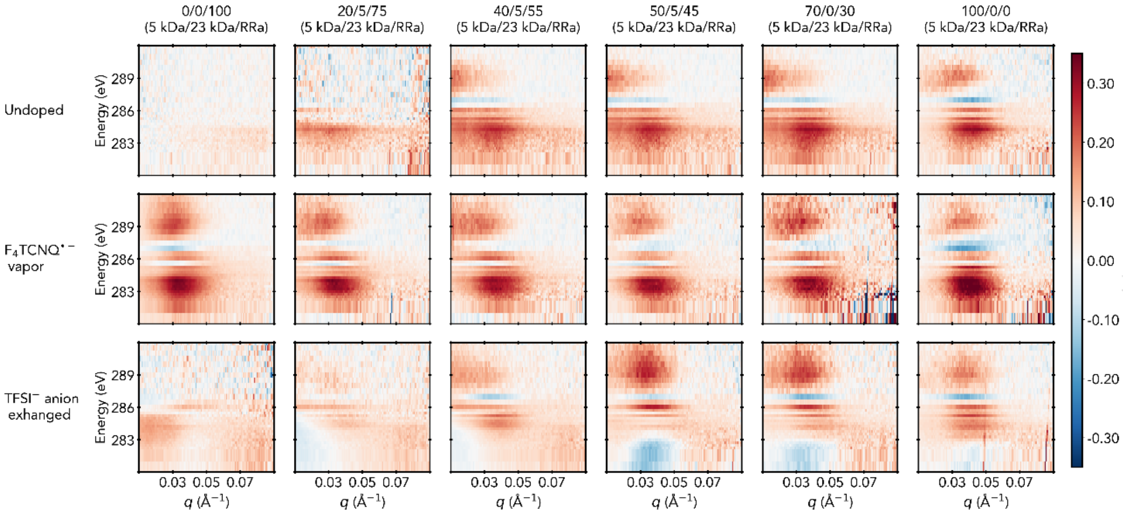

Figure 94. C K Edge Scattering Anisotropy

*C K Edge scattering anisotropy maps of different P3HT blend compositions (outlined along top axis) and dopant incorporation identity (outlined along vertical axis). Distinct changes are observed experimentally with increasing crystallinity (q position of scattering anisotropy) and dopant ion incorporation (energies at which scattering anisotropy is observed).*

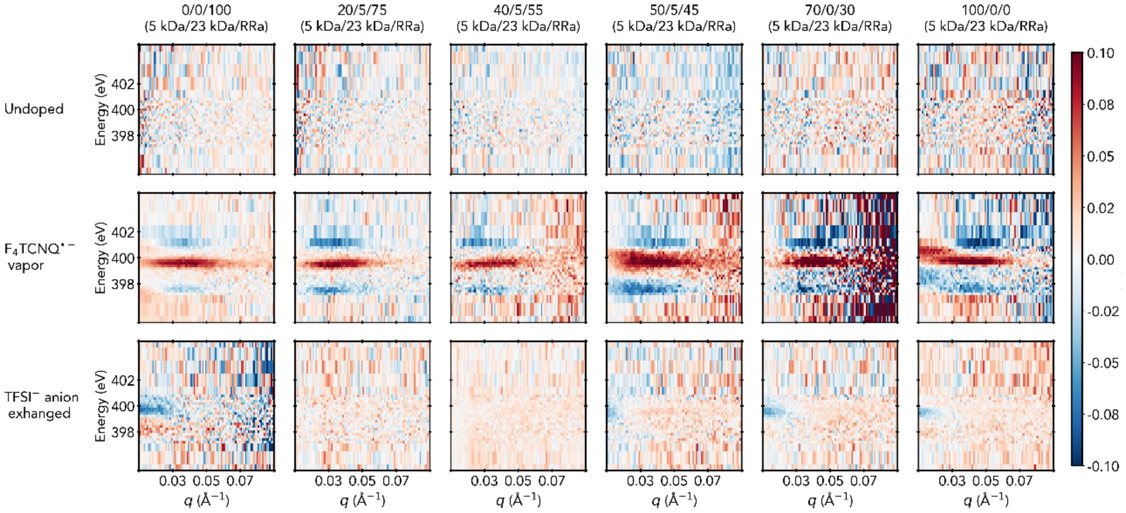

Figure 95. N K Edge Scattering Anisotropy

*N K Edge scattering anisotropy maps of different P3HT blend compositions (outlined along top axis) and dopant incorporation identity (outlined along vertical axis). Distinct changes are observed experimentally with dopant ion incorporation (energies at which scattering anisotropy is observed).*

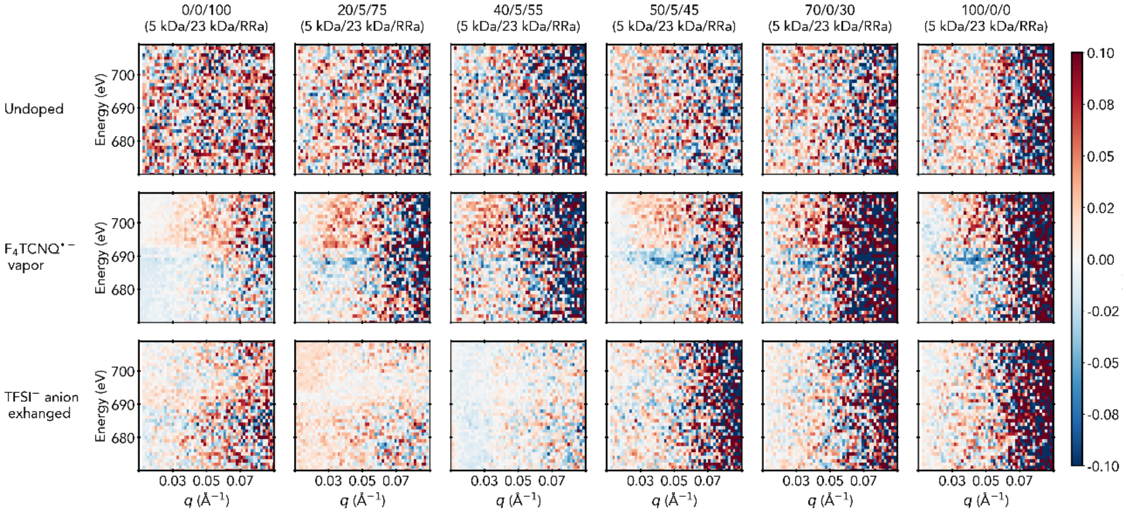

Figure 96. F K Edge Scattering Anisotropy

*F K Edge scattering anisotropy maps of different P3HT blend compositions (outlined along top axis) and dopant incorporation identity (outlined along vertical axis).*

### 4.6.18 Simulated Scattering Anisotropy Versus Dopant Distribution and Orientation

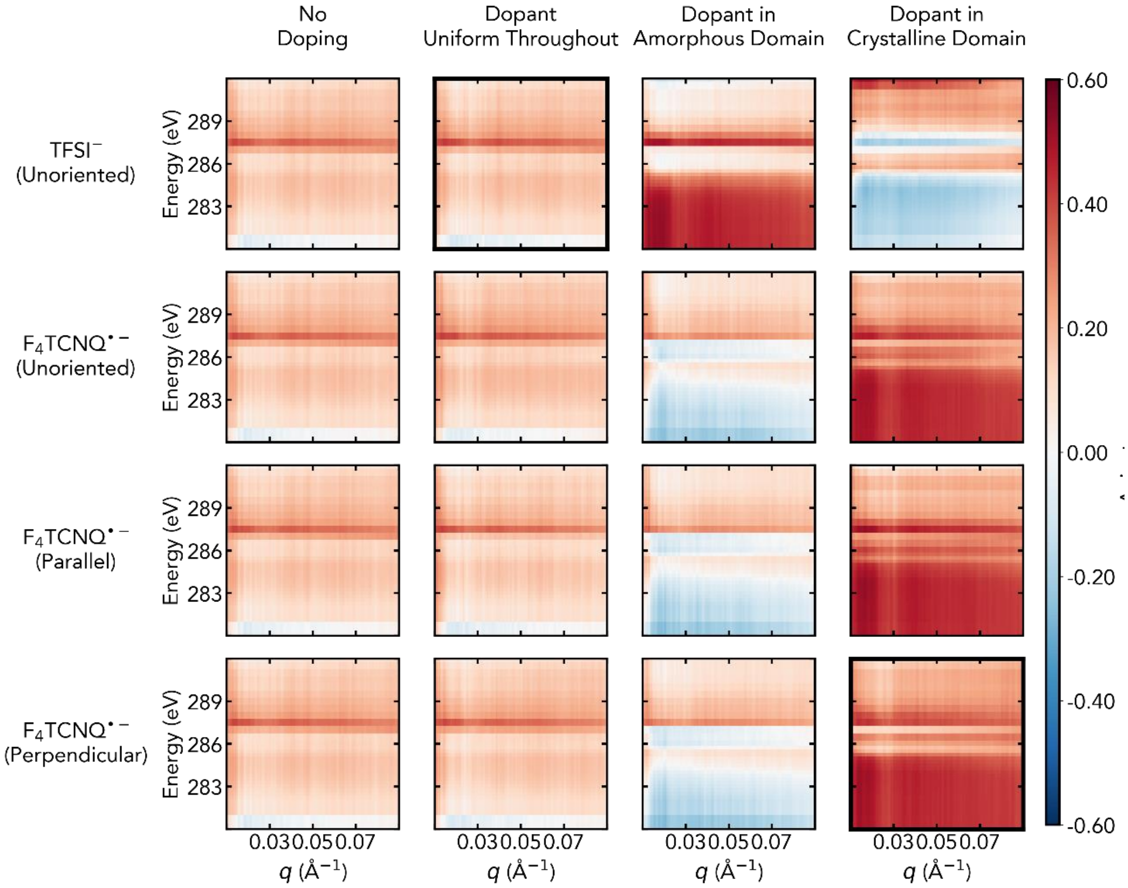

**Figure 97. Simulated Scattering Anisotropy Versus Dopant Distribution and Orientation for Doped P3HT at the C K-Edge**

*Simulated scattering anisotropy maps for different dopant incorporation/distribution (labeled above the top row) and dopant identity/orientation relative to P3HT thiophene plane normal (labeled along the left column) for approximately 36% crystalline P3HT morphologies at the C K-edge. Changes observed along q and energy for dopant distribution, identity, and orientation, further discussed in the main text. Scattering*

*anisotropy maps that best correspond to observed scattering anisotropy are outlined with thicker black borders.*

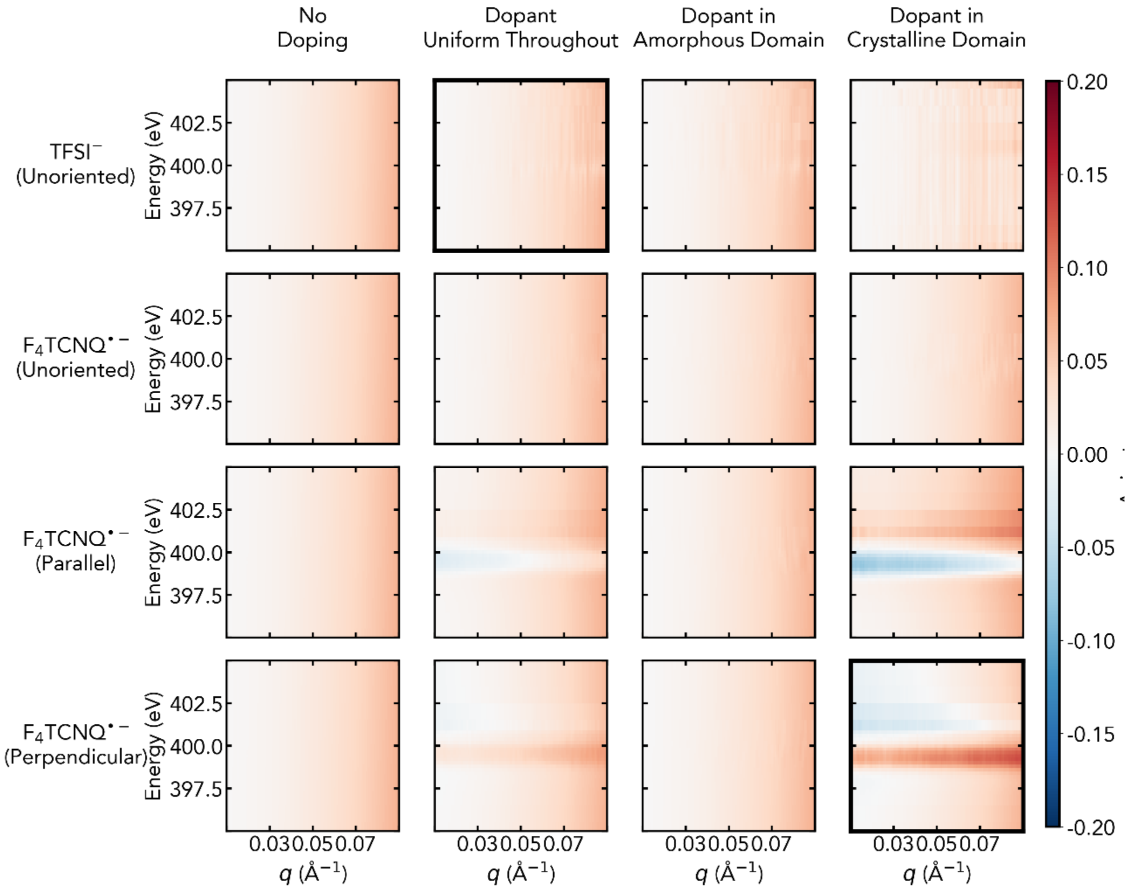

**Figure 98. Simulated Scattering Anisotropy Versus Dopant Distribution and Orientation for Doped P3HT at the C K-Edge**

*Simulated scattering anisotropy maps for different dopant incorporation/distribution (labeled above the top row) and dopant identity/orientation relative to P3HT thiophene plane normal (labeled along the left column) for approximately 36% crystalline P3HT morphologies at the N K-edge. Changes observed along q and energy for dopant distribution, identity, and orientation, further discussed in the main text. Scattering*

*anisotropy maps that best correspond to observed scattering anisotropy are outlined with thicker black borders.*

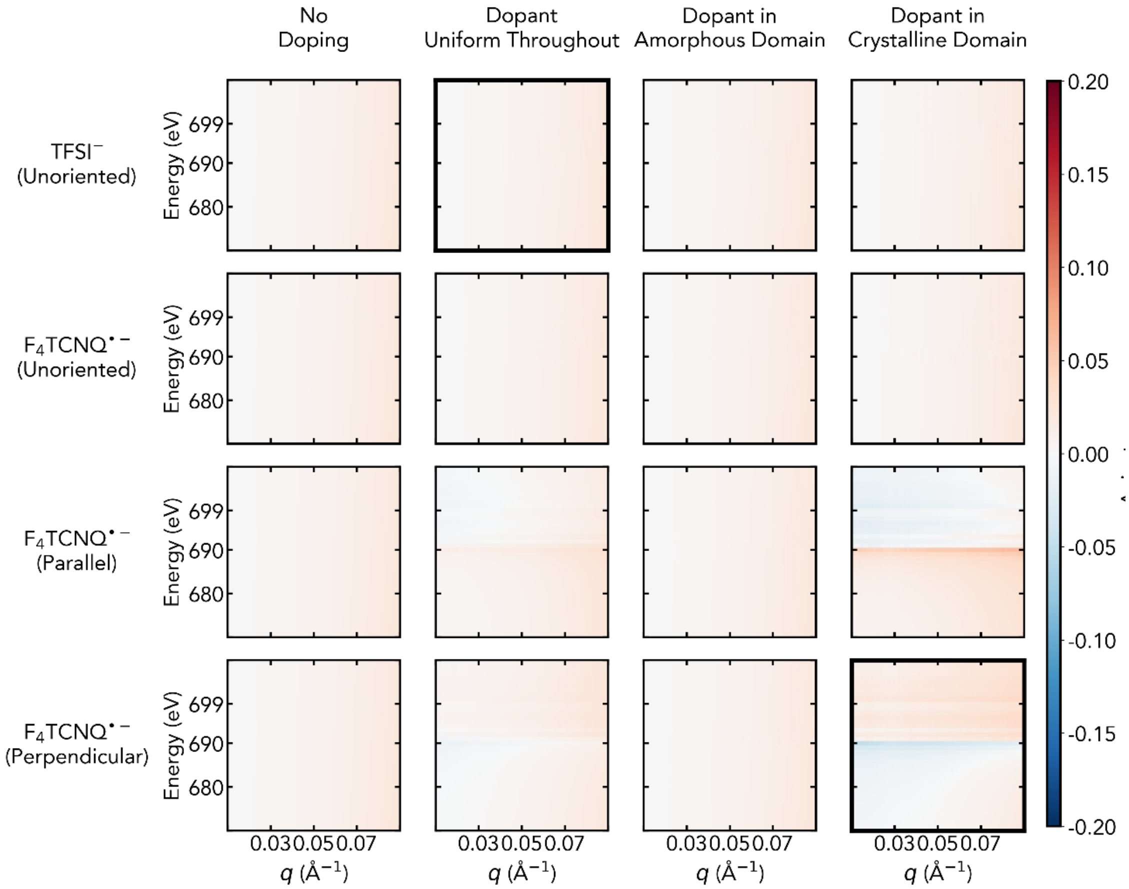

**Figure 99. Simulated Scattering Anisotropy Versus Dopant Distribution and Orientation for Doped P3HT at the C K-Edge**

*Simulated scattering anisotropy maps for different dopant incorporation/distribution (labeled above the top row) and dopant identity/orientation relative to P3HT thiophene plane normal (labeled along the left column) for approximately 36% crystalline P3HT morphologies at the F K-edge. Changes observed along q and energy for dopant distribution, identity, and orientation, further discussed in the main text. Scattering*

*anisotropy maps that best correspond to observed scattering anisotropy are outlined with thicker black borders.*

# Chapter 5 – Conclusions and Future Outlook

This dissertation has presented studies of ionically and electronically conducting polymers, a class of materials distinguished by their unique blend of conductive properties, flexibility, and processability. Our investigations have elucidated the complex interplay between the structure and function of these polymers, demonstrating how their structural characteristics can lead to significant advancements in their conductive properties. In our detailed examination of the doping process, we found that Brønsted acidic doping in conjugated polymers, such as poly(3-hexylthiophene) (P3HT), is primarily limited by proton transfer. This was evidenced by observing a kinetic isotope effect when doping P3HT films with bis(trifluoromethane)sulfonimide (HTFSI). Techniques like X-ray photoelectron spectroscopy and dynamic secondary ion mass spectrometry were instrumental in revealing dopant enrichment at the P3HT surface, underscoring that dopant diffusivity is inversely related to dopant concentration due to structural changes in the polymer. The formation of a highly stable dopant gradient as a result of this process opens new avenues in the design and fabrication of next-generation electronic materials and devices.

Our work on understanding the role of polymer-ion interactions in polyelectrolytes showcased the potential of light-responsive materials in modulating ionic conductivity. The significant change in ion conductivity triggered by the reversible isomerization of azobenzene indicated that the coordination of the *cis* isomer with $Li^+$ ions is chiefly responsible for its lower conductivity. This discovery challenges conventional understanding, which typically associates higher ionic conductivity with disordered, amorphous structures (attributed to the inefficient packing of the *cis* azobenzene) and suggests that careful control of polymer crystallinity and polymer-ion interactions can be powerful in designing functional polyelectrolytes. This insight paves the way for developing innovative photo-responsive polyelectrolyte materials, potentially transforming the design and application of such materials in various technological fields.

Finally, our exploration of scattering anisotropy using Polarized Resonant Soft X-ray Scattering (p-RSoXS) in P3HT blends yielded new insights into sample composition, morphology, and molecular orientation. The development of a model system, coupled with methods such as atomic force microscopy, UV-vis absorbance spectroscopy, X-ray photoelectron spectroscopy, and grazing incidence wide-angle X-ray scattering, led to the creation of a computational model that enhanced our understanding of how structure, chemistry, and orientation in these materials can be interpreted from p-RSoXS contrasts. Our findings reveal that the distributions of dopant counterions vary depending on the dopant's identity and significantly influence the sample's optical properties, thereby affecting scattering anisotropy. This approach paves the way for employing machine learning methods to gain quantitative insights into sample composition and orientation.

In conclusion, this dissertation contributes to the understanding of doping, charge conduction, and polymer morphology in ionically and electronically conducting semicrystalline polymers. By exploring the disorder inherent in these materials and the intricate interplay between structure and transport, our research lays a foundation for future technological advancements in the fields enabled by conductive polymers. Future research may delve into the evolution of ion conduction mechanisms and addressing the complex roles of hydration in both the polymer and the ion. With the advent of higher dielectric constant conjugated polyelectrolytes, a key focus will be understanding how dielectric constant affects the efficacy of doping and dopant-induced structural evolution, thus far difficult to characterize with traditional means. The potential of resonant scattering methods to probe orientational correlations in amorphous domains may offer further insight for these nominally disordered, emerging materials.

## References

(1) Onorato, J. W.; Luscombe, C. K. Morphological Effects on Polymeric Mixed Ionic/Electronic Conductors. *Mol. Syst. Des. Eng.* **2019**, *4* (2), 310–324. https://doi.org/10.1039/C8ME00093J.

(2) Paulsen, B. D.; Tybrandt, K.; Stavrinidou, E.; Rivnay, J. Organic Mixed Ionic–Electronic Conductors. *Nature Materials* **2020**, *19* (1), 13–26. https://doi.org/10.1038/s41563-019-0435-z.

(3) Inal, S.; Rivnay, J.; Leleux, P.; Ferro, M.; Ramuz, M.; Brendel, J. C.; Schmidt, M. M.; Thelakkat, M.; Malliaras, G. G. A High Transconductance Accumulation Mode Electrochemical Transistor. *Advanced Materials* **2014**, *26* (44), 7450–7455. https://doi.org/10.1002/adma.201403150.

(4) Zhao, Z.; Richardson, G. F.; Meng, Q.; Zhu, S.; Kuan, H.-C.; Ma, J. PEDOT-Based Composites as Electrode Materials for Supercapacitors. *Nanotechnology* **2015**, *27* (4), 042001. https://doi.org/10.1088/0957-4484/27/4/042001.

(5) Gaupp, C. L.; Welsh, D. M.; Reynolds, J. R. Poly(ProDOT-Et2): A High-Contrast, High-Coloration Efficiency Electrochromic Polymer. *Macromolecular Rapid Communications* **2002**, *23* (15), 885–889. https://doi.org/10.1002/1521-3927(20021001)23:15<885::AID-MARC885>3.0.CO;2-X.

(6) Miyamoto, T.; Shibayama, K. Free-volume Model for Ionic Conductivity in Polymers. *Journal of Applied Physics* **1973**, *44* (12), 5372–5376. https://doi.org/10.1063/1.1662158.

(7) Sirringhaus, H.; Brown, P. J.; Friend, R. H.; Nielsen, M. M.; Bechgaard, K.; Langeveld-Voss, B. M. W.; Spiering, A. J. H.; Janssen, R. A. J.; Meijer, E. W. Microstructure–Mobility Correlation in Self-Organised, Conjugated Polymer Field-Effect Transistors. *Synthetic Metals* **2000**, *111–112*, 129–132. https://doi.org/10.1016/S0379-6779(99)00326-4.

(8) Noriega, R.; Rivnay, J.; Vandewal, K.; Koch, F. P. V.; Stingelin, N.; Smith, P.; Toney, M. F.; Salleo, A. A General Relationship between Disorder, Aggregation and Charge Transport in Conjugated Polymers. *Nature Materials* **2013**, *12* (11), 1038–1044. https://doi.org/10.1038/nmat3722.

(9) Chabinyc, M. L.; Endicott, F.; Vogt, B. D.; DeLongchamp, D. M.; Lin, E. K.; Wu, Y.; Liu, P.; Ong, B. S. Effects of Humidity on Unencapsulated Poly(Thiophene) Thin-Film Transistors. *Appl. Phys. Lett.* **2006**, *88* (11), 113514. https://doi.org/10.1063/1.2181206.

(10) Chang, W. B.; Fang, H.; Liu, J.; Evans, C. M.; Russ, B.; Popere, B. C.; Patel, S. N.; Chabinyc, M. L.; Segalman, R. A. Electrochemical Effects in Thermoelectric Polymers. *ACS Macro Lett.* **2016**, *5* (4), 455–459. https://doi.org/10.1021/acsmacrolett.6b00054.

(11) Patel, S. N.; Javier, A. E.; Balsara, N. P. Electrochemically Oxidized Electronic and Ionic Conducting Nanostructured Block Copolymers for Lithium Battery Electrodes. *ACS Nano* **2013**, *7* (7), 6056–6068. https://doi.org/10.1021/nn4018685.

(12) Gu, Z.; Kanto, T.; Tsuchiya, K.; Ogino, K. Synthesis of Poly(3-Hexylthiophene)-b-Poly(Ethylene Oxide) for Application to Photovoltaic Device. *Journal of Photopolymer Science and Technology* **2010**, *23* (3), 405–406. https://doi.org/10.2494/photopolymer.23.405.

(13) Moon, H. C.; Kim, J. K. Phase Segregation of Poly(3-Dodecylthiophene)-Block-Poly(Methyl Methacrylate) Copolymers. *Polymer* **2013**, *54* (20), 5437–5442. https://doi.org/10.1016/j.polymer.2013.07.063.

(14) Stavrinidou, E.; Winther-Jensen, O.; Shekibi, B. S.; Armel, V.; Rivnay, J.; Ismailova, E.; Sanaur, S.; Malliaras, G. G.; Winther-Jensen, B. Engineering Hydrophilic Conducting Composites with Enhanced Ion Mobility. *Phys. Chem. Chem. Phys.* **2014**, *16* (6), 2275–2279. https://doi.org/10.1039/C3CP54061H.

(15) Lai, C.-H.; Ashby, D. S.; Lin, T. C.; Lau, J.; Dawson, A.; Tolbert, S. H.; Dunn, B. S. Application of Poly(3-Hexylthiophene-2,5-Diyl) as a Protective Coating for High Rate Cathode Materials. *Chem. Mater.* **2018**, *30* (8), 2589–2599. https://doi.org/10.1021/acs.chemmater.7b05116.

(16) Jiang, H.; Taranekar, P.; Reynolds, J. R.; Schanze, K. S. Conjugated Polyelectrolytes: Synthesis, Photophysics, and Applications. *Angewandte Chemie International Edition* **2009**, *48* (24), 4300–4316. https://doi.org/10.1002/anie.200805456.

(17) Evans, C. M.; Bridges, C. R.; Sanoja, G. E.; Bartels, J.; Segalman, R. A. Role of Tethered Ion Placement on Polymerized Ionic Liquid Structure and Conductivity: Pendant versus Backbone Charge Placement. *ACS Macro Lett.* **2016**, *5* (8), 925–930. https://doi.org/10.1021/acsmacrolett.6b00534.

(18) Kang, K.; Watanabe, S.; Broch, K.; Sepe, A.; Brown, A.; Nasrallah, I.; Nikolka, M.; Fei, Z.; Heeney, M.; Matsumoto, D.; Marumoto, K.; Tanaka, H.; Kuroda, S.; Sirringhaus, H. 2D Coherent Charge Transport in Highly Ordered Conducting Polymers Doped by Solid State Diffusion. *Nature Materials* **2016**, *15* (8), 896–902. https://doi.org/10.1038/nmat4634.

(19) Arkhipov, V. I.; Heremans, P.; Emelianova, E. V.; Bässler, H. Effect of Doping on the Density-of-States Distribution and Carrier Hopping in Disordered Organic Semiconductors. *Phys. Rev. B* **2005**, *71* (4), 045214. https://doi.org/10.1103/PhysRevB.71.045214.

(20) Wang, S.; Ha, M.; Manno, M.; Frisbie, C. D.; Leighton, C. Hopping Transport and the Hall Effect near the Insulator–Metal Transition in Electrochemically Gated Poly(3-Hexylthiophene) Transistors. *Nat Commun* **2012**, *3* (1), 1–7. https://doi.org/10.1038/ncomms2213.

(21) Volkov, A. V.; Wijeratne, K.; Mitraka, E.; Ail, U.; Zhao, D.; Tybrandt, K.; Andreasen, J. W.; Berggren, M.; Crispin, X.; Zozoulenko, I. V. Understanding the Capacitance of PEDOT:PSS. *Advanced Functional Materials* **2017**, *27* (28), 1700329. https://doi.org/10.1002/adfm.201700329.

(22) Newman, J.; Thomas-Alyea, K. E. Transport Laws. In *Electrochemical Systems*; John Wiley & Sons: Hoboken, N.J, 2004; pp 271–274.

(23) Buck, R. P. General Voltage-Step Responses and Impedances of Mixed-Conductor Films and Diodes: Metal-Contact Cells with Mobile Anions or Cations. *The Journal of Physical Chemistry* **1989**, *93* (16), 6212–6219.

(24) Buck, R. P. Electron Hopping in One Dimension: Mixed Conductor Membranes. *The Journal of Physical Chemistry* **1988**, *92* (14), 4196–4200.

(25) Nahir, T. M.; Buck, R. P. Transport Processes in Membranes Containing Neutral Ion Carriers, Positive Ion Complexes, Negative Mobile Sites, and Ion Pairs. *The Journal of Physical Chemistry* **1993**, *97* (47), 12363–12372.

(26) Nowak, M.; Rughooputh, S.; Hotta, S.; Heeger, A. J. Polarons and Bipolarons on a Conducting Polymer in Solution. *Macromolecules* **1987**, *20* (5), 965–968.

(27) Jia, H.; Lei, T. Emerging Research Directions for N-Type Conjugated Polymers. *Journal of Materials Chemistry C* **2019**, *7* (41), 12809–12821. https://doi.org/10.1039/C9TC02632K.

(28) Rawlings, D.; Thomas, E. M.; Segalman, R. A.; Chabinyc, M. L. Controlling the Doping Mechanism in Poly(3-Hexylthiophene) Thin-Film Transistors with Polymeric Ionic Liquid Dielectrics. *Chem. Mater.* **2019**, *31* (21), 8820–8829. https://doi.org/10.1021/acs.chemmater.9b02803.

(29) Mills, T.; Kaake, L. G.; Zhu, X.-Y. Polaron and Ion Diffusion in a Poly(3-Hexylthiophene) Thin-Film Transistor Gated with Polymer Electrolyte Dielectric. *Appl. Phys. A* **2009**, *95* (1), 291–296. https://doi.org/10.1007/s00339-008-5026-9.

(30) Kaneto, K.; Agawa, H.; Yoshino, K. Cycle Life, Stability, and Characteristics of Color Switching Cells Utilizing Polythiophene Films. *Journal of Applied Physics* **1987**, *61* (3), 1197–1205. https://doi.org/10.1063/1.338167.

(31) Bischak, C. G.; Flagg, L. Q.; Yan, K.; Rehman, T.; Davies, D. W.; Quezada, R. J.; Onorato, J. W.; Luscombe, C. K.; Diao, Y.; Li, C.-Z.; Ginger, D. S. A Reversible Structural Phase Transition by Electrochemically-Driven Ion Injection into a Conjugated Polymer. *J. Am. Chem. Soc.* **2020**, *142* (16), 7434–7442. https://doi.org/10.1021/jacs.9b12769.

(32) Bocharova, V.; Sokolov, A. P. Perspectives for Polymer Electrolytes: A View from Fundamentals of Ionic Conductivity. *Macromolecules* **2020**, *53* (11), 4141–4157. https://doi.org/10.1021/acs.macromol.9b02742.

(33) Albinsson, I.; Mellander, B. -E.; Stevens, J. R. Ionic Conductivity in Poly(Propylene Glycol) Complexed with Lithium and Sodium Triflate. *J. Chem. Phys.* **1992**, *96* (1), 681–690. https://doi.org/10.1063/1.462453.

(34) Wang, Y.; Fan, F.; Agapov, A. L.; Yu, X.; Hong, K.; Mays, J.; Sokolov, A. P. Design of Superionic Polymers—New Insights from Walden Plot Analysis. *Solid State Ionics* **2014**, *262*, 782–784. https://doi.org/10.1016/j.ssi.2013.09.026.

(35) Cohen, M. H.; Turnbull, D. Molecular Transport in Liquids and Glasses. *J. Chem. Phys.* **1959**, *31* (5), 1164–1169. https://doi.org/10.1063/1.1730566.

(36) Turnbull, D.; Cohen, M. H. On the Free-Volume Model of the Liquid-Glass Transition. *J. Chem. Phys.* **1970**, *52* (6), 3038–3041. https://doi.org/10.1063/1.1673434.

(37) A. Ratner, M.; Nitzan, A. Conductivity in Polymer Ionics. Dynamic Disorder and Correlation. *Faraday Discussions of the Chemical Society* **1989**, *88* (0), 19–42. https://doi.org/10.1039/DC9898800019.

(38) Aziz, S. B.; Woo, T. J.; Kadir, M. F. Z.; Ahmed, H. M. A Conceptual Review on Polymer Electrolytes and Ion Transport Models. *Journal of Science: Advanced Materials and Devices* **2018**, *3* (1), 1–17. https://doi.org/10.1016/j.jsamd.2018.01.002.

(39) Boden, N.; Leng, S. A.; Ward, I. M. Ionic Conductivity and Diffusivity in Polyethylene Oxode/Electrolyte Solutions as Models for Polymer Electrolytes. *Solid State Ionics* **1991**, *45* (3), 261–270. https://doi.org/10.1016/0167-2738(91)90160-D.

(40) Chung, S. H.; Such, K.; Wieczorek, W.; Stevens, J. R. An Analysis of Ionic Conductivity in Polymer Electrolytes. *Journal of Polymer Science Part B: Polymer Physics* **1994**, *32* (16), 2733–2741. https://doi.org/10.1002/polb.1994.090321619.

(41) Meyer, W. H. Polymer Electrolytes for Lithium-Ion Batteries. *Advanced Materials* **1998**, *10* (6), 439–448. https://doi.org/10.1002/(SICI)1521-4095(199804)10:6<439::AID-ADMA439>3.0.CO;2-I.

(42) Mao, G.; Saboungi, M.-L.; Price, D. L.; Armand, M.; Mezei, F.; Pouget, S. α-Relaxation in PEO−LiTFSI Polymer Electrolytes. *Macromolecules* **2002**, *35* (2), 415–419. https://doi.org/10.1021/ma010108e.

(43) Loo, W. S.; Mongcopa, K. I.; Gribble, D. A.; Faraone, A. A.; Balsara, N. P. Investigating the Effect of Added Salt on the Chain Dimensions of Poly(Ethylene Oxide) through Small-Angle Neutron Scattering. *Macromolecules* **2019**, *52* (22), 8724–8732. https://doi.org/10.1021/acs.macromol.9b01509.

(44) Mongcopa, K. I. S.; Tyagi, M.; Mailoa, J. P.; Samsonidze, G.; Kozinsky, B.; Mullin, S. A.; Gribble, D. A.; Watanabe, H.; Balsara, N. P. Relationship between Segmental Dynamics Measured by Quasi-Elastic Neutron Scattering and Conductivity in Polymer Electrolytes. *ACS Macro Lett.* **2018**, *7* (4), 504–508. https://doi.org/10.1021/acsmacrolett.8b00159.

(45) Hall, L. M.; Seitz, M. E.; Winey, K. I.; Opper, K. L.; Wagener, K. B.; Stevens, M. J.; Frischknecht, A. L. Ionic Aggregate Structure in Ionomer Melts: Effect of Molecular Architecture on Aggregates and the Ionomer Peak. *J. Am. Chem. Soc.* **2012**, *134* (1), 574–587. https://doi.org/10.1021/ja209142b.

(46) Yan, L.; Rank, C.; Mecking, S.; Winey, K. I. Gyroid and Other Ordered Morphologies in Single-Ion Conducting Polymers and Their Impact on Ion Conductivity. *J. Am. Chem. Soc.* **2020**, *142* (2), 857–866. https://doi.org/10.1021/jacs.9b09701.

(47) Yan, L.; Bustillo, K. C.; Panova, O.; Minor, A. M.; Winey, K. I. Solution-Grown Crystals of Precise Acid- and Ion-Containing Polyethylenes. *Polymer* **2018**, *135*, 111–119. https://doi.org/10.1016/j.polymer.2017.12.007.

(48) Young, W.-S.; Epps, T. H. Salt Doping in PEO-Containing Block Copolymers: Counterion and Concentration Effects. *Macromolecules* **2009**, *42* (7), 2672–2678. https://doi.org/10.1021/ma802799p.

(49) Singh, M.; Odusanya, O.; Wilmes, G. M.; Eitouni, H. B.; Gomez, E. D.; Patel, A. J.; Chen, V. L.; Park, M. J.; Fragouli, P.; Iatrou, H.; Hadjichristidis, N.; Cookson, D.; Balsara, N. P. Effect of Molecular Weight on the Mechanical and Electrical Properties of Block Copolymer Electrolytes. *Macromolecules* **2007**, *40* (13), 4578–4585. https://doi.org/10.1021/ma0629541.

(50) Xie, S.; Meyer, D. J.; Wang, E.; Bates, F. S.; Lodge, T. P. Structure and Properties of Bicontinuous Microemulsions from Salt-Doped Ternary Polymer Blends. *Macromolecules* **2019**, *52* (24), 9693–9702. https://doi.org/10.1021/acs.macromol.9b01963.

(51) Knychała, P.; Banaszak, M. Simulations on a Swollen Gyroid Nanostructure in Thin Films Relevant to Systems of Ionic Block Copolymers. *The European Physical Journal E* **2014**, *37* (7), 67. https://doi.org/10.1140/epje/i2014-14067-4.

(52) Park, M. J.; Balsara, N. P. Phase Behavior of Symmetric Sulfonated Block Copolymers. *Macromolecules* **2008**, *41* (10), 3678–3687. https://doi.org/10.1021/ma702733f.

(53) Coropceanu, V.; Cornil, J.; da Silva Filho, D. A.; Olivier, Y.; Silbey, R.; Brédas, J.-L. Charge Transport in Organic Semiconductors. *Chem. Rev.* **2007**, *107* (4), 926–952. https://doi.org/10.1021/cr050140x.

(54) Tietze, M. L.; Pahner, P.; Schmidt, K.; Leo, K.; Lüssem, B. Doped Organic Semiconductors: Trap-Filling, Impurity Saturation, and Reserve Regimes. *Advanced Functional Materials* **2015**, *25* (18), 2701–2707. https://doi.org/10.1002/adfm.201404549.

(55) Thomas, E. M.; Davidson, E. C.; Katsumata, R.; Segalman, R. A.; Chabinyc, M. L. Branched Side Chains Govern Counterion Position and Doping Mechanism in Conjugated Polythiophenes. *ACS Macro Lett.* **2018**, *7* (12), 1492–1497. https://doi.org/10.1021/acsmacrolett.8b00778.

(56) Liu, C.; Huang, K.; Park, W.-T.; Li, M.; Yang, T.; Liu, X.; Liang, L.; Minari, T.; Noh, Y.-Y. A Unified Understanding of Charge Transport in Organic Semiconductors: The Importance of Attenuated Delocalization for the Carriers. *Mater. Horiz.* **2017**, *4* (4), 608–618. https://doi.org/10.1039/C7MH00091J.

(57) Baranovskii, S. D. Theoretical Description of Charge Transport in Disordered Organic Semiconductors. *physica status solidi (b)* **2014**, *251* (3), 487–525. https://doi.org/10.1002/pssb.201350339.

(58) Bässler, H.; Köhler, A. Charge Transport in Organic Semiconductors. In *Unimolecular and Supramolecular Electronics I: Chemistry and Physics Meet at Metal-Molecule Interfaces*; Metzger, R. M., Ed.; Topics in Current Chemistry; Springer: Berlin, Heidelberg, 2012; pp 1–65. https://doi.org/10.1007/128_2011_218.

(59) Glaudell, A. M.; Cochran, J. E.; Patel, S. N.; Chabinyc, M. L. Impact of the Doping Method on Conductivity and Thermopower in Semiconducting Polythiophenes. *Advanced Energy Materials* **2015**, *5* (4), 1401072. https://doi.org/10.1002/aenm.201401072.

(60) Thomas, E. M.; Popere, B. C.; Fang, H.; Chabinyc, M. L.; Segalman, R. A. Role of Disorder Induced by Doping on the Thermoelectric Properties of Semiconducting Polymers. *Chem. Mater.* **2018**, *30* (9), 2965–2972. https://doi.org/10.1021/acs.chemmater.8b00394.

(61) Zuo, G.; Abdalla, H.; Kemerink, M. Impact of Doping on the Density of States and the Mobility in Organic Semiconductors. *Phys. Rev. B* **2016**, *93* (23), 235203. https://doi.org/10.1103/PhysRevB.93.235203.

(62) Yee, P. Y.; Scholes, D. T.; Schwartz, B. J.; Tolbert, S. H. Dopant-Induced Ordering of Amorphous Regions in Regiorandom P3HT. *J. Phys. Chem. Lett.* **2019**, *10* (17), 4929–4934. https://doi.org/10.1021/acs.jpclett.9b02070.

(63) Duong, D. T.; Toney, M. F.; Salleo, A. Role of Confinement and Aggregation in Charge Transport in Semicrystalline Polythiophene Thin Films. *Phys. Rev. B* **2012**, *86* (20), 205205. https://doi.org/10.1103/PhysRevB.86.205205.

(64) Wirix, M. J. M.; Bomans, P. H. H.; Friedrich, H.; Sommerdijk, N. A. J. M.; de With, G. Three-Dimensional Structure of P3HT Assemblies in Organic Solvents Revealed by Cryo-TEM. *Nano Lett.* **2014**, *14* (4), 2033–2038. https://doi.org/10.1021/nl5001967.

(65) Liu, W.; Müller, L.; Ma, S.; Barlow, S.; Marder, S. R.; Kowalsky, W.; Köhn, A.; Lovrincic, R. Origin of the π–π Spacing Change upon Doping of Semiconducting Polymers. *J. Phys. Chem. C* **2018**, *122* (49), 27983–27990. https://doi.org/10.1021/acs.jpcc.8b10845.

(66) Bridges, C. R.; Ford, M. J.; Thomas, E. M.; Gomez, C.; Bazan, G. C.; Segalman, R. A. Effects of Side Chain Branch Point on Self Assembly, Structure, and Electronic

Properties of High Mobility Semiconducting Polymers. *Macromolecules* **2018**, *51* (21), 8597–8604. https://doi.org/10.1021/acs.macromol.8b01906.

(67) Ma, Z.; Geng, H.; Wang, D.; Shuai, Z. Influence of Alkyl Side-Chain Length on the Carrier Mobility in Organic Semiconductors: Herringbone vs. Pi–Pi Stacking. *J. Mater. Chem. C* **2016**, *4* (20), 4546–4555. https://doi.org/10.1039/C6TC00755D.

(68) Zhou, K.; Zhou, X.; Xu, X.; Musumeci, C.; Wang, C.; Xu, W.; Meng, X.; Ma, W.; Inganäs, O. π–π Stacking Distance and Phase Separation Controlled Efficiency in Stable All-Polymer Solar Cells. *Polymers* **2019**, *11* (10), 1665. https://doi.org/10.3390/polym11101665.

(69) Kroon, R.; Kiefer, D.; Stegerer, D.; Yu, L.; Sommer, M.; Müller, C. Polar Side Chains Enhance Processability, Electrical Conductivity, and Thermal Stability of a Molecularly p-Doped Polythiophene. *Advanced Materials* **2017**, *29* (24), 1700930. https://doi.org/10.1002/adma.201700930.

(70) Liu, J.; Qiu, L.; Alessandri, R.; Qiu, X.; Portale, G.; Dong, J.; Talsma, W.; Ye, G.; Sengrian, A. A.; Souza, P. C. T.; Loi, M. A.; Chiechi, R. C.; Marrink, S. J.; Hummelen, J. C.; Koster, L. J. A. Enhancing Molecular N-Type Doping of Donor–Acceptor Copolymers by Tailoring Side Chains. *Advanced Materials* **2018**, *30* (7), 1704630. https://doi.org/10.1002/adma.201704630.

(71) Aubry, T. J.; Axtell, J. C.; Basile, V. M.; Winchell, K. J.; Lindemuth, J. R.; Porter, T. M.; Liu, J.-Y.; Alexandrova, A. N.; Kubiak, C. P.; Tolbert, S. H.; Spokoyny, A. M.; Schwartz, B. J. Dodecaborane-Based Dopants Designed to Shield Anion Electrostatics Lead to Increased Carrier Mobility in a Doped Conjugated Polymer. *Advanced Materials* **2019**, *31* (11), 1805647. https://doi.org/10.1002/adma.201805647.

(72) Giovannitti, A.; Maria, I. P.; Hanifi, D.; Donahue, M. J.; Bryant, D.; Barth, K. J.; Makdah, B. E.; Savva, A.; Moia, D.; Zetek, M.; Barnes, P. R. F.; Reid, O. G.; Inal, S.; Rumbles, G.; Malliaras, G. G.; Nelson, J.; Rivnay, J.; McCulloch, I. The Role of the Side Chain on the Performance of N-Type Conjugated Polymers in Aqueous Electrolytes. *Chem. Mater.* **2018**, *30* (9), 2945–2953. https://doi.org/10.1021/acs.chemmater.8b00321.

(73) Hynynen, J.; Kiefer, D.; Yu, L. Y.; Kroon, R.; Munir, R.; Amassian, A.; Kemerink, M.; Muller, C. Enhanced Electrical Conductivity of Molecularly P-Doped Poly(3-Hexylthiophene) through Understanding the Correlation with Solid-State Order. *Macromolecules* **2017**, *50*, 8140–8148. https://doi.org/10.1021/acs.macromol.7b00968.

(74) Lim, E.; Glaudell, A. M.; Miller, R.; Chabinyc, M. L. The Role of Ordering on the Thermoelectric Properties of Blends of Regioregular and Regiorandom Poly(3-Hexylthiophene). *Advanced Electronic Materials* **2019**, *5* (11), 1800915. https://doi.org/10.1002/aelm.201800915.

(75) Collins, B. A.; Cochran, J. E.; Yan, H.; Gann, E.; Hub, C.; Fink, R.; Wang, C.; Schuettfort, T.; McNeill, C. R.; Chabinyc, M. L.; Ade, H. Polarized X-Ray Scattering Reveals Non-Crystalline Orientational Ordering in Organic Films. *Nature Materials* **2012**, *11* (6), 536–543. https://doi.org/10.1038/nmat3310.

(76) Patel, S. N.; Glaudell, A. M.; Kiefer, D.; Chabinyc, M. L. Increasing the Thermoelectric Power Factor of a Semiconducting Polymer by Doping from the Vapor Phase. *Acs Macro Lett* **2016**, *5*, 268–272. https://doi.org/10.1021/acsmacrolett.5b00887.

(77) Patel, S. N.; Glaudell, A. M.; Peterson, K. A.; Thomas, E. M.; O'Hara, K. A.; Lim, E.; Chabinyc, M. L. Morphology Controls the Thermoelectric Power Factor of a Doped

Semiconducting Polymer. *Science Advances* **2017**, *3* (6), e1700434. https://doi.org/10.1126/sciadv.1700434.

(78) Gu, K.; Snyder, C. R.; Onorato, J.; Luscombe, C. K.; Bosse, A. W.; Loo, Y.-L. Assessing the Huang–Brown Description of Tie Chains for Charge Transport in Conjugated Polymers. *ACS Macro Lett.* **2018**, *7* (11), 1333–1338. https://doi.org/10.1021/acsmacrolett.8b00626.

(79) Himmelberger, S.; Vandewal, K.; Fei, Z.; Heeney, M.; Salleo, A. Role of Molecular Weight Distribution on Charge Transport in Semiconducting Polymers. *Macromolecules* **2014**, *47* (20), 7151–7157. https://doi.org/10.1021/ma501508j.

(80) Mindemark, J.; Lacey, M. J.; Bowden, T.; Brandell, D. Beyond PEO—Alternative Host Materials for Li+-Conducting Solid Polymer Electrolytes. *Progress in Polymer Science* **2018**, *81*, 114–143. https://doi.org/10.1016/j.progpolymsci.2017.12.004.

(81) MacFarlane, D. R.; Forsyth, M.; Izgorodina, E. I.; Abbott, A. P.; Annat, G.; Fraser, K. On the Concept of Ionicity in Ionic Liquids. *Phys. Chem. Chem. Phys.* **2009**, *11* (25), 4962–4967. https://doi.org/10.1039/B900201D.

(82) Hayashi, A.; Noi, K.; Sakuda, A.; Tatsumisago, M. Superionic Glass-Ceramic Electrolytes for Room-Temperature Rechargeable Sodium Batteries. *Nature Communications* **2012**, *3* (1), 856. https://doi.org/10.1038/ncomms1843.

(83) Chiang, C. K.; Fincher, C. R.; Park, Y. W.; Heeger, A. J.; Shirakawa, H.; Louis, E. J.; Gau, S. C.; MacDiarmid, A. G. Electrical Conductivity in Doped Polyacetylene. *Phys. Rev. Lett.* **1977**, *39* (17), 1098–1101. https://doi.org/10.1103/PhysRevLett.39.1098.

(84) Vijayakumar, V.; Zhong, Y.; Untilova, V.; Bahri, M.; Herrmann, L.; Biniek, L.; Leclerc, N.; Brinkmann, M. Bringing Conducting Polymers to High Order: Toward Conductivities beyond 105 S Cm−1 and Thermoelectric Power Factors of 2 mW M−1 K−2. *Advanced Energy Materials* **2019**, *9* (24), 1900266. https://doi.org/10.1002/aenm.201900266.

(85) Thomas, E. M.; Brady, M. A.; Nakayama, H.; Popere, B. C.; Segalman, R. A.; Chabinyc, M. L. X-Ray Scattering Reveals Ion-Induced Microstructural Changes During Electrochemical Gating of Poly(3-Hexylthiophene). *Advanced Functional Materials* **2018**, *28* (44), 1803687. https://doi.org/10.1002/adfm.201803687.

(86) Pingel, P.; Neher, D. Comprehensive Picture of P-Type Doping of P3HT with the Molecular Acceptor F4TCNQ. *Phys. Rev. B* **2013**, *87* (11), 115209. https://doi.org/10.1103/PhysRevB.87.115209.

(87) Jamnik, J.; Maier, J. Generalised Equivalent Circuits for Mass and Charge Transport: Chemical Capacitance and Its Implications. *Physical Chemistry Chemical Physics* **2001**, *3* (9), 1668–1678. https://doi.org/10.1039/B100180I.

(88) Kim, Y.; Han, M.; Kim, J.; Kim, E. Electrochromic Capacitive Windows Based on All Conjugated Polymers for a Dual Function Smart Window. *Energy Environ. Sci.* **2018**, *11* (8), 2124–2133. https://doi.org/10.1039/C8EE00080H.

(89) Heimburg, T. The Capacitance and Electromechanical Coupling of Lipid Membranes Close to Transitions: The Effect of Electrostriction. *Biophys J* **2012**, *103* (5), 918–929. https://doi.org/10.1016/j.bpj.2012.07.010.

(90) Gopal, C. B.; Gabaly, F. E.; McDaniel, A. H.; Chueh, W. C. Origin and Tunability of Unusually Large Surface Capacitance in Doped Cerium Oxide Studied by Ambient-Pressure X-Ray Photoelectron Spectroscopy. *Advanced Materials* **2016**, *28* (23), 4692–4697. https://doi.org/10.1002/adma.201506333.

(91) Zhao, D.; Fabiano, S.; Berggren, M.; Crispin, X. Ionic Thermoelectric Gating Organic Transistors. *Nature Communications* **2017**, *8* (1), 14214. https://doi.org/10.1038/ncomms14214.

(92) Moser, M.; Hidalgo, T. C.; Surgailis, J.; Gladisch, J.; Ghosh, S.; Sheelamanthula, R.; Thiburce, Q.; Giovannitti, A.; Salleo, A.; Gasparini, N.; Wadsworth, A.; Zozoulenko, I.; Berggren, M.; Stavrinidou, E.; Inal, S.; McCulloch, I. Side Chain Redistribution as a Strategy to Boost Organic Electrochemical Transistor Performance and Stability. *Advanced Materials n/a* (n/a), 2002748. https://doi.org/10.1002/adma.202002748.

(93) Gladisch, J.; Stavrinidou, E.; Ghosh, S.; Giovannitti, A.; Moser, M.; Zozoulenko, I.; McCulloch, I.; Berggren, M. Reversible Electronic Solid–Gel Switching of a Conjugated Polymer. *Advanced Materials* **2019**, 1901144. https://doi.org/10.1002/advs.201901144@10.1002/(ISSN)1521-4095.polymer-technology.

(94) Friedlein, J. T.; Donahue, M. J.; Shaheen, S. E.; Malliaras, G. G.; McLeod, R. R. Microsecond Response in Organic Electrochemical Transistors: Exceeding the Ionic Speed Limit. *Advanced Materials* **2016**, *28* (38), 8398–8404. https://doi.org/10.1002/adma.201602684.

(95) Berggren, M.; Malliaras, G. G. How Conducting Polymer Electrodes Operate. *Science* **2019**, *364* (6437), 233–234. https://doi.org/10.1126/science.aaw9295.

(96) Khodagholy, D.; Rivnay, J.; Sessolo, M.; Gurfinkel, M.; Leleux, P.; Jimison, L. H.; Stavrinidou, E.; Herve, T.; Sanaur, S.; Owens, R. M.; Malliaras, G. G. High Transconductance Organic Electrochemical Transistors. *Nature Communications* **2013**, *4* (1), 2133. https://doi.org/10.1038/ncomms3133.

(97) Patel, S. N.; Javier, A. E.; Stone, G. M.; Mullin, S. A.; Balsara, N. P. Simultaneous Conduction of Electronic Charge and Lithium Ions in Block Copolymers. *ACS Nano* **2012**, *6* (2), 1589–1600. https://doi.org/10.1021/nn2045664.

(98) Newman, J.; Thomas-Alyea, K. E. *Electrochemical Systems*.

(99) Ma, Y.; Doyle, M.; Fuller, T. F.; Doeff, M. M.; Jonghe, L. C. D.; Newman, J. The Measurement of a Complete Set of Transport Properties for a Concentrated Solid Polymer Electrolyte Solution. *J. Electrochem. Soc.* **1995**, *142* (6), 1859. https://doi.org/10.1149/1.2044206.

(100) Schauser, N. S.; Seshadri, R.; Segalman, R. A. Multivalent Ion Conduction in Solid Polymer Systems. *Molecular Systems Design & Engineering* **2019**, *4* (2), 263–279. https://doi.org/10.1039/C8ME00096D.

(101) Klett, M.; Giesecke, M.; Nyman, A.; Hallberg, F.; Lindström, R. W.; Lindbergh, G.; Furó, I. Quantifying Mass Transport during Polarization in a Li Ion Battery Electrolyte by in Situ 7Li NMR Imaging. *J. Am. Chem. Soc.* **2012**, *134* (36), 14654–14657. https://doi.org/10.1021/ja305461j.

(102) Thomas, E. M.; Popere, B. C.; Fang, H.; Chabinyc, M. L.; Segalman, R. A. Role of Disorder Induced by Doping on the Thermoelectric Properties of Semiconducting Polymers. *Chem. Mater.* **2018**, *30* (9), 2965–2972. https://doi.org/10.1021/acs.chemmater.8b00394.

(103) Choi, J.-H.; Xie, W.; Gu, Y.; Frisbie, C. D.; Lodge, T. P. Single Ion Conducting, Polymerized Ionic Liquid Triblock Copolymer Films: High Capacitance Electrolyte Gates for n-Type Transistors. *ACS Appl. Mater. Interfaces* **2015**, *7* (13), 7294–7302. https://doi.org/10.1021/acsami.5b00495.

(104) Prigodin, V. N.; Hsu, F. C.; Park, J. H.; Waldmann, O.; Epstein, A. J. Electron-Ion Interaction in Doped Conducting Polymers. *Phys. Rev. B* **2008**, *78* (3), 035203. https://doi.org/10.1103/PhysRevB.78.035203.

(105) Moia, D.; Giovannitti, A.; Szumska, A. A.; Maria, I. P.; Rezasoltani, E.; Sachs, M.; Schnurr, M.; Barnes, P. R. F.; McCulloch, I.; Nelson, J. Design and Evaluation of Conjugated Polymers with Polar Side Chains as Electrode Materials for Electrochemical Energy Storage in Aqueous Electrolytes. *Energy Environ. Sci.* **2019**, *12* (4), 1349–1357. https://doi.org/10.1039/C8EE03518K.

(106) Christie, A. M.; Lilley, S. J.; Staunton, E.; Andreev, Y. G.; Bruce, P. G. Increasing the Conductivity of Crystalline Polymer Electrolytes. *Nature* **2005**, *433* (7021), 50–53. https://doi.org/10.1038/nature03186.

(107) Beckingham, B. S.; Ho, V.; Segalman, R. A. Formation of a Rigid Amorphous Fraction in Poly(3-(2′-Ethyl)Hexylthiophene). *ACS Macro Lett.* **2014**, *3* (7), 684–688. https://doi.org/10.1021/mz500262d.

(108) Martín, J.; Stingelin, N.; Cangialosi, D. Direct Calorimetric Observation of the Rigid Amorphous Fraction in a Semiconducting Polymer. *J. Phys. Chem. Lett.* **2018**, *9* (5), 990–995. https://doi.org/10.1021/acs.jpclett.7b03110.

(109) Thomas, E. M.; Peterson, K. A.; Balzer, A.; Rawlings, D.; Stingelin, N.; Segalman, R. A.; Chabinyc, M. L. Effects of Counter-Ion Size on Delocalization of Carriers and Stability of Doped Semiconducting Polymers. *Submitted.* **2020**.

(110) Kiefer, D.; Kroon, R.; Hofmann, A. I.; Sun, H.; Liu, X.; Giovannitti, A.; Stegerer, D.; Cano, A.; Hynynen, J.; Yu, L.; Zhang, Y.; Nai, D.; Harrelson, T. F.; Sommer, M.; Moulé, A. J.; Kemerink, M.; Marder, S. R.; McCulloch, I.; Fahlman, M.; Fabiano, S.; Müller, C. Double Doping of Conjugated Polymers with Monomer Molecular Dopants. *Nature Materials* **2019**, *18* (2), 149–155. https://doi.org/10.1038/s41563-018-0263-6.

(111) Mazaheripour, A.; Thomas, E. M.; Segalman, R. A.; Chabinyc, M. L. Nonaggregating Doped Polymers Based on Poly(3,4-Propylenedioxythiophene). *Macromolecules* **2019**, *52* (5), 2203–2213. https://doi.org/10.1021/acs.macromol.8b02389.

(112) Wen, H.-F.; Wu, H.-C.; Aimi, J.; Hung, C.-C.; Chiang, Y.-C.; Kuo, C.-C.; Chen, W.-C. Soft Poly(Butyl Acrylate) Side Chains toward Intrinsically Stretchable Polymeric Semiconductors for Field-Effect Transistor Applications. *Macromolecules* **2017**, *50* (13), 4982–4992. https://doi.org/10.1021/acs.macromol.7b00860.

(113) Ashizawa, M.; Zheng, Y.; Tran, H.; Bao, Z. Intrinsically Stretchable Conjugated Polymer Semiconductors in Field Effect Transistors. *Progress in Polymer Science* **2019**, 101181. https://doi.org/10.1016/j.progpolymsci.2019.101181.

(114) Kelly, T.; Ghadi, B. M.; Berg, S.; Ardebili, H. In Situ Study of Strain-Dependent Ion Conductivity of Stretchable Polyethylene Oxide Electrolyte. *Scientific Reports* **2016**, *6* (1), 1–9. https://doi.org/10.1038/srep20128.

(115) Reynolds, V. G.; Oh, S.; Xie, R.; Chabinyc, M. L. Model for the Electro-Mechanical Behavior of Elastic Organic Transistors. *J. Mater. Chem. C* **2020**. https://doi.org/10.1039/D0TC01181A.

(116) Jacobs, I. E.; Moulé, A. J. Controlling Molecular Doping in Organic Semiconductors. *Advanced Materials* **2017**, *29* (42), 1703063. https://doi.org/10.1002/adma.201703063.

(117) Zokaei, S.; Kim, D.; Järsvall, E.; Fenton, A. M.; Weisen, A. R.; Hultmark, S.; Nguyen, P. H.; Matheson, A. M.; Lund, A.; Kroon, R.; Chabinyc, M. L.; Enrique, G. D.; Zozoulenko, I.; Müller, C. Tuning of the Elastic Modulus of a Soft Polythiophene

through Molecular Doping. *Materials Horizons* **2022**, *9* (1), 433–443. https://doi.org/10.1039/D1MH01079D.

(118) Lim, E.; Glaudell, A. M.; Miller, R.; Chabinyc, M. L. The Role of Ordering on the Thermoelectric Properties of Blends of Regioregular and Regiorandom Poly(3-Hexylthiophene). *Advanced Electronic Materials* **2019**, *5* (11), 1800915. https://doi.org/10.1002/aelm.201800915.

(119) Cendra, C.; Giovannitti, A.; Savva, A.; Venkatraman, V.; McCulloch, I.; Salleo, A.; Inal, S.; Rivnay, J. Role of the Anion on the Transport and Structure of Organic Mixed Conductors. *Advanced Functional Materials* **2019**, *29* (5), 1807034. https://doi.org/10.1002/adfm.201807034.

(120) Li, J.; Koshnick, C.; Diallo, S. O.; Ackling, S.; Huang, D. M.; Jacobs, I. E.; Harrelson, T. F.; Hong, K.; Zhang, G.; Beckett, J.; Mascal, M.; Moulé, A. J. Quantitative Measurements of the Temperature-Dependent Microscopic and Macroscopic Dynamics of a Molecular Dopant in a Conjugated Polymer. *Macromolecules* **2017**, *50* (14), 5476–5489. https://doi.org/10.1021/acs.macromol.7b00672.

(121) E. Jacobs, I.; W. Aasen, E.; L. Oliveira, J.; N. Fonseca, T.; D. Roehling, J.; Li, J.; Zhang, G.; P. Augustine, M.; Mascal, M.; J. Moulé, A. Comparison of Solution-Mixed and Sequentially Processed P3HT:F4TCNQ Films: Effect of Doping-Induced Aggregation on Film Morphology. *Journal of Materials Chemistry C* **2016**, *4* (16), 3454–3466. https://doi.org/10.1039/C5TC04207K.

(122) Lim, E.; Peterson, K. A.; Su, G. M.; Chabinyc, M. L. Thermoelectric Properties of Poly(3-Hexylthiophene) (P3HT) Doped with 2,3,5,6-Tetrafluoro-7,7,8,8-Tetracyanoquinodimethane (F4TCNQ) by Vapor-Phase Infiltration. *Chem. Mater.* **2018**, *30* (3), 998–1010. https://doi.org/10.1021/acs.chemmater.7b04849.

(123) DiTusa, M. F.; Grocke, G. L.; Ma, T.; Patel, S. N. Probing the Evolution of Conductivity and Structural Changes in Vapor-F4TCNQ Doped P3HT. *Mol. Syst. Des. Eng.* **2022**, *7* (7), 788–797. https://doi.org/10.1039/D1ME00192B.

(124) Dai, A.; Wan, A.; Magee, C.; Zhang, Y.; Barlow, S.; Marder, S. R.; Kahn, A. Investigation of P-Dopant Diffusion in Polymer Films and Bulk Heterojunctions: Stable Spatially-Confined Doping for All-Solution Processed Solar Cells. *Organic Electronics* **2015**, *23*, 151–157. https://doi.org/10.1016/j.orgel.2015.04.023.

(125) Reiser, P.; Müller, L.; Sivanesan, V.; Lovrincic, R.; Barlow, S.; Marder, S. R.; Pucci, A.; Jaegermann, W.; Mankel, E.; Beck, S. Dopant Diffusion in Sequentially Doped Poly(3-Hexylthiophene) Studied by Infrared and Photoelectron Spectroscopy. *J. Phys. Chem. C* **2018**, *122* (26), 14518–14527. https://doi.org/10.1021/acs.jpcc.8b02657.

(126) Kolesov, V. A.; Fuentes-Hernandez, C.; Chou, W.-F.; Aizawa, N.; Larrain, F. A.; Wang, M.; Perrotta, A.; Choi, S.; Graham, S.; Bazan, G. C.; Nguyen, T.-Q.; Marder, S. R.; Kippelen, B. Solution-Based Electrical Doping of Semiconducting Polymer Films over a Limited Depth. *Nature Mater* **2017**, *16* (4), 474–480. https://doi.org/10.1038/nmat4818.

(127) Thomas, E. M.; Peterson, K. A.; Balzer, A. H.; Rawlings, D.; Stingelin, N.; Segalman, R. A.; Chabinyc, M. L. Effects of Counter-Ion Size on Delocalization of Carriers and Stability of Doped Semiconducting Polymers. *Advanced Electronic Materials* **2020**, *6* (12), 2000595. https://doi.org/10.1002/aelm.202000595.

(128) Fontana, M. T.; Stanfield, D. A.; Scholes, D. T.; Winchell, K. J.; Tolbert, S. H.; Schwartz, B. J. Evaporation vs Solution Sequential Doping of Conjugated Polymers:

F4TCNQ Doping of Micrometer-Thick P3HT Films for Thermoelectrics. *J. Phys. Chem. C* **2019**, *123* (37), 22711–22724. https://doi.org/10.1021/acs.jpcc.9b05069.

(129) Yu, L.; Scheunemann, D.; Lund, A.; Kiefer, D.; Müller, C. Sequential Doping of Solid Chunks of a Conjugated Polymer for Body-Heat-Powered Thermoelectric Modules. *Appl. Phys. Lett.* **2021**, *119* (18), 181902. https://doi.org/10.1063/5.0075789.

(130) Poverenov, E.; Zamoshchik, N.; Patra, A.; Ridelman, Y.; Bendikov, M. Unusual Doping of Donor–Acceptor-Type Conjugated Polymers Using Lewis Acids. *J. Am. Chem. Soc.* **2014**, *136* (13), 5138–5149. https://doi.org/10.1021/ja501024n.

(131) Simón Marqués, P.; Londi, G.; Yurash, B.; Nguyen, T.-Q.; Barlow, S.; R. Marder, S.; Beljonne, D. Understanding How Lewis Acids Dope Organic Semiconductors: A “Complex” Story. *Chemical Science* **2021**, *12* (20), 7012–7022. https://doi.org/10.1039/D1SC01268A.

(132) Han, C. C.; Elsenbaumer, R. L. Protonic Acids: Generally Applicable Dopants for Conducting Polymers. *Synthetic Metals* **1989**, *30* (1), 123–131. https://doi.org/10.1016/0379-6779(89)90648-6.

(133) Bridges, C. R.; Baumgartner, T. Lewis Acids and Bases as Molecular Dopants for Organic Semiconductors. *Journal of Physical Organic Chemistry* **2020**, *33* (9), e4077. https://doi.org/10.1002/poc.4077.

(134) Suh, E. H.; Oh, J. G.; Jung, J.; Noh, S. H.; Lee, T. S.; Jang, J. Brønsted Acid Doping of P3HT with Largely Soluble Tris(Pentafluorophenyl)Borane for Highly Conductive and Stable Organic Thermoelectrics Via One-Step Solution Mixing. *Advanced Energy Materials* **2020**, *10* (47), 2002521. https://doi.org/10.1002/aenm.202002521.

(135) Gregory, S. A.; Li, Y.; Monroe, T. D.; Li, J.; Yee, S. K.; Losego, M. D. Vapor Phase Infiltration Doping of the Semiconducting Polymer Poly(Aniline) with TiCl4 + H2O: Mechanisms, Reaction Kinetics, and Electrical and Optical Properties. *ACS Appl. Polym. Mater.* **2021**, *3* (2), 720–729. https://doi.org/10.1021/acsapm.0c01014.

(136) Arvind, M.; Tait, C. E.; Guerrini, M.; Krumland, J.; Valencia, A. M.; Cocchi, C.; Mansour, A. E.; Koch, N.; Barlow, S.; Marder, S. R.; Behrends, J.; Neher, D. Quantitative Analysis of Doping-Induced Polarons and Charge-Transfer Complexes of Poly(3-Hexylthiophene) in Solution. *J. Phys. Chem. B* **2020**, *124* (35), 7694–7708. https://doi.org/10.1021/acs.jpcb.0c03517.

(137) Pallini, F.; Mattiello, S.; Manfredi, N.; Mecca, S.; Fedorov, A.; Sassi, M.; Kurdi, K. A.; Ding, Y.-F.; Pan, C.-K.; Pei, J.; Barlow, S.; Marder, S. R.; Nguyen, T.-Q.; Beverina, L. Direct Detection of Molecular Hydrogen upon P- and n-Doping of Organic Semiconductors with Complex Oxidants or Reductants. *J. Mater. Chem. A* **2023**, *11* (15), 8192–8201. https://doi.org/10.1039/D3TA00231D.

(138) Raamat, E.; Kaupmees, K.; Ovsjannikov, G.; Trummal, A.; Kütt, A.; Saame, J.; Koppel, I.; Kaljurand, I.; Lipping, L.; Rodima, T.; Pihl, V.; Koppel, I. A.; Leito, I. Acidities of Strong Neutral Brønsted Acids in Different Media. *Journal of Physical Organic Chemistry* **2013**, *26* (2), 162–170. https://doi.org/10.1002/poc.2946.

(139) Aguirre, J. C.; Hawks, S. A.; Ferreira, A. S.; Yee, P.; Subramaniyan, S.; Jenekhe, S. A.; Tolbert, S. H.; Schwartz, B. J. Sequential Processing for Organic Photovoltaics: Design Rules for Morphology Control by Tailored Semi-Orthogonal Solvent Blends. *Advanced Energy Materials* **2015**, *5* (11), 1402020. https://doi.org/10.1002/aenm.201402020.

(140) Scholes, D. T.; Yee, P. Y.; Lindemuth, J. R.; Kang, H.; Onorato, J.; Ghosh, R.; Luscombe, C. K.; Spano, F. C.; Tolbert, S. H.; Schwartz, B. J. The Effects of Crystallinity on Charge Transport and the Structure of Sequentially Processed F4TCNQ-Doped Conjugated Polymer Films. *Advanced Functional Materials* **2017**, *27* (44), 1702654. https://doi.org/10.1002/adfm.201702654.

(141) Melander, L.; Saunders, W. H. *Reaction Rates of Isotopic Molecules*; Wiley, 1980.

(142) Jhulki, S.; Un, H.-I.; Ding, Y.-F.; Risko, C.; Mohapatra, S. K.; Pei, J.; Barlow, S.; Marder, S. R. Reactivity of an Air-Stable Dihydrobenzoimidazole n-Dopant with Organic Semiconductor Molecules. *Chem* **2021**, *7* (4), 1050–1065. https://doi.org/10.1016/j.chempr.2021.01.020.

(143) Maliakal, A. J. Characterization of Dopant Diffusion within Semiconducting Polymer and Small-Molecule Films Using Infrared-Active Vibrational Modes and Attenuated Total Reflectance Infrared Spectroscopy. *ACS Appl. Mater. Interfaces* **2013**, *5* (17), 8300–8307. https://doi.org/10.1021/am401799k.

(144) Vijayakumar, V.; Zaborova, E.; Biniek, L.; Zeng, H.; Herrmann, L.; Carvalho, A.; Boyron, O.; Leclerc, N.; Brinkmann, M. Effect of Alkyl Side Chain Length on Doping Kinetics, Thermopower, and Charge Transport Properties in Highly Oriented F4TCNQ-Doped PBTTT Films. *ACS Appl. Mater. Interfaces* **2019**, *11* (5), 4942–4953. https://doi.org/10.1021/acsami.8b17594.

(145) Zhong, Y.; Untilova, V.; Muller, D.; Guchait, S.; Kiefer, C.; Herrmann, L.; Zimmermann, N.; Brosset, M.; Heiser, T.; Brinkmann, M. Preferential Location of Dopants in the Amorphous Phase of Oriented Regioregular Poly(3-Hexylthiophene-2,5-Diyl) Films Helps Reach Charge Conductivities of 3000 S Cm−1. *Advanced Functional Materials* **2022**, *32* (30), 2202075. https://doi.org/10.1002/adfm.202202075.

(146) Aguirre, A.; Gast, P.; Orlinskii, S.; Akimoto, I.; Groenen, E. J. J.; Mkami, H. E.; Goovaerts, E.; Doorslaer, S. V. Multifrequency EPR Analysis of the Positive Polaron in I2-Doped Poly(3-Hexylthiophene) and in Poly[2-Methoxy-5-(3,7-Dimethyloctyloxy)]-1,4-Phenylenevinylene. *Phys. Chem. Chem. Phys.* **2008**, *10* (47), 7129–7138. https://doi.org/10.1039/B811419F.

(147) Deline, V. R.; Katz, W.; Evans, C. A.; Williams, P. Mechanism of the SIMS Matrix Effect. *Appl. Phys. Lett.* **1978**, *33* (9), 832–835. https://doi.org/10.1063/1.90546.

(148) Surana, S.; Conard, T.; Fleischmann, C.; Tait, J. G.; Bastos, J. P.; Voroshazi, E.; Havelund, R.; Turbiez, M.; Louette, P.; Felten, A.; Poleunis, C.; Delcorte, A.; Vandervorst, W. Understanding Physico-Chemical Aspects in the Depth Profiling of Polymer:Fullerene Layers. *J. Phys. Chem. C* **2016**, *120* (49), 28074–28082. https://doi.org/10.1021/acs.jpcc.6b09911.

(149) Smentkowski, V. S.; Zorn, G.; Misner, A.; Parthasarathy, G.; Couture, A.; Tallarek, E.; Hagenhoff, B. ToF-SIMS Depth Profiling of Organic Solar Cell Layers Using an Ar Cluster Ion Source. *Journal of Vacuum Science & Technology A* **2013**, *31* (3), 030601. https://doi.org/10.1116/1.4793730.

(150) Kosco, J.; Sachs, M.; Godin, R.; Kirkus, M.; Francas, L.; Bidwell, M.; Qureshi, M.; Anjum, D.; Durrant, J. R.; McCulloch, I. The Effect of Residual Palladium Catalyst Contamination on the Photocatalytic Hydrogen Evolution Activity of Conjugated Polymers. *Advanced Energy Materials* **2018**, *8* (34), 1802181. https://doi.org/10.1002/aenm.201802181.

(151) Sachs, M.; Cha, H.; Kosco, J.; Aitchison, C. M.; Francàs, L.; Corby, S.; Chiang, C.-L.; Wilson, A. A.; Godin, R.; Fahey-Williams, A.; Cooper, A. I.; Sprick, R. S.; McCulloch, I.; Durrant, J. R. Tracking Charge Transfer to Residual Metal Clusters in Conjugated Polymers for Photocatalytic Hydrogen Evolution. *J. Am. Chem. Soc.* **2020**, *142* (34), 14574–14587. https://doi.org/10.1021/jacs.0c06104.

(152) Thomas, E. M.; Davidson, E. C.; Katsumata, R.; Segalman, R. A.; Chabinyc, M. L. Branched Side Chains Govern Counterion Position and Doping Mechanism in Conjugated Polythiophenes. *ACS Macro Lett.* **2018**, *7* (12), 1492–1497. https://doi.org/10.1021/acsmacrolett.8b00778.

(153) Patel, S. N.; Glaudell, A. M.; Kiefer, D.; Chabinyc, M. L. Increasing the Thermoelectric Power Factor of a Semiconducting Polymer by Doping from the Vapor Phase. *ACS Macro Lett.* **2016**, *5* (3), 268–272. https://doi.org/10.1021/acsmacrolett.5b00887.

(154) Kroon, R.; Hofmann, A. I.; Yu, L.; Lund, A.; Müller, C. Thermally Activated in Situ Doping Enables Solid-State Processing of Conducting Polymers. *Chem. Mater.* **2019**, *31* (8), 2770–2777. https://doi.org/10.1021/acs.chemmater.8b04895.

(155) Treat, N. D.; Mates, T. E.; Hawker, C. J.; Kramer, E. J.; Chabinyc, M. L. Temperature Dependence of the Diffusion Coefficient of PCBM in Poly(3-Hexylthiophene). *Macromolecules* **2013**, *46* (3), 1002–1007. https://doi.org/10.1021/ma302337p.

(156) Berriman, G. A.; Holdsworth, J. L.; Zhou, X.; Belcher, W. J.; Dastoor, P. C. Molecular versus Crystallite PCBM Diffusion in P3HT:PCBM Blends. *AIP Advances* **2015**, *5* (9), 097220. https://doi.org/10.1063/1.4932212.

(157) Cussler, E. L.; Cussler, E. L. *Diffusion: Mass Transfer in Fluid Systems*; Cambridge university press, 2009.

(158) Moulton, J.; Smith, P. Electrical and Mechanical Properties of Oriented Poly(3-Alkylthiophenes): 2. Effect of Side-Chain Length. *Polymer* **1992**, *33* (11), 2340–2347. https://doi.org/10.1016/0032-3861(92)90525-2.

(159) Hynynen, J.; Järsvall, E.; Kroon, R.; Zhang, Y.; Barlow, S.; Marder, S. R.; Kemerink, M.; Lund, A.; Müller, C. Enhanced Thermoelectric Power Factor of Tensile Drawn Poly(3-Hexylthiophene). *ACS Macro Lett.* **2019**, *8* (1), 70–76. https://doi.org/10.1021/acsmacrolett.8b00820.

(160) Dudenko, D.; Kiersnowski, A.; Shu, J.; Pisula, W.; Sebastiani, D.; Spiess, H. W.; Hansen, M. R. A Strategy for Revealing the Packing in Semicrystalline π-Conjugated Polymers: Crystal Structure of Bulk Poly-3-Hexyl-Thiophene (P3HT). *Angewandte Chemie International Edition* **2012**, *51* (44), 11068–11072. https://doi.org/10.1002/anie.201205075.

(161) Hofmann, A. I.; Kroon, R.; Yu, L.; Müller, C. Highly Stable Doping of a Polar Polythiophene through Co-Processing with Sulfonic Acids and Bistriflimide. *J. Mater. Chem. C* **2018**, *6* (26), 6905–6910. https://doi.org/10.1039/C8TC01593G.

(162) Thomas, E. Operando X-Ray Scattering Reveals Ion-Induced Structural Changes During Electrochemical Gating of Poly(3-Hexylthiophene), 2018.

(163) Liu, W.; Müller, L.; Ma, S.; Barlow, S.; Marder, S. R.; Kowalsky, W.; Köhn, A.; Lovrincic, R. Origin of the π–π Spacing Change upon Doping of Semiconducting Polymers. *J. Phys. Chem. C* **2018**, *122* (49), 27983–27990. https://doi.org/10.1021/acs.jpcc.8b10845.

(164) Joseph Kline, R.; McGehee, M. D.; Toney, M. F. Highly Oriented Crystals at the Buried Interface in Polythiophene Thin-Film Transistors. *Nature Mater* **2006**, *5* (3), 222–228. https://doi.org/10.1038/nmat1590.

(165) Jiang, Z.; Lee, D. R.; Narayanan, S.; Wang, J.; Sinha, S. K. Waveguide-Enhanced Grazing-Incidence Small-Angle x-Ray Scattering of Buried Nanostructures in Thin Films. *Phys. Rev. B* **2011**, *84* (7), 075440. https://doi.org/10.1103/PhysRevB.84.075440.

(166) Gann, E.; Caironi, M.; Noh, Y.-Y.; Kim, Y.-H.; McNeill, C. R. Diffractive X-Ray Waveguiding Reveals Orthogonal Crystalline Stratification in Conjugated Polymer Thin Films. *Macromolecules* **2018**, *51* (8), 2979–2987. https://doi.org/10.1021/acs.macromol.8b00168.

(167) Factor, B. J.; Russell, T. P.; Toney, M. F. Grazing Incidence X-Ray Scattering Studies of Thin Films of an Aromatic Polyimide. *Macromolecules* **1993**, *26* (11), 2847–2859. https://doi.org/10.1021/ma00063a033.

(168) Qian, W.; Texter, J.; Yan, F. Frontiers in Poly(Ionic Liquid)s: Syntheses and Applications. *Chem. Soc. Rev.* **2017**, *46* (4), 1124–1159. https://doi.org/10.1039/C6CS00620E.

(169) Ding, L.; Shi, J.; Yang, C.; Dong, S. Ionic Conductivity of Solid Polymer Electrolytes Based on Modified Alternating Maleic Anhydride Copolymer with Oligo(Oxyethylene) Side Chains. *Polym. J.* **1997**, *29* (5), 410–416. https://doi.org/10.1295/polymj.29.410.

(170) Andreozzi, L.; Galli, G.; Giordano, M.; Zulli, F. A Rheological Investigation of Entanglement in Side-Chain Liquid-Crystalline Azobenzene Polymethacrylates. *Macromolecules* **2013**, *46* (12), 5003–5017. https://doi.org/10.1021/ma400260n.

(171) Tong, X.; Wang, G.; Soldera, A.; Zhao, Y. How Can Azobenzene Block Copolymer Vesicles Be Dissociated and Reformed by Light? *J. Phys. Chem. B* **2005**, *109* (43), 20281–20287. https://doi.org/10.1021/jp0524274.

(172) Kumar, G. S.; Neckers, D. C. Photochemistry of Azobenzene-Containing Polymers. *Chem. Rev.* **1989**, *89* (8), 1915–1925. https://doi.org/10.1021/cr00098a012.

(173) Norikane, Y.; Uchida, E.; Tanaka, S.; Fujiwara, K.; Koyama, E.; Azumi, R.; Akiyama, H.; Kihara, H.; Yoshida, M. Photoinduced Crystal-to-Liquid Phase Transitions of Azobenzene Derivatives and Their Application in Photolithography Processes through a Solid–Liquid Patterning. *Org. Lett.* **2014**, *16* (19), 5012–5015. https://doi.org/10.1021/ol502223u.

(174) Nakayama, K.; Jiang, L.; Iyoda, T.; Hashimoto, K.; Fujishima, A. Photo-Induced Structural Transformation on the Surface of Azobenzene Crystals. *Jpn. J. Appl. Phys.* **1997**, *36* (6S), 3898. https://doi.org/10.1143/JJAP.36.3898.

(175) Bléger, D.; Schwarz, J.; Brouwer, A. M.; Hecht, S. O-Fluoroazobenzenes as Readily Synthesized Photoswitches Offering Nearly Quantitative Two-Way Isomerization with Visible Light. *J. Am. Chem. Soc.* **2012**, *134* (51), 20597–20600. https://doi.org/10.1021/ja310323y.

(176) Scheuermann, A. M.; Wakidi, H.; Lill, A. T.; Oh, S.; Llanes, L. C.; D’Ambra, C. A.; Antoine, S.; Wang, M.; Chabinyc, M. L.; Nguyen, T.-Q.; Read de Alaniz, J.; Bates, C. M. Multiwavelength Photodetectors Based on an Azobenzene Polymeric Ionic Liquid. *ACS Appl. Polym. Mater.* **2021**, *3* (10), 5125–5133. https://doi.org/10.1021/acsapm.1c00884.

(177) Li, Z.; Yuan, X.; Feng, Y.; Chen, Y.; Zhao, Y.; Wang, H.; Xu, Q.; Wang, J. A Reversible Conductivity Modulation of Azobenzene-Based Ionic Liquids in Aqueous

Solutions Using UV/Vis Light. *Phys. Chem. Chem. Phys.* **2018**, *20* (18), 12808–12816. https://doi.org/10.1039/C8CP01617H.

(178) Kang, N.; Li, P.; Tan, S.; Wang, C. Azobenzene Based Inorganic Salts for Light Modulated Ionic Conductivity in Aqueous Solution. *Soft Matter* **2019**, *15* (40), 7992–7995. https://doi.org/10.1039/C9SM01411J.

(179) Wei, S.; Zhang, Z.; Dong, W.; Liang, T.; Ji, J.; Tian, W.; Tan, S.; Zhao, Q.; Wang, C.; Wu, Y. Specific Ion Effects of Azobenzene Salts on Photoresponse of PNIPAm in Aqueous Solutions. *Macromol. Rapid Commun.* **2021**, *42* (16), 2100232. https://doi.org/10.1002/marc.202100232.

(180) Ichimura, K. Reversible Photoisomerisability and Particle Size Changes of Mill-Dispersed Azobenzene Crystals in Water. *Chem. Commun.* **2009**, No. 12, 1496–1498. https://doi.org/10.1039/B820022J.

(181) Yamamoto, T.; Norikane, Y.; Akiyama, H. Photochemical Liquefaction and Softening in Molecular Materials, Polymers, and Related Compounds. *Polym. J.* **2018**, *50* (8), 551–562. https://doi.org/10.1038/s41428-018-0064-4.

(182) Zhou, H.; Xue, C.; Weis, P.; Suzuki, Y.; Huang, S.; Koynov, K.; Auernhammer, G. K.; Berger, R.; Butt, H.-J.; Wu, S. Photoswitching of Glass Transition Temperatures of Azobenzene-Containing Polymers Induces Reversible Solid-to-Liquid Transitions. *Nat. Chem.* **2017**, *9* (2), 145–151. https://doi.org/10.1038/nchem.2625.

(183) Shang, C.; Xiong, Z.; Liu, S.; Yu, W. Molecular Dynamics of Azobenzene Polymer with Photoreversible Glass Transition. *Macromolecules* **2022**, *55* (9), 3711–3722. https://doi.org/10.1021/acs.macromol.2c00073.

(184) Nanasawa, M.; Nishiyama, T.; Kamogawa, H. Synthesis and Photoregulated Metal Coordination of Azobenzene Polymer Having Ion Binding Sites. *Polym. J.* **1991**, *23* (2), 127–134. https://doi.org/10.1295/polymj.23.127.

(185) Nanasawa, M.; Horikago, Y.; Hirai, M. Photo-Regulated Metal Coordination of Azobenzene Polymer Having Sterically Controlled Ion Binding Sites. *Polym. Bull.* **1995**, *35* (1), 103–108. https://doi.org/10.1007/BF00312900.

(186) Yang, Y.; Hughes, R. P.; Aprahamian, I. Near-Infrared Light Activated Azo-BF2 Switches. *J. Am. Chem. Soc.* **2014**, *136* (38), 13190–13193. https://doi.org/10.1021/ja508125n.

(187) Tylkowski, B.; Jastrząb, R.; Skrobańska, M. Photo-Sensitive Complexes Based on Azobenzene. *Physical Sciences Reviews* **2016**, *1* (4). https://doi.org/10.1515/psr-2016-0002.

(188) Bazhenova, T. A.; Emelyanova, N. S.; Shestakov, A. F.; Shilov, A. E.; Antipin, M. Yu.; Lyssenko, K. A. Molecular Structure and Reactions of Azobenzene Complexes with Iron-Lithium Compounds. *Inorganica Chimica Acta* **1998**, *280* (1), 288–294. https://doi.org/10.1016/S0020-1693(98)00177-7.

(189) Oka, Y.; Tamaoki, N. Structure of Silver(I) Complex Prepared from Azobenzenonaphthalenophane, Photochemical Coordination Change of Silver(I) and Silver(I)-Induced Acceleration of Z−E Thermal Isomerization of Azobenzene Unit. *Inorg. Chem.* **2010**, *49* (11), 4765–4767. https://doi.org/10.1021/ic100317p.

(190) Markiewicz, G.; Walczak, A.; Perlitius, F.; Piasecka, M.; M. Harrowfield, J.; R. Stefankiewicz, A. Photoswitchable Transition Metal Complexes with Azobenzene-Functionalized Imine-Based Ligands: Structural and Kinetic Analysis. *Dalton Transactions* **2018**, *47* (40), 14254–14262. https://doi.org/10.1039/C8DT00590G.

(191) Yamamura, M.; Yamakawa, K.; Okazaki, Y.; Nabeshima, T. Coordination-Driven Macrocyclization for Locking of Photo- and Thermal Cis→trans Isomerization of Azobenzene. *Chemistry – A European Journal* **2014**, *20* (49), 16258–16265. https://doi.org/10.1002/chem.201404620.

(192) Tazuke, S.; Kurihara, S.; Ikeda, T. Amplified Image Recording in Liquid Crystal Media by Means of Photochemically Triggered Phase Transition. *Chem. Lett.* **1987**, *16* (5), 911–914. https://doi.org/10.1246/cl.1987.911.

(193) Weis, P.; Wu, S. Light-Switchable Azobenzene-Containing Macromolecules: From UV to Near Infrared. *Macromol. Rapid Commun.* **2018**, *39* (1), 1700220. https://doi.org/10.1002/marc.201700220.

(194) Theato, P. Synthesis of Well-Defined Polymeric Activated Esters. *J. Polym. Sci. A Polym. Chem.* **2008**, *46* (20), 6677–6687. https://doi.org/10.1002/pola.22994.

(195) Suga, T.; Aoki, K.; Yashiro, T.; Nishide, H. "Click" Incorporation of Radical/Ionic Sites into a Reactive Block Copolymer: A Facile and On-Demand Domain Functionalization Approach toward Organic Resistive Memory. *Macromol. Rapid Commun.* **2016**, *37* (1), 53–59. https://doi.org/10.1002/marc.201500492.

(196) Bandara, H. M. D.; Burdette, S. C. Photoisomerization in Different Classes of Azobenzene. *Chem. Soc. Rev.* **2012**, *41* (5), 1809–1825. https://doi.org/10.1039/C1CS15179G.

(197) Dyck, R. H.; McClure, D. S. Ultraviolet Spectra of Stilbene, p-Monohalogen Stilbenes, and Azobenzene and the Trans to Cis Photoisomerization Process. *J. Chem. Phys.* **1962**, *36* (9), 2326–2345. https://doi.org/10.1063/1.1732885.

(198) Yue, Y.; Norikane, Y.; Azumi, R.; Koyama, E. Light-Induced Mechanical Response in Crosslinked Liquid-Crystalline Polymers with Photoswitchable Glass Transition Temperatures. *Nat Commun* **2018**, *9* (1), 3234. https://doi.org/10.1038/s41467-018-05744-x.

(199) Kuenstler, A. S.; Clark, K. D.; Read de Alaniz, J.; Hayward, R. C. Reversible Actuation via Photoisomerization-Induced Melting of a Semicrystalline Poly(Azobenzene). *ACS Macro Lett.* **2020**, *9* (6), 902–909. https://doi.org/10.1021/acsmacrolett.0c00328.

(200) Vetráková, L.; Ladányi, V.; Al Anshori, J.; Dvořák, P.; Wirz, J.; Heger, D. The Absorption Spectrum of Cis-Azobenzene. *Photochem Photobiol Sci* **2017**, *16* (12), 1749–1756. https://doi.org/10.1039/c7pp00314e.

(201) Weis, P.; Tian, W.; Wu, S. Photoinduced Liquefaction of Azobenzene-Containing Polymers. *Chemistry – A European Journal* **2018**, *24* (25), 6494–6505. https://doi.org/10.1002/chem.201704162.

(202) Ishiba, K.; Morikawa, M.; Chikara, C.; Iwase, K.; Kawakita, M.; Kimizuka, N. Photoliquefiable Ionic Crystals: A Phase Crossover Approach for Photon Energy Storage Materials with Functional Multiplicity. **2015**, *54* (5), 1532–1536.

(203) Stumpel, J. E.; Liu, D.; Broer, D. J.; Schenning, A. P. H. J. Photoswitchable Hydrogel Surface Topographies by Polymerisation-Induced Diffusion. *Eur. J. Chem.* **2013**, *19* (33), 10922–10927. https://doi.org/10.1002/chem.201300852.

(204) Das, A.; Theato, P. Multifaceted Synthetic Route to Functional Polyacrylates by Transesterification of Poly(Pentafluorophenyl Acrylates). *Macromolecules* **2015**, *48* (24), 8695–8707. https://doi.org/10.1021/acs.macromol.5b02293.

(205) Jaacks, V. Novel Method of Determination of Reactivity Ratios in Binary and Ternary Copolymerizations. *Makromol. Chem.* **1972**, *161* (1), 161–172. https://doi.org/10.1002/macp.1972.021610110.

(206) Sharon, D.; Bennington, P.; Liu, C.; Kambe, Y.; Dong, B. X.; Burnett, V. F.; Dolejsi, M.; Grocke, G.; Patel, S. N.; Nealey, P. F. Interrogation of Electrochemical Properties of Polymer Electrolyte Thin Films with Interdigitated Electrodes. *J. Electrochem. Soc.* **2018**, *165* (16), H1028. https://doi.org/10.1149/2.0291816jes.

(207) Tong, X.; Pelletier, M.; Lasia, A.; Zhao, Y. Fast Cis–Trans Isomerization of an Azobenzene Derivative in Liquids and Liquid Crystals under a Low Electric Field. *Angewandte Chemie International Edition* **2008**, *47* (19), 3596–3599. https://doi.org/10.1002/anie.200705699.

(208) Goulet-Hanssens, A.; Utecht, M.; Mutruc, D.; Titov, E.; Schwarz, J.; Grubert, L.; Bléger, D.; Saalfrank, P.; Hecht, S. Electrocatalytic Z → E Isomerization of Azobenzenes. *J. Am. Chem. Soc.* **2017**, *139* (1), 335–341. https://doi.org/10.1021/jacs.6b10822.

(209) Arkhipov, V. I.; Heremans, P.; Emelianova, E. V.; Bässler, H. Effect of Doping on the Density-of-States Distribution and Carrier Hopping in Disordered Organic Semiconductors. *Phys. Rev. B* **2005**, *71* (4), 045214. https://doi.org/10.1103/PhysRevB.71.045214.

(210) Litofsky, J. H.; Lee, Y.; Aplan, M. P.; Kuei, B.; Hexemer, A.; Wang, C.; Wang, Q.; Gomez, E. D. Polarized Soft X-Ray Scattering Reveals Chain Orientation within Nanoscale Polymer Domains. *Macromolecules* **2019**, *52* (7), 2803–2813. https://doi.org/10.1021/acs.macromol.8b02198.

(211) Jacobs, I. E.; D’Avino, G.; Lemaur, V.; Lin, Y.; Huang, Y.; Chen, C.; Harrelson, T. F.; Wood, W.; Spalek, L. J.; Mustafa, T.; O’Keefe, C. A.; Ren, X.; Simatos, D.; Tjhe, D.; Statz, M.; Strzalka, J. W.; Lee, J.-K.; McCulloch, I.; Fratini, S.; Beljonne, D.; Sirringhaus, H. Structural and Dynamic Disorder, Not Ionic Trapping, Controls Charge Transport in Highly Doped Conducting Polymers. *J. Am. Chem. Soc.* **2022**, *144* (7), 3005–3019. https://doi.org/10.1021/jacs.1c10651.

(212) Lim, E.; Glaudell, A. M.; Miller, R.; Chabinyc, M. L. The Role of Ordering on the Thermoelectric Properties of Blends of Regioregular and Regiorandom Poly(3-Hexylthiophene). *Advanced Electronic Materials* **2019**, *5* (11), 1800915. https://doi.org/10.1002/aelm.201800915.

(213) Rivnay, J.; Noriega, R.; Kline, R. J.; Salleo, A.; Toney, M. F. Quantitative Analysis of Lattice Disorder and Crystallite Size in Organic Semiconductor Thin Films. *Phys. Rev. B* **2011**, *84* (4), 045203. https://doi.org/10.1103/PhysRevB.84.045203.

(214) Watts, K. E.; Neelamraju, B.; Ratcliff, E. L.; Pemberton, J. E. Stability of Charge Transfer States in F4TCNQ-Doped P3HT. *Chem. Mater.* **2019**, *31* (17), 6986–6994. https://doi.org/10.1021/acs.chemmater.9b01549.

(215) Valencia, A. M.; Cocchi, C. Electronic and Optical Properties of Oligothiophene-F4TCNQ Charge-Transfer Complexes: The Role of the Donor Conjugation Length. *J. Phys. Chem. C* **2019**, *123* (14), 9617–9623. https://doi.org/10.1021/acs.jpcc.9b01390.

(216) Neelamraju, B.; Watts, K. E.; Pemberton, J. E.; Ratcliff, E. L. Correlation of Coexistent Charge Transfer States in F4TCNQ-Doped P3HT with Microstructure. *J. Phys. Chem. Lett.* **2018**, *9* (23), 6871–6877. https://doi.org/10.1021/acs.jpclett.8b03104.

(217) Untilova, V.; Zeng, H.; Durand, P.; Herrmann, L.; Leclerc, N.; Brinkmann, M. Intercalation and Ordering of F6TCNNQ and F4TCNQ Dopants in Regioregular Poly(3-Hexylthiophene) Crystals: Impact on Anisotropic Thermoelectric Properties of Oriented Thin Films. *Macromolecules* **2021**, *54* (13), 6073–6084. https://doi.org/10.1021/acs.macromol.1c00554.

(218) Giridharagopal, R.; Flagg, L. Q.; Harrison, J. S.; Ziffer, M. E.; Onorato, J.; Luscombe, C. K.; Ginger, D. S. Electrochemical Strain Microscopy Probes Morphology-Induced Variations in Ion Uptake and Performance in Organic Electrochemical Transistors. *Nature Mater* **2017**, *16* (7), 737–742. https://doi.org/10.1038/nmat4918.

(219) Flagg, L. Q.; Onorato, J. W.; Luscombe, C. K.; Bhat, V.; Risko, C.; Levy-Wendt, B.; Toney, M. F.; McNeill, C. R.; Freychet, G.; Zhernenkov, M.; Li, R.; Richter, L. J. Resonant X-Ray Diffraction Reveals the Location of Counterions in Doped Organic Mixed Ionic Conductors. *Chem. Mater.* **2023**, *35* (10), 3960–3967. https://doi.org/10.1021/acs.chemmater.3c00180.

(220) Jackson, S. R.; Kingsford, R. L.; Collins, G. W.; Bischak, C. G. Crystallinity Determines Ion Injection Kinetics and Local Ion Density in Organic Mixed Conductors. *Chem. Mater.* **2023**. https://doi.org/10.1021/acs.chemmater.3c00657.

(221) Scholes, D. T.; Yee, P. Y.; Lindemuth, J. R.; Kang, H.; Onorato, J.; Ghosh, R.; Luscombe, C. K.; Spano, F. C.; Tolbert, S. H.; Schwartz, B. J. The Effects of Crystallinity on Charge Transport and the Structure of Sequentially Processed F4TCNQ-Doped Conjugated Polymer Films. *Advanced Functional Materials* **2017**, *27* (44), 1702654. https://doi.org/10.1002/adfm.201702654.

(222) Duong, D. T.; Wang, C.; Antono, E.; Toney, M. F.; Salleo, A. The Chemical and Structural Origin of Efficient P-Type Doping in P3HT. *Organic Electronics* **2013**, *14* (5), 1330–1336. https://doi.org/10.1016/j.orgel.2013.02.028.

(223) Gao, J.; Niles, E. T.; Grey, J. K. Aggregates Promote Efficient Charge Transfer Doping of Poly(3-Hexylthiophene). *J. Phys. Chem. Lett.* **2013**, *4* (17), 2953–2957. https://doi.org/10.1021/jz401555x.

(224) Harris, J. K.; Neelamraju, B.; Ratcliff, E. L. Intersystem Subpopulation Charge Transfer and Conformational Relaxation Preceding in Situ Conductivity in Electrochemically Doped Poly(3-Hexylthiophene) Electrodes. *Chem. Mater.* **2019**, *31* (17), 6870–6879. https://doi.org/10.1021/acs.chemmater.9b01298.

(225) Cochran, J. E.; Junk, M. J. N.; Glaudell, A. M.; Miller, P. L.; Cowart, J. S.; Toney, M. F.; Hawker, C. J.; Chmelka, B. F.; Chabinyc, M. L. Molecular Interactions and Ordering in Electrically Doped Polymers: Blends of PBTTT and F4TCNQ. *Macromolecules* **2014**, *47* (19), 6836–6846. https://doi.org/10.1021/ma501547h.

(226) Jacobs, I. E.; Lin, Y.; Huang, Y.; Ren, X.; Simatos, D.; Chen, C.; Tjhe, D.; Statz, M.; Lai, L.; Finn, P. A.; Neal, W. G.; D'Avino, G.; Lemaur, V.; Fratini, S.; Beljonne, D.; Strzalka, J.; Nielsen, C. B.; Barlow, S.; Marder, S. R.; McCulloch, I.; Sirringhaus, H. High-Efficiency Ion-Exchange Doping of Conducting Polymers. *Advanced Materials* **2022**, *34* (22), 2102988. https://doi.org/10.1002/adma.202102988.

(227) Untilova, V.; Biskup, T.; Biniek, L.; Vijayakumar, V.; Brinkmann, M. Control of Chain Alignment and Crystallization Helps Enhance Charge Conductivities and Thermoelectric Power Factors in Sequentially Doped P3HT:F4TCNQ Films. *Macromolecules* **2020**, *53* (7), 2441–2453. https://doi.org/10.1021/acs.macromol.9b02389.

(228) Hynynen, J.; Kiefer, D.; Müller, C. Influence of Crystallinity on the Thermoelectric Power Factor of P3HT Vapour-Doped with F4TCNQ. *RSC Advances* **2018**, *8* (3), 1593–1599. https://doi.org/10.1039/C7RA11912G.

(229) Collins, B. A.; Gann, E. Resonant Soft X-Ray Scattering in Polymer Science. *Journal of Polymer Science* **2022**, *60* (7), 1199–1243. https://doi.org/10.1002/pol.20210414.

(230) Freychet, G.; Chantler, P.; Huang, Y.; Tan, W. L.; Zhernenkov, M.; Nayak, N.; Kumar, A.; Gilhooly-Finn, P. A.; Nielsen, C. B.; Thomsen, L.; Roychoudhury, S.; Sirringhaus, H.; Prendergast, D.; McNeill, C. R. Resolving the Backbone Tilt of Crystalline Poly(3-Hexylthiophene) with Resonant Tender X-Ray Diffraction. *Mater. Horiz.* **2022**, *9* (6), 1649–1657. https://doi.org/10.1039/D2MH00244B.

(231) Saurabh, K.; Dudenas, P. J.; Gann, E.; Reynolds, V. G.; Mukherjee, S.; Sunday, D.; Martin, T. B.; Beaucage, P. A.; Chabinyc, M. L.; DeLongchamp, D. M.; Krishnamurthy, A.; Ganapathysubramanian, B. CyRSoXS: A GPU-Accelerated Virtual Instrument for Polarized Resonant Soft X-Ray Scattering (p-RSoXS). arXiv September 26, 2022. https://doi.org/10.48550/arXiv.2209.13121.

(232) Reynolds, V. G.; Callan, D. H.; Saurabh, K.; Murphy, E. A.; Albanese, K. R.; Chen, Y.-Q.; Wu, C.; Gann, E.; Hawker, C. J.; Ganapathysubramanian, B.; Bates, C. M.; Chabinyc, M. L. Simulation-Guided Analysis of Resonant Soft X-Ray Scattering for Determining the Microstructure of Triblock Copolymers. *Mol. Syst. Des. Eng.* **2022**, *7* (11), 1449–1458. https://doi.org/10.1039/D2ME00096B.

(233) Litofsky, J. H.; Gomez, E. D. Connecting Soft X-Ray Anisotropy with Local Order in Conjugated Polymers. *MRS Communications* **2019**, *9* (4), 1168–1173. https://doi.org/10.1557/mrc.2019.119.

(234) McCulloch, B.; Ho, V.; Hoarfrost, M.; Stanley, C.; Do, C.; Heller, W. T.; Segalman, R. A. Polymer Chain Shape of Poly(3-Alkylthiophenes) in Solution Using Small-Angle Neutron Scattering. *Macromolecules* **2013**, *46* (5), 1899–1907. https://doi.org/10.1021/ma302463d.

(235) Nagai, M.; Huang, J.; Zhou, T.; Huang, W. Effect of Molecular Weight on Conformational Characteristics of Poly(3-Hexyl Thiophene). *Journal of Polymer Science Part B: Polymer Physics* **2017**, *55* (17), 1273–1277. https://doi.org/10.1002/polb.24389.

(236) Clark, J.; Chang, J.-F.; Spano, F. C.; Friend, R. H.; Silva, C. Determining Exciton Bandwidth and Film Microstructure in Polythiophene Films Using Linear Absorption Spectroscopy. *Appl. Phys. Lett.* **2009**, *94* (16), 163306. https://doi.org/10.1063/1.3110904.

(237) Yamashita, Y.; Tsurumi, J.; Ohno, M.; Fujimoto, R.; Kumagai, S.; Kurosawa, T.; Okamoto, T.; Takeya, J.; Watanabe, S. Efficient Molecular Doping of Polymeric Semiconductors Driven by Anion Exchange. *Nature* **2019**, *572* (7771), 634–638. https://doi.org/10.1038/s41586-019-1504-9.

(238) Murrey, T. L.; Riley, M. A.; Gonel, G.; Antonio, D. D.; Filardi, L.; Shevchenko, N.; Mascal, M.; Moulé, A. J. Anion Exchange Doping: Tuning Equilibrium to Increase Doping Efficiency in Semiconducting Polymers. *J. Phys. Chem. Lett.* **2021**, *12* (4), 1284–1289. https://doi.org/10.1021/acs.jpclett.0c03620.

(239) E, G.; B.a, C.; M, T.; J.r, T.; S, M.; H, A. Origins of Polarization-Dependent Anisotropic X-Ray Scattering from Organic Thin Films. *Journal of Synchrotron Radiation* **2016**, *23* (1), 219–227. https://doi.org/10.1107/S1600577515019074.

(240) Collins, B. A.; Cochran, J. E.; Yan, H.; Gann, E.; Hub, C.; Fink, R.; Wang, C.; Schuettfort, T.; McNeill, C. R.; Chabinyc, M. L.; Ade, H. Polarized X-Ray Scattering Reveals Non-Crystalline Orientational Ordering in Organic Films. *Nature Mater* **2012**, *11* (6), 536–543. https://doi.org/10.1038/nmat3310.

(241) Mukherjee, S.; Gann, E.; Nahid, M. M.; McAfee, T.; Herzing, A. A.; DeLongchamp, D. M.; Ade, H. Orientational Ordering within Semiconducting Polymer Fibrils. *Advanced Functional Materials* **2021**, *31* (28), 2102522. https://doi.org/10.1002/adfm.202102522.

(242) Su, G. M.; Patel, S. N.; Pemmaraju, C. D.; Prendergast, D.; Chabinyc, M. L. First-Principles Predictions of Near-Edge X-Ray Absorption Fine Structure Spectra of Semiconducting Polymers. *J. Phys. Chem. C* **2017**, *121* (17), 9142–9152. https://doi.org/10.1021/acs.jpcc.7b01353.

(243) Ferron, T.; Pope, M.; Collins, B. A. Spectral Analysis for Resonant Soft X-Ray Scattering Enables Measurement of Interfacial Width in 3D Organic Nanostructures. *Phys. Rev. Lett.* **2017**, *119* (16), 167801. https://doi.org/10.1103/PhysRevLett.119.167801.

(244) Nahid, M. M.; Gann, E.; Thomsen, L.; McNeill, C. R. NEXAFS Spectroscopy of Conjugated Polymers. *European Polymer Journal* **2016**, *81*, 532–554. https://doi.org/10.1016/j.eurpolymj.2016.01.017.

(245) Watts, B.; Swaraj, S.; Nordlund, D.; Lüning, J.; Ade, H. Calibrated NEXAFS Spectra of Common Conjugated Polymers. *J. Chem. Phys.* **2011**, *134* (2), 024702. https://doi.org/10.1063/1.3506636.

(246) Gann, E.; Collins, B. A.; Tang, M.; Tumbleston, J. R.; Mukherjee, S.; Ade, H. Origins of Polarization-Dependent Anisotropic X-Ray Scattering from Organic Thin Films. *J Synchrotron Rad* **2016**, *23* (1), 219–227. https://doi.org/10.1107/S1600577515019074.

(247) Wang, C.-H.; Mukherjee, S.; Maidul Islam, A. K. M.; Yang, Y.-W.; Mukherjee, M. Role of Interfacial Interaction in Orientation of Poly(N-Isopropylacrylamide) Chains on Silicon Substrate. *Macromolecules* **2011**, *44* (14), 5750–5757. https://doi.org/10.1021/ma200614w.

(248) O'Connor, B.; Kline, R. J.; Conrad, B. R.; Richter, L. J.; Gundlach, D.; Toney, M. F.; DeLongchamp, D. M. Anisotropic Structure and Charge Transport in Highly Strain-Aligned Regioregular Poly(3-Hexylthiophene). *Advanced Functional Materials* **2011**, *21* (19), 3697–3705. https://doi.org/10.1002/adfm.201100904.

(249) Spano, F. C. Modeling Disorder in Polymer Aggregates: The Optical Spectroscopy of Regioregular Poly (3-Hexylthiophene) Thin Films. *The Journal of chemical physics* **2005**, *122* (23), 234701.

(250) Spano, F. C. Absorption in Regio-Regular Poly(3-Hexyl)Thiophene Thin Films: Fermi Resonances, Interband Coupling and Disorder. *Chemical Physics* **2006**, *325* (1), 22–35. https://doi.org/10.1016/j.chemphys.2005.08.019.

(251) Ilavsky, J. Nika: Software for Two-Dimensional Data Reduction. *J Appl Cryst* **2012**, *45* (2), 324–328. https://doi.org/10.1107/S0021889812004037.

(252) Gann, E.; Crofts, T.; Holland, G.; Beaucage, P.; McAfee, T.; Kline, R. J.; Collins, B. A.; McNeill, C. R.; Fischer, D. A.; DeLongchamp, D. M. A NIST Facility for Resonant Soft X-Ray Scattering Measuring Nano-Scale Soft Matter Structure at NSLS-II. *J. Phys.: Condens. Matter* **2021**, *33* (16), 164001. https://doi.org/10.1088/1361-648X/abdffb.

(253) Kieffer, J.; Valls, V.; Blanc, N.; Hennig, C. New Tools for Calibrating Diffraction Setups. *J Synchrotron Rad* **2020**, *27* (2), 558–566. https://doi.org/10.1107/S1600577520000776.

(254) Bunău, O.; Calandra, M. Projector Augmented Wave Calculation of X-Ray Absorption Spectra at the ${L}_{2,3}$ Edges. *Phys. Rev. B* **2013**, *87* (20), 205105. https://doi.org/10.1103/PhysRevB.87.205105.

(255) Gougoussis, C.; Calandra, M.; Seitsonen, A. P.; Mauri, F. First-Principles Calculations of x-Ray Absorption in a Scheme Based on Ultrasoft Pseudopotentials: From $\ensuremath{\alpha}$-Quartz to High-${T}_{c}$ Compounds. *Phys. Rev. B* **2009**, *80* (7), 075102. https://doi.org/10.1103/PhysRevB.80.075102.

(256) Taillefumier, M.; Cabaret, D.; Flank, A.-M.; Mauri, F. X-Ray Absorption near-Edge Structure Calculations with the Pseudopotentials: Application to the K Edge in Diamond and $\ensuremath{\alpha}$-Quartz. *Phys. Rev. B* **2002**, *66* (19), 195107. https://doi.org/10.1103/PhysRevB.66.195107.

(257) Giannozzi, P.; Baroni, S.; Bonini, N.; Calandra, M.; Car, R.; Cavazzoni, C.; Ceresoli, D.; Chiarotti, G. L.; Cococcioni, M.; Dabo, I.; Corso, A. D.; Gironcoli, S. de; Fabris, S.; Fratesi, G.; Gebauer, R.; Gerstmann, U.; Gougoussis, C.; Kokalj, A.; Lazzeri, M.; Martin-Samos, L.; Marzari, N.; Mauri, F.; Mazzarello, R.; Paolini, S.; Pasquarello, A.; Paulatto, L.; Sbraccia, C.; Scandolo, S.; Sclauzero, G.; Seitsonen, A. P.; Smogunov, A.; Umari, P.; Wentzcovitch, R. M. QUANTUM ESPRESSO: A Modular and Open-Source Software Project for Quantum Simulations of Materials. *J. Phys.: Condens. Matter* **2009**, *21* (39), 395502. https://doi.org/10.1088/0953-8984/21/39/395502.

(258) Giannozzi, P.; Andreussi, O.; Brumme, T.; Bunau, O.; Nardelli, M. B.; Calandra, M.; Car, R.; Cavazzoni, C.; Ceresoli, D.; Cococcioni, M.; Colonna, N.; Carnimeo, I.; Corso, A. D.; Gironcoli, S. de; Delugas, P.; DiStasio, R. A.; Ferretti, A.; Floris, A.; Fratesi, G.; Fugallo, G.; Gebauer, R.; Gerstmann, U.; Giustino, F.; Gorni, T.; Jia, J.; Kawamura, M.; Ko, H.-Y.; Kokalj, A.; Küçükbenli, E.; Lazzeri, M.; Marsili, M.; Marzari, N.; Mauri, F.; Nguyen, N. L.; Nguyen, H.-V.; Otero-de-la-Roza, A.; Paulatto, L.; Poncé, S.; Rocca, D.; Sabatini, R.; Santra, B.; Schlipf, M.; Seitsonen, A. P.; Smogunov, A.; Timrov, I.; Thonhauser, T.; Umari, P.; Vast, N.; Wu, X.; Baroni, S. Advanced Capabilities for Materials Modelling with Quantum ESPRESSO. *J. Phys.: Condens. Matter* **2017**, *29* (46), 465901. https://doi.org/10.1088/1361-648X/aa8f79.

(259) Zhugayevych, A.; Mazaleva, O.; Naumov, A.; Tretiak, S. Lowest-Energy Crystalline Polymorphs of P3HT. *J. Phys. Chem. C* **2018**, *122* (16), 9141–9151. https://doi.org/10.1021/acs.jpcc.7b11271.

(260) Watts, B. Calculation of the Kramers-Kronig Transform of X-Ray Spectra by a Piecewise Laurent Polynomial Method. *Opt. Express, OE* **2014**, *22* (19), 23628–23639. https://doi.org/10.1364/OE.22.023628.

(261) Gann, E.; McNeill, C. R.; Tadich, A.; Cowie, B. C. C.; Thomsen, L. Quick AS NEXAFS Tool (QANT): A Program for NEXAFS Loading and Analysis Developed at the Australian Synchrotron. *Journal of Synchrotron Radiation* **2016**, *23* (1), 374–380. https://doi.org/10.1107/S1600577515018688.

(262) Nguyen, P. H.; Schmithorst, M. B.; Mates, T. E.; Segalman, R. A.; Chabinyc, M. Diffusion of Brønsted Acidic Dopants in Conjugated Polymers. *Journal of Materials Chemistry C* **2023**, *11* (22), 7462–7470. https://doi.org/10.1039/D3TC00415E.